PREPARATION AND PROPERTIES OF POLY-LACTIC ACID / NANO-HYDROXYAPATITE/GRAPHENE NANOCOMPOSITE BLEND FOR LOAD BEARING BONE IMPLANTS

FEVEN MATTEWS MICHAEL, BEng.

Thesis submitted to the University of Nottingham

for the degree of Doctor of Philosophy

OCTOBER 2016

ABSTRACT

Naturally, bones have a remarkable capacity to regenerate in case of minor injury and continuously remodel throughout an adult life. However, major injuries involving the load bearing bones, such as spine, hips and knee, require orthopaedic surgeries. These bone implants are made from biomaterials. As a result, this study investigates the use of biomaterials such as poly-lactic acid (PLA), nanohydroxyapatite (NHA) and graphene nanoplatelets (GNP) for applications related to bone implants.

In this study, NHA was synthesised using precipitation method assisted with ultrasonication. The process parameters (reaction temperature, ultrasonic time and amplitude) were optimised using response surface methodology (RSM) based on 3 factors and 5 level central composite design (CCD). Upon characterisation, the synthesised NHA was confirmed to mimic the HA present in the human bone both chemically and morphologically.

The synthesised NHA was then compounded with PLA matrix via melt-mixing by varying the NHA loading (1-5wt%). The impact strength of the PLA-NHA nanocomposites increased with NHA loading, attaining 21.6% enhancement in comparison to neat PLA. In contrast, the tensile strength and modulus of the PLA-NHA nanocomposites exhibited an initial increase of 0.7% and 10.6%, respectively, for 1wt% NHA loading, but deteriorated with the increasing NHA loading. The FESEM microstructures of the impact fractured samples also depicted agglomeration of NHA particles and poor interfacial adhesion between NHA and PLA. Hence, to improve the dispersion, NHA was surface modified (mNHA) using three different surface modifiers namely, 3-aminopropyl triethoxysilane (APTES), sodium n-dodecyl sulfate (SDS) and poly-ethylenimine (PEI). The FESEM analysis revealed an improved interfacial adhesion between PLA matrix and mNHA(APTES), which, enhanced the mechanical, thermal and dynamic mechanical properties of the PLA-5wt%mNHA(APTES). Meanwhile, mNHA(SDS) and mNHA (PEI) had no significant effect on interfacial adhesion, ultimately, failing to improve the properties of the PLA-5wt%mNHA(SDS) and PLA-5wt%mNHA (PEI), respectively.

GNP was added into the mNHA in order to further improve the properties of the PLA-5wt%mNHA(APTES) nanocomposite. With the addition of only 0.01wt% of GNP, the impact strength of the PLA-mNHA-GNP nanocomposite was increased by 22.1% (neat PLA) and 7.9% (PLA-5wt%mNHA(APTES)). Nonetheless, the tensile strength recorded a drop of 8.7% (neat PLA) and 9.7% (PLA-5wt%mNHA(APTES)). It is important to note the tensile strength obtained for the PLA-mNHA-GNP nanocomposite was within the acceptable limit of bone strength requirements.

Biocompatibility of the nanocomposites (PLA, PLA-NHA, PLA-mNHA and PLA-mNHA-GNP) was investigated using in-vitro analysis. The results show the MG63 cells adhere and grow well on the nanocomposites. Moreover, the nanocomposites encouraged the cells to proliferate and differentiate within 7 days and 21 days of incubation period, respectively. Thus, the in-vitro analysis evidenced the prepared nanocomposites were biocompatible with the MG63 cells. Finally, possible extensions and future works for these prepared nanocomposites as bone implants have been highlighted.

LIST OF PUBLICATIONS

Refereed journals

MICHAEL, F. M., KHALID, M., WALVEKAR, R., RATNAM, C. T., RAMARAD, S., SIDDIQUI, H. & HOQUE, M. E. 2016c. Effect of nanofillers on the physico-mechanical properties of load bearing bone implants. *Materials Science and Engineering: C,* 67, 792-806.

MICHAEL, F. M., KHALID, M., RATNAM, C., CHEE, C. Y., RASHMI, W. & HOQUE, M. 2016a. Sono-synthesis of nanohydroxyapatite: Effects of process parameters. *Ceramics International,* 42, 6263-6272.

MICHAEL, F. M., KHALID, M., RATNAM, C. T., RASHMI, W., HOQUE, M. E. & KETABCHI, M. R. 2016b. Nanohydroxyapatite synthesis using optimized process parameters for load-bearing implant. *Bulletin of Materials Science*, 1-13.

MICHAEL, F. M., KHALID, M., RATNAM, C. T., RASHMI, W., 2016. Effect of nanohydroxyapatite surface modification on the properties of polylactic acid nanocomposites. *Polymer Composites (accepted)*

Conference presentations

MICHAEL, F.M., KHALID, M., HOQUE, M.E., RATNAM, C.T., 2015. PLA/GNP/NHA- Application of Poly-lactic Acid Reinforced with Graphene Nanoplatelets and Nano-hydroxyapatite hybrids in Load Bearing Bone Implants. *5th International Conference on Nanotek and Expo, San Antonio, USA*.

MICHAEL, F.M., KHALID, M., RATNAM, C.T., HOQUE, M.E., 2015. Effect of Solvents on the Dispersion of Graphene Nanoplatelets in Nanohydroxyapatite for Load Bearing Body Implants. *2nd Edition Nanotech Dubai Conference & Exhibition, Dubai*

I dedicate this thesis to my loving and supportive parents,
Mr. Matthews Michael and Mrs. Brikti Berhane.

Thank you.

ACKNOWLEDGEMENT

TABLE OF CONTENTS

LIST OF FIGURES

xiii

LIST OF TABLES

LIST OF NOMENCLATURE

PLA	poly-lactic acid,
PGA	poly-glycolide acid,
PLGA	poly-lactic-co-glycolic acid,
PLLA	poly-L-lactic acid,
PPF	poly-propylene fumarate,
PE	poly-ethylene,
PEEK	poly-ether-ether ketone,
PSU	poly-sulphone,
UHMWPE	ultrahigh molecular weight poly-ethylene,
PS	poly-styrene,
PMMA	poly-methyl methacrylate,
PCL	poly-caprolactone,
EVA	ethylene-vinyl acetate copolymer,
MAPP	maleic anhydride grafted polypropylene,
PA-6	polyamide-6,
HDPE	high density polyethylene,
HDPE-HDMA	high density polyethylene – hexamethylene diamine,
PVA	poly-vinyl alcohol,
PP	poly-propylene,
PLA-g-AA	poly-lactic acid grafted acrylic acid,
PEI	poly-ethylenimine,
SDS	sodium n-dodecyl sulfate,
APTES	(3-Aminopropyl) triethoxysilane,
CNTs	carbon nanotubes,
MWNTs	multi walled carbon nanotubes,
SWNTs	single walled carbon nanotubes,
HA	hydroxyapatite,
nHA or NHA	nanohydroxyapatite,
Sr-HA	strontium-hydroxyapatite,
β-TCP	tricalcium phosphate,

MMT	montmorillonite clay,
GNP	graphene nanoplatelets,
TAIC	triallyl isocyanurate,
DGEBA	bisphenol A diglycidyl ether,
PI	propidium iodide,
MEM	minimum essential medium,
FBS	fetal bovine serum,
PBS	phosphate buffered saline,
pNPP	*p*-nitrophenyl phosphate,
HMDS	hexamethyldisilazane,
DMSO	dimethyl sulphoxide,
ECM	extracellular matrix,
MW	molecular weight,
CVD	chemical vapour deposition,
MFI	melt flow index,
OD	optical density
TGA	thermogravimetric analysis,
DSC	differential scanning calorimetry,
FESEM	field emission scanning electron microscope,
BET	Brunauer-Emmett-Teller,
XRD	X-ray Diffraction,
DOE	design of experiments,
CCD	central composite design,

CHAPTER 1

INTRODUCTION

1.1. Background study

In the 20th century, the average life expectancy was reported to have increased from less than 45 years in 1950 to more than 74 years (U.S. department of health and human service). This can be credited to the continuous improvement in the human healthcare provided nowadays, especially with the development of devices such as pacemakers, heart valves, aortic grafts and endovascular stent grafts and many more. Nonetheless, with respect to the human bones, this worldwide increase of human average age has raised the likelihood of the bones to fracture; to an average of twice in a lifetime. This is because with aging, bones, particularly the load-bearing bones like spine, hips and knee bones become prone to ailments. As a result, an increasing interest within the biomedical field to develop supports/scaffolds to restore the function of the damaged bone has arisen (Hutmacher 2001, Dhandayuthapani et al. 2011). These scaffolds are fabricated from biomaterials such as polymers, ceramics, metals and their composites. Thus, highlighting the role biomaterials play in improving the quality of human life and prolonging life in general (Teo et al. 2016).

It is important to note that the choice of biomaterial depends on the bone to be repaired or restored. For instance, load bearing bones, ligaments and articular cartilage require scaffolds that are capable of withstanding stresses. Also, another factor that can determine the choice of biomaterial is the interaction between the biomaterial and the human body. This means that, the biomaterial is required to be biocompatible with the body and be able to encourage bone healing or growth (Parchi et al. 2013).

So far, the biomaterials favoured for load bearing bone implants were prepared from metal-ceramic or metal-polymer due to the high strength of the metals. In the early 1960s, Sir John Charnley developed the first successful hip replacement from stainless steel and ultrahigh molecular weight polyethylene (UHMWPE) (Charnley 1960). Following this, a total knee replacement was developed between 1968-1972. However, these metal-based implants suffered from premature failure due to formation of wear particles or the accumulation

of corrosion products in the tissue surrounding the implant (Campbell et al. 2006). In other words, the inability of the metal-based implants to adapt to the biological environment caused the scaffold to crumple before the bone healed. As a result, the metal-based implants are required to be changed/replaced, reaching a revision rate as high as 10 percent in 10 years (Sargeant and Goswami 2006).

1.2. Problem statement

Considering the drawbacks of metal-polymer and metal-ceramic implants, the need for an improved novel biomaterial formulation has arisen. Individually, polymers have been used successfully in different medical related applications (pacemakers, heart valves and contact lenses), due to their ability to adapt to the biological environment (human body). Nonetheless, their strength has limited them for the load bearing implants related applications. Similarly, even though ceramics are bioactive materials with bone bonding ability, they also possess low tensile strength and fracture toughness, limiting their use in bulk form for load bearing implants. However, the combination of these two biomaterials (polymers and ceramics) is becoming the new choice for bone implant as it offer the advantages of avoiding the problem of stress shielding and also the elimination of the ion release problem of metal implants. Hence, nowadays researchers are investigating ways to overcome their individual limitations in order to develop polymer-ceramic composites that could meet not only the biocompatibility requirement, but also the strength required for the load bearing implants.

1.3. Scope of study

Preparation of nanofillers − first NHA will be synthesised via precipitation methods, assisted by ultrasonication. The optimised process parameters were determined using Design Expert® by designing a number of experiments. Central Composite Design (CCD) method will be carried out to optimise

experimental conditions for the preparation of NHA. Second, the NHA will further be surface modified using three materials; APTES, SDS and PEI, to get mNHA. The third nanofiller (mNHA-GNP nanohybrid) will be prepared by mixing the mNHA with GNP at different GNP loading. Finally, the nanofillers will be characterised using FTIR, XRD, FESEM, BET, and TGA.

Preparation of nanocomposite- the nanocomposites will be prepared via a series of processes; i.e. blending followed by injection moulding. Filler loading (NHA, mNHA and mNHA-GNP) will be varied to attain the preferred nanocomposite for load bearing bone implant application.

Characterisation of nanocomposites- the mechanical, thermal, and dynamic properties of the nanocomposite will be investigated. Tensile and impact strength of the nanocomposite will be the properties of interest. The thermal and viscoelastic including creep properties will be also analysed using TGA, DSC and DMA. Morphological analysis using FESEM will be carried out to study the dispersion pattern and matrix-nanofiller interfacial adhesion as well.

***In-vitro* analysis-** the upon identifying the best performing nanocomposites, the biocompatibility of the nanocomposites will be studied based on three *in-vitro* assays ; using human MG63 cells, an osteosarcoma cell line.

1.4. Aims and objectives

This study aims to develop a bio-mechanically stable nanocomposite by reinforcing PLA with nanofillers including (1) NHA, (2) surface modified NHA (mNHA) and (3) mNHA-GNP nanohybrid.

Therefore, the aim of this study is met by considering the following objectives:

   i.   To synthesis, optimise and characterise NHA.

  ii.   To assess the mechanical and surface morphological properties of PLA reinforced with NHA

iii.   To investigate the effect of surface modification of NHA in the mechanical, thermal, dynamical mechanical as well as the surface morphology of the PLA-mNHA nanocomposite.

iv.   To determine the influence of GNP addition into PLA-mNHA nanocomposite and analyse its mechanical, thermal, dynamical mechanical properties.

v.   To make a recommendation on biocompatibility of the nanocomposite.

1.5. Thesis outline

This thesis contains nine chapters and an appendix. The outlines of the chapters in the thesis are as follows:

Chapter 1- includes the background study, the problem statement, aims and objectives, scope and chapter outline of this study.

Chapter 2- presents a thorough review of the literatures related to the reinforcement of polymers with different nanofillers and their influence on the physico-mechanical properties and biocompatibility of the nanocomposites.

Chapter 3- details the materials and methodology employed in executing the experimental work of this study. Methods of synthesising the nanofillers as well as mixing and injection moulding of the nanocomposites along with characterisation have been detailed. Specific attention has been given to the mechanical, thermal, dynamic mechanical properties and *in-vitro* analysis of the nanocomposites.

Chapter 4- addresses the synthesis of NHA and the optimisation of the process parameter. Moreover, the thermal, chemical and morphological properties of the synthesised NHA were discussed.

Chapter 5- reports the reinforcement of PLA using the synthesised NHA. The change in mechanical and thermal properties of the nanocomposite in respect to NHA loading was described.

Chapter 6- addresses the surface modification of the NHA prior to reinforcing the PLA. The variation in mechanical, thermal and dynamic mechanical properties of the nanocomposites in respect to different surface modifiers used was discussed.

Chapter 7- addresses the reinforcement of PLA with mNHA-GNP nanohybrids and its effect on the properties of the nanocomposite was highlighted.

Chapter 8- reports the *in-vitro* analysis of the prepared nanocomposite. Particular attention was given to the MTT, ALP as well as the FESEM *in-vitro* analysis tests.

Chapter 9- concludes the main findings based on the aim and objectives of the study as well as make recommendation for future works.

1.6. Significance of the study

Global market for the orthopaedic implant is forecasted to reach USD 46.5 billion by 2017 (Rezler 2011). As Malaysia enters the next stage in its development, the manufacturing and health sector will need to play a prominent role in securing and enhancing the nation's prosperity. However, there had been sporadic development of Malaysia innovation on orthopaedic implants in the past years. To ensure the right balance of breadth and depth of coverage, the Healthcare National Key Economic Area (NKEA) support is developed for the whole ecosystem, from the Government policies including the Medical Device Act 2012. In 2011, the Malaysian statistics department reported Malaysia had exported orthopaedic implants worth RM 11.5 million (~USD 2.6 million). According to the Healthcare NKEA (2013), by 2020, the medical devices are projected to generate RM 35.3 billion (~USD 8 billion) incremental Gross National Impact (GNI) from the entry point projects (EPPs) and business opportunities on top of baseline growth and conduct 1,000 clinical trials, all of which will result in approximately 181,000 new jobs. Thus, this study will contribute to the body of knowledge for manufacturing implants locally.

CHAPTER 2

LITERATURE REVIEW

2.1. Introduction

This chapter presents a review of literature related to nanocomposites that could potentially be used for load bearing bone implants. An overview of the human bones mainly the load bearing bones are discussed in section 2.2. The biomaterials and the preparation techniques for nanocomposites are highlighted in section 2.3. In addition, the dispersion modification techniques are also discussed in section 2.5. Finally, specific focus is given to the effects of nanofillers loading and the preparation techniques on the physico-mechanical and biocompatibility properties of the nanocomposites in sections 2.6 to 2.8. A review based on this chapter has been published as "effect of nanofillers on the physico-mechanical properties of load bearing bone implants" (Michael et al. 2016).

2.2. Bones

Bones are complex connective tissues that are continuously torn down and replaced by biological remodelling. There are mainly two types of bones: cortical (about 80% of the total skeleton present in the body) and cancellous bone (the remaining 20% of the skeleton). The cortical forms the outer wall of all the bones whereas the cancellous is found in the inner part of bones. At the molecular/primary level, bones can be considered as a composite material consisting of inorganic mineral chiefly calcium phosphates along with other organic proteins (Datta et al. 2005). These proteins are made of 85-90% of collagen while the remaining percentage is non-collagenous in nature (Currey 2013). They are strengthened by the extremely dense filling surrounding of calcium phosphates mainly hydroxyapatite (Habibovic et al. 2010). In other words, presence of collagen contributes to the bone flexibility whereas the calcium phosphates (CaP) contributes to the bone strength (Wang et al. 2010). By varying the compositions of collagen and calcium phosphates, the flexibility and strength properties of bones can be balanced.

Moreover, presence of water in the bone is also an important determinant factor in the mechanical behaviour of the bones, as hydrated bones tend to have lower strength and higher flexibility (Lee et al. 2012). It is important to note that, bone

strength refers to its ability to withstand force (pulling or pushing) whereas flexibility is its ability to stretch without being deformed. Hence, bone strength is measured in terms of compressive/tensile strength and flexibility is measured by the elasticity. Table 2.1 compares the compositions of cortical and cancellous bones and their respective strength and elasticity. From the table, it can be observed that in spite of cortical bone having almost similar composition and elasticity with cancellous bone, the strength of cortical bone is ~85% greater than cancellous. This is due to cortical bone being more dense and solid with 5-30% porosity compared to cancellous bone which is spongy type and has porosity of 70-95% (Keaveny et al. 2004). This indicates that bones strength not only depends on its composition but also on bones mass, geometry and microstructure (Clarke 2008).

Generally, bones possess high compressive strength of 170MPa, but low tensile strength of 104-121MPa and very low shear stress strength of 51.6 MPa (Turner et al. 2001). In other words, bones are likely to fail due to tensile loading compared to compressive loading. Thus, in the case of bone failure, the bones have the ability to self-heal or remodel.

Table 2.1: Bone composition and mechanical properties

Type of Bone	Composition (wt%)			Mechanical Properties		Reference
	Protein	CaP	Water	Strength (MPa)	Elasticity (GPa)	
Cortical	28	60	12	50-150 (T) 70-200 (C)	3-30	(Currey 1998, Mozafari et al. 2010)
Cancellous	26	54	20	0.1-30 (T) 4-12 (C)	0.02-0.5	(Keaveny 1998, Mozafari, Rabiee et al. 2010)

T= Tensile strength; C= compressive strength

However, with time, increased remodelling of damaged bone often leads to a decrease in bone mass density due to increase in porosity which tends to cause an imbalance between the bone loss and gain, leading to bone deterioration. However, most of the bone damages in the body are commonly caused by a progressive bone disorder known as osteoporosis (Bono and Einhorn 2003). In osteoporosis, the bone tends to decrease in mass and density, ultimately making the bone prone to fracture. The most common targeted sites are around hips, spine, knee and wrist. These bones are referred to as the load bearing bones as

they carry most of the body's load. Aside from osteoporosis, these load bearing bones can also be damaged from injuries sustained or failure due to fatigue. Based on the biomechanical studies, knee joint consistently undergoes estimated maximum joint compressive forces of 4 to 4.5 times body weight during daily activities (Jang et al. 2009). This range of values has become a design criterion for most currently used knee prostheses. Nonetheless, recent studies have indicated that loading can be much higher even during level walking. This finding is consistent with the increasing incidence of reports on severe wear in joint replacements; in which the most destructive wear process has been found to be is fatigue, which occurs through repeated high loads and cyclic stressing (Liebschner and Wettergreen 2003). This load is dependent both on physical activity and body weight.

Considering the importance and the impact of damaged load bearing bones can cause to vital functioning of the human health, scaffolds mainly meant for load bearing applications are required. Thus, the need to bring forth the field of *tissue engineering* where the knowledge of science and engineering is combined to regenerate tissues/organs using scaffolds and living cells (Nerem and Sambanis 1995). Tissue engineering aims to develop tissue substitutes that could mimic the structure and properties of the damaged tissue to be replaced (Navarro et al. 2008). Figure 2.1 shows parts of the load bearing bones that can be replaced in case of damage. For instance, scaffolds are developed for the broken femur around the hips (Figure 2.1(a)), or articular cartilage in the knee (Figure 2.1 (b)) or the intervertebral disk found between vertebra of the spine or the facet joints (Figure 2.1 (c)). This can be done through three possible approaches, (1) substituting the cells that supply a needed function (Yaszemski et al. 1996); (2) delivering the tissue-inducing substances such as growth factors (GF) to a targeted location (Tabata 2003); and (3) by growing cells in a three-dimensional (3D) scaffold (Seitz et al. 2005). The first approach deals with replacing the damaged cell with new one while the second approach adds growth factors; which are naturally occurring substances capable of stimulating cellular growth, proliferation, healing and cellular differentiation. The third approach on the other hand requires fabrication of 3D scaffold from biomaterials that encourage cell growth. Generally, the first two approaches are

more suited for smaller and well-contained damages whereas the last one is applicable for generating a larger tissue blocks with pre-designed shapes.
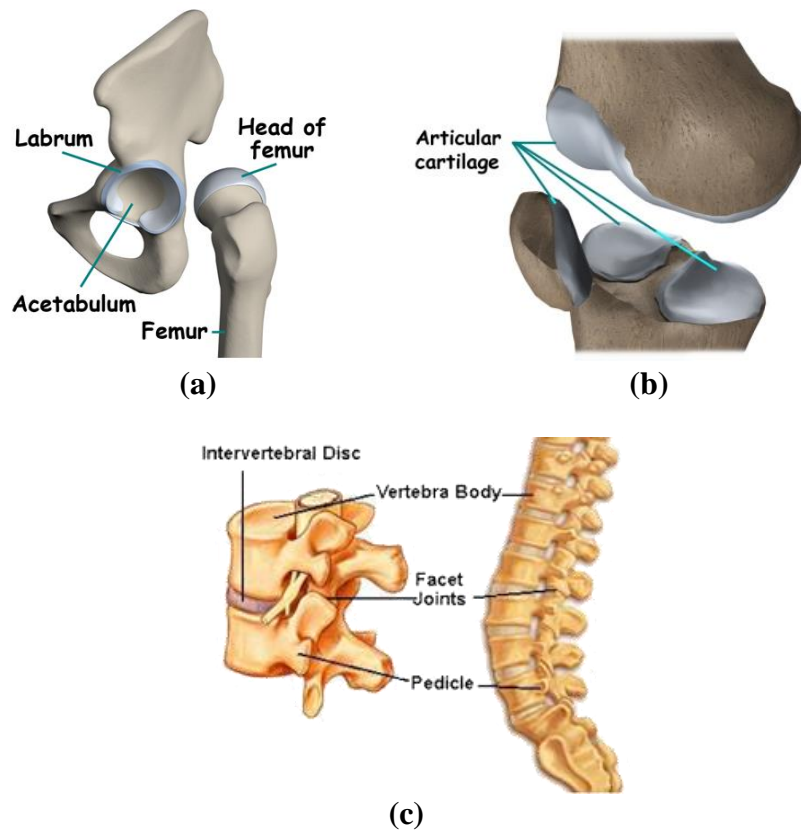
Figure 2.1: Types of load bearing bones (a) hip, (b) knee and (c) spine

The properties of the scaffolds, mainly the mechanical properties are greatly affected by several microstructural parameters such as: (1) properties of the matrix; (2) properties and distribution of the fillers in the matrix; (3) the interfacial bonding between the filler and matrix; (4) techniques used to prepare the scaffold (Fu et al. 2008). The understanding of mechanical properties of scaffolds is an important aspect in establishing a balance between the strength and elasticity, especially when dealing with load bearing bone implants. Recent designs have been unsuccessful to produce a scaffold that is able to stay feasible throughout the period from implantation to the last stage of the healing under load-bearing conditions (Guarino et al. 2007). Thus, failing to fulfil the aim of an optimised and restructured bone architecture that is as efficient and stable as the original bone (Liu and Ma 2004). Therefore, to improve this limitation, many researchers are studying on the effect of reinforcement of the composite

with nanofillers. As a result, this review focuses mainly on load bearing bone implants prepared from polymers reinforced with nanofillers. Furthermore, the effect of nanofillers dispersion into the polymer matrix and its effect on the physio-mechanical and thermo-physical properties of load bearing bone implants are also discussed thoroughly.

2.3. Biomaterials used for Load Bearing Bone Implants

2.3.1. Categories of biomaterials

Biomaterials are synthetic materials mainly used to make devices that are meant to replace a part of living system due to their unique biocompatibility such as scaffolds used as load bearing implants. The most common classes of biomaterials used are metals, ceramics and polymers. These three biomaterials can be used either individually or in combination known as composite, for bone implant applications (Li et al. 2013, Mahyudin et al. 2016). Table 2.2 summarises the advantages and disadvantages of these biomaterials and their application in tissue engineering. However, in this chapter, more attention is given to polymers, ceramics and polymer-ceramic composites. In addition, the biomaterials especially used for load bearing implants are expected to be:

- **Biocompatible:** should be able to co-exist and not harm the cells and tissues
- **Biodegradable:** should readily degrade and allow the bone to regenerate and heal.
- **No immune rejection:** biomaterials should not provoke an immunological reaction in the body.
- **Mechanical properties:** must be strong enough to function properly from the implantation time to the completion of the regeneration process.

Table 2.2: Classification of Biomaterials

Biomaterial	Advantages	Disadvantages	Applications	Example
Metals and Alloys	Strong, tough, ductile	Dense, may corrode, difficult to make	Load-bearing bone implants, dental restoration, etc.	Nanostructured titanium and Ti-6Al-4V alloys
Ceramics	Bioinert, bioactive, bioresorbable, high resistance to wear, corrosion resistance	Brittle, low toughness, not resilient	Low weight bearing bone implants, dental restoration, tissue scaffolds, bone drug delivery, etc.	Nanoclay, HA, TCP
Polymers	Flexible, low density, resilient, surface modifiable, chemical functional groups	Low stiffness, may degrade	Tissue scaffolds, drug delivery, breast implant, sutures, skin augmentation, blood vessels, heart valves, etc.	Collagen and PLLA nanofibers
Composites	Strong, design flexibility, enhanced mechanical reliability than monolithic	Properties may vary with respect to fabrication methodology	Tissue scaffolds, drug delivery, dental restoration, spinal surgery, load bearing bone implants etc.	HA-collagen, HA-PLA

2.3.1.1. Ceramics

Ceramics represent a wide class of biomaterials which can be categorised into three groups, bioinert (alumina and zirconia), bioactive (HA and bioglasses) and bioresorbable (tricalcium phosphate) ceramics. They are not mechanically tough to be used in bulk for large scale bone fracture; limiting their application in load bearing implants. In spite of this, their ionic bonding mechanisms make them favourable for osteoblast function; which is the production and secreting of matrix proteins and transport of mineral into the matrix. Osteoblast is a cell that secretes the matrix for bone formation. Due to this property, ceramics have found an application as a bioactive coating in bone tissue engineering (Zhou and Lee 2011).

As mentioned in section 2.2, bone is a composite of organic and inorganic materials consisting of collagen fibres and calcium phosphates, respectively. Among the calcium phosphates (CP) present in bone, dicalcium phosphate dehydrate (DCPD), tricalcium phosphate (TCP), tetracalcium phosphate (TTCP), octacalcium phosphate (OCP) and hydroxyapatite (HA) have been

studied for application in the medical fields. Mainly TCP (resorbable material) and HA (bioactive ceramic), are used as bone-substitute materials due to their ability to induce bone formation on their surface (Koutsopoulos 2002, Ramay and Zhang 2003, Parhi et al. 2004, Marchi et al. 2007). Moreover, HA is osteoconductive, non-toxic and non-immunogenic (Murugan and Ramakrishna 2005). Despite of HA being an integral bone material, the application of pure HA is very limited due to its property of brittleness (He et al. 2008). Other than HA, the other bioactive ceramic is bioglass which is composed of SiO_2, CaO, Na_2O, P_2O_5. Bioactive glasses are covered with a double layer of silica gel and apatite; this in turn promotes adsorption and concentration of protein used by osteoblasts to form a mineralised extracellular matrix (ECM) (Narang and Chava 2000).

2.3.1.2. Polymers

Polymers are the largest class of biomaterials, which are being extensively studied in medical applications. This is due to their unique properties like viscosity, malleability, moldability and their mechanical strength that is comparable with many soft tissues in the body (Park and Webster 2005). Unlike metals, polymers have excellent friction properties, and have been used as the main components of the orthopaedic joint replacements (Fang et al. 2006). These polymers are either natural or synthetic. In Table 2.3, the applications of some natural and synthetic biodegradable and non-biodegradable polymers are mentioned.

Natural polymers (collagen and chitosan) are usually abundant, biodegradable and offer good biocompatibility. Collagen is one of the components of the human bone as mentioned in section 2.2, whereas chitosan is a biodegradable, biocompatible and nontoxic natural polymer with high strength (Dash et al. 2011). As results, these natural polymers have attracted considerable attention as wound healing agents (Kumar 2000).

Synthetic polymers (biodegradable and non-biodegradable) are human-made polymers. The non-biodegradable polymers like poly methyl methacrylate (PMMA), poly ether ether ketone (PEEK) and ultra-high molecular weight polyethylene (UHMWPE) have been heavily studied due to their excellent

properties (Navarro et al. 2008). For instance, PMMA is a biocompatible material and also the principal material ingredient of bone cement. In spite of PMMA suffering from fatigue related cracking or impact induced breakage, it can still be used to strengthen a weakened vertebral disc (spine) (Polikeit et al. 2003). UHMWPE on the other hand, has unique properties like high abrasion resistance, low friction and high impact strength. This makes UHMWPE favourable for acetabular (hip), tibia (knee) and intervertebral disc (spine) applications (Kurtz et al. 1999). More recently, scientists have been focusing on PEEK, a hard radiolucent plastic that has bone-like mechanical properties. The clear transparent nature of PEEK, allows the doctors to accurately place the scaffold and helps in easy monitoring of the healing process of the patient through imaging methods such as X-ray (Ventura et al. 2014). As a result, PEEK can be used to manufacture implants for cervical vertebrae (spine). Other synthetic polymers such as nylon 6 (PA 6) (Das et al. 2003), polyvinyl chloride (PVC) (Paul and Sharma 2006), poly caprolactone (PCL) (Kim et al. 2004), polypropylene (PP) (Liao et al. 2013), and poly vinyl alcohol (PVA) (Kim et al. 2008) have been used for bone implants as well.

Another group of synthetic polymers that have attracted attention in the tissue engineering application are biodegradable polymers; in particular polyesters like polyglycolide acid (PGA), polylactic acid (PLA) and poly lactic-co-glycolic acid (PLGA) (Rezwan et al. 2006). In contrast to metals or ceramics, these biodegradable polymers minimise the times of surgery one has to undergo through degradation of the polymers into biocompatible products such as carbon dioxide and water. This happens due to the polyesters containing ester functional group in their main chain, which allows them to degrade into natural products. However, this degradation process is greatly affected by temperature, as the reaction is reversible and can be accelerated by heat. As a result, the thermal stability of the biodegradable polymers (polyesters) is the key factor that limits their applications (Armentano et al. 2010).

Table 2.3: Different types of polymer and their application

Polymers	Application
PMMA, PVA, PLGA, collagen	Ophthalmic (Intraocular lenses, contact lenses)
PLA, PGA, PGLA, PLGA	Liver
PLGA, PGA, collagen	Nerve (Hydrocephalus shunts)
PCL, PE (UHMWPE), collagen, PGA, PGLA, nylon-6	Skin (Facial and hip prostheses, artificial skin)
PMMA, PEEK, nylon-6, PP, HA, PGA, PLLA, PGLA-HA fibres, PCL	Orthopaedic and cartilage (Bone cement for fracture fixation, sutures, bone repair)
PE, PGA	Heart (Heart valves, artificial heart, ventricular assist devices, pacemaker leads)
PU, PGA, PLA, PGLA, PVC, collagen	Vascular graft (Blood substitutes)
PCL, PLA	Stem cells
PLA, PGA, PLGA	Drug delivery systems

2.3.1.3. Composite

Composite biomaterials are designed by mixing two or more biomaterials in order to have enhanced properties of the individual biomaterial. To date, the conventional composites made from ceramic/metal have failed before the completion of the healing process of the damaged bone. This is due to the weak link between the metal and the ceramic (Bonfield et al. 1981, Custers et al. 2009). The other challenge with the metal-alloy/ceramic implants is their durability. Considering that the lifespan of bone implants ranges only about 10-12 years, at least one revision surgery will be required years (Sargeant and Goswami 2006). However, the second replacement of the implant becomes very difficult for elderly patients and impossible in case of spine, hips and knee joint.

Recently, the use of composite made from polymer matrix and ceramic filler is becoming the new material of interest for load bearing implant (Hutmacher et al. 2007). This is because the strength of the polymer matrix is improved to mimic the natural bone properties by reinforcing them with ceramic fillers. Moreover, these composites offer the advantages of avoiding the problem of stress shielding and the elimination of the ion release caused by the metal implants. Therefore, from this point on, this review will focus mainly on how

to overcome the drawbacks of the polymers discussed in section 2.3.1.2., and explore their application as load bearing bone implants.

2.3.2. Nanofillers and their Synthesis

With the introduction and advancement of nanotechnology in the recent years, it has become possible to enhance the composite by reinforcing the polymer matrix by nanofillers. Nanofillers improve the strength, wear resistance, optical and conductive properties of the composites. This is due to the large surface to volume ratio of the nanofiller which further contributes in increasing the number of filler-polymer matrix interactions (Pradhan et al. 2013). Generally, these nanofillers are categorised into three groups: fibre or tube nanofiller (carbon nanotubes (CNTs), diameter <100nm), plate-like nanofillers (hydroxyapatite (HA), nanoclay and bioactive glasses, thickness 1nm) and 3D nanofillers (metallic fillers, any dimension <100nm). As ceramic fillers such as CNTs, HA, nanoclay and bioactive glasses are biocompatible with the human body, they will be discussed from this point on.

CNTs are long cylinders of 3-coordinated carbon having mechanical properties measured in the gigapascals with a high surface area (Fischer 2006). For this reason, CNTs mainly single walled carbon nanotubes (SWNT) and multi walled carbon nanotubes (MWNT) are used to reinforce the polymer matrix and improve the mechanical properties of the composite. SWNTs consists of one cylindrical nanotube, whereas MWNT comprises of many nested cylinders. The most promising technique to synthesis large scale MWNT is via chemical vapour deposition (CVD) (Andrews et al. 2002). On the other hand SWNTs can be synthesised through electric arc (Journet et al. 1997), laser ablation (Gorbunov et al. 1999), CVD (Kong et al. 1998) and catalytic pyrolysis of n-hexane (Zhu et al. 2002).

Hydroxyapatite is another nanofiller that can be used to reinforce polymers for load bearing implants. This is because of its bioactive and biocompatible nature which also happens to be a major constituent of the inorganic segment of human bone (Rezwan et al. 2006). HA has proven to be more effective in nanoscale compared to microscale. Therefore, researchers have used different methods to

synthesis HA via wet-chemical (Wang et al. 2010), solid-state (Pramanik et al. 2007), hydrothermal (Liu et al. 1997) and mechanochemical (Rhee 2002). Furthermore, nanoclays which are nanoparticles layered with mineral silicates can be used to reinforce polymers. Based on their chemical composition and morphology, nanoclays can be classified into montmorillonite, bentonite, kaolinite, hectorite and halloysite. Organoclays, a mixture of organic and inorganic nanomaterials is preferable for applications which include rheological modifiers, gas absorbents and drug delivery carriers. Last but not least, bioactive glasses used as nanofillers are categorised by their fast formation of a hydroxycarbonate apatite layer on their surface that encourages their bond formation to the bone apatite. So far, researchers have found sol-gel method (Rámila et al. 2002) produced a more nanostructured and bioactive compound compared to those prepared through melt method (Unnikrishnan et al. 2011). Recently, Kaur *et. al*. (2014) has conducted a thorough review on the use of bioactive glasses in bone implants.

2.3.3. Preparation of Nanocomposites

Nanocomposites are designed from two or more biomaterials; with at least one of it being nano in size. The ability of the nanocomposites to adapt to a specific orthopaedic application makes them attractive for load bearing implants, chiefly because of their mechanical properties and biocompatibility. In other words, nanocomposites are "biomechanically compatible" with the host tissue and do not crumple during patient's normal routine (Amini et al. 2012). Moreover, the mechanical properties are greatly affected by the technique used to prepare the nanocomposite which will be discussed further in section 2.6.

Table 2.4 presents collection of different nanocomposites prepared through different techniques. From the table, the most common technique used is melt-mixing. Melt-mixing involves blending, compounding, twin-screw extrusion, followed by moulding either by injection moulding or compression moulding. Melt-mixing is operated at the melting temperature of polymer matrix. This is to melt the polymer and increase the viscosity in order to allow the nanofiller to disperse within the polymer matrix. Some of the nanocomposites prepared through melt-mixing include PA 6-nanoclay-glass (Akkapeddi 2000), MAPP-

nanoclay (Ling et al. 2003), PA 6-MWNT (Liu et al. 2004, Zhang et al. 2004), UHMWPE-HA (Fang, Leng et al. 2006) and EVA-MWNT (K.A. Dubey 2009).

Self-assembly technique is also one of the techniques used to prepare a well-defined multilevel nanostructure by assembling block of polymers and nanofillers into hierarchical structures spontaneously (Liao et al. 2007, Jiao et al. 2015). Other techniques used to prepare nanocomposites include electrodeposition (Sen et al. 2004, Hudson Zanin 2013), compacting and sintering (Batra 2010), in-situ polymerization (Saeed and Park 2007), wet casting (Paiva et al. 2004, Ismail Zainol 2008, Wang et al. 2008), co-precipitation (Ramírez et al. 2005) and freeze granulation (Jiang et al. 2008, Singh et al. 2008). To date, thorough reviews have been made on the preparation of nanocomposites and their characterisation (Chronakis 2005, Hussain et al. 2006). However, in this research, special focus was given to the effect of these techniques on the physico-mechanical properties of the nanocomposites.

2.4. Dispersion of Nanofillers in Polymer Matrix

It is important to understand the meaning behind dispersion and agglomeration and how these two influence the properties of the nanocomposite. Dispersion is a process of creating a liquid in which discrete particles are homogeneously distributed throughout a continuous fluid phase and breaks down the agglomerates into their principal component particles. Agglomeration on the other hand is the assemblages of particles by relatively weak forces such as van der Waals or electrostatic forces (Taurozzi et al. 2011). Both dispersion and agglomeration have crucial role in influencing the physico-mechanical properties of the nanocomposites which will be discussed in section 2.6.

Generally, the nanoparticles can be dispersed and the agglomerates can easily be broken apart into smaller particles using sonication; which is an act of applying sound energy to agitate the particles. The primary part of a sonication device is the ultrasonic electric generator. This device creates a signal (>20 kHz) that powers a transducer. This transducer converts the electric signal by using piezoelectric crystals, or crystals that respond directly to the electricity by

creating a mechanical vibration. This vibration, molecular in origin, is carefully preserved and amplified by the sonicator, until it is passed through to the probe (Taurozzi, Hackley et al. 2011). As a result, many researchers have employed sonication to disperse nanofillers, as shown in Table 2.4 due to their availability and relatively inexpensive cost.

In addition to dispersion and deagglomeration techniques, the solvent used can also influence the dispersion of the nanofiller in the polymer matrix. For instance, its known that incorporating CNTs into a polymer matrix will improve the nanocomposite properties. However, the dispersion of CNTs in liquid mainly in water and organic solvents is difficult due to their chemical nature; where the CNTs molecules are held together in bundles by van der Waals force. As a result, some entanglement were observed in the scanning electron microscope (SEM) images of a PA-6 matrix reinforced with MWNTs dispersed in nitric acid (HNO_3) (Zhang, Shen et al. 2004). This was further complemented by another study (Liu, Phang et al. 2004). The entanglement and poor dispersion of these MWNTs in the polymeric matrix can be improved via chemical modification of the dispersant/solvent during the purification stage (Andrews, Jacques et al. 2002). Thus, upon chemically treating the MWNTs in HNO_3, the dispersion of MWNTs in PA-6 matrix was improved (Saeed and Park 2007).

In another study, the dispersion of SWNTs in epoxy matrix by using three organic solvents was reported [acetone, ethanol and dimethylformamide (DMF)] (Lau et al. 2005). In here, SWNTs were dispersed as bundles rather than fully isolated individuals whereby the SEM microscopy showed formation of no significant agglomerates as well as no homogenous dispersion of SWNTs in all solvents was observed. However, DMF solvent had the greatest unreacted epoxide functional groups detected from the Fourier transform infrared (FTIR) compared to ethanol and acetone. This in turn caused the mechanical and thermal properties of the epoxy/SWNTs to decrease, compared to the pure epoxy or epoxy/SWNTs dispersed in acetone or ethanol. Moreover, dispersing SWNTs using acetone solvent improved the thermal properties of the nanocomposite by acting as a heat sink to accelerate the heat absorption of the epoxy matrix.

Table 2.4: Techniques of synthesising nanofillers and preparing nanocomposites

Biomaterials	Nanofiller Synthesis	Dispersion method	Nanofiller Composition	Nanocomposite Preparation	Reference
Acrylic bone cement and MWNTs	Chemical vapour deposition		0.5–10 wt.% of MWNTs	Mixing, hot pressing and curing in air	(Marrs et al. 2006)
Chitosan and HA	Freeze-drying	Ultrasonically dispersed in deionised water	0-2 wt% of Nha	Mixing, lyophilisation, aseptic treatment and buffering	(Thein-Han and Misra 2009)
HDPE and HA	Chemical coupling and acrylic acid grafting		7-40 vol% HA	Silanation, blending, compounding, pelletizing, powdering and compression moulding	(Wang and Bonfield 2001)
PMMA and SWNTs	Laser ablation	Sonication dispersion in DMF	0.26 wt% of SWNTs	Melt mixing, drying, hot pressed, moulded, irradiation	(Muisener et al. 2002)
EVA and MWNT	Sol-gel		0-5 wt% of MWNTs	Melt mixing, compression moulding, cutting and irradiation	(K.A. Dubey 2009)
MAPP and nanoclay	Ion-modification of montmorillonite		0-50 wt% of nanoclay	Melt mixing, injection moulding, ultrathin sectioning	(Ling, Shing-Chung et al. 2003)
PMMA, HA and MWNTs	Freeze-granulation	Dispersed in distilled water and kept in Ultrasonication bath	0-1 wt% of MWNTs	Ball milling and drying	(Singh, Shokuhfar et al. 2008)
Water soluble chitosan and nHA in presence of glycerol	In laboratory	Mixed in distilled water and kept in ultrasonication bath	0-30 wt% nHA and 30 wt% glycerol	Mixing in water, mould and dry	(Ismail Zainol 2008)
PEEK and Sr-HA	Wet precipitation	Electronic blender	0-30 vol% of Sr-HA	Mixing, moulding, drying, cut	(Wong et al. 2009)
MAPP and HA	Wet precipitation		0-30 wt% of HA	Melt mixing, compression moulding, cut and irradiation	(Ramírez, Albano et al. 2005)
Chitosan, carboxymethyl cellulose and HA	In laboratory (Wang et al. 2002)		15-40 wt% of carboxymethyl cellulose	Mixing, freezing-drying	(Jiang, Li et al. 2008)

Collagen, HA and MWNTs	Chemical vapour deposition			Mixing and self-assembly	(Liao, Xu et al. 2007)
PEEK and HA	Wet precipitation		0-40 vol% of HA	Compounding, granulating and injection moulding	(Abu Bakar et al. 2003)
Bioactive glass and polysulfone			20 vol% of bioactive glass	Compression moulding	(Marcolongo et al. 1998)
Chitosan, gelatine and bioactive glass			0-70 wt% of bioactive glass	Stirring and freeze drying	(Gentile et al. 2012)
Reduced graphene oxide and HA		Immersed in DMF and dried for 2 hrs		Direct electrodeposition	(Hudson Zanin 2013)
Bioglass and HA			2-10 wt% of bioglass	Compacting and sintering	(Batra 2010)
PCL and bioactive glass	Electrospinning	Dissolved and stirred in THF for 24 hrs	10-30 wt % of bioactive glass	Stirring, dried and moulded	(Jo et al. 2009)
Magnetic mesoporous bioactive glass and carbon			0-10 wt% of Magnetic mesoporous bioactive glass		(Zhu et al. 2013)
Nylon 6 and MWNTs	Catalytic chemical vapour deposition		0-2 wt% of MWNTs	Melt compounding, compression moulding and quenching	(Liu, Phang et al. 2004)
Nylon 6 and MWNTs	Catalytic chemical vapour deposition		0-1 wt% of MWNTs	Melt compounding, compression moulding and quenching	(Zhang, Shen et al. 2004)
Nylon 6 and MWNTs	Thermal chemical vapour deposition	Sonicated for 2 hrs in HNO_3	0-7 wt% of MWNTs	In-situ polymerization including heating and mechanical stirring	(Saeed and Park 2007)
HDPE and MWNTs	Chemically treated	Sonicated for an hour in water	0-0.44 vol% of MWNTs	Heating and magnetically stirring	(Kanagaraj et al. 2007)
Epoxy and MWNTs	Thermal chemical vapour deposition	Dispersed in methanol under magnetic agitation	0-4 wt% of MWNTs	Mixing and injection moulding	(Allaoui et al. 2002)
Chitosan and MWNTs	Catalytic chemical vapour deposition	Dispersed in ultrasonic bath for an hour	0-2 wt% of MWNTs	Mechanical stirring, sonication and heating	(Wang et al. 2005)
PVA and MWNTs PVA and SWNTs	Arc discharge (SWNTs) and	Dispersed in water	10-20 wt% of CNTs	Wet-casting	(Paiva, Zhou et al. 2004)

	chemical vapour deposition (MWNTs)				
Polystyrene, polyurethane and SWNTs		Sonication dispersion in DMF for 4-5 hrs	0-1 wt% of SWNTs	Electrospinning/electrospraying	(Sen, Zhao et al. 2004)
PVA and SWNTs			0-0.8 wt% of SWNTs	Simple mixing,	(Liu et al. 2005)
PP and SWNTs	Arc discharge		0-1 wt% of SWNTs	Melt mixing, compression and cutting	(Manchado et al. 2005)
Epoxy and SWNTs	Arc discharge	Dispersed in ethanol and sonicated for 30 min	0.5-7 wt% of SWNTs	Solution casting, compression and cutting	(Wang, Dai et al. 2008)
Epoxy and SWNTs	Grinding bucky pearls	Dispersed in water and sonicated for 30-200 min.	0-39 wt% of SWNTs	Hot press moulding	(Wang et al. 2004)
Epoxy and SWNTs	Chemical vapour deposition	Dispersed in acetone, ethanol or DMF for an hr	0.5 wt% of SWNTs	Cast in a PP mould and cured	(Lau, Lu et al. 2005)
Chitosan and nHA	In laboratory in presence of 2 vol% of acetic acid		5-10 wt% of nHA	Casting, moulding, soaked in water for 8 hrs and air-dried	(Hu et al. 2004)
UHMWPE and HA	Wet precipitation	Dispersed on paraffin oil	0-50 wt% of HA	Compounded, hot-pressed and cut	(Fang, Leng et al. 2006)
PMMA and nanoclay	Modified by cloisite 20A via ion exchange reaction	Dispersed in toluene and sonicated in ultrasonic bath for an hr	0-2 wt% of MMT	Co-precipitation method or blending and compression method	(Fu and Naguib 2006)
PMMA and nanoclay	Modified by cloisite 10A, cloisite 30B, cloisite 93A		3-5 wt% of nanoclays	Mixing, compression moulding, cutting	(Unnikrishnan, Mohanty et al. 2011)
PMMA epoxy and nanoclay	Modified by cloisite 30B		0-30 wt% of nanoclay	Stirring, drying and internal mixing	(Park and Jana 2003)

DGEBA based epoxy resin and nanoclay	Modified by Na$^+$ or 30B or I.30E or CFC	Mechanically stirred for 2 hrs	2-10 wt% of nanoclay	Drying, blending, moulding and curing	(Qi et al. 2006)
Chitosan, polygalacturonic acid and nanoclay	Wet precipitation (HA) Modified by Na$^+$ (nanoclay)	Dispersed in deionised water by sonicator	ChiPgA (0 wt% HA + 0 wt% clay), ChiPgAHAP (20 wt% HA + 0 wt% clay), ChiPgAMMT (0 wt% HA + 10 wt% clay) ChiPgAHAPMMT (20 wt% HA + 10 wt% clay)	Freeze drying	(Ambre et al. 2010)
HDPE and nanoclay	Modified with dimethyl dialkyl ammonium		4 wt% of nanoclay	Mixing by twin crew extruder and injection moulding	(Tanniru et al. 2006)
Agarose and nanoclay	Modified with Na$^+$	Dispersed in distilled water and sonicated for an hr	0-80 wt% of nanoclay	Gelation method	(Li et al. 2005)
Phenolic resin and nanoclay			0-8 wt% of nanoclay	In-situ polymerization and compression moulding	(Pappas et al. 2005)
Polyamide-6, glass fibre and nanoclay	Organo modified montmorillonite		10-15 wt% of glass fibre 2-5wt % of nanoclay	Melt compounding	(Akkapeddi 2000)

In another research conducted, the effect of particle size on the dispersion of the fillers within the polymer matrix was considered (Takayama et al. 2009). In this study, HA (micro, nano and bimodal sizes) was dispersed in poly L-lactic acid (PLLA) matrix. The micro HA showed good dispersion where no agglomeration could be seen compared to nano HA which showed many agglomerates up to a size of 50-300µm. This in turn indicated that nano HA agglomerates easily. When bimodal HA was used to reinforce the PLLA, reduced amount of agglomerates measuring to 10-20µm were observed (Takayama, Todo et al. 2009). In contrast to the agglomeration of particles, the mechanical properties of nano HA reinforced PLLA was higher compared to micro HA reinforced PLLA which will further be discussed in section 2.6. The microstructure of chitosan matrix reinforced with MWNTs and HA clearly show the homogeneous dispersion of MWNTs in the chitosan matrix compared to the HA (Wang, Shen et al. 2005, Pang and Zhitomirsky 2007). This suggested that MWNTs has a good interfacial interaction with chitosan compared to HA.

2.5. Nanocomposite Modification Techniques

The prime techniques used to modify the nanocomposites are through grafting and crosslinking, where the polymer chains are linked together chemically or induced by irradiation (Nielsen 1969). When the polymer chains are linked together, their ability to move freely decreases, becoming less flexible and harder. In other words, once the polymer matrix is cross-linked, the molecular movement is impended, making it stable against heat. This in turn improves the tensile strength and fatigue life of the nanocomposite. However, the polymer can end up degrading if irradiated at higher irradiation dosage. For instance, PLA matrix was seen to diminish with increasing irradiation dosage; indicating sample degradation (Malinowski et al. 2011). On the other hand, addition of crosslinking agent triallyl isocyanurate (TAIC) improved the degradation of PLA. Similarly, a nanocomposite of PP-HA showed decrease in its properties as a result of PP degradation during irradiation (Ramírez, Albano et al. 2005). In contrary, EVA reinforced with MWNTs improved when irradiated; inducing crosslink between the filler and matrix which in turn enhanced the interfacial

interaction between EVA and MWNTs (K.A. Dubey 2009). Apart from cross-linking, irradiation has the potential to enhance the curing, sterilisation and in modifying the surface of the nanocomposite. However, more studies need to be conducted regarding irradiated nanocomposites for load bearing implants.

The properties of the nanocomposites can also be modified using coupling reagent known as silane coupling agents. Silane coupling agents are compounds whose molecules contain functional groups that bond with both organic (polymer) and inorganic (nanofiller) biomaterials. These agents are used in forms of diluted aqueous solutions. The most effective method used to modify the nanocomposite is by treating the nanofillers with the silane coupling agent before they are being added to the polymer matrix. This can be done either by dry or wet treatment. In dry treatment, the silane is added and evenly dispersed in the nanofiller by a high speed stirring mixer whereas in wet treatment the nanofiller is immersed in a diluted silane solution. As a result, upon reinforcing polyurethane (PU) with surface treated MWNTs using 3-triethoxysilylpropyl amine (ESPA) through a wet treatment technique, the mechanical properties of the nanocomposite enhanced due to the improved dispersion of MWNTs in the PU matrix (Zhou et al. 2012).

2.6. Physico-Mechanical Properties

One of the most notable properties of nanoparticles is their extremely high strength which makes them attractive for structural applications where strength and weight are critical. The mechanical properties of scaffolds are determined not only on the structure and the material properties, but also the technique used to prepare the nanocomposite. Therefore, the key to building a successful design of scaffold for load bearing implants is to match the strength and elasticity of the scaffold to that of natural bone. This in turn gives the tissue enough time to heal without any mechanical failure of the scaffold. In this section, we will discuss how different types of nanofillers can enhance the mechanical properties of the nanocomposite such as tensile and compressive strength, toughness and hardness, young's modulus and bending modulus, as well as strain. Table 2.5 summarises the physico-mechanical properties of different

nanocomposites prepared by many researchers in comparison with human cortical and cancellous bones.

2.6.1. Mechanical Strength

As mentioned in section 2.2, the load bearing bones carry the load of the body. As a result, bones (cortical and cancellous) should possess a certain amount of strength in order to withstand the load. However, when the bone is damaged, the designed load bearing implant (scaffold) should have similar strength as the original bone. For this to happen, the biomaterial (polymer) needs to be reinforced with nanofiller that has excellent mechanical strength. This mechanical strength of the nanocomposite is determined using tensile and compressive strength as mentioned earlier.

2.6.1.1. Effect of filler loading

One of the fillers that can be used to reinforce polymers is carbon nanotubes (MWNTs and SWNTs), which have very high ratio of volume to surface area with an exceptional mechanical strength; making them an outstanding reinforcement material for nanocomposites (Singh, Shokuhfar et al. 2008). MWNTs have a bending strength and compression strength of 14 GPa, and 100 GPa, respectively (Muisener, Clayton et al. 2002). On the other hand, SWNTs have a tensile strength of ~50-200 GPa (Ren et al. 2003, Wang, Liang et al. 2004, Liu, Barber et al. 2005). Consequently, incorporating either MWNTs or SWNTs into different polymer matrices have proven to enhance the strength of the nanocomposite.

For instance, PMMA suffers from fatigue related cracking or impact induced breakage, thereby limiting its application in load bearing implants. In an attempt to correct this problem, PMMA was reinforced with 2wt% MWNTs contributing to its improvement in the flexural strength and flexural yield strength of PMMA by 12.8% and 13.1%, respectively (Marrs, Andrews et al. 2006). Further increase in MWNTs loading (5-10wt%) caused the properties to decrease due to MWNTs agglomeration, leading to inadequate dispersion of MWNTs in the PMMA matrix. In another work, a unique nanocomposite material containing PMMA/HA reinforced with 0.1wt% MWNTs was prepared

(Singh, Shokuhfar et al. 2008). This nanocomposite showed a homogenous dispersion of MWNTs and good interaction between the materials, attaining a suitable level of interfacial stress transfer. Below 0.1wt% MWNTs loading, the mutual interaction of MWNTs with the matrix is non-existent, leading to decrease in homogenous dispersion of MWNTs into PMMA-HA. On the other hand, MWNTs loading above 0.1wt% lead to decrease in strength due to MWNTs agglomeration. Therefore, by adding 0.1wt% MWNTs the hardness of the nanocomposite increased from 0.288GPa to 3.460GPa (Singh, Shokuhfar et al. 2008). Aside from PMMA, MWNTs showed good homogenous dispersion and strong interfacial interaction with the polymeric matrix such as chitosan (0.4wt% MWNTs) (Wang, Shen et al. 2005), nylon-6 (2wt% and 1wt% MWNTs) (Liu, Phang et al. 2004, Zhang, Shen et al. 2004) and epoxy (4wt% MWNTs) (Allaoui, Bai et al. 2002). As a result, the tensile properties increased with increase in MWNTs loading.

Same as MWNTs, SWNTs have excellent homogeneity and strong interfacial interaction with the polymeric matrix (Xie et al. 2005). Consequently, the mechanical properties of the polymers reinforced with SWNTs are seen to increase with increase in SWNTs loading. For example, the yield stress and tensile strength of PVA nanocomposite increased by 55% when reinforced with 5wt% SWNTs (Paiva, Zhou et al. 2004) and 45% when 0.8wt% functionalized SWNTs with multiple surface hydroxyl groups was used (Liu, Barber et al. 2005). Moreover, with addition of 0.01wt% ester functionalized SWNTs into PU matrix, the tensile strength was enhanced by 104% compared to pure PU (Sen, Zhao et al. 2004). Likewise, PP reinforced by 0.75wt% SWNTs nanocomposite showed yield strength improvement by 26.5% compared to pure PP nanocomposite (Manchado, Valentini et al. 2005).

Unlike CNTs, HA has low compressive strength of 6.5MPa (Li et al. 2005). In spite of that, incorporating HA into polymeric matrix can enhance the mechanical properties of the nanocomposite, and find application in load bearing implants. For instance, the properties of polymers like chitosan which are flexible with low mechanical properties compared to natural bone can be improved by incorporating with high a composition of HA. This was proven when chitosan was incorporated with 70wt% of HA and the compressive

strength of the nanocomposite increased to 120 MPa (Li, Yubao et al. 2005). Similarly, the mechanical properties of a three-dimensional scaffold consisting of HA, chitosan and carboxymethyl cellulose increased due to enhanced dispersion of HA in the polymer matrix (Jiang, Li et al. 2008). Generally, increasing HA loading showed an increase in the tensile properties of chitosan-HA nanocomposite, especially when using high molecular weight chitosan rather than medium molecular weight (Jiang, Li et al. 2008, Thein-Han and Misra 2009).

Nanoclay as a filler has the ability to align and produce barrier layers that allows it to easily disperse within the polymer matrix. As a result, tensile properties of polymeric matrix such as MAPP reinforced with 50wt% nanoclay was seen to increase by 120% (Ling, Shing-Chung et al. 2003). Similarly, PMMA reinforced with 0.5wt% nanoclay showed an increase in tensile strength by 54% (Fu and Naguib 2006). In contrast, increasing the nanoclay loading to 3.8wt% resulted in a decrease of the tensile strength of PMMA by 50% (Park and Jana 2003). Further incorporation of 20wt% epoxy to the PMMA-2wt% nanoclay nanocomposite resulted in the increase of tensile strength by 40% (Park and Jana 2003). However, bisphenol A diglycidyl ether (DGEBA) based epoxy reinforced with nanoclay showed decrease by 20% in tensile strength with an increase of nanoclay loading (Qi, Zhang et al. 2006). In all these nanocomposites prepared, with further increase in nanoclay loading, the mechanical strength of the polymeric matrix was seen to deteriorate due to increase in agglomeration of nanoparticles.

Bioactive glass has fairly high mechanical strength which decreases gradually under load-bearing conditions in the body (Kokubo 1991). Hence, when polymers were reinforced with bioactive glass, the mechanical strength was seen to increase. For instance, incorporating 1wt% nanoclay into the epoxy-bioactive glass nanocomposite contributed to 24% and 187% increase in mechanical strength compared to the epoxy-bioactive glass nanocomposite and pure epoxy, respectively (Haque et al. 2003). Similarly, PCL reinforced with 40wt% bioactive glass showed a 233% increase in the tensile strength (Yoo and Rhee 2004). In addition, gelatine reinforced with 50wt% bioactive glass showed a 100% increase in compressive strength (Mozafari, Rabiee et al. 2010).

2.6.1.2. Effect of preparation technique

Another factor that enhances the mechanical strength of the nanocomposite, is the technique used to prepare them. As mentioned in section 2.3.3 and summarised in Table 2.4, nanocomposites can be prepared mainly by melt-mixing, in-situ polymerization and hybridization, or wet-casting. Other techniques include ball milling, freeze drying, direct electrodeposition and electrospinning. These techniques help to improve the dispersion of the filler in the polymer matrix by either breaking down the agglomerates or by providing a better mixing method depending on the polymer matrix.

Nonetheless, the selection of the technique depends on the polymer and filler compatibility (Oliveira and Machado 2013). Melt-mixing is the most desirable technique; however, it poses a challenge in preparing a nanocomposite with uniform dispersion. In-situ polymerization on the other hand, is suitable for polymers, especially that are insoluble and thermally unstable, which cannot be processed through solution or melt-mixing (Coleman et al. 2006). For instance, chitosan being thermally unstable polymer has weaker interfacial bonding with HA when prepared by melt-mixing compared to in-situ. As a result, chitosan-HA nanocomposite prepared using in-situ hybridization showed an increase in tensile properties by 8%, whereas decreased by 15% when prepared using melt-mixing technique (Hu, Li et al. 2004). In contrast to chitosan, Nylon-6 which is a thermally stable polymer, showed an increase in tensile strength by 162% (Liu, Phang et al. 2004) and 123% (Zhang, Shen et al. 2004) when reinforced with MWNTs using melt-mixing technique, and 27% increase when prepared by in-situ polymerization technique (Saeed and Park 2007).

Other technique like ball milling, a mixing process with intensive stirring of the powder was found to effectively break the agglomeration of the filler. This in turn, increases the surface area and favours interfacial interaction between the filler and polymer matrix, which enhances the mechanical properties of the nanocomposite. Here, to avoid re-aggregating of the filler in the matrix, ethanol is used as a dispersant to generate a homogenous dispersion. Thus, UHMWPE matrix reinforced with HA dispersed in ethanol through ball milling technique reported increase in the yield strength of by 50% (Fang et al. 2005). Similarly,

electronspinning technique improves the dispersion of the filler in the polymer matrix by depositing the filler on the electrostatically stretched polymer. As a result, the tensile strength of electrospinning prepared PU-SWNTs nanocomposite was reported to increase by 46% (Sen, Zhao et al. 2004). Lastly, wet-casting technique is a technique used to prepare a nanocomposite by dissolving the polymer and dispersing filler in the solutions, consequently SWNTs were homogenously dispersed in PVA dissolved in water and increase in the tensile strength by 55% was reported (Paiva, Zhou et al. 2004).

2.6.2. Elasticity

Human bones are hard but at the same time are elastic to some extent. Polymers, however, are too elastic (rubbery like) limiting their application in load bearing implants. However, when reinforced with ceramic fillers, the elasticity reduces. In other word, the nanocomposite becomes stiffer and less elastic. The elasticity of the nanocomposite can be determined using Young's modulus, compressive modulus and shear modulus. The relationship between elasticity and modulus properties is inversely proportional, where increase in modulus properties reduces the elasticity nature of the nanocomposite. This is favourable as long as the reduction in elasticity is within the range of cortical (3-30 GPa) and cancellous (0.02-0.5 GPa) bones.

2.6.2.1. Effect of filler loading

CNTs are ceramic materials and have a brittle nature. The young' modulus of MWNTs is 200-4000 GPa (Muisener, Clayton et al. 2002) and SWNTs have a tensile modulus and young's modulus, ~1TPa and 800 GPa, respectively (Ren, Li et al. 2003, Wang, Liang et al. 2004, Liu, Barber et al. 2005). Furthermore, as mentioned in section 2.3.1.1, HA is also ceramic material with brittle nature. So, when these fillers (CNTs and HA) are added to the polymer, the elasticity of the nanocomposites is always seen to decrease with increase in filler loading. Similarly, the elasticity of polymers was found dependent on the amount of nanoclay and bioactive glasses were added, where the elasticity of the nanocomposite decreased with further addition of the nanofillers. This is due to

increase in restriction to the mobility of polymer chains caused by the increased loading of filler (Paiva, Zhou et al. 2004, Liu, Barber et al. 2005, Unnikrishnan, Mohanty et al. 2011). Generally, continuous increase in filler loading leads to reduction in the elasticity of the nanocomposite (favourable), however, the strength of the nanocomposite will also decrease due to agglomeration (not favourable). For instance, a nanocomposite of PCL reinforced with 20 wt% bioglass, both the elasticity and strength were seen to reduce by 25%, and 30%, respectively (Jo et al. 2009) In other words, the nanocomposite becomes less rubbery along with reduced strength which was less than the natural bone strength. Thus, the challenge is finding the balance between the elasticity and strength of nanocomposite to match with the natural bone.

Table 2.5 shows some of the nanocomposites that meet not only the strength requirement but also the elasticity. For instance, the tangential modulus of PU (Sen, Zhao et al. 2004) and Young's modulus of PP (Manchado, Valentini et al. 2005) reinforced with SWNTs showed increase up to 250% and 40%, respectively. Moreover, the Young's modulus of PEEK (Abu Bakar et al. 2003) and UHMWPE (Fang, Leng et al. 2006) reinforced with HA showed increase up to 165% and 750%, respectively. In other studies, further increase in nanoclay loading improved the Young's modulus by 34% (Chan et al. 2011) and 40% (Unnikrishnan, Mohanty et al. 2011). Addition of bioactive glass also showed to improve the Young's modulus of epoxy and gelatine by 880% (Haque, Shamsuzzoha et al. 2003) and 53% (Mozafari, Rabiee et al. 2010), respectively. All these increase in modulus properties lead to reduction in elasticity of the nanocomposites, which in turn made the nanocomposites stiffer and favourable for load bearing bone implants.

2.6.2.2. Effect of preparation technique

Like mechanical strength, the elasticity of the nanocomposite is also affected by the preparation technique of the nanocomposite. For example, the elasticity of the chitosan-HA nanocomposite prepared using in-situ hybridization showed no change but was decreased by 18% when prepared using melt-mixing technique (Hu, Li et al. 2004). On contrary, the elasticity of nylon-6 reinforced with MWNTs increased for both techniques by 214% (Liu, Phang et al. 2004),

115% (Zhang, Shen et al. 2004) and 85% (Saeed and Park 2007). Other techniques such as ball milling and electrospinning deposition also reduced the elasticity of the nanocomposite. For instance, UHMWPE and PU reinforced with HA and SWNTs, through ball milling and electrospinning technique, respectively showed increase in young modulus by 90% (Fang, Leng et al. 2005) and 215% (Sen, Zhao et al. 2004). Hence indicating reduction in elasticity. Wet-casting technique as well showed decrease in elasticity of the nanocomposite, such as PVA reinforced with SWNTs (Paiva, Zhou et al. 2004).

In general, the nanocomposites presented in Table 2.5, can be considered as a good choice for bone implants. This is because they can meet either the tensile strength, compressive strength and elasticity requirement of the cortical bone ranging from 5-150 MPa, 70-200 MPa and 3-30 GPa, respectively, (Abu Bakar, Cheang et al. 2003, Fang, Leng et al. 2006, Jiang, Li et al. 2008) or the compressive strength and elasticity of cancellous bone which are 4-12 MPa and 20-500 GPa, respectively (Mozafari, Rabiee et al. 2010).

Table 2.5: Physico-mechanical properties of the natural bone and nanocomposite materials prepared

Polymer Matrix	Nanofiller	Optimum composition of nanofiller	Mechanical Properties						Reference
			Strength			Elasticity			
			Flexural (F)/ Tensile (T) strength (MPa)	Flexural yield (FY)/Compressive (C) strength (MPa)	Hardness	Young's (Y)/ Compression (C) modulus (MPa)	Strain (%)	Bending modulus (MPa)	
Cortical bone	NA		50-150 (T)	70-200 (C)		3-30 (GPa) (Y)	1-3		(Abu Bakar, Cheang et al. 2003, Fang, Leng et al. 2006, Jiang, Li et al. 2008)
Cancellous bone			0.1-30 (T)	4-12 (C)		20-500 (Y)	1-2		(Mozafari, Rabiee et al. 2010)
PMMA/HA	MWNT	0.1 wt%			3.460 (GPa)	69.528 (Y)			(Singh, Shokuhfar et al. 2008)
PMMA		2 wt%	90.6±3.2 (F)	89.8±2.6 (FY)			0.036± 0.006	3528±66	(Marrs, Andrews et al. 2006)
Nylon 6		2 wt%		47.2 Yield strength		1241.8 (GPa) (Y)			(Liu, Phang et al. 2004)
Nylon 6		1 wt%	40.3±3.1 (T)		0.1±0.002 (GPa)	852.4±77.0 (Y)			(Zhang, Shen et al. 2004)
Nylon 6		7 wt%	24.08±1.87 (T)			921.30±96.62 (Y)			(Saeed and Park 2007)
EVA		5 wt%			93 (shore A value)				(K.A. Dubey 2009)

Material	Type	Loading						Reference
HDPE		0.44 vol%				1.338 (GPa) (Y)		(Kanagaraj, Varanda et al. 2007)
Chitosan		0.4 wt%	73.1±6.3 (T)			1.92±0.07 (GPa) (Y)		(Wang, Shen et al. 2005)
Epoxy resin		4 wt%		6 &10(MPa) Yield strength (2% and 10% strain level)		465 (Y)		(Allaoui, Bai et al. 2002)
Polystyrene and polyurethane		1 wt%	~13 (T)			~24.5 Tangent modulus		(Sen, Zhao et al. 2004)
PVA		0.8 wt%		107 (MPa) Tensile yield strength		4.3 (GPa) (Y)		(Liu, Barber et al. 2005)
PVA		5 wt%		128 (MPa) Yield stress		6.2 (GPa) (Y)	0.038 yield strain	(Paiva, Zhou et al. 2004)
PP		0.75 wt%	35.5 (T)	31 (MPa) yield strength		1187 (Y)		(Manchado, Valentini et al. 2005)
Epoxy resin	**SWNT**	3 wt%	21.1 (T)			843 (Y)		(Wang, Dai et al. 2008)
Epoxy resin		31.3 wt%				15.1 (GPa) (storage modulus)		(Wang, Liang et al. 2004)
Epoxy resin		0.5 wt% (cured and dispersed in acetone)	75.6 (F)		18.0±0.11 (VHN)			(Lau, Lu et al. 2005)
Chitosan		1 wt%				9.20 (kPa) (C)		(Thein-Han and Misra 2009)

Chitosan		5 wt%	86 (Bending strength)					3400	(Hu, Li et al. 2004)
HDPE		40 vol%	23.16±0.40 (T)			3.87±0.21 (GPa) (Y)	6.8±0.6		(Wang and Bonfield 2001)
PEEK		30 vol% of Sr-HA						10600±600	(Wong, Wong et al. 2009)
PEEK		40 vol%	49 (T)		37.47±1.54 (VHN)	11.4 (GPa) (Y)	1		(Abu Bakar, Cheang et al. 2003)
PP	**HA**	20 wt%					5.1		(Ramírez, Albano et al. 2005)
Chitosan		70wt%		120 (C)					(Li, Yubao et al. 2005)
Chitosan/ carboxymethyl cellulose		30wt/v% of HA and 30 wt/v% of carboxymethyl cellulose		40 (C) dry state and 12 (C) wet state					(Jiang, Li et al. 2008)
PLA		20wt%	48.3 (T)			3.44 (GPa) (Y)			(Wan et al. 2015)
PLA		5wt%	62.5-75 (T)						(Liu et al. 2015)
PLA/PCL		30wt%	140 (T)			14 (GPa) (Y)	0.25		(Torabinejad et al. 2014)
MAPP		50 wt%		~10.5 (FY)		~2.9 (Y)			(Ling, Shing-Chung et al. 2003)
PMMA		0.5 wt%	43.84 (T)			1.72 (GPa) (Y)			(Fu and Naguib 2006)
Epoxy resin (Na$^+$/30B/I.30E)		10 wt%				3.44/3.12/3.04 (GPa) (Y)			(Qi, Zhang et al. 2006)

Polyurethane		1 wt%	33.6 (T)		79 (Shore A value)			(Kim et al. 2003)
Chitosan/polygalacturonic acid/HA	**Nanoclay**	20 wt% HA and 10 wt% MMT				4-6 (C)			(Ambre, Katti et al. 2010)
HDPE		4 wt%	24.6 Yield strength			767 (Y)			(Tanniru, Yuan et al. 2006)
Agarose		60 wt%	109 (T)		~0.25 (GPa)	21.4±2.5 (Y)			(Li, Gao et al. 2005)
Phenolic resin		2.7 wt%	24.9 (T)			1.53 (GPa) (Y)	3.6		(Pappas, Patel et al. 2005)
PMMA epoxy		15.5 wt%				1109 (Y)			(Park and Jana 2003)
Epoxy/bioactive glass		1wt%	298.51 (F)			2.78 (GPa) Flexural modulus			(Haque, Shamsuzzoha et al. 2003)
Chitosan/gelatine	**Bioactive glass**	70 wt%	374.0±7.1 (kPa) collapse strength			2120.6±106.9 (kPa) (Y) 737.2±38.6 (kPa) collapse modulus	17.5±2.1		(Gentile, Mattioli-Belmonte et al. 2012)
PCL		20 wt%	10 (T)			150 (Y)			(Jo, Lee et al. 2009)
Gelatine		50 wt%	5.6 Yield strength			78±1.2 (MPa)			(Mozafari, Rabiee et al. 2010)

2.7. Thermo-Physical Properties of the Nanocomposites

Thermo-physical properties of nanocomposites refer to the materials properties that vary with temperature without having to change its chemical identity. This property is usually classified into two parts. The first part deals with the heat capacity, thermal conductivity and diffusivity whereas the second part is mainly on the thermal behaviour of the polymer under deformation and fracture. Considering that this review is about nanocomposites for load bearing implants, in this section we will focus on the second part of thermo-physical properties. We will start with the thermal properties of biodegradable polymers and later discuss how change in temperature will affect the deformation and fracture properties of the nanocomposites also known as creep and fatigue, respectively.

2.7.1. Thermal Properties

Thermal properties such as melting, crystallization and glass transition temperatures of the nanocomposite help in understanding the nature of the polymer. Melting temperature (T_m) is the temperature at which a polymer will start to change from solid to liquid, whereas glass transition temperature (T_g) is the temperature where a polymer will convert from a glassy to a rubbery material. Crystallization temperature (T_c) is in between T_m and T_g, representing the temperature at which the polymer starts to crystalline. These temperatures are measured using differential scanning calometry (DSC). It is important to analyse these temperatures that can be used in the preparation of the nanocomposites meant for load bearing implant. For instance, as the temperature of a polymer drops below T_g, its brittleness increases. In contrary, when the temperature rises above the T_g, the polymer becomes rubbery. Moreover, heating the polymer at its T_m causes the polymer chains to come out of their arrangement, allowing them to move freely. This allows the fillers to disperse within the polymer matrix easily, thereby improving the final physico-mechanical properties of the nanocomposite which are discussed in the next section.

Another thermal factor that is important is the temperature at which thermal breakdown of polymer chains occur, known as decomposition/degradation temperature (T_{deg}). This temperature is measured by thermogravimetric analysis (TGA), where the weight loss of the nanocomposite is monitored after being subjected to a controlled heating at a specific environment. As a result, T_{deg} is sensitive to not only heating rate but also to presence of oxygen. This temperature in turn determines the thermal stability of the polymer. Based on the thermal stability criteria, polymers are classified either as thermally stable or unstable for those that decompose at process or ambient temperature. Though both polymers can be used to prepare nanocomposite for load bearing implants, the technique used to prepare them and loading filler will vary. The key point here is, the T_{deg} should not be comparable to the T_m. Otherwise, preparing the nanocomposite through melt-mixing will be difficult.

Generally, the thermal stability of the composite prepared shown in Table 2.6 are expected to be higher than of the pure polymer. This is because, the filler used can act as a heat-sink to accelerate heat absorption to the polymer matrix, improving the thermal stability of the nanocomposite (Lau, Lu et al. 2005). However, presence of agglomerates can decrease the thermal stability of the nanocomposite. Consequently, nylon 6-nanoclay improved its thermal stability at a lower nanoclay loading; however further increase in nanoclay loading contributed to decrease in thermal stability due to formation of agglomerates (Pramoda et al. 2003).

2.7.2. Deformation and Fracture Properties of the Nanocomposite

By definition, creep is the tendency of nanocomposite to deform when subjected to long-term stress whereas fatigue failure occurs when the nanocomposite is subjected to repeated loading and unloading. Nevertheless, fatigue and creep are greatly influenced by time and temperature especially for polymers who can easily go under transition from brittle to ductile over narrow temperature change (Lichte et al. 2011). Consequently, creep property becomes significant at 40-50% of the T_m for ceramics and above 200°C for polymers (Liu et al. 2013). In spite of that, ceramics are relatively resistant to creep at physiological (human body) temperature but not polymers (Lichte, Pape et al. 2011).

Table 2.6: Thermal properties of nanocomposites

Polymer matrix	Nanofiller	Filler Wt (%)	TGA Analysis		DCS Analysis			Reference
			$T_{peakdeg}$ (°C)	Residual Wt (%)	T_c (°C)	T_m (°C)	T_g (°C)	
PP	**HA**	20	Not reported		119	165	Not reported	(Ramírez, Albano et al. 2005)
PLLA		10			59.5	161.2		(Hong et al. 2005)
Chitosan		80	500	18.4	Not reported			(Yamaguchi et al. 2001)
PLA	**MWNTs**	10	348	3	Not reported			(Hapuarachchi and Peijs 2010)
PLA		3	Not reported		Not reported	156.5	61.3	(Wu and Liao 2007)
PLA-g-AA		3	378	15		152	65.9	(Wu and Liao 2007)
Chitosan		0.20g	270	35		Not reported	Not reported	(Chen et al. 2011)
Chitosan		1	272	~35	279		166	(He et al. 2011)
Nylon 6		5	500	~10	208		Not reported	(Saeed and Park 2007)
PP	**SWNTs**	0.75	Not reported		119.85	161.12		(Manchado, Valentini et al. 2005)
PEEK		1	576	~1	300			(Naffakh et al. 2011)
PMMA		0.5	370	~1	Not reported			(Kashiwagi et al. 2007)
PMMA		8	380	10				(Dai et al. 2007)
PVA		5	249	35				(Konidari et al. 2012)
Epoxy	**Nanoclay**	2	370	10	Not reported		115	(Zainuddin et al. 2010)
PMMA-epoxy		6	~375	~10			Not reported	(Park and Jana 2003)
Nylon 6		2.5	476	1.9				(Pramoda, Liu et al. 2003)
HDPE-HDMA		3	448	~8	115.9	133.9		(Minkova et al. 2009)

Considering cortical and cancellous bones are loaded regularly during everyday activities, fatigue and creep responses become important aspects of their mechanical behaviour. A thorough study on the fatigue and creep properties of human bone has been reported (Ker 2008). Therefore, while preparing a load bearing implant, the nanocomposite material should have high fatigue endurance and low creep (Ogle et al. 2001). However, compared to the strength and elasticity properties of the nanocomposite, relatively few studies have been conducted on the fatigue and creep properties (Gloria et al. 2007, Kane et al. 2008). As a result, it's hard to conclude the nanocomposites prepared and as shown in Table 2.5, are suitable for a long period of time under different factor such as change in temperature. For instance, HDPE reinforced with 40 vol% HA showed increase in strength and elasticity by 29% and 495%, respectively (Wang and Bonfield 2001) which was within the limit of natural bone, however, the fatigue life of the nanocomposite decreased by 200% when HA loading increased from 20 vol% to 40vol % (Kane, Converse et al. 2008). This was due to the nanocomposite becoming more brittle and less resistant to crack initiation and propagation which ultimately lead to failure by fatigue.

Overall, the thermo-physical properties of the nanocomposite are dependent on the properties of polymer matrix and the nanofiller individually. In addition, the interfacial bonding strength between the nanofiller and polymer matrix is also an important factor (Piggott et al. 1985). Considering the interfacial bonding of the nanocomposite is weaker than the pure polymer matrix, the fatigue fractures usually occur at the interface of nanofiller and polymer. Hence, their uncertain lifespans and degradation under complex states of stress, and their low mechanical strengths could limit their application. Hence, it is of great importance to study the fatigue and creep properties of the nanocomposite especially when dealing with load bearing implants.

2.8. Biocompatibility and Immune rejection

In the past decade many reviews on the biocompatibility analysis of nanocomposites have been reported (Smart et al. 2006, Harrison and Atala

2007, Onuki et al. 2008, Maisanaba et al. 2015). Biocompatibility- the ability of the biomaterial to be accepted by the cellular and biological responses of the tissue host, can be analysed either by *in-vitro* or *in-vivo* technique. *In-vitro* refers to the technique of performing the test in a controlled environment outside the living cells. Whereas *in-vivo* technique refers to the interaction of the biomaterials within the living cells. Among these two techniques, *in-vivo* has the potential to offer conclusive insights about the nature of the interaction. Bone implants (scaffolds) aside from having a desirable mechanical integrity to maintain the predesigned bone structure, requires having a biocompatible nature and no immune rejection towards the tissue host. Thus, a review on bone implant would not be complete without reviewing the biocompatibility of the biomaterials,

Generally, exposure to engineered nanoparticles may lead to harmful biological responses i.e. immune rejection. Immune rejection occurs when the designed bone implant is rejected by the immune system, destroying the hosting tissue. This can be prevented by selecting biomaterials that are biocompatible with the hosting tissue. These biomaterials can be permanent or biodegradable. They can be also naturally occurring biomaterials, synthetic or composites. The biocompatibility analysis of some nanocomposites is summarised in Table 2.7.

As mentioned in sections 2.3.1.1, one of the reasons for choosing HA as a nanofiller is due to its biocompatibility as it is already present in the bones. In addition, given that HA is osteoinductive, it has ability to encourage bone regeneration. This bone regeneration is normally starts by initially the cells attachment, followed by growth and proliferation of the living cells and then differentiation of the living cells (Polo-Corrales et al. 2014). Up to date, several *in-vitro* and *in-vivo* studies have reported that polymers incorporated with HA are biocompatible with the tissue host and have no immune rejection. Moreover, the higher the loading of HA (>20wt%) in the nanocomposites, the better chances of cell growth. As such, the prepared PA-HA nanocomposite was not only mechanically stable but also biocompatible with the tissue host after conducting both an *in-vitro* and *in-vivo* analysis (Wang et al. 2007). Similarly, PLA-HA nanocomposites have also showed to have no negative reaction with

the tissue host (biocompatible) through *in-vivo* (Wan, Wu et al. 2015) and *in-vitro* (Torabinejad, Mohammadi-Rovshandeh et al. 2014) analysis.

Nonetheless, it is important to note that the size, shape, loading and particle agglomeration of the nanofiller within the polymer matrix can affect the biocompatibility of the nanocomposite (Lordan et al. 2011). As a result, though the mechanical properties of polymers incorporated with CNTs and nanoclays are enhanced greatly, their biocompatibility is still debatable. Moreover, their ability to boost the cell growth depends on the preparation technique of the nanocomposite (Harrison and Atala 2007, Hussain et al. 2009). For instance, agglomerated CNTs significantly decrease the cell growth and proliferation (Wick et al. 2007). Moreover, it is reported that highly dispersed SWNTs are biocompatible compared to agglomerated SWNTs nanocomposites (Mutlu et al. 2010). For instance, *in-vitro* analysis of a well dispersed PPF-SWNTs nanocomposite confirmed its biocompatibility with the tissue host, however, further *in vivo* analysis is required to make decision on the cell growth and proliferation (Shi et al. 2008). Similarly, nanoclays can also result to considerable cell death, especially at a higher loading (>20wt%) (Lordan, Kennedy et al. 2011, Verma et al. 2012). An *in-vitro* analysis of chitin-nanoclays nanocomposite at a lower loading (2wt% nanoclay), however, was reported to be biocompatible and have no immune rejection (Zia et al. 2011).

Bioactive glasses are the second preferred nanofillers (after HA) due to their good interaction with living cells by forming a carbonated apatite layer on the surface. Also, bioactive glasses are biocompatible and osteoconducitve in nature, hence encouraging cell growth and proliferation (Srinivasan et al. 2012). Thorough reviews on both *in-vivo* and *in-vitro* analysis of bioactive glasses have been done (Gorustovich et al. 2009, Rahaman et al. 2011).

Table 2.7: Biocompatibility of some nanocomposites with the tissue host

Nanocomposite	Cell culture	Staining Liquid	Incubation Period	Observation	Outcome	Reference
Chitosan-nHA	Mouse preosteoblasts cultured in DMWM consisting 10% FBS and penicillin-streptomycin	Nucleic acid dye, PI	14 days	Fluorescence microscope	Increase in cell density up to 0.66 OD	(Thein-Han and Misra 2009)
Collagen-TCP	Mouse fibroblasts cultured in DMEM consisting 10% calf serum, 100μ/mL penicillin, 100 U/mL streptomycin		12 weeks	MTT assay	None showed toxic effects with 0.37 OD increase	(Zou et al. 2005)
	White rabbit	Villanueva bone stain embedded in methyl methacrylate resin		Fluorescence microscope	Newly formed and matured bone filled the defected sites and surrounding of the composite	
Halloysite clay nanotubes	Human epithelial adenocarcinoma and human breast cancer cultured in 10% FBS, 100 U/mL penicillin, 100μg/mL streptomycin, 5% glutamine and 5% sodium pyruvate		72 hrs	MTT assay	70% of cells survived at 75 μg/mL halloysite clay nanotube	(Vergaro et al. 2010)
		Amino-propyltriethoxysilane	2 days	Confocal Laser Scanning Fluorescence Microscopy	Effective internalization within the cells	
PEEK-Sr-HA	Human osteoblast cultured in 10% FBS	Alizarin	14 days	Microscope (Nikon Eclipse 80i)	More stained area compared to pure PEEK	(Wong, Wong et al. 2009)

			14 days	ALP	Normalized absorbance of 0.95 per unit cell number x 10^5	
			7 days	MTT	Rapid proliferation of osteoblasts after cell attachment	
PLLA solutions	Osteoblast-like cells, MC3T3-E1 cultured in α-MEM supplements with1% penincillin-streptomycin and 10% FBS		12 days	FESEM and MTT	Better adhesion behavior and proliferation behavior with the cell	(Park and Todo 2011)

2.9. Summary

It is worth noting that from the literature surveyed in this chapter, researchers have devoted more attention towards the nanocomposites (polymers reinforced with ceramics) in the recent years for tissue engineering related applications. However, there are still drawbacks faced especially with balancing the mechanical strength and biocompatibility of the nanocomposites. In addition, thorough characterisations on the properties of the nanocomposites are yet to be reported. Hence, in this study; nanocomposites of PLA reinforced with three nanofillers (NHA, mNHA and mNHA-GNP nanohybrid) will be prepared in hopes of meeting the required mechanical strength as well as the biocompatibility properties that mimics the human bones.

CHAPTER 3

METHODOLOGY

3.1. Introduction

This chapter lists the materials and sample preparation methods used in this study. The details of the sample preparation methods have been clearly described here as well. Figure 3.1 represents the overall schematic representation of the sample preparation steps and properties tested.
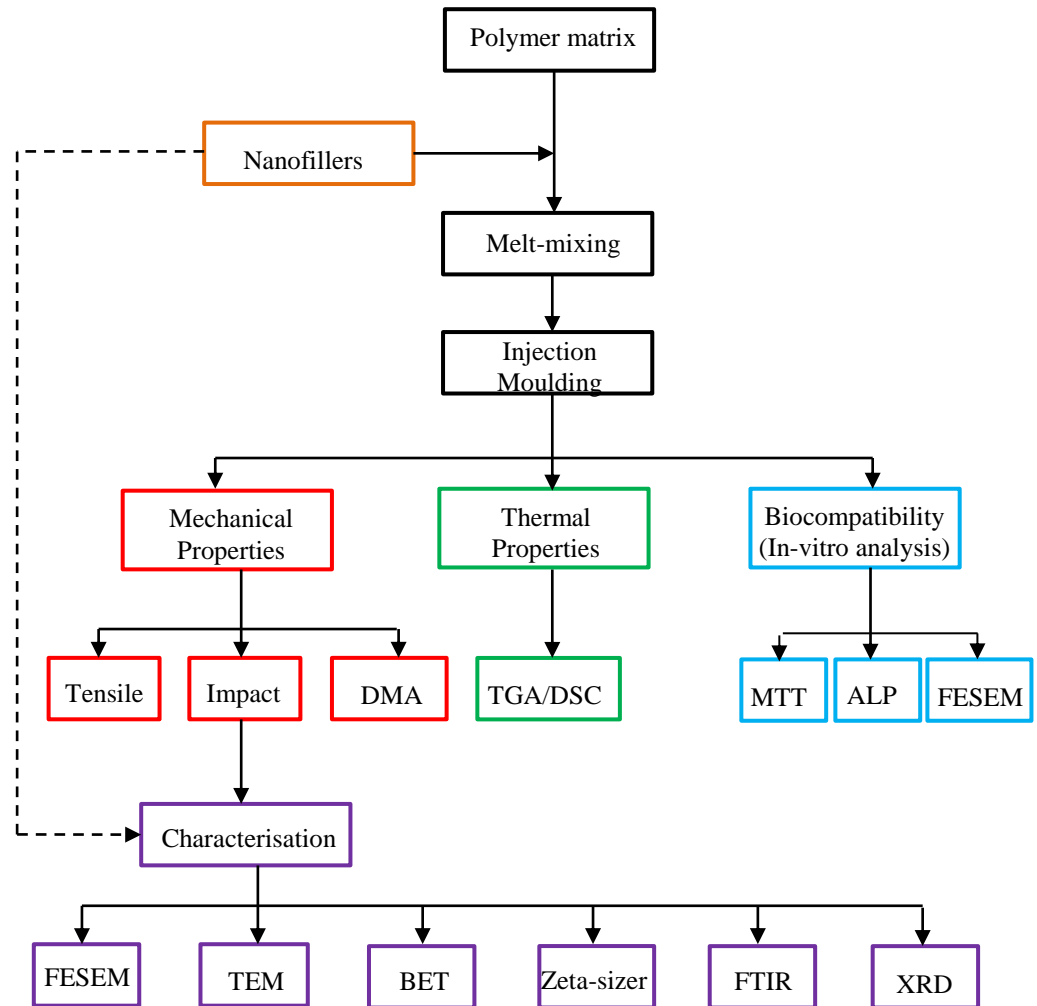
Figure 3.1: Schematic representation of the methodology of the study

3.2. Raw Materials and Chemicals

3.2.1. Raw Materials

Poly-lactic acid (Ingeo[TM] biopolymer 3052D), PLA, having melt flow index, MFI, value of 14 g/10min and specific gravity of 1.24 was supplied by

NatureWorks LLC, USA. The graphene nanoplatelets, GNP, used in this study as a raw material was purchased from Graphene supermarket, USA. The general properties of the GNP with particle size of 8nm are bulk density of 0.03 to 0.1 g/cc, an oxygen content of <1%, a carbon content of >99.5wt% and a residual acid content of <0.5wt%, and are offered as black granules.

3.2.2. Chemicals

The chemicals used to synthesis the nanohydroxyapatite, NHA, such as di-ammonium hydrogen phosphate, calcium nitrate tetrahydrate, ammonium solution (30%), and absolute alcohol 99.7% (Denatured) were purchased from LGC scientific, Malaysia. The chemicals used to surface treat the NHA, 3-aminopropyl triethoxysilane, APTES, 98% and sodium n-dodecyl sulfate, SDS, 99% (dry wt.) and water <1.5% were purchased from Alfa Aesar, UK. Moreover, polyethylenimine, PEI, branched with average molecular weight of ~25,000 by LS was also purchased from Sigma-Aldrich, Germany, to surface treat NHA.

The chemicals used for cell culturing, including minimum essential medium powder, MEM and pen-strep antibiotics were purchased from Gibco, while sodium bicarbonate (cell culture grade), sodium pyruvate and fetal bovine serum, FBS, were all purchased from Sigma-Aldrich, USA. In addition, the chemicals used to prepare phosphate buffered saline, PBS, such as sodium chloride, potassium chloride, sodium hydrogen phosphate, potassium dihydrogen phosphate, hydrochloric acid were purchased from R&M marketing, Essex, U.K. In order to detach the cells, trypsin was purchased from Gibco.

Other chemicals purchased for cell fixing, MTT and ALP assays include ascorbic acid (Fluka, UK), β-glycerophosphate (Sigma-Aldrich, USA), PRO-PREP protein extraction solution (Intron, Korea), *p*-nitrophenyl phosphate, *p*NPP, (Sigma-Aldrich, USA), hexamethyldisilazane, HMDS (Sigma-Aldrich, USA), dimethyl sulphoxide, DMSO (Sigma-Aldrich, USA), MTT 3-(4,5-dimethylthiazol-2-yl)-2,5-diphenyltetrazolium bromide (Invitrogen, USA).

All these chemicals were analytical grade and were used without further modification.

3.3. Preparation of the Nanofillers

The nanofillers used in this study were synthesised through precipitation method aided with ultrasonicator (Cole Palmer ultrasonic processor having a power of 750-watts and equipped with stainless steel probe). The processing parameters for the ultrasonicator such as ultrasonic time and amplitude are presented in Table 3.1.

Figure 3.2 shows the schematic representation of the preparation of the three nanofillers. The preparation of the nanofillers was classified into three categories as per the objectives of the study. The first category was further divided into two parts: (1) the synthesis of NHA using precipitation method (solid red line), and (2) optimisation of the process parameters using a software called Design of Experiment, DOE (Design-Expert 6.0.8). The second category was to prepare nanofiller by improving the quality of the synthesised NHA through surface modification (solid green line). Finally, hybrid nanofiller preparation by adding GNP into the surface modified NHA (solid blue line).

3.3.1. Synthesis and Optimisation of NHA

3.3.1.1. Synthesis of NHA

The NHA was synthesised by mixing 50 ml of 1M calcium nitrate tetrahydrate and 35mL of 0.6M diammonium hydrogen phosphate. The pH of the solution was adjusted with ammonium solution. Upon completion of the reactions, the solutions were vacuum filtered and washed with water and ethanol. The washed precipitate (NHA) was collected and kept in the oven at 70°C for overnight. The properties of the NHA powder were characterised. The range of process parameters used is presented in Table 3.1**.** These ranges were collected and determined from other studies.
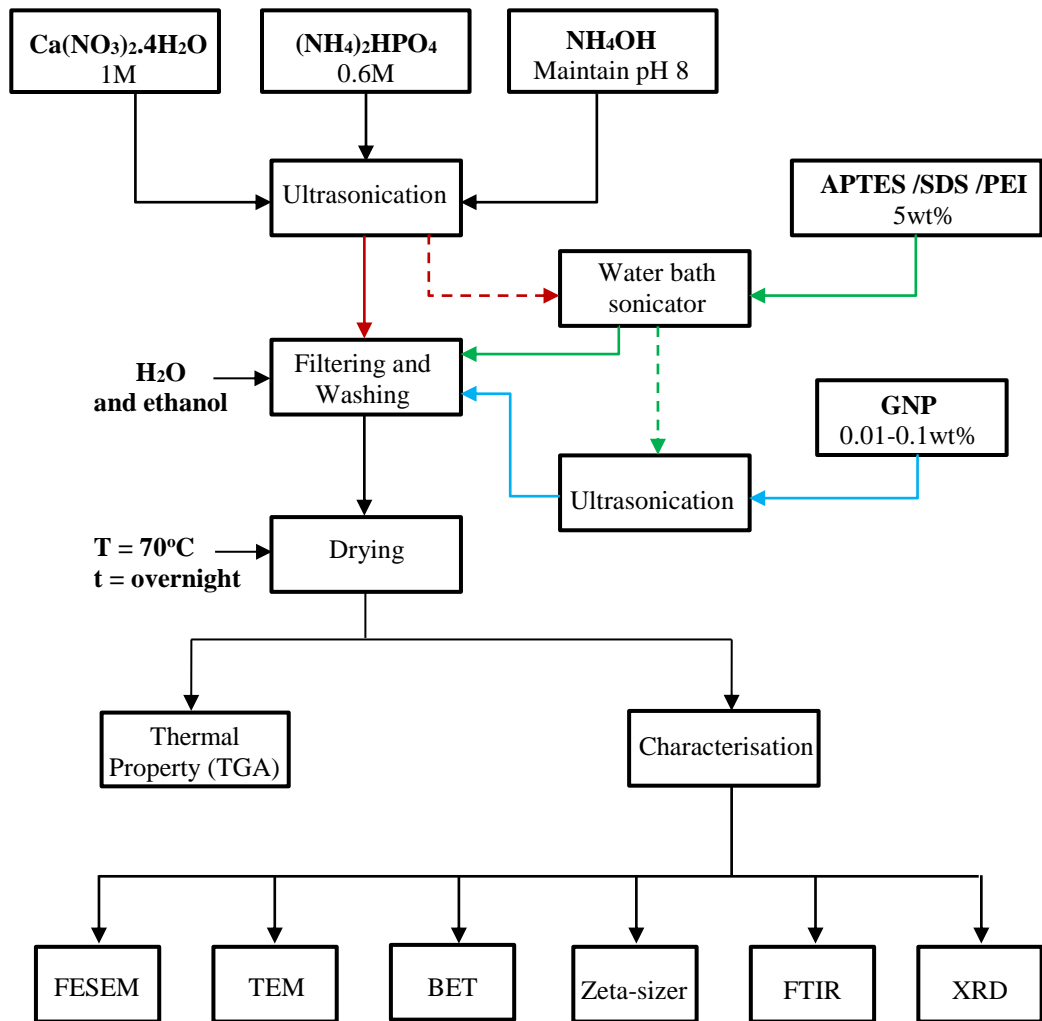
Figure 3.2: Schematic representation of the synthesis and surface modification of the nanofillers

Table 3.1: Process parameters influencing the synthesis of NHA

Studied Parameters	Constant Parameters
pH of solution **7, 8 and 9**	• **reaction temperature** at 60°C • **ultrasonic amplitude** at 60% • **ultrasonic time** at 20mins
Ultrasonic Time **10mins, 15mins, 20mins, 25mins and 30mins.**	• **pH** of 8, • **reaction temperature** at 60°C • **ultrasonic amplitude** at 60%
Ultrasonic amplitude **50%, 55%, 60%, 65% and 70%**	• **pH** of 8, • **reaction temperature** at 60°C • **ultrasonic time** at 20mins
Reaction Temperature **50°C, 60°C, 70°C, 80°C and 90°C**	• **pH** of 8, • **ultrasonic amplitude** at 60% • **ultrasonic time** at 20mins

3.3.1.2. Experimental Design and Statistical Analysis

The optimisation of process parameters was conducted using one of the Design of Experiments, DOE, methods called Response Surface Methodology, RSM, based on the Central Composite Design, CCD, with 3 factors and 5 levels as shown in Table 3.2. The three independent process parameters used for further studies are reaction temperature (T), ultrasonic time (t) and amplitude (A). The complete design consisted of 20 runs, where runs 15-20 were used to evaluate the pure error, whereas run 13 and 14 were outliers as shown in Table 3.3. The responses chosen to optimise the parameters are particle size, surface area and the weight loss or thermal degradation. The data collected in Table 3.3, were analysed using multiple regressions to fit the quadratic polynomial model. Once the optimum conditions were determined, the NHA powder was synthesised again using the optimum conditions.

Table 3.2: Independent parameters used for synthesis of NHA using CCD

Parameters/Factors	Levels				
	$-\alpha$	-1	0	+1	$+\alpha$
Temperature (T)	63.18	70	80	90	96.82
Ultrasonic time (t)	16.59	20	25	30	33.41
Amplitude (A)	56.59	60	65	70	73.41

3.3.2. Surface Modification of NHA (mNHA)

The synthesised NHA was further treated with 5wt% APSTE, SDS or PEI in order to improve the interfacial adhesion between the nanofiller and the polymer matrix. The treating agents were first activated by mixing with water in presence of ethanol as a catalyst for 1 hour at 70°C. Then, the synthesised NHA was added and mixed further for 1 hour in magnetic stirrer followed by water bath sonicator for 1 hour more. The precipitate (mNHA) was vacuum filtered and kept in the oven at 70°C for overnight. The properties of the mNHA powder were characterised.

3.3.3.   Preparation of Nano-hybrids (mNHA-GNP)

GNP (0.01-0.1 wt%) was first dispersed in ethanol using ultrasonication at 70°C for 1 hour. Then, the dispersed GNP was added into the mNHA solution (prepared in section 3.3.2). The solutions were vacuum filtered and washed with water and ethanol. The washed precipitates (mNHA-GNP) were then collected and kept in the oven to dry at 70°C for overnight. The properties of the mNHA-GNP powder were characterised. Table 3.4 shows the designation of the overall sets of nanofillers prepared.

3.4. Preparation of Nanocomposite

PLA as a matrix and the prepared nanofillers in section 3.3 were melt-mixed using an internal mixer (Haake Remix Polydrive R600/610 equipped with twin-screw and volumetric capacity of $69cm^3$). The rotor speed was set at 100 rpm while the mixing temperature was set at 170°C. The processing parameters were determined from a preliminary work.

Melt-mixing of the nanocomposites was done according to three categories as per the objectives of the study. At first, PLA-NHA nanocomposites were prepared by varying NHA loading. The second category was the preparation of PLA-mNHA nanocomposite by varying the mNHA loading. Lastly, PLA-mNHA-GNP nanocomposite was prepared by varying the GNP loading while keeping mNHA loading constant. The designations of the sets of nanocomposites prepared are presented in Table 3.5.

PLA was first charged in the mixing chamber and allowed to melt for 2 minutes, followed by the addition of the nanofillers (NHA, mNHA or mNHA-GNP). Both the PLA matrix and the nanofiller were continued to mix for another 8 minutes before collecting the nanocomposites from the internal mixer. The melt-mixing torque readings were detected by pressure transducer and recorded using the built-in software (Haake Remix Polydrive R600/610 Mixer Program, version 3.2.31). Analysis was conducted using fusion behaviour evaluation to obtain melt-mixing torque-time curves and data. Total mixing time was kept

constant to 10 minutes for PLA and all the nanocomposites to ensure similar thermal history. The collected nanocomposites were immediately cut into smaller pieces and kept in sealed plastic bags for injection moulding.

3.5. Injection Moulding

Nanocomposites collected from the internal mixer were injection moulded (Ray-Ran injection moulding machine) to obtain test specimens. The barrel and moulds of the injection moulder were first pre-heated to 170°C and 90°C, respectively (determined from the melting temperature of PLA). The moulding cycles include 6 minutes of heating in the barrel, followed by 9 seconds of pressure cycling of 6 bars to distribute the melted nanocomposite into the mould and avoid any air bubbles. The moulds used were based on ASTM D638 and ASTM D256 standards for tensile and impact testing, respectively. Upon cooling, the specimens were removed from the mould cavity.

3.6. Mechanical Properties

The mechanical properties such as tensile and impact properties of the nanocomposite were tested as follows.

3.6.1. Tensile properties test

The tensile specimens were prepared according to ASTM D638 standard with a gauge length of 25 mm, width of 6 mm and thickness of 3 mm. The tensile properties tests were conducted at ambient temperature using computerised tensile tester (Toyoseiki, Japan) with a load cell of 1kN and crosshead speed of 5 mm/min. Data for tensile strength and tensile modulus were recorded. At least 7 specimens were used for each set of nanocomposite and average results were taken as the resultant value. The standard deviation of the results was less than 10% (tensile strength) and 40% (tensile modulus).

Table 3.3: Factors and levels for CCD experimental design and their actual and predicted results

Run	T (°C)	t (min)	A (%)	FESEM- Particle size (nm)		BET- Particle size (nm)		BET- surface area (m^2/g)		TGA- Wt remaining (wt%)	
				Actual	Predicted	Actual	Predicted	Actual	Predicted	Actual	Predicted
1	70	30	60	165.017	170.11	19.169	21.69	99.0501	93.34	65.776	63.68
2	90	20	60	136.088	138.99	26.344	27.91	72.0744	67.98	76.7873	75.55
3	90	30	70	152.713	157.08	26.088	28.00	72.7812	69.54	63.6909	61.97
4	80	33.41	65	153.338	148.97	39.21	37.30	48.425	51.67	56.7622	58.48
5	90	20	70	187.79	182.70	28.365	25.84	66.9387	72.65	66.5943	68.69
6	70	20	70	156.275	158.46	25.927	26.88	73.2326	71.61	72.021	71.16
7	70	20	60	150.73	146.36	20.953	19.04	90.6207	93.86	74.1495	75.87
8	80	16.59	65	148.85	153.22	34.677	36.59	54.7545	51.51	62.1142	60.39
9	80	25	56.59	139.82	138.38	30.732	29.51	61.7831	66.72	62.0851	62.84
10	80	25	73.41	137.46	138.90	28.319	29.54	67.0476	62.11	58.9614	58.21
11	70	30	70	142.95	140.04	31.881	30.31	59.5572	63.65	54.7941	56.03
12	90	30	60	182.62	180.44	42.995	42.04	44.1613	45.78	48.2089	49.07
13	63.18	25	65	188.26	-	25.43	-	74.666	-	75.5886	-
14	96.82	25	65	158.47	-	36.127	-	52.557	-	64.0314	-
15-20	80	25	65	123.08	124.78	23.194	24.03	81.8621	79.96	69.9123	69.21

Table 3.4: Designation of the nanofillers

Designation	Process Parameters				mNHA		GNP (wt%)
	Temperature (°C)	Amplitude (%)	Time (mins)	pH	NHA (wt%)	Modifying agent (wt%)	
Neat NHA	-	-	-	-	-	-	-
NHA at T=90°C	90	60	20	8	-	-	-
NHA at A=65%	60	65	20	8	-	-	-
NHA at t=25mins	60	60	25	8	-	-	-
NHA	75	61	23.52	8	-	-	-
mNHA (APTES)	75	61	23.52	8	95	5	-
mNHA (SDS)	75	61	23.52	8	95	5	-
mNHA (PEI)	75	61	23.52	8	95	5	-
mNHA-0.01wt%GNP	75	61	23.52	8	95	5	0.01
mNHA-0.05wt%GNP	75	61	23.52	8	95	5	0.05
mNHA-0.1wt%GNP	75	61	23.52	8	95	5	0.1

Table 3.5: Designation of the nanocomposites

Designation	PLA (wt%)	NHA (wt%)	mNHA (wt%)		GNP (wt%)
			NHA	Modifying agent	
PLA	100	-	-	-	-
PLA- 1wt% NHA	99	1	-	-	-
PLA- 2wt% NHA	98	2	-	-	-
PLA- 3wt% NHA	97	3	-	-	-
PLA- 5wt% NHA	95	5	-	-	-
PLA- 5wt% mNHA(APTES)	95	-	5	5	-
PLA- 10wt% mNHA(APTES)	90	-	10	5	-
PLA- 20wt% mNHA(APTES)	80	-	20	5	-
PLA- 30wt% mNHA(APTES)	70	-	30	5	-
PLA- 5wt% mNHA(SDS)	95	-	5	5	-
PLA- 30wt% mNHA(SDS)	70	-	30	5	-
PLA- 5wt% mNHA(PEI)	95	-	5	5	-
PLA- 30wt% mNHA(PEI)	70	-	30	5	-
PLA- 5wt% (mNHA-0.01wt%GNP)	95	-	5	5	0.01
PLA- 5wt% (mNHA-0.05wt%GNP)	95	-	5	5	0.05
PLA- 5wt% (mNHA-0.1wt%GNP)	95	-	5	5	0.1

3.6.2. Izod Impact test

The impact specimens, 6mm wide and 3mm thick were prepared according to ASTM D256 standard. The specimens were notched to 2.59 mm. The impact properties tests were performed using Ceast Izod impact test machine equipped with 4-Joule pendulum. The energy required to break the specimens was recorded, and impact strength was calculated using the Equation 3.1. At least, 7 specimens were used for each set of nanocomposite and average results were taken as the resultant value. Standard deviation of the results was less than 10%.

$$\text{Impact strength} = \frac{\text{Energy required to break sample}}{\text{Thickness of sample}} \qquad \textbf{Equation 3.1}$$

3.7. Thermal Properties

3.7.1. Thermogravimetric Analysis

Thermal degradation and stability of the nanofillers and nanocomposites was measured using computerised thermogravimetric analyser (TGA, Mettler Toledo TGA/DSC 1 equipped with STAR^e System). The thermal stability of the samples was assessed by dynamic thermogravimetric analysis (TGA) experiments. The test was conducted at a heating rate of 10°C/min from 30°C to 1000°C (nanofillers) and 500°C (nanocomposites), under nitrogen atmosphere with a flow rate of 10ml/min. The PLA-mNHA-GNP nanocomposites were also heated at a rate of 3°C/min, for comparison purpose. All analysis was carried out using 5-10mg of the sample. The results were analysed using STARe System software, whereby the normalised weight loss vs temperature curve was smoothed using least-squares averaging technique before analysis. For the nanofillers, T_1, T_2 and T_3 represent the temperatures at which the three stages of starts to degrade. For the nanocomposites on the other hand, $T_{5\%}$, $T_{10\%}$, and $T_{50\%}$ are defined as the temperature at 5%, 10% and 50% weight loss, respectively. T_{max} is defined as temperature at which the nanocomposite losses its maximum weight, that is identified by the peak of derivative (dW/dT) curve. These temperatures are used to indicate the thermal degradation and stability of the nanofillers and nanocomposites.

3.7.2. Differential Scanning Calorimetry

The crystallisation and melting temperatures along with their respective heat flux of the nanocomposites were determined using computerized differential scanning calorimeter (DSC, Mettler Toledo TGA/DSC 1 equipped with STAR^e System). Analysis was carried out using 5-10mg of nanocomposites in nitrogen atmosphere (10ml/min). The samples were heated from 80°C to 200°C at 10°C/min. The results were analysed using STARe System software, whereby the heat flux vs temperature curve was smoothed using least-squares averaging technique before analysis. The T_c and T_m were defined as the crystallisation and melting temperatures obtained from the peak of the DSC curve, respectively.

The HF_c and HF_m are the heat flux of the samples determined at T_c and T_m, respectively.

3.8. Dynamic Mechanical Analysis

The viscoelastic properties of the nanocomposites were tested using a dual cantilever mode using dynamic mechanical analyser (DMA, TA instrument TA01 DMA 2980). The specimens were prepared in a dimension of 25 x 6 x 3 mm from the extra remaining moulded specimens. The specimen dimensions were kept as similar as possible in order to obtain an accurate comparison. The temperature range was 30 to 150°C with a heating rate of 5°C, using a frequency of 1 Hz. The storage modulus and peak of tan delta at the glass transition temperature (T_g) of the nanocomposites were recorded.

The creep properties of the nanocomposites (dimension of 25 x 6 x 3 mm) were also determined by the dual cantilever mode using DMA. Creep recovery cycles were conducted at an isothermal temperature of 70°C (T_g of neat PLA). To study the effect of temperature on the creep properties, an isothermal temperature of 10°C above and below the T_g was applied. For each temperature, 10% of the average tensile strength of neat PLA was applied for 20mins followed by 20mins of recovery period. For all the nanocomposites, a graph of static strain versus time was plotted in order to analyse their creep properties.

3.9. *In-vitro* Analysis

3.9.1. Cell Culturing and Trypsinization Process

Cell studies were conducted by using human MG63 cells, an osteosarcoma cell line. The cells were maintained in a 75ml flask in complete medium consisting of MEM and 5vol% FBS. The preparation method of complete MEM is highlighted in the appendix (Figure A.1). The cells were incubated at 37°C in a 5% CO_2 atmosphere. Moreover, the cells were passaged every 2-3days. After 10-14 days, the cells had grown to 90-100% confluence. Upon confluence, the complete medium was poured out and the flask was washed with PBS. The

preparation of PBS is presented in appendix (Figure A.2). Then, 2mL of 0.25% trypsin was added and the cells were incubated at 37°C in a 5% CO_2 atmosphere for 5 minutes in order to facilitate the trypsinization process (i.e. detachment of the cells from the flask). Upon detachment, the cells were centrifuged at 1800 rpm for 5 min followed by resuspension in the complete medium. Then, cell numbers were counted using haemacytometer and then diluted with the help of Equation 3.2. The m_1 and m_2 represent the cells number/ml while V_1 and V_2 are the volume of complete MEM. The m_2 and V_2 are fixed, i.e. $2x10^4$ cells/ml and number of wells x 1.5ml, respectively. Meanwhile, m_1 is the counted cell number and V_1 is the volume of complete MEM required to dilute with the cells.

$$m_1 V_1 = m_2 V_2$$

Equation 3.2

3.9.2. Cell fixing for FESEM analysis

The nanocomposites used for *in-vitro* analysis were prepared based on (8 x 8 x 3 mm) (Islam and Todo 2016). After 4 hours of cell seeding onto the nanocomposites, the cell-nanocomposite construct was rinsed with PBS once. Then, the fixing solution was added to fully immerse each nanocomposite and incubated at 4°C for 30 minutes. The nanocomposites were washed with PBS again prior to the dehydration at room temperature using ethanol of graded concentrations 70%, 95%, and 99.5% and absolute alcohol for 20 minutes, respectively. Subsequently, the final two drying steps were executed by first immersing the nanocomposites in the solution of 50% pure ethanol mixed with 50% HMDS and secondly in 100% HMDS, whereby the nanocomposites where then gently shook for 5 and 10 minutes, respectively. The excess drying solution was removed and samples were air dried for overnight. The morphology of cells cultured on the nanocomposite was examined by using FESEM at an accelerating voltage of 10kV.

3.9.3. MTT Assay

The cell proliferation analyses on the surface of the nanocomposites (8 x 8 x 3 mm) were conducted through MTT assay at 3, 5, and 7 days incubation period. The culture medium was removed from each well every 2-3 days. One millilitre

of fresh complete medium and 100 µl of MTT solution (5mg/ml) was added to each well for further 4 hr incubation. MTT was reduced by mitochondrial succinate dehydrogenase and formed an insoluble and dark purple formazan. Then, 1 ml of dimethyl sulphoxide was added to dissolve the formazan formed in each well. An aliquot resulting solution of 200 µl was transferred to a 96-well plate in triplicate, and the absorbance at 570 nm was measured using Varioskan^{TM} Flash Multimode Reader (Thermo Scientific, USA). Three independent experiments for each prescribed time period were performed.

3.9.4. Alkaline Phosphatase (ALP) Assay

Osteoblast early differentiation marker, ALP, was used to evaluate the cell differentiation potential of the prepared nanocomposites. The complete medium (MEM and 5vol% FBS) was mixed with 2.16µg/ml ascorbic acid and 0.05mg/ml β-glycerophosphate for the ALP assay. Prior to seeding, the nanocomposites were sterilised using 70vol% ethanol and UV light. The cells were then seeded on the nanocomposites (8 x 8 x 3 mm) and placed in 24-well plate followed by incubation at 37°C in a 5% CO_2 atmosphere for 7, 14, 21, and 28 days. The medium was changed with complete medium every 2-3 days. Upon the required day, the medium was completely removed from each well and washed with PBS twice. The nanocomposites with cells were scraped from the well and kept in 1ml of PRO-PREP protein extraction solution and finally placed on ice bath for 15 minutes. In between, the nanocomposites with cell lysates were centrifuged at 10,000rpm and 4°C for 10 minutes. ALP activity was determined as the rate of *p*-nitrophenyl phosphate (*p*NPP) hydrolysed by ALP into *p*-nitrophenol. In a 96-well plate, 100µl of *p*-NPP substrate was added to 100µl of supernatant of cell lysates and incubated for 2 hours at 37°C and 5% CO_2 atmosphere. Sodium hydroxide (0.2M) of 100µl volume was added per well and resuspended slowly without introducing bubbles in the mixture. Then, absorbance was measured at 405nm by using Varioskan^{TM} Flash Multimode Reader (Thermo Scientific, USA) to detect *p*-nitrophenol. The experiments for each nanocomposite were performed in triplicate.

3.9.5. ANOVA Analysis

The statistical significance was determined by ANOVA (single factor) to examine the correlation between the incubation period and the MTT and ALP assays. The $p<0.05$ was taken as a significant result i.e. the results obtained are 95% confidence level.

3.10. Characterisation tests

The chemical compositions, particle size and shape, dispersion properties of the synthesised nanofillers and prepared nanocomposites were analysed using Field Emission Scanning Electron Microscope (FESEM), Transmission Electron Microscope (TEM), Brunauer-Emmett-Teller (BET), zeta-sizer, Fourier Transform Infrared Spectroscopy (FTIR) and X-ray Diffraction (XRD).

3.10.1. Field Emission Scanning Electron Microscopy

The particle size and elemental composition of the nanofillers were examined using field emission scanning electron microscope (FESEM, FEI Quanta 400). The nanofiller were subjected to low vacuum at an accelerating voltage of 20kV, current of 60-90mA and working distance of ~8mm. An average of few measurements of the particle size was taken and standard deviation was calculated. Similarly, the microstructure of the impact fractured surfaces of the nanocomposites was also examined using FESEM (FEI Quanta 400).

3.10.2. Transmission Electron Microscopy

The morphology and the particle size of the nanofillers were evaluated using transmission electron microscope (TEM, Jeol-JEM-2100). The sample was prepared by dispersing the nanofillers into ethanol using 1 hr sonication. Later, the samples were observed under TEM using a voltage of 200 kV.

3.10.3. Gas Adsorption

The specific surface area of the nanofillers was determined by Brunauer-Emmett-Teller method (BET, micromeritics ASAP 2020 surface area and

porosity analyser). The powdered samples were degassed using a Unit 1 - S/N: 720, port 1 at 300°C for 1 hr prior to analyses. BET analysis provides a precise specific surface area, pore size and porosity volume of the sample. The particle size of nanofillers was calculated using Equation 3.3 with the help of BET surface area and the theoretical density of NHA which is 3.156g/cm^3 (Scalera et al. 2013).

$$\mathbf{D(nm)} = \frac{6}{S_w \rho_w} \qquad \qquad \textbf{Equation 3.3}$$

3.10.4. Zeta-sizer

The particle size distribution of the nanofillers was measured using Zetasizer (Malvern Zeta sizer nano ZS). The sample was prepared by dispersing the nanofillers into water using 1 hr sonication. A drop of the prepared sample was then diluted with distilled water in the disposable cuvette and measured.

3.10.5. Fourier Transform Infrared Analysis

The chemical functional groups of the nanofillers and nanocomposites were characterised using Fourier transform infrared spectroscopy (FTIR, Perkin Elmer Spectrum 2000). The spectrometer was operated with 50 scans at 4 cm^{-1} resolution and within the range of 4000-400 cm^{-1} for each sample. All FTIR spectra were recorded in transmittance unit. The test was conducted by preparing a disk from a mixture of nanofillers and KBr at a weight ratio of 0.2% to 1%.

3.10.6. X-ray Diffraction

The XRD patterns of the nanofillers were collected with help of X-ray diffraction (XRD, Panalytical X'Pert Pro model) using Cu-K$_\alpha$ radiation (λ=0.15418nm). Data were collected over the range of 2θ values from 15° to 80° with step size of 0.2° and step time of 2.5 sec.

CHAPTER 4

SYNTHESIS, OPTIMISATION AND CHARACTERISATION OF NANOHYDROXYAPATITE

4.1. Introduction

This chapter addresses the first objective of this study that includes (1) the synthesis of NHA, (2) the optimisation of the process parameters and (3) the characterisation of the NHA. The NHA nanofiller was prepared via precipitation technique, aided with ultrasonication. Initially, the effects of different process parameters such as the ultrasonication time (10-30 minutes) and amplitude (50-70%) as well as reaction temperature (50-90°C) and solution pH (7-9) were investigated using single factor analysis. Then, the optimisation of these process parameters using Design Expert 6.0.8 was discussed. The surface morphologies, particle sizes, thermal properties and chemical functional groups of the synthesised nanofiller in respect to neat NHA were also discussed. This chapter has been published in two separate journals (Michael et al. 2016, Michael et al. 2016).

4.2. Chemical Functional Group and Elemental Analysis

4.2.1. EDX

Table 4.1 compares the EDX semi-quantitatively measured data of the calcium and phosphorus contents of the synthesised NHA powder in comparison to the pure NHA. This data was then used in determining the molar ratio of calcium and phosphorus content (Ca/P) within the NHA powder. From the table, it is noticed that the Ca/P ratio of the synthesised NHA was higher than the theoretical stoichiometric molar ratio (Ca/P=1.67). However, the Ca/P ratio should be within the range of 1.67 to 1.82; acceptable Ca/P ratio for a successful synthesis of NHA (Bonfield and Gibson 2003). Meanwhile, the increase in Ca/P ration attained for the synthesised NHA indicates presence of calcium hydroxide (Ansari et al. 2011). The presence of calcium hydroxide is advantageous as it has antibacterial characteristics among others including enhancing enzymes and growth factors release (Ansari, Naghib et al. 2011).. This is important because as mentioned in section 2.2., release of growth factors is important as they are naturally occurring substances capable of stimulating cellular growth, proliferation, healing and cellular differentiation. Hence, from

the table, the process parameters producing the closest Ca/P ratio to the stoichiometric value of NHA were chosen for further analysis. This include NHA synthesised at t=25mins, T=90°C, A=65% and pH=8 in comparison to pure NHA.

Table 4.1: Semi-quantitative calcium and phosphorus content of NHA powder

Processing Parameter		Calcium (wt%)	Phosphorus (wt%)	Ca/P
Pure NHA		16.37	9.23	**1.77**
Time (mins)	**10**	27.48	14.98	**1.83**
	15	24.72	13.31	**1.85**
	20	28.54	15.99	**1.78**
	25	25.12	14.35	**1.75**
	30	29.79	13.56	**2.19**
Temperature (°C)	**50**	25.78	12.59	**2.05**
	70	24.98	13.47	**1.85**
	80	21.18	11.50	**1.84**
	90	11.34	6.52	**1.74**
Amplitude (%)	**50**	17.86	9.89	**1.81**
	55	16.56	9.13	**1.81**
	65	19.02	11.27	**1.69**
	70	19.09	10.75	**1.76**
pH	**7**	18.09	10.60	**1.71**
	8	24.20	13.9	**1.73**
	9	21.56	12.17	**1.77**

4.2.2. FTIR

Figure 4.1 displays the FTIR spectra of the NHA synthesised at different process parameters in respect to neat NHA. The peaks observed at 1075.88 cm^{-1}, 1028.10 cm^{-1}, and 1029.72 cm^{-1} are associated with the stretching modes of PO_4^{3-} functional groups for NHA synthesised t=25mins, T=90°C and A=65%, respectively (Gopi et al. 2008, Scalera, Gervaso et al. 2013). Other peaks present at 653.89cm^{-1}, 601.81 cm^{-1}, and 604.08 cm^{-1} correspond to the bending modes of PO_4^{3-} functional groups. From the FTIR spectra, a stretching and bending mode of PO_4^{3-} peaks are observed for the pure NHA at 1042.06 cm^{-1} and 601.97 cm^{-1} wavelength, respectively. Furthermore, at wavelength of ~825cm^{-1} presence of acidic phosphate group (HPO_4^{2-}) was detected for NHA synthesised at T=90°C.

Nitrate groups were detected at a wavelength of 1404.19 cm^{-1}, 1394.26 cm^{-1} and 1355.74 cm^{-1} for NHA synthesised at t=25mins, T=90°C and A=65%, respectively (Singh 2012). The presence of nitrate group is from the ammonium solution added during the synthesis of NHA to adjust the pH of the solution. Presence of carbonate group with a low intensity was spotted for the pure NHA at a wavelength of 1456.47 cm^{-1}. This could be due to the absorption of carbon dioxide from the atmosphere during the synthesis process (Gopi, Govindaraju et al. 2008).

Peaks shown at 1635 cm^{-1}, 1636 cm^{-1} and 1640cm^{-1} corresponds to the bending mode of OH$^-$ for the NHA synthesised at t=25mins, T=90°C and A=65%, respectively. Furthermore, a stretching mode of OH$^-$ was seen with a broader intensity at 3420.49cm^{-1} for t=25 mins, 3178.74 cm^{-1} for T=90°C, and 3444.16 cm^{-1} for A=65% (Singh 2012). Similarly, presence of OH$^-$ ions was detected at 3571.78 cm^{-1} for pure NHA. Thus, confirming the successful synthesis of NHA through precipitation method.
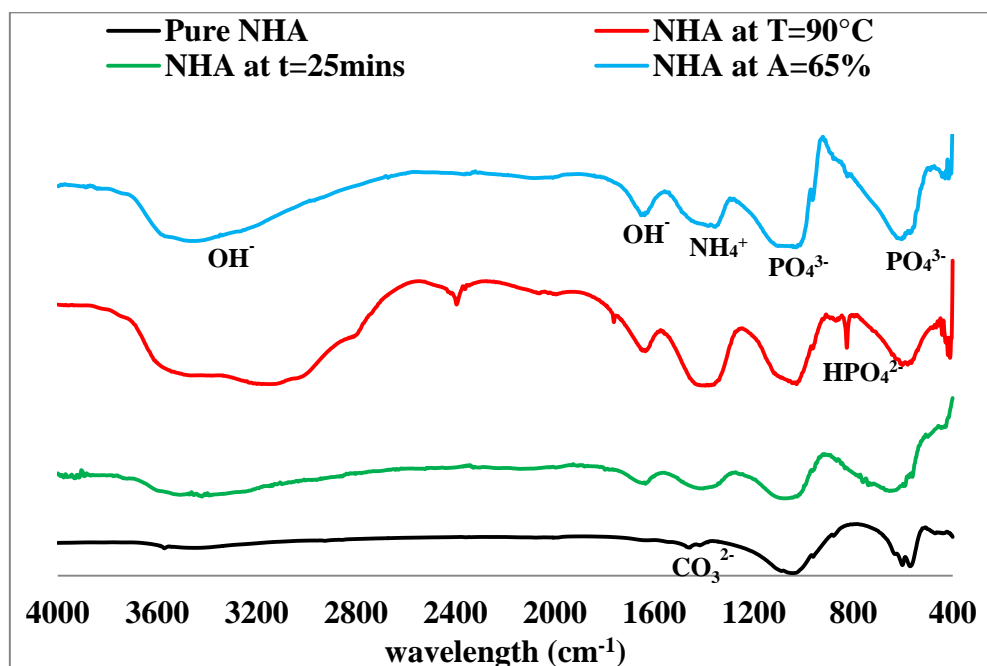
Figure 4.1: FTIR spectrum of synthesised NHA at different parameters in comparison with pure NHA

4.2.3. XRD

The XRD pattern of NHA synthesised at different process parameters is presented in Figure 4.2, in comparison to pure NHA. From the figure, the synthesised NHA powder showed blunt peaks compared to the sharp peaks of pure NHA. From the figure, it can be observed that the most intense and sharp lines are found between the 2θ angle of 20-60º (Granados-Correa et al. 2010). The peaks found at 2θ angle of 27º, 32-35º, 40-42º, 47-48º, 50º, and 54º indicate presence of NHA (Han et al. 2006, Hui et al. 2010). The sharp peaks at 26° (2θ) indicate the crystallisation of hydroxyl-deficient areas to form oxyapatite (Gross et al. 1998). These peaks with the lower intensities indicate presence of amorphous phase in the form of other phosphate related compounds (Liu et al. 2002). It has been reported that samples showing broader peaks at 30-35° (2θ) with high intensity, indicate the presence of crystalline phase which corresponds to NHA and tricalcium phosphate (TCP) (Bonfield and Gibson 2003). Considering the crystallinity of NHA is affected by sintering (Michael et al. 2016), the synthesised NHA was not sintered; thus the crystallinity of NHA reduced compared to the pure NHA.

4.3. Particle Size and Microstructure

4.3.1. FESEM

Figure 4.3, Figure 4.5, Figure 4.7 and Figure 4.9 depict the FESEM microstructural images of the NHA synthesised at different ultrasonic time, amplitude, reaction temperature and pH, respectively. Figure 4.4, Figure 4.6, Figure 4.8 and Figure 4.10 on the other hand, exemplify the effect of these process parameters on the particle sizes of the synthesised NHA measured by the FESEM. From these figures, the size and dispersion of NHA particles were observed vary as the ultrasonication parameters changed. This could be as a result of varying the amount of energy applied that could potentially influence the dispersion of the NHA particles. This energy applied is a factor of ultrasonic power and total amount of time that the NHA was sonicated. Thus, when the ultrasonic energy increases, the bubbles collapse with more force, causing the

particles to break down and disperse in smaller size (Wu et al. 2013). However, if too much ultrasonic energy is applied, the bubbles do not have enough time to grow and collapse, thus rapid collision of particles takes place, causing the particles to collide and re-agglomerate (Wu, Guo et al. 2013). As a result, in another study, when metal nanoparticles were sonicated, an extensive agglomeration of metal nanoparticles was observed due to increased collision frequency between the particles upon sonication (Pradhan et al. 2016).

Therefore, in this chapter, varying the ultrasonic parameters resulted in the dispersion of the synthesised NHA while in some cases the NHA particles were seen to agglomerate. For instance, lower ultrasonic time (10-15 mins) resulted in the formation of agglomerated NHA particles (Figure 4.3 a-b). Increasing the ultrasonic time (25-30 mins), however, improved the size of the agglomerates by breaking them into smaller particles (Figure 4.3 c-d). This is further complemented by the particle sizes measured (Figure 4.4), whereby a decrease of 68.4% is observed when the time increased from 10 mins to 25 mins. Further increase to 30 mins, however, increased the particle size by 20.2% compared to 25mins. This is caused by the re-agglomeration of the NHA particles as a result of the collisions between the particles The NHA synthesised at different amplitude (Figure 4.5) was observed to be better dispersed and less agglomerated compared to the NHA synthesised at different time (Figure 4.3). This shows that ultrasonic time has more influence on the homogeneity of the NHA powder than ultrasonic amplitude. In other words, increasing the ultrasonic time significantly changed the surface morphology of the NHA powder (reducing the agglomeration), whereas increasing ultrasonic amplitude had no effect on the surface morphology (mostly dispersed). Moreover, the particle size of the NHA synthesised by varying the amplitude produced finer powder (Figure 4.6) compared to the one synthesised by varying time (Figure 4.4). Increasing the amplitude from 50% to 65% reduced the particle size of the NHA by 30.2%. Further increase to amplitude of 70% caused the particle size to increase by 9.9%. This could be caused by the re-agglomeration of the NHA powder.
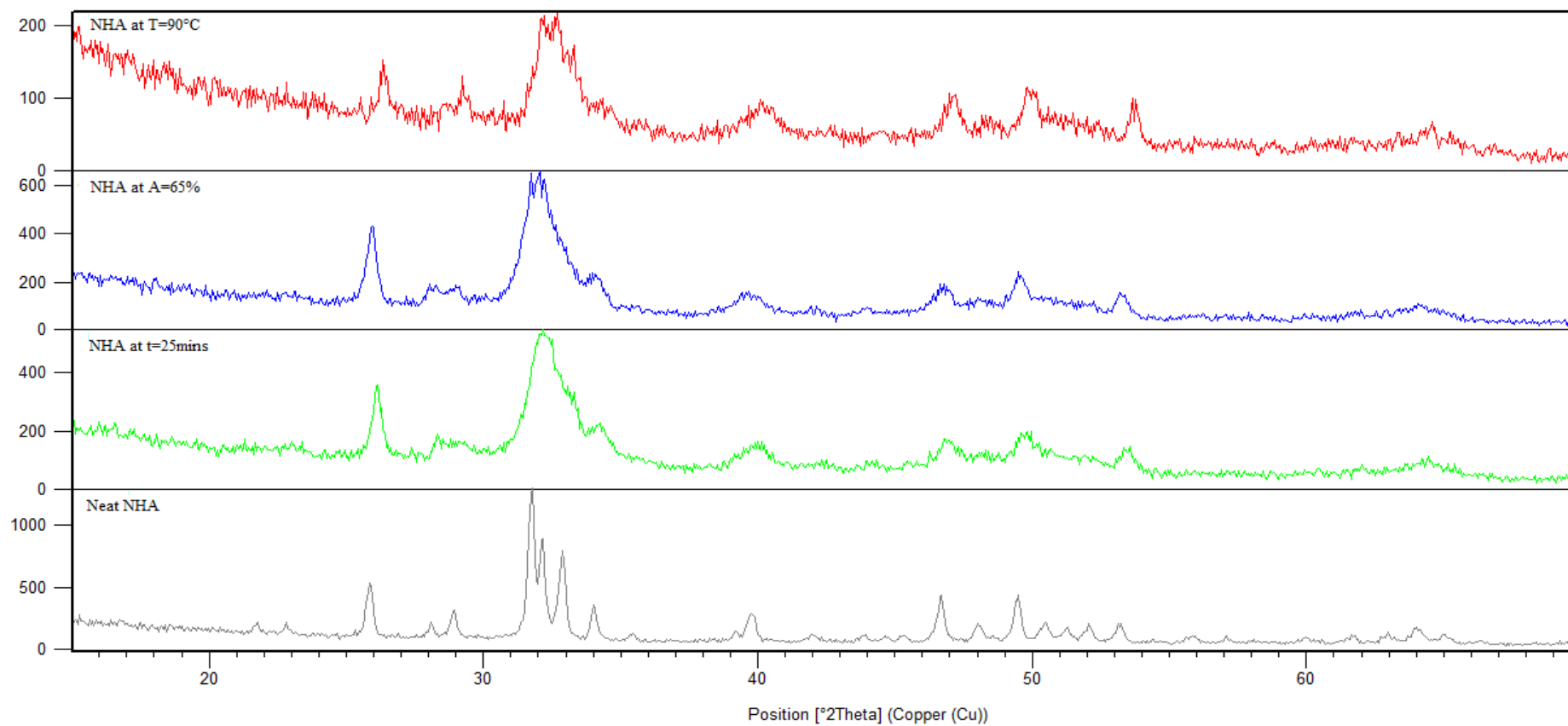
Figure 4.2: XRD pattern of synthesised NHA at different parameters in comparison with neat NHA
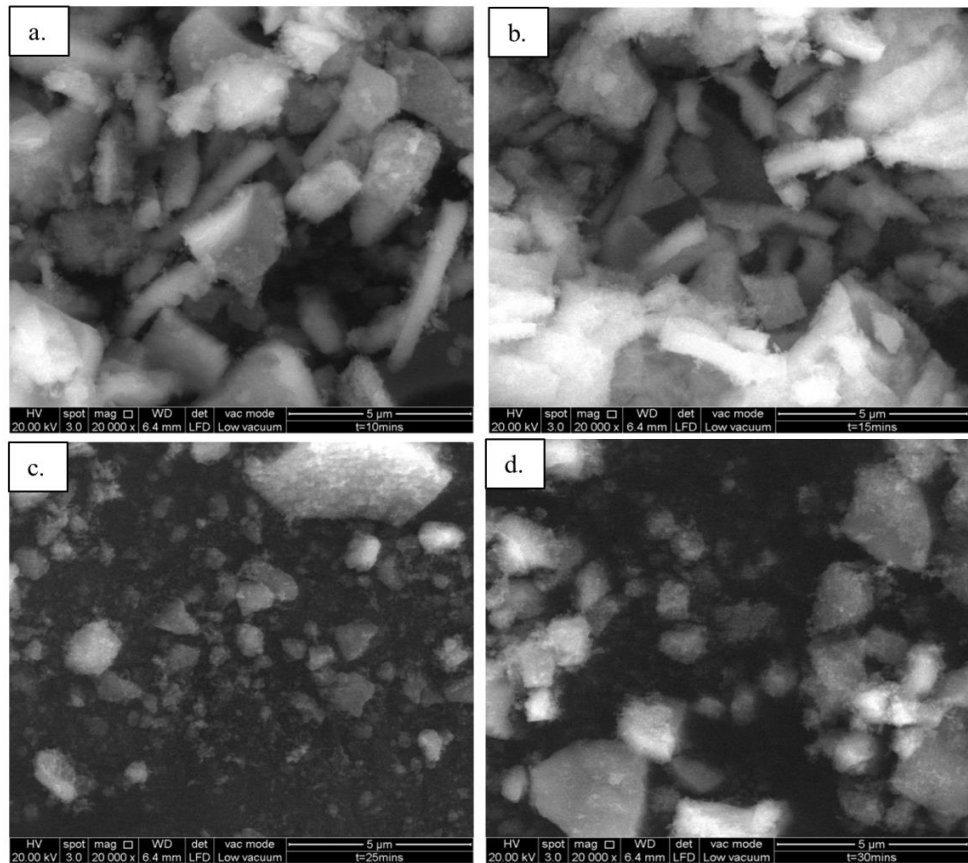
Figure 4.3: Microstructural images of NHA synthesised at time of (a) 10mins, (b) 15mins, (c) 25mins and (d) 30mins
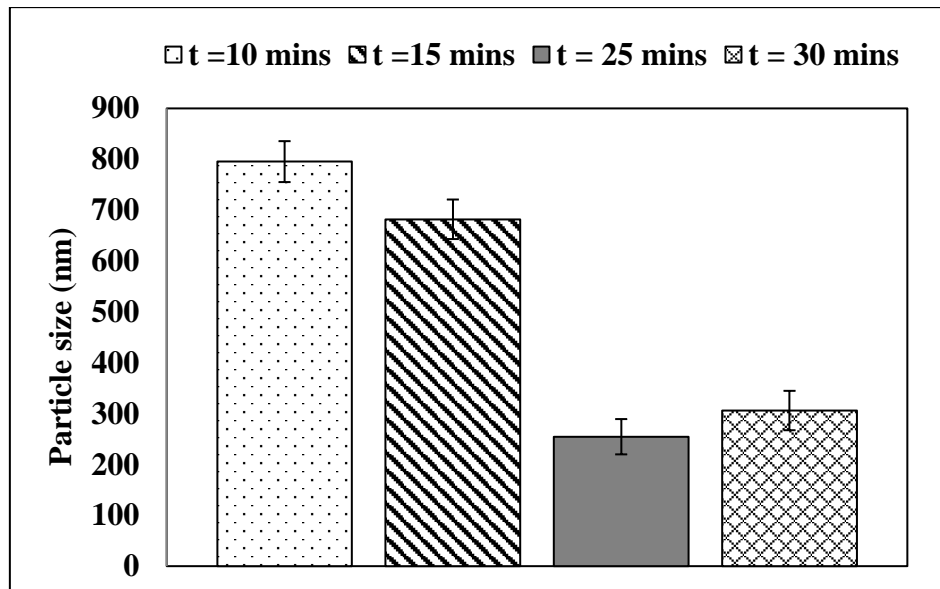
Figure 4.4: Particle size of NHA synthesised at different ultrasonic time
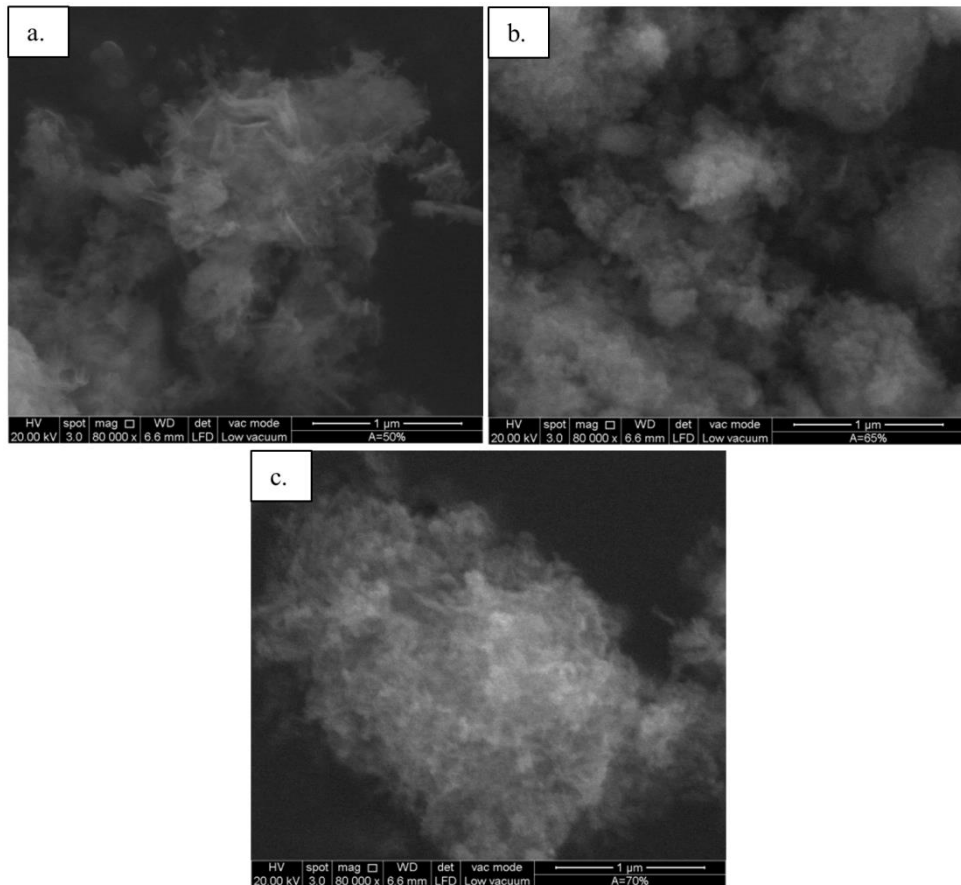
Figure 4.5: Microstructural images of NHA synthesised at an ultrasonic amplitude of (a) 50%, (b) 65% and (c) 70%
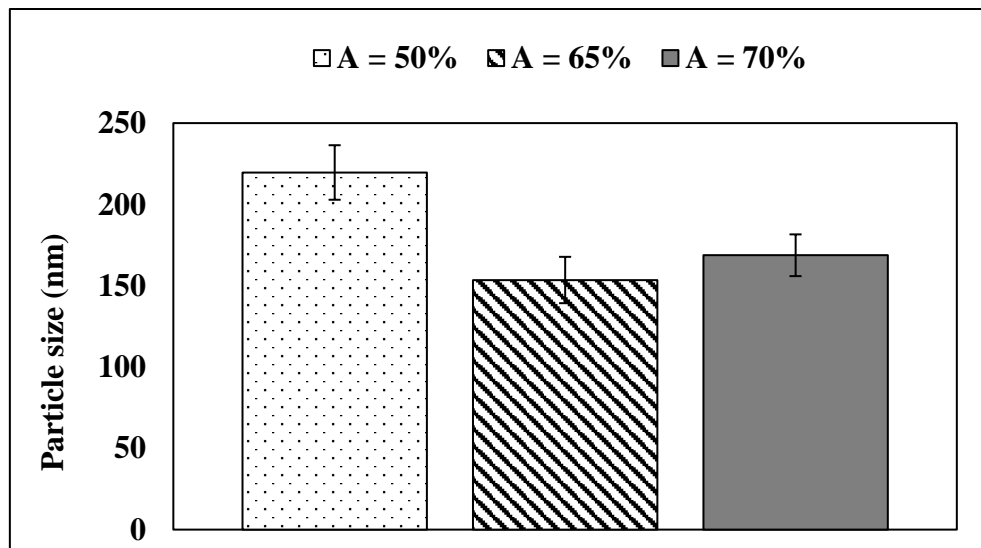
Figure 4.6: Particle size of NHA synthesised at different ultrasonic amplitude

NHA was also observed to be affected by the temperature, whereby lower temperature (T=50°C) is not favourable as agglomerated NHA particles are formed (Figure 4.7 (a)). Temperature above 70°C produced a well dispersed NHA powder (Figure 4.7 (b and c)). This is further complemented with the particle size measured and shown in Figure 4.8. The finest particle size was obtained at a temperature of 90°C (reduced by 37.8% compared to 50°C).

The microstructural images of the synthesised NHA powder depict the dispersion of NHA powder was not significantly affected by the change of pH (Figure 4.9 (a-c)). The particle size on the other hand is observed to reduce by 53.6% when the pH increased from 7 to 9. Therefore, from this point onwards, more characterisation tests were focused on the NHA synthesised at pH=8 for selected parameters that are t=25mins, T=90°C and A=65%.
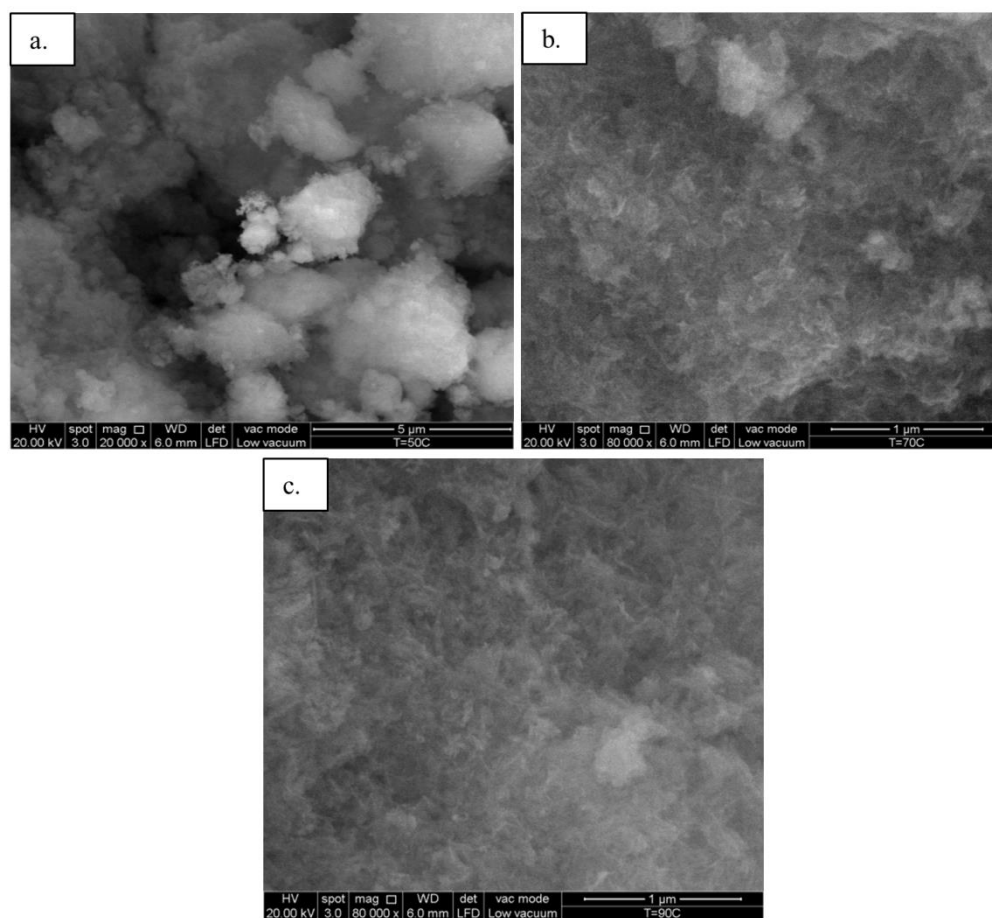
Figure 4.7: Microstructural images of NHA synthesised at temperature of (a) 50°C, (b) 70°C and (c) 90°C
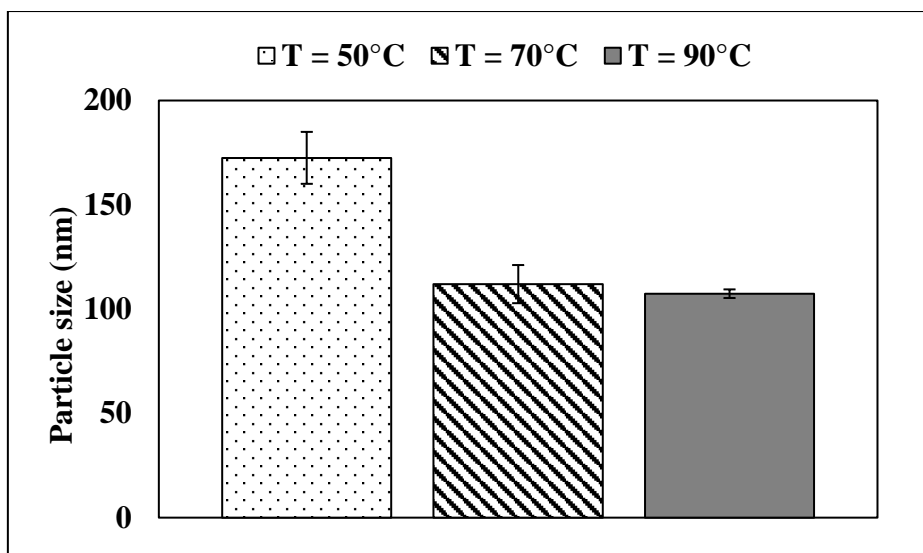
Figure 4.8: Particle size of NHA synthesised at different temperature
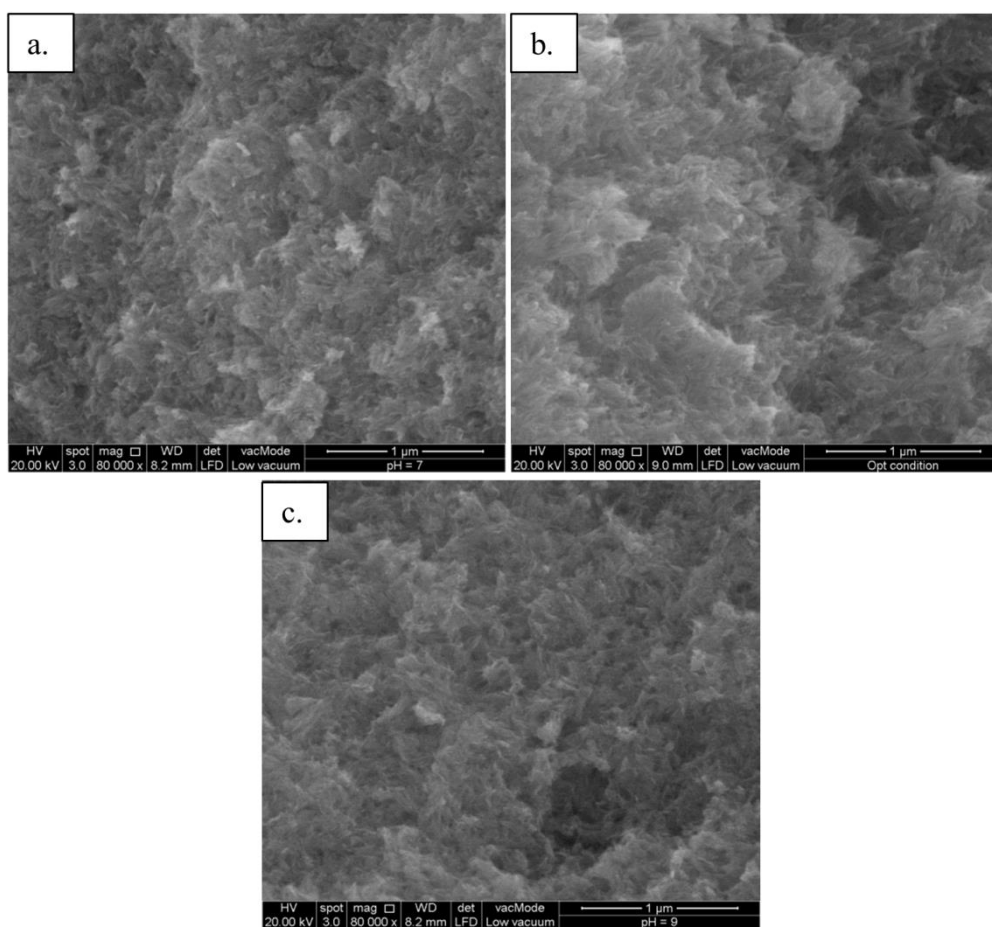
Figure 4.9: Microstructural images of NHA synthesised at pH of (a) 7, (b) 8 and (c) 9
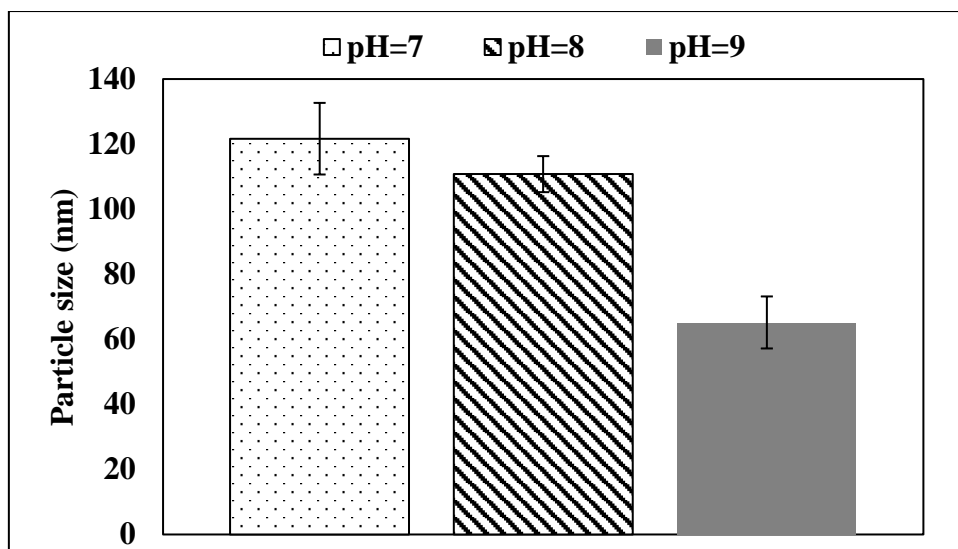
Figure 4.10: Particle size of NHA synthesised at different pH

4.3.2. Zeta-sizer

Figure 4.11 depicts the particle size distribution obtained using zeta-sizer for the NHA synthesised at selected process parameters. The average particle sizes of NHA powder measured were found to be 165.5nm, 255nm, 396.1nm and 660.7nm for T=90°C, A=65%, pH=8 and t=25mins, respectively. This in turn, confirmed the synthesis of nano-sized NHA, hence complementing the particle size measured by the FESEM. However, comparing the two particle sizes measured by FESEM and zeta-sizer, the former gave smaller size compared to the latter. This is due to the variation associated with the measurement technique (Cengiz et al. 2008). For instance, the particle size measurement using zeta-sizer is based on dynamic light scattering (DLS), whereby the shape of the particle affects the scattering angle (Chandrasekar et al. 2013). Thus, more accurate measurement can be obtained for particles having spherical shape. Besides that, the observed difference in the particle size measurement between the two techniques is also attributed to the agglomeration of the very fine particles which tend to occur in zeta sizer.
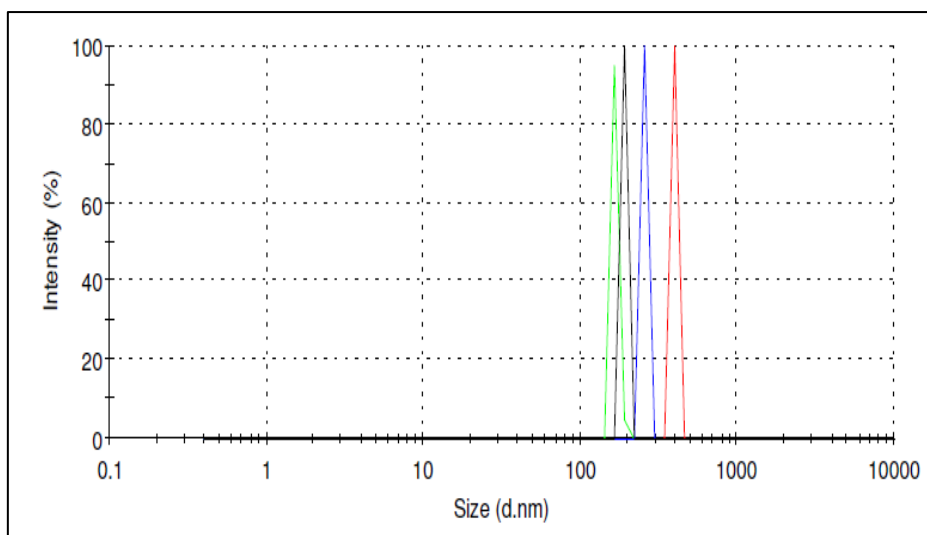
Figure 4.11: Particle size distribution using Zeta sizer for NHA at different process parameter, green (T=90°C), black (A=65%), blue (pH=8) and red (t=25mins)

4.3.3. TEM

Figure 4.12 shows the TEM micrographs of the synthesised NHA at (a) t=25mins, (b) A=65%, (c) T=90°C and (d) pH=8 in comparison to neat NHA. As indicated by the arrows in the Figure 4.12 (a-b), the synthesised NHA is observed to have needle shaped particles with particle sizes ranging 40-100nm and 35-85nm for NHA synthesised at t=25mins and A=65%, respectively. This is in line with the previous reported studies, where the needle shaped NHA has been synthesised (Cengiz, Gokce et al. 2008, Agrawal et al. 2011, Ansari et al. 2011).

In literature, it is stated that both reaction temperature and solution pH play crucial roles in determining the particle shape of the NHA (Liu et al. 2003). Hence, in comparison to NHA synthesised at t=25mins and A=65%, the morphology of the needle-shaped NHA is observed to change into spherical shape at an increased reaction temperature of 90°C, as indicated by the arrows in Figure 4.12 (c). Consequently, the length of the NHA particles synthesised at T=90°C reduced to 45-65nm. Similar observations were reported by (Puvvada et al. 2013) where increasing the reaction temperature contributed in change of the NHA particle shape from needle-like to spherical. This change in the NHA

75

particle shape is attributed to the difference in the interaction between the molecules as the reaction temperature increases.

The second crucial process parameter, solution pH, produced a needle shaped NHA with particle size ranging between 55-95nm, as presented by the arrows in Figure 4.12 (d). However, the NHA particles were agglomerated, as designated by the circles in the Figure 4.12 (d). This could be due to the lower ultrasonic amplitude (i.e. A=60%) applied, that was not enough to break down the NHA agglomerates.

In comparison to the synthesised NHA, the particle size of the pure NHA is spherical shaped as shown in Figure 4.12 (e). The difference in the particle shape of the synthesised NHA in respect to the pure NHA could be due to the preparation technique (Zhou and Lee 2011). In addition, calcination of NHA will produce a spherical-shaped NHA compared to uncalcinated NHA (Bouyer et al. 2000, Michael, Khalid et al. 2016). In general, the results obtained by the TEM further complemented the FESEM and zeta-sizer particle size measurements, confirming the synthesis of nano-sized NHA through precipitation technique.

4.3.4. Gas Adsorption

The BET method was used to further determine the specific surface area from which the particle size was calculated. The data obtained for the synthesised NHA in respect with pure NHA are summarised in Table 4.2 in conjunction with the TEM, zeta-sizer and FESEM results. Therefore, by comparing all the particle sizes summarised in Table 4.2 and the TEM micrographs in Figure 4.12, it can be concluded that NHA that mimics the morphology of the NHA present in the bones has been synthesised at different parameters. This further complements the previous studies that reported the hydroxyapatite in the natural bone has a thickness of 2-7nm, length of 15-200nm and width of 10-80nm. It is also worth noting that the hydroxyapatite present in the natural bone is described as being needle-shaped (Kalia et al. 2014).
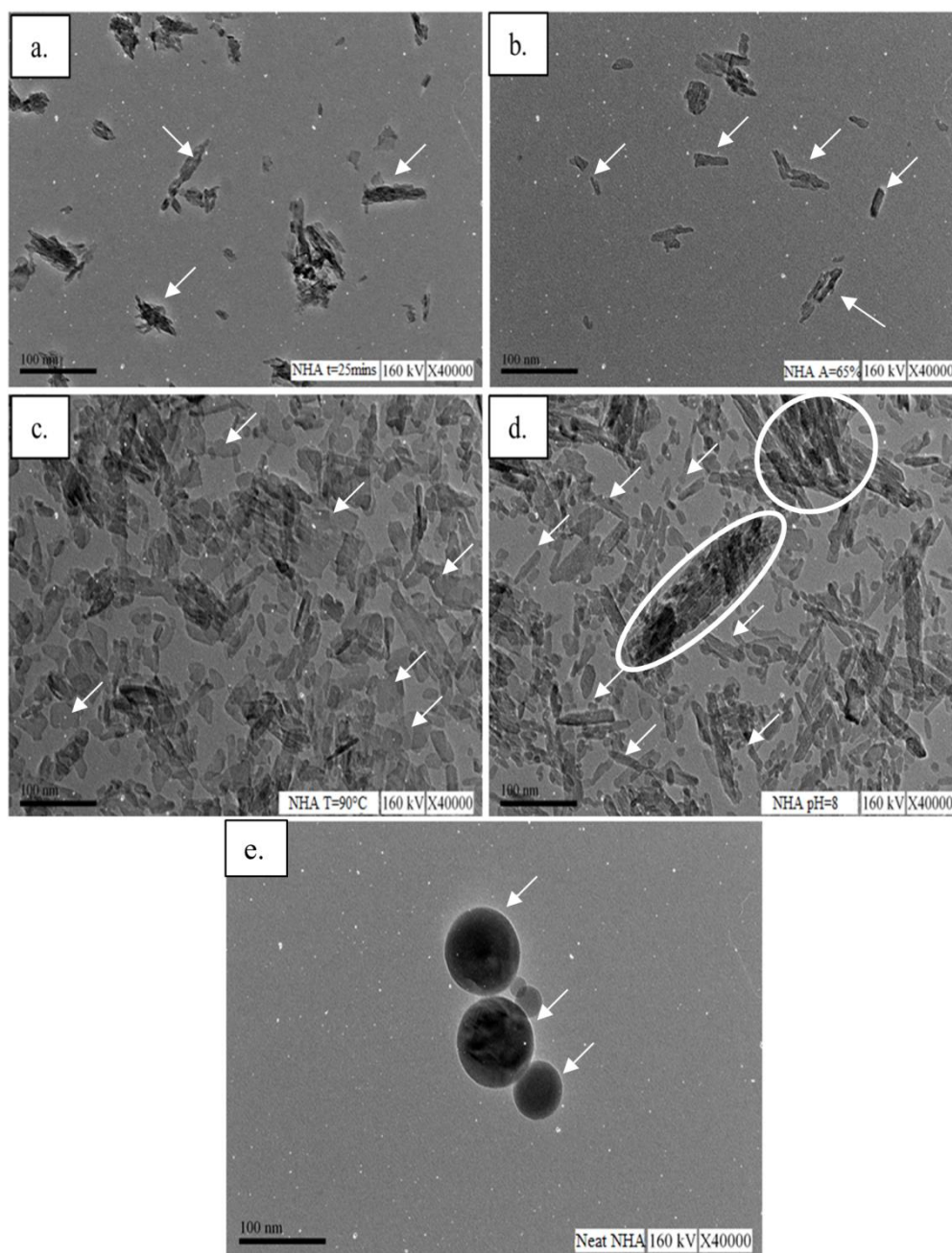
Figure 4.12: TEM micrographs of NHA synthesised at (a) t=25mins, (b) A=65%, (c) T=90°C and (d) pH=8 in comparison to (e) neat NHA

Table 4.2: Comparison between the particle size of the synthesised NHA measured by gas adsorption (BET), TEM, and Zeta-sizer

Sample	BET		TEM	Zeta-sizer	FESEM
	Surface area (m²/g)	Particle size (nm)	Particle size (nm)	Average diameter (nm)	Particle size (nm)
Pure NHA	9.4	200	30-90	-	215.15 ± 3.4
NHA at t=25mins	1.64	115.51	40-100	660.7	254.5 ± 34.5
NHA at A=65%	1.59	119.31	35-85	255.0	153.5 ± 14.25
NHA at T=90ºC	2.65	71.43	45-65	165.5	107.4 ± 2.06
NHA at pH=8	1.74	46.90	55-95	396.1	110.8 ± 6.1

To this point, the effect of four process parameters including reaction temperature (T), solution pH, ultrasonic amplitude (A) and ultrasonic time (t) at a wide range of 50-90°C, 7-9, 50-70% and 10-30mins, respectively, on the synthesis of NHA were studied. With the help of single factor analysis and based on the Ca/P ratio and particle sizes of the synthesised NHA, these ranges were further narrowed down to T= 70-90°C, pH=8, A=60-70% and t=20-25mins. Thus, from this point on, the second part of the first objective i.e. the optimisation of the process parameters using Design of Experiment (DOE) will be discussed.

4.4. Design of Experiment

In this section, the DOE used to optimise the process parameters (reaction temperature, ultrasonic time and amplitude) is response surface methodology (RSM). RSM is an effective statistical technique used in the optimisation of process parameters having three or more factors (Bezerra et al. 2008). The advantage of using RSM is the reduction in the number of experimental runs needed to evaluate multiple process parameters and their interaction. In addition, it is more efficient, easier to arrange and interpret the experimental results compared to others. Therefore, in this chapter central composite design (CCD), one of the RSMs based on 3 factors and 5 level designs is used to obtain the optimum process parameters to synthesis NHA (Bezerra, Santelli et al.

2008) This analysis was based on the thermal stability, particle size and surface area of the NHA.

4.4.1. Modelling of NHA characterisation

The statistical testing of the model was performed in the form of f-test analysis of variance (ANOVA) where the fitted quadratic polynomial model of the characterisation tests is summarised in Table 4.3. Through multiple regression analysis on the experimental data, the model for the predicted responses of particle size (FESEM) (Y1), particle size (BET) (Y2), surface area (Y3), and the remaining weight (Y4) could be expressed by the following quadratic polynomial equations in terms of coded factors as shown in Equation 4.1-Equation **4.4**, respectively, where A= reaction temperature, B= ultrasonic time and C= ultrasonic amplitude.

$$Y_1 = 127.34 + 7.22A + 4.64B + 0.26C + 16.14A^2 + 18.35B^2 - 0.87C^2 - 2.10AB + 2.80AC - 15.34BC \qquad \textbf{Equation 4.1}$$

$$Y_2 = 25.42 + 4.11A + 3.85B + 0.016C - 3.30A^2 + 8.69B^2 - 2.22C^2 - 0.50AB - 5.13AC - 2.27BC \qquad \textbf{Equation 4.2}$$

$$Y_3 = 77.33 - 9.93A - 6.39B - 2.31C + 13.50A^2 - 19.72B^2 - 0.43C^2 + 1.76AB + 12.21AC + 3.07BC \qquad \textbf{Equation 4.3}$$

$$Y_4 = 65.04 - 3.68A - 9.95B - 2.31C - 11.62A^2 - 0.25B^2 + 9.83C^2 + 2.24AB + 4.68AC + 4.35BC \qquad \textbf{Equation 4.4}$$

From Table 4.3, the determination coefficient (R^2) for particle size (FESEM and BET), surface area (BET) and weight remaining (TGA) was 0.9659, 0.9148, 0.9076 and 0.9547, respectively. This implies that 96.59%, 91.48%, 90.76% and 95.47% of the variations could be explained by the fitted model. For a good statistical model, R^2 adj should be close to R^2 where the R^2 adj for particle size (FESEM and BET), surface area (BET) and weight remaining (TGA) was

0.9044, 0.7615, 0.7413 and 0.8732, respectively. This in turn would mean that only 9.56%, 23.85%, 25.87% and 12.68% of the total variations were not explained by the model. However, the reliability and correlation between the actual and predicted values are indicated by the coefficient of variance (CV). From Table 4.3, the relatively low CV values for particle size (FESEM) (4.48%), particle size (BET) (11.52%), surface area (BET) (10.17%) and weight remaining (TGA) (4.02%) indicate high degree of correlation between the actual and predicted values. Furthermore, the significance of the model was also analysed by the F-value and p-value as shown in Table 4.3. This is because, the R^2 and CV values become more significant if the F-value is greater and p-value is less. As a result, the F-value and p-value of the model for particle size (FESEM and BET), surface area (BET) and weight remaining (TGA) were 15.72 and 0.037, 5.97 and 0.0317, 5.46 and 0.0381, 11.71 and 0.0072, respectively. This implies that the model is significant since all the p-values are less than 0.05.

Table 4.3: Analysis of variance for the fitted quadratic model of the characterisation of NHA synthesised

Source	FESEM Particle size (nm)					BET Particle size (nm)					BET surface area (m^2/g)					TGA Wt remaining (wt %)				
	SS	DF	MS	F-value	p-value	SS	DF	MS	F-value	p-value	SS	DF	MS	F-value	p-value	SS	DF	MS	F-value	p-value
Model	5876	9	652.9	15.72	0.0037	536.5	9	59.61	5.97	0.0317	2655.9	9	295.1	5.46	0.038	733.7	9	81.52	11.71	0.0072
Residual	207.7	5	41.54			49.96	5	9.99			270.40	5	54.08			34.80	5	6.96		
Lack of fit	207.7	2	103.8			49.96	2	24.98			270.40	2	135.2			34.80	2	17.40		
Pure error	0	3	0			0	3	0			0	3	0			0	3	0		
Cor. total	6983	17				689	17				3599.9	17				921.6	17			
	R^2=0.9659, Adj R^2=0.9044, C.V.=4.48					R^2=0.9148, Adj R^2=0.7615, C.V.=11.52					R^2=0.9076, Adj R^2=0.7413, C.V.=10.17					R^2=0.9547, Adj R^2=0.8732, C.V.=4.02				

4.4.2.   Analysis of response surface

Figures 4.13 - 4.16 depict the relationship between the independent and dependent variables by a 3-D representation of the response surfaces and 2-D contours generated by the model. Generally, contour plots relate the different interactions between the variables, indicating the significance of the interactions between the variables. The 3-D response surfaces on the other hand indicate the direction in which the original design must be placed to reach optimal conditions. These response surfaces are characterised based on their points located within the experimental regions, for instance, as either maximum, minimum or saddle (Bezerra, Santelli et al. 2008). Saddle points are inflexion points between relatively maximum and minimum points. In this case, increasing or decreasing both variables at the same time will lead to a decrease in response. Nevertheless, increasing one variable while decreasing the other will increase in the response.

Table 4.4 summarises the descriptions of the response surfaces and contour plots of the model. As a result, the 3-D response surfaces, from Figure 4.13 showed minimum points located within the experimental regions for all variable interactions. However, Figures 4.14 − 4.16 showed maximum points located within the experimental regions, especially for combinations of temperature and amplitude, amplitude and time as well as time and temperature, respectively. For the rest of variable interactions, Figures 4.14 − 4.16 presented saddle points. That being said, the contour plots for all the variables showed a significant interaction between each other. These were further complemented with the p-value obtained from the quadratic model, which was 0.0455, 0.0277, 0.0215 and 0.0242 for particle size (FESEM and BET), surface area (BET) and weight remaining (TGA), respectively.

Table 4.4: Summarised description of the response surfaces and contour plots

Figures	Variable interaction	Response surface plot
4.13	Ultrasonic time vs temperature	Minimum point located inside the experimental region
	Amplitude vs temperature	Minimum point located inside the experimental region
	Amplitude vs ultrasonic time	Minimum point located inside the experimental region
4.14	Ultrasonic time vs temperature	Saddle points -inflexion points between relatively maximum and minimum
	Amplitude vs temperature	Maximum point located inside the experimental region
	Amplitude vs ultrasonic time	Saddle points which are inflexion points between relatively maximum and minimum
4.15	Ultrasonic time vs temperature	Saddle points which are inflexion points between relatively maximum and minimum
	Amplitude vs temperature	Minimum point located inside the experimental region
	Amplitude vs ultrasonic time	Maximum point located inside the experimental region
4.16	Ultrasonic time vs temperature	Maximum point located inside the experimental region
	Amplitude vs temperature	Saddle points which are inflexion points between relatively maximum and minimum
	Amplitude vs ultrasonic time	Minimum point located inside the experimental region
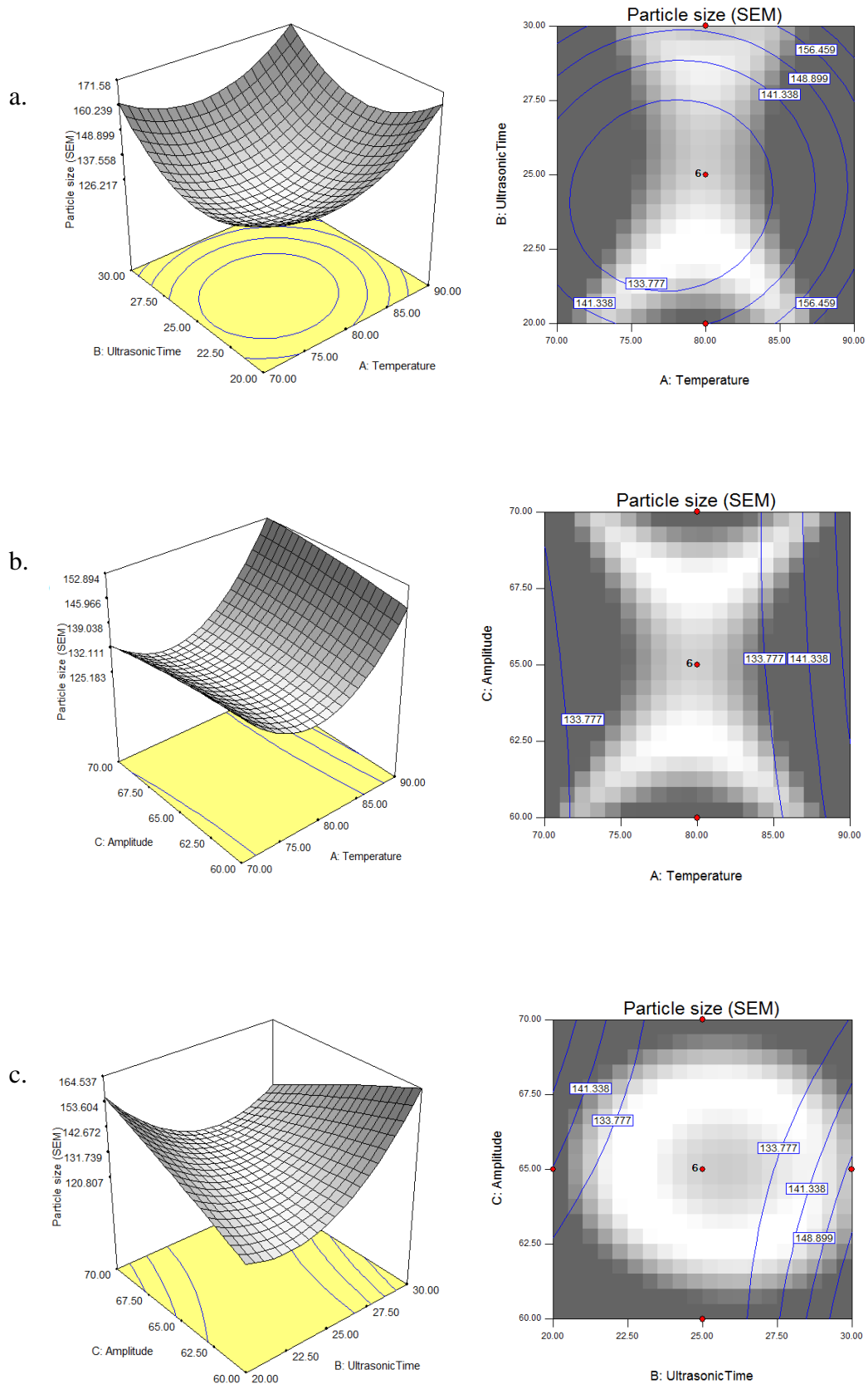
Figure 4.13: Response surface plot and contour plot of reaction temperature, ultrasonic time and amplitude and their effect on the particle size of NHA measured through FESEM
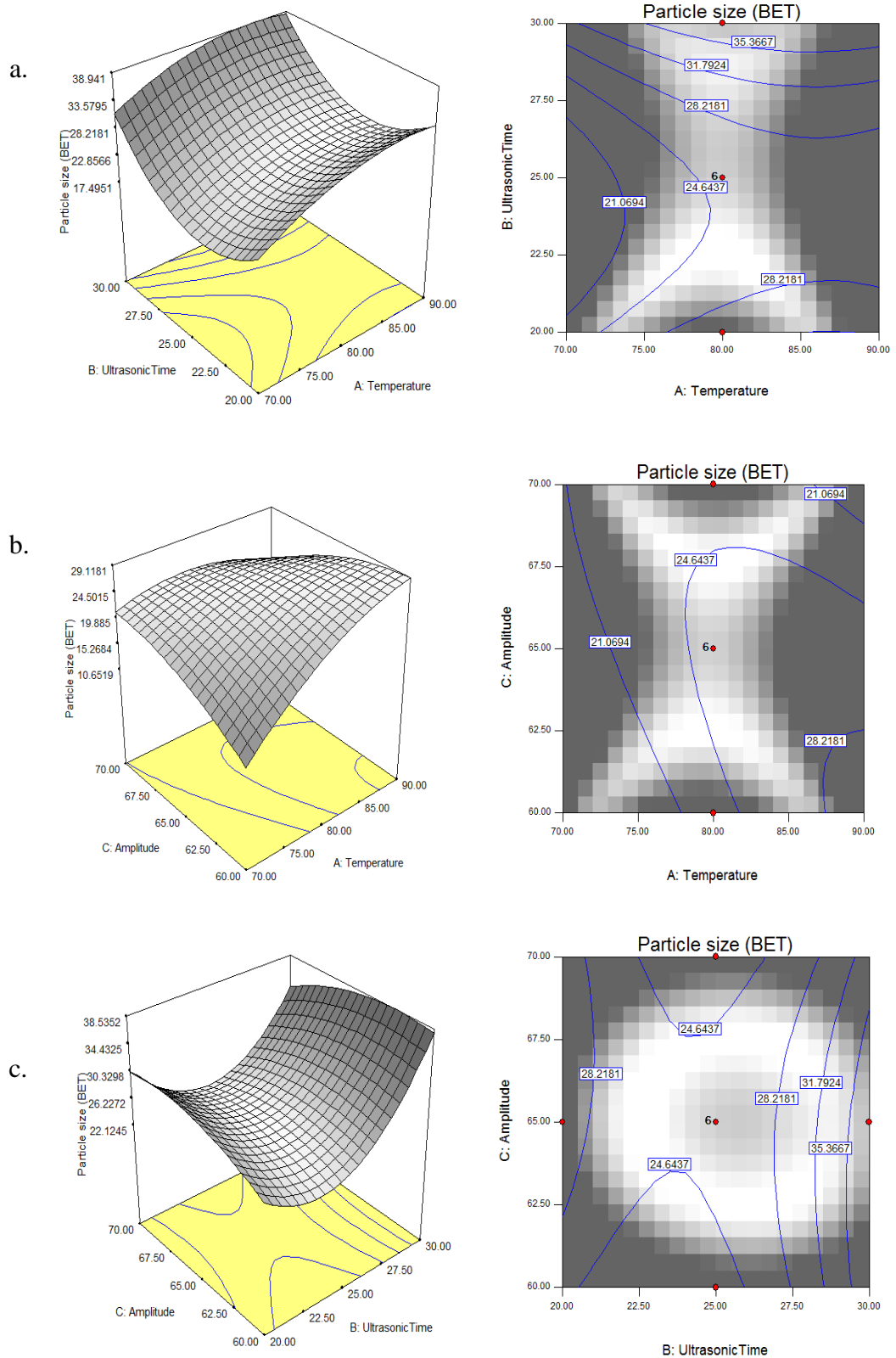
Figure 4.14: Response surface plot and contour plot of reaction temperature, ultrasonic time and amplitude and their effect on the particle size of NHA measured through BET
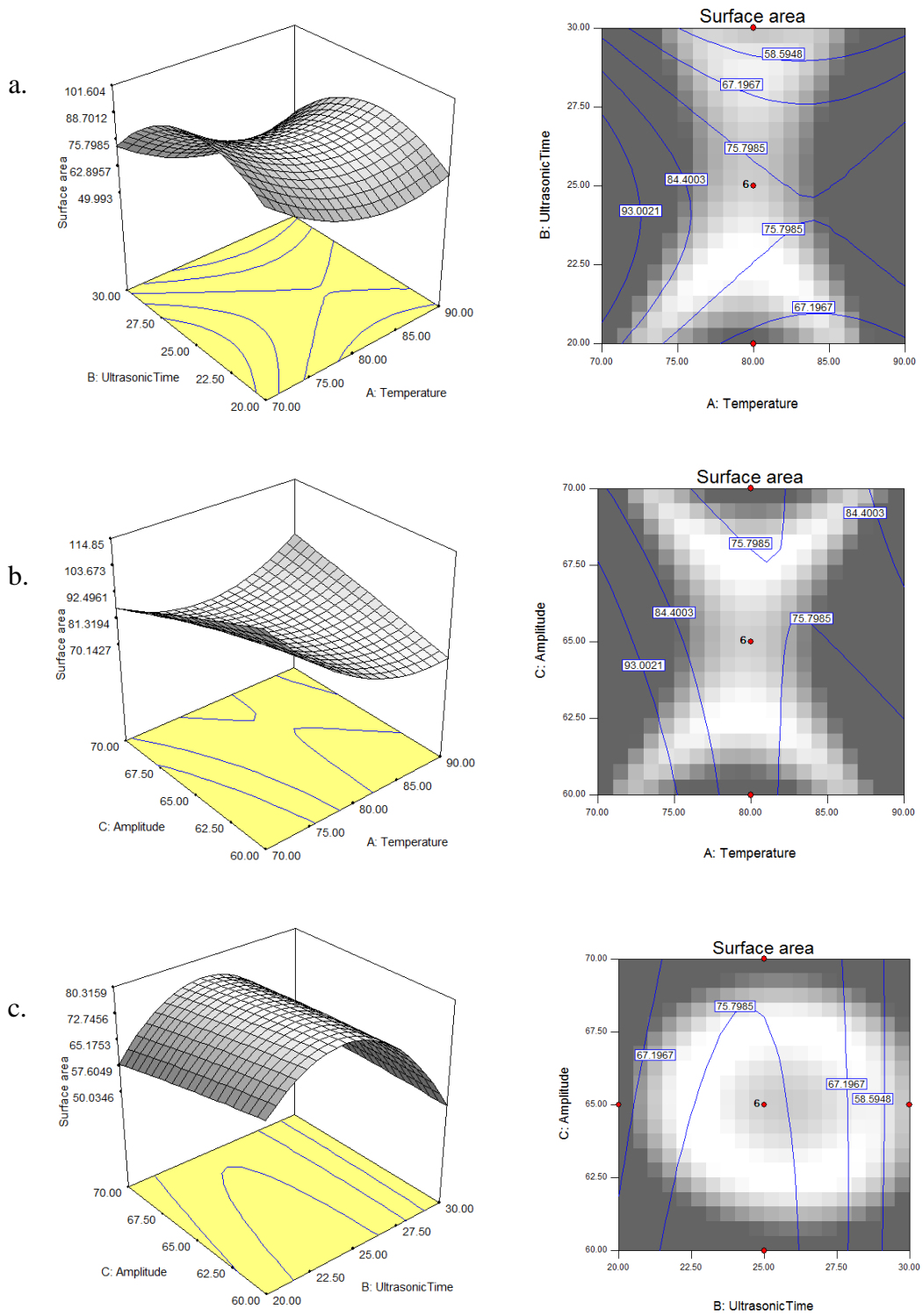
Figure 4.15: Response surface plot and contour plot of reaction temperature, ultrasonic time and amplitude and their effect on the surface area of NHA measured through BET
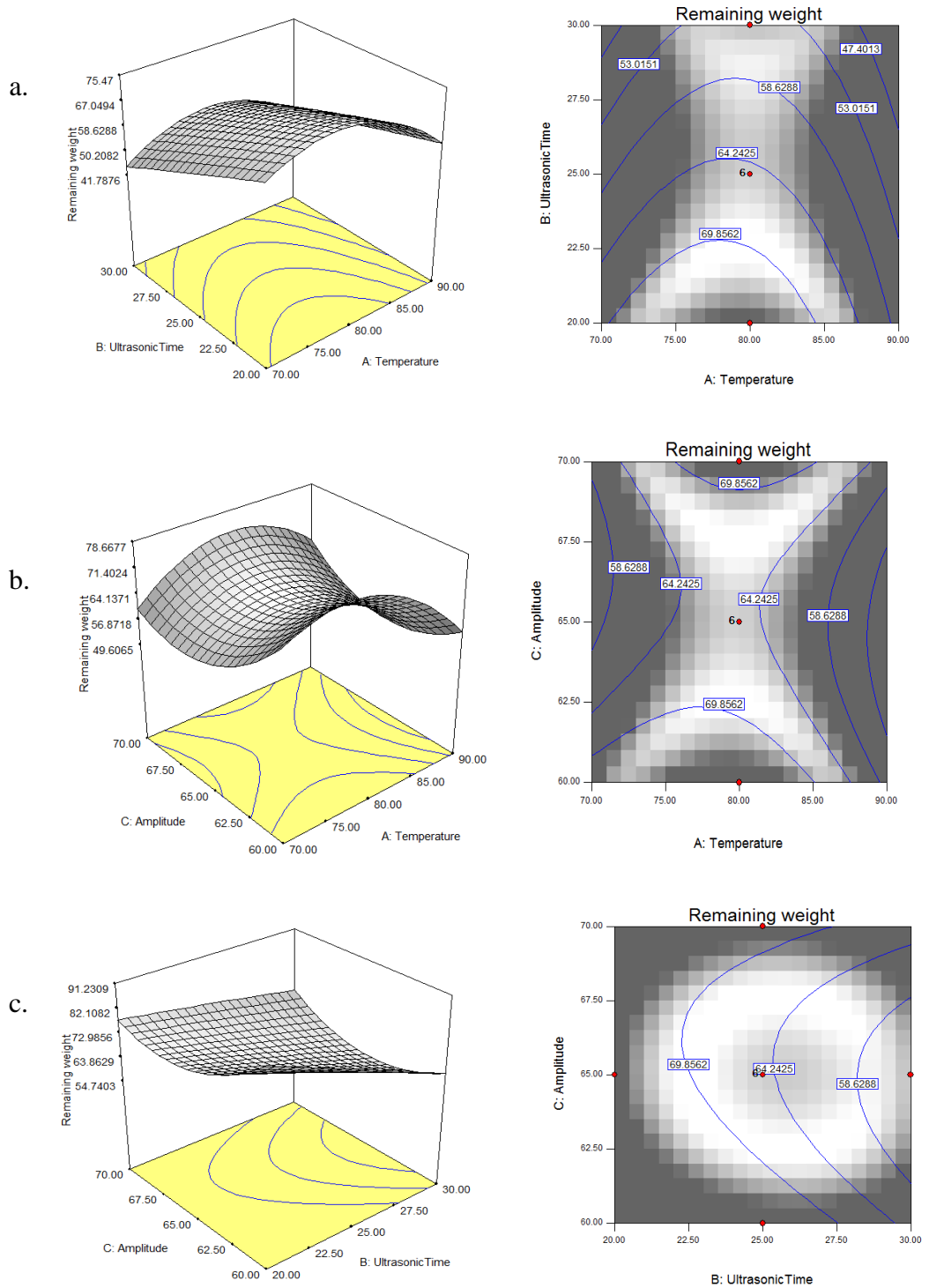
Figure 4.16: Response surface plot and contour plot of reaction temperature, ultrasonic time and amplitude and their effect on the weight loss of NHA after TGA analysis

4.4.3. Optimisation of process parameters

The optimum process parameters for synthesis of NHA powder were determined from the 3-D plots and their respective contour plots. The predicted values for the particle size (FESEM and BET), surface area (BET) and weight remaining (TGA) at the predicted optimum process parameters are shown in Table 4.5. These predicted values were compared with the actual value by synthesising the NHA powder at the optimum process parameters. However, considering the operability of the ultrasonication machine in the actual process, the parameters were modified from T=76.26°C, t=23.52mins, and A=61.43% to T=75°C, t=23.52mins, and A=61%. Therefore, the results obtained based on the modified process parameters were almost similar to the predicted values as the percentage errors were less than ±8% as shown in Table 4.5.

Table 4.5: Optimised conditions and the predicted and actual value of the responses at optimum conditions

	T (°C)	t (min)	A (%)	FESEM-Particle size (nm)	BET-Particle size (nm)	BET-Surface area (m^2/g)	TGA- Wt remaining (wt %)
Predicted value	76.26	23.52	61.43	123.775	20	88.6316	76.7871
Actual value	75	23.52	61	132.9526	20.16	94.1963	72.0847
Percentage error	1.7	0	0.7	-7.4	-0.8	-6.3	6.1

4.4.4. Properties of the synthesised NHA powder

Figure 4.17 depicts the TGA analysis on the thermal degradation properties of the NHA synthesised at an optimised condition. From the figure, the thermal degradation of the synthesised NHA is observed to take place in three stages. The first stage corresponds to the removal of the adsorbed water, whereas the second stage is for the lattice water, each removed at T_1 (25-100°C) and T_2 (200-400°C), respectively (Pramanik et al. 2007). The former is a reversible stage which occurs through dehydration of precipitating complex and loss of physically absorbed water molecules. While the removal of lattice water, is

caused by contraction in the α-lattice dimension during heating. The last stage of degradation of NHA is due to dehydroxylation process which corresponds to weight loss at T_3 (>500°C) (Rhee 2002, Eslami et al. 2010).

Figure 4.18 presents the XRD patterns obtained for the NHA synthesised at an optimised condition. From the result obtained, the synthesis of NHA was confirmed as the peaks present at 2θ angle of 27°, 32-35°, 40-42°, 47-48°, 50°, and 54°, indicate presence of NHA as mentioned in section 4.2.3. Moreover, Figure 4.19 shows the chemical functional groups (FTIR spectrum) and elemental analysis (EDX) as well as the morphology (FESEM and TEM) of the NHA powder synthesised at the optimum parameter. From the FTIR spectrum in Figure 4.19 (a), similar peaks observed in Figure 4.1 are detected, confirming the synthesis of NHA. In particular, the two peaks for stretching and bending modes of PO_4^{3-} are identified at 1029.93 cm^{-1} and 603.52 cm^{-1}, respectively. Furthermore, at wavelength of 825cm^{-1} presence of acidic phosphate group (HPO_4^{2-}) was detected. Other peaks shown at 1636.43 cm^{-1} and 3138.29 cm^{-1} indicates presence of OH$^-$ ions in the synthesised NHA. Furthermore, presence of nitrate group was detected at bandwidth of 1393.88 cm^{-1}. This is complemented with the EDX result obtained in Figure 4.19 (b), where the presence of nitrogen element is detected due to the ammonium solution used. The elemental analysis further confirmed the synthesis of NHA with a Ca/P ratio of 1.80.

From Figure 4.19 (c), the synthesised NHA was observed to disperse homogeneously. Moreover, the synthesised NHA is a nano-sized and needle-like shape as shown in Figure 4.19 (d). The particle size ranged from 45-65nm. This is more complemented by the particle size distribution measured using zeta-sizer, where the particle size distribution ranged between 50-100nm. Hence, overall the synthesised NHA is indeed nano-sized that resembles the properties of the natural hydroxyapatite found in the bones; chemically and morphologically.
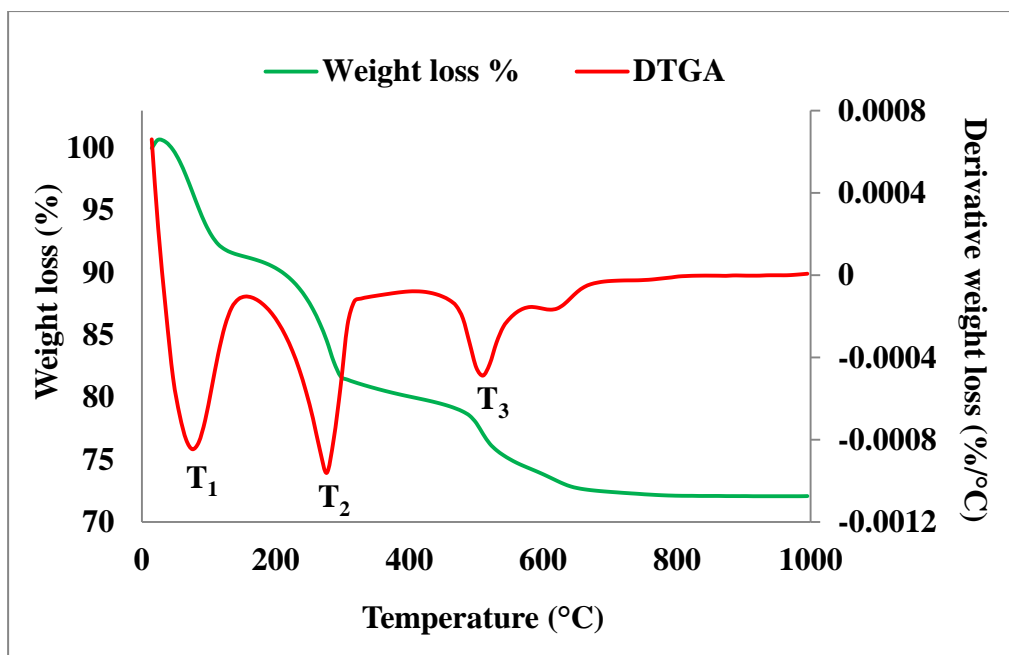
Figure 4.17: TGA result for the NHA synthesised at the optimised condition
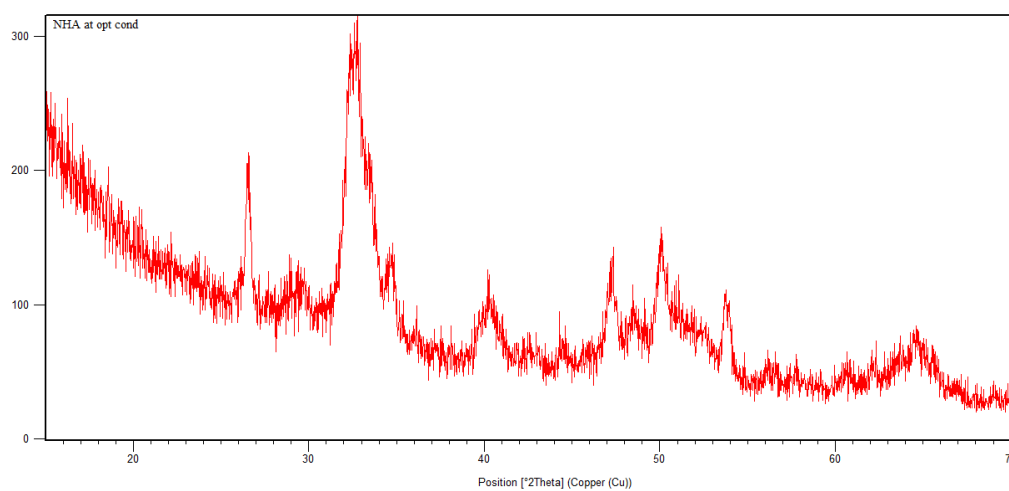
Figure 4.18: XRD patterns for the NHA synthesised at the optimised condition
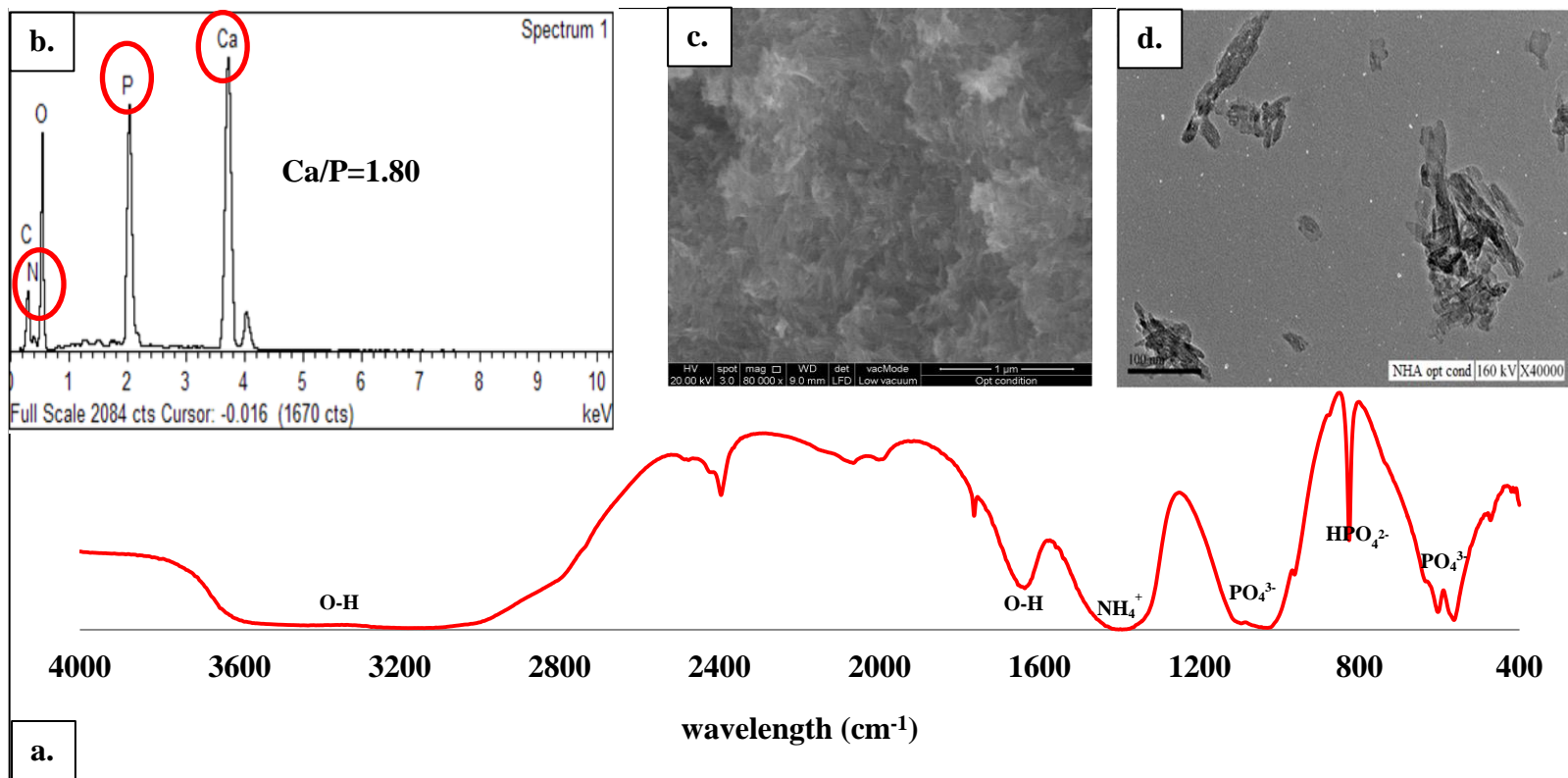
Figure 4.19: Characterisation of NHA synthesised at the optimised condition (a) FTIR spectrum, (b) EDX elementary analysis, (c) FESEM microscopic image and (d) TEM microscopic image

4.5. Summary

The synthesis of NHA using ultrasonication was greatly influenced by process parameters such as reaction temperature, solution pH, ultrasonic amplitude and time. This is because, the energy applied for the ultrasonication to operate is a factor of ultrasonic power (amplitude) and total amount of time that the NHA was sonicated. Thus, alteration of the parameters could cause the NHA particles to either breakdown or in some cases to agglomerate. Consequently, the results of the elementary analysis (EDX), chemical functional groups (FTIR and XRD), particle sizes (FESEM, TEM, BET and zeta-sizer) and particle shapes (TEM) revealed that the synthesised NHA through precipitation method aided with ultrasonication does mimic the NHA present in the human bone, chemically and morphologically. Moreover, with the help of DOE the process parameters for the synthesis of NHA were optimised.

CHAPTER 5

PREPARATION OF POLY-LACTIC ACID NANOCOMPOSITES REINFORCED WITH NHA

5.1. Introduction

In this chapter, the second objective of this study is addressed, whereby the reinforcement of PLA matrix using the synthesised NHA is discussed. Based from the elemental analysis, chemical functional groups, particle size and shapes of the synthesised NHA, it is evident that the synthesised NHA mimics the properties of the hydroxyapatite present in the human bone. Thus, the PLA matrix is reinforced with the synthesised NHA through melt mixing which could be used for load bearing implants related applications. The NHA loading was varied at 1, 2, 3 and 5wt%. Neat PLA was also prepared as a control sample. The changes in mixing torque, chemical, mechanical, thermal and morphological properties of the PLA-NHA nanocomposites with different NHA loading were discussed.

5.2. Mixing Torque

Figure 5.1 depicts the mixing torque-time curve of PLA-NHA nanocomposites in comparison to neat PLA. In general, the first peak at 30 seconds represents the loading peak of PLA. A sharp increase is observed when PLA was charged into the mixing chamber followed by a gradual drop in the torque at about 1 minute. The torque started to stabilise at around 2 minutes, indicating that the PLA underwent full melting and fusion. Hence, when the NHA was charged in at 2 minutes, the mixing torque was observed to increase slightly for 3wt% and 5wt% NHA loading. This is due to the increased viscosity upon the addition of NHA. After a few seconds, the torque is observed to decrease as PLA and NHA melted, signifying the nanocomposite underwent mixing and homogenisation.
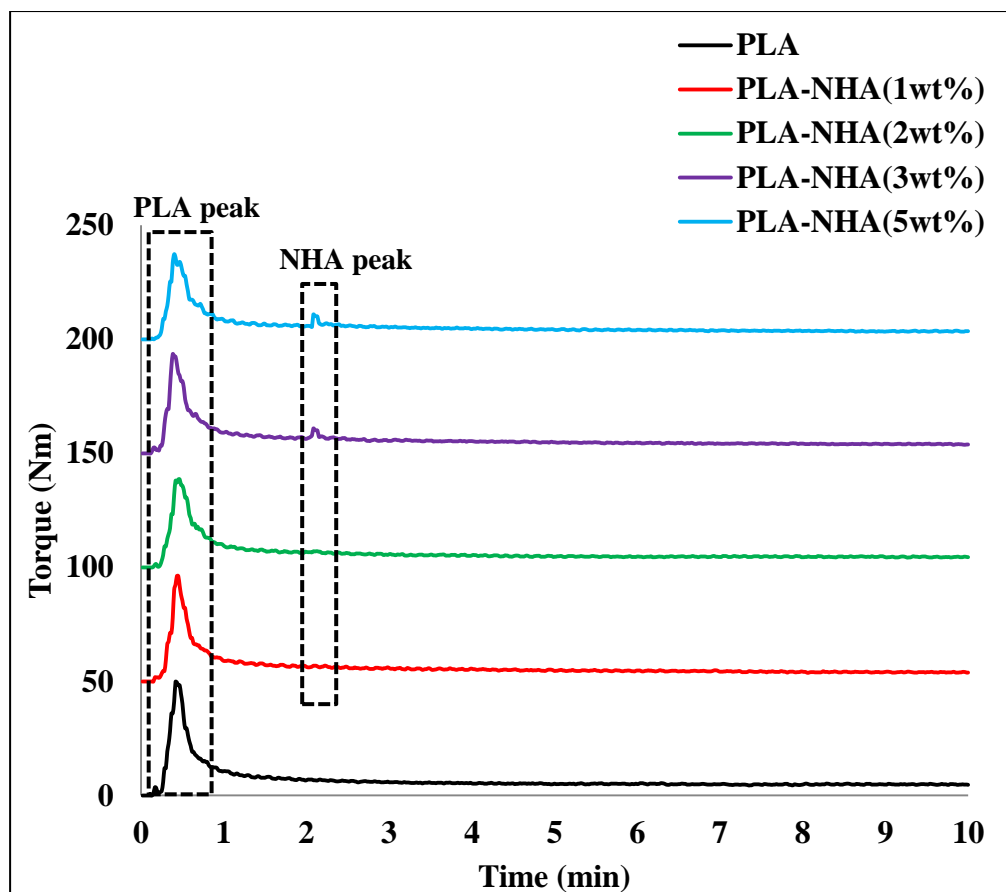
Figure 5.1: Mixing torque graph for PLA and PLA-NHA nanocomposites

5.3. FTIR and Elemental analysis

Figure 5.2 depicts the FTIR spectra of the neat PLA, synthesised NHA and PLA-NHA nanocomposite. The peaks detected at 2989 and 2930cm^{-1} are assigned to the stretching C-H bands present in the PLA matrix. At 1780cm^{-1} wavelength, the stretching C=O band of the PLA matrix is identified. Moreover, the stretching O-H mode of the PLA matrix is also detected at 3600cm^{-1}. However, the peaks spotted within the regions of 600-1400cm^{-1} are usually overlapping peaks, whereby identifying the functional groups present within this region is difficult. Nonetheless, the C-C and C-O modes of the PLA matrix are present within the 900-1100cm^{-1} wavelength. These peaks confirms the presence of PLA (Hoidy et al. 2010, Xu et al. 2012). Similar peaks are detected within the PLA-NHA nanocomposites.

It is evident from previous discussion (chapter 4) that the stretching and bending modes of PO_4^{3-} groups present in the NHA are detected within the wavelength of 600-1000cm^{-1}, also as presented in Figure 5.2. Thus, in comparison to the FTIR spectrum of the synthesised NHA, it can be confirmed that NHA is indeed present in the PLA-NHA nanocomposite as the peaks of PO_4^{3-} groups are detected within the regions of 600-700cm^{-1} wavelength, as indicated by arrow.

Moreover, Figure 5.3 presents the elementary analysis of the neat PLA, synthesised NHA and PLA-NHA nanocomposite. In comparison to the neat PLA (Figure 5.3 (a)) and NHA (Figure 5.3 (b)), the PLA-NHA nanocomposite (Figure 5.3 (c)) consist all the elements present in the PLA matrix and NHA, confirming the presence of both materials in the nanocomposite.
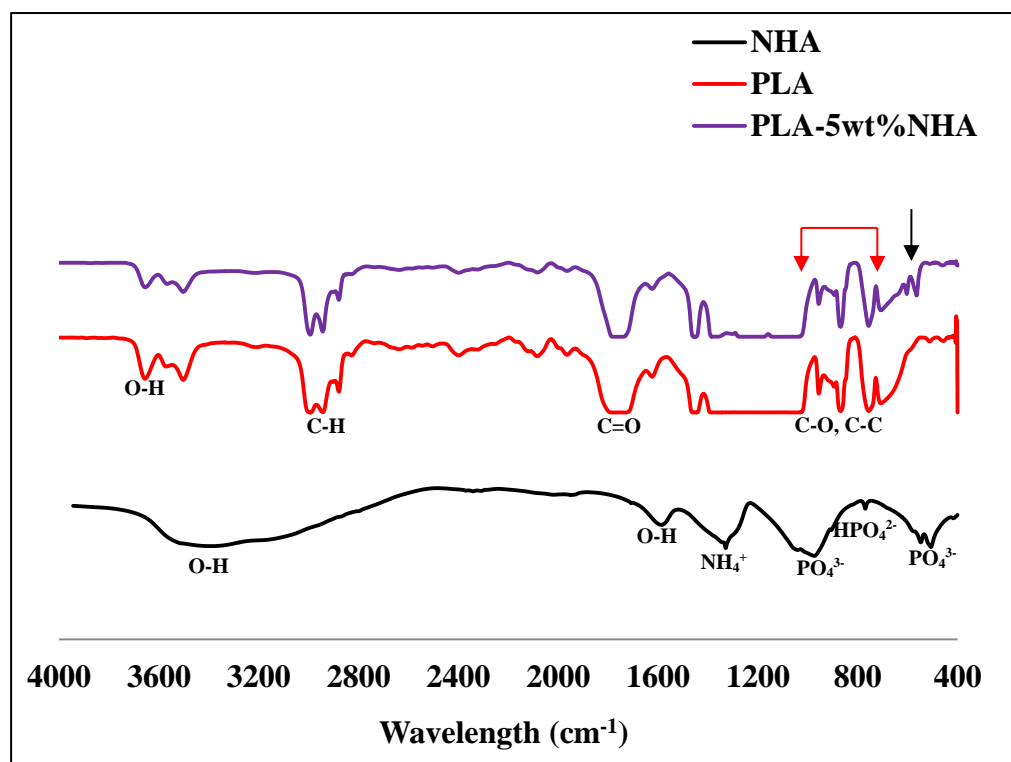
Figure 5.2: FTIR spectra of PLA-NHA nanocomposite with comparison to neat PLA and NHA
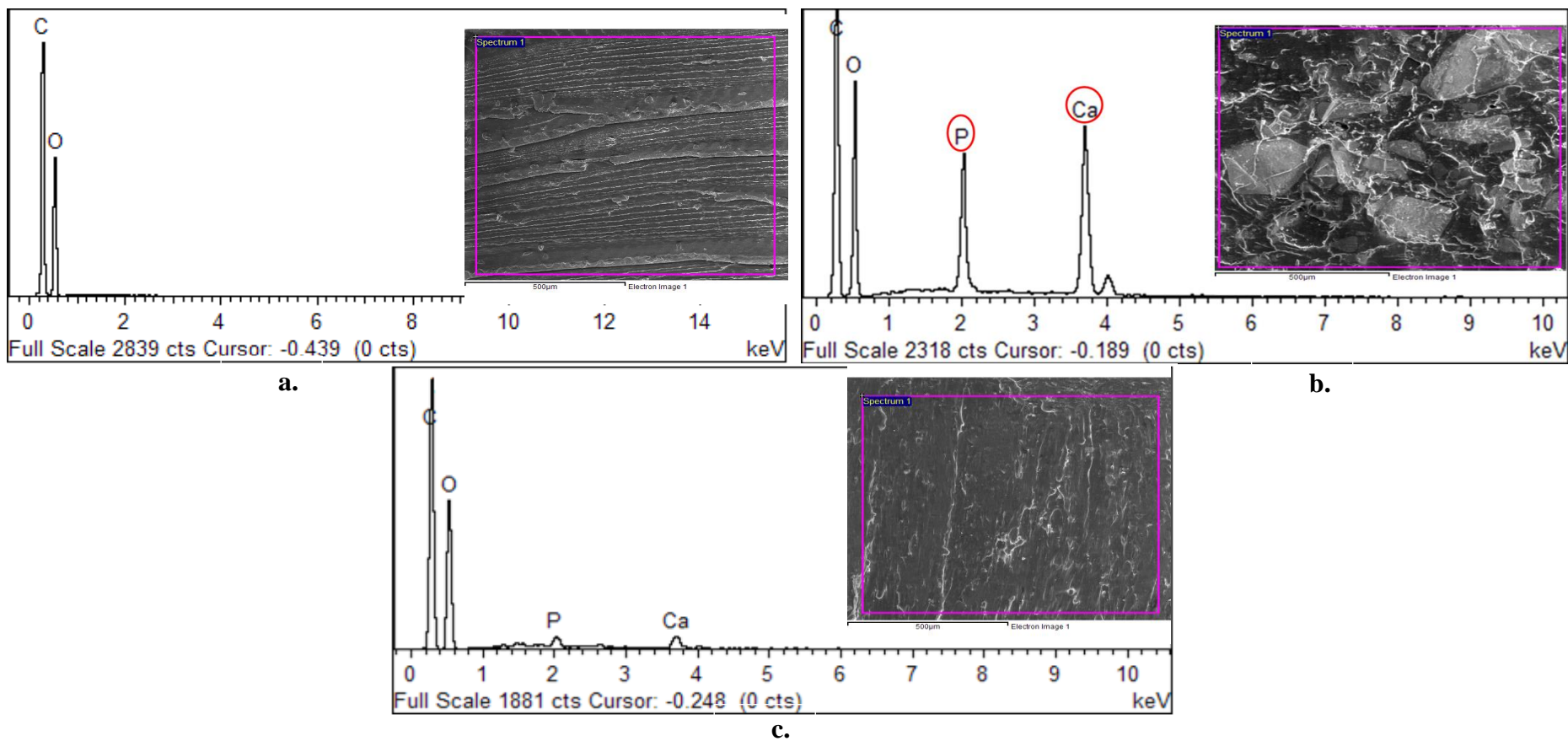
Figure 5.3: Microstructure image and EDX analysis of (a) PLA, (b) NHA and (c) PLA-NHA nanocomposite

5.4. Mechanical Properties

5.4.1. Tensile Properties

Figure 5.4 presents the tensile properties of the PLA-NHA nanocomposites prepared in comparison to neat PLA. Initially, improvement in the tensile strength and modulus of the nanocomposite was observed, followed by a gradual decline. With an addition of 1wt% of NHA, the tensile strength and modulus increased by 0.7% and 10.6%, respectively, in respect to neat PLA. Further increase in NHA loading to 5wt% of NHA caused the tensile strength and modulus to decrease by 15.6% and 1.1%, respectively, in comparison to neat PLA. In addition, in respect to the PLA-1wt%NHA, the tensile strength and modulus of the PLA-5wt%NHA decreased by 16.1% and 10.6%, respectively.

Generally, the improvement noted in the tensile properties of PLA-NHA nanocomposite at a lower NHA loading (1wt%) can be credited to the well dispersed NHA in the PLA matrix, thus reinforcing the PLA matrix. Aside from dispersion, the interfacial adhesion between the PLA matrix and NHA also played role in the improvement of the tensile properties. As such, the weak van der Waals forces formed between the PLA matrix and NHA helped transferring stress between the NHA and PLA matrix, subsequently, contributing to the increase in tensile modulus and strength to some extent. Nonetheless, after the formation of agglomeration (at a higher NHA loading) the tensile strength tends to decrease due to stress reinforcement around NHA (Fu and Naguib 2006). The formation of agglomeration could be due to melt mixing being not suitable technique to prepare nanocomposites with higher nanofiller loading (Roeder et al. 2008). The presence of agglomeration and the weak interfacial adhesion between the PLA matrix and NHA at a higher loading can be observed in the FESEM micrographs, discussed later in section 5.6.

It is worth noting that, even though the tensile strength decreased upon increase in NHA loading, the results obtained for PLA-(1-3)wt% NHA nanocomposites are able to mimic the tensile strength of cortical bones (50-60MPa) (Roeder, Converse et al. 2008). Similarly, the tensile strength and modulus of the PLA-

5wt%NHA nanocomposite is still within the range of cancellous bones which are 0.1-30MPa and 20-500MPa, respectively (Keaveny 1998, Mozafari, Rabiee et al. 2010).
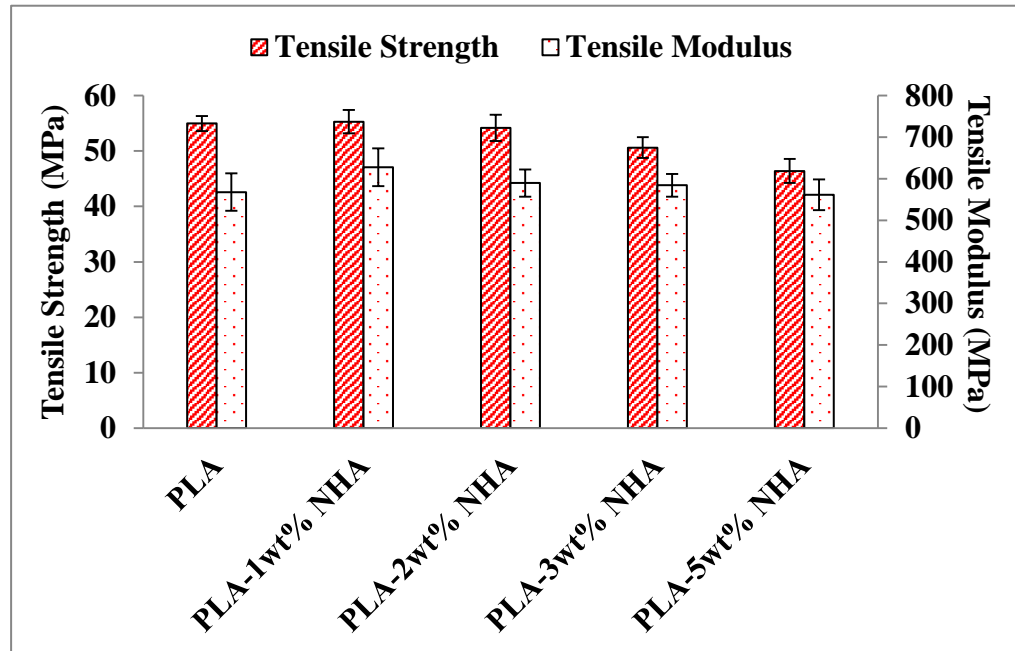
Figure 5.4: Tensile properties of the PLA-NHA nanocomposites in comparison to neat PLA

5.4.2. Impact Strength

Figure 5.5 shows the impact strength of the PLA-NHA nanocomposites prepared in comparison to neat PLA. In contrast to the tensile properties, the impact strength of the PLA-NHA nanocomposites displayed a general increase upon increased NHA loading. For instance, with addition of only 1wt% NHA, the impact strength of neat PLA increased by 14.8%. Optimum impact strength was obtained upon addition of 3wt% NHA; which was 27.2% and 10.8% higher than the neat PLA and PLA-1wt%NHA nanocomposite, respectively. However, further increase to 5wt% NHA loading contributed to slight decrease in the impact strength of the nanocomposite by 4.4% in respect to the PLA-3wt% NHA, while the value is still 21.6% higher than the neat PLA (Wetzel et al. 2002).

The continuous increase in the impact strength of the PLA nanocomposites observed as the NHA loading increased, suggests the PLA became less brittle upon addition of NHA (Kumar et al. 2010). Generally, incorporating nanofillers into polymer matrix reduces the mobility of the polymer chain segments, hence inducing lower impact resistance. However, formation of agglomerates causes the stress to be concentrated around the filler, hence increasing the impact strength (Salehi Vaziri et al. 2011), while causing the tensile strength to reduce as reported earlier upon higher NHA loading.
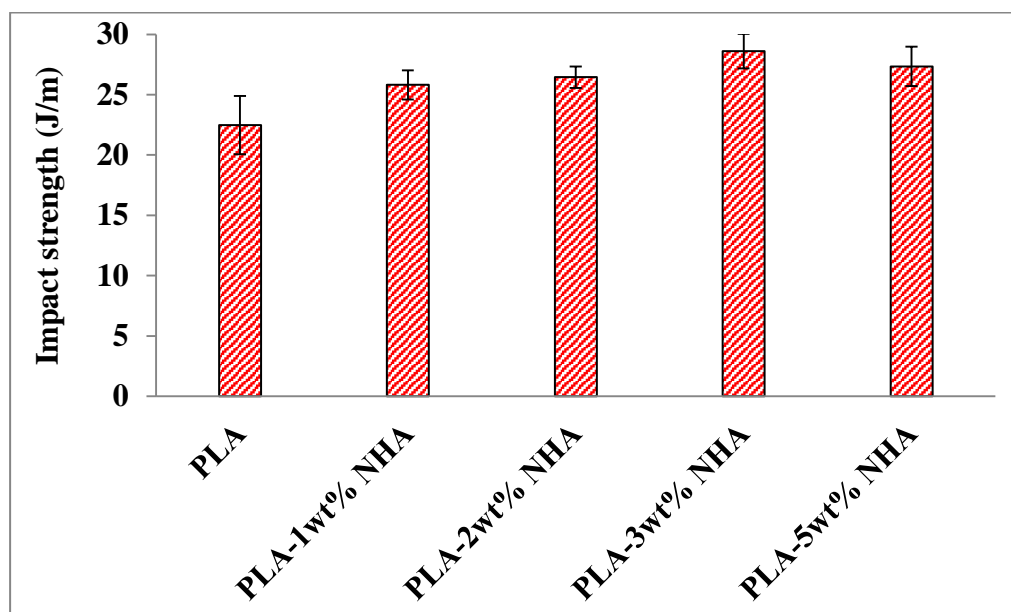
Figure 5.5: Impact strength of the PLA-NHA nanocomposites in comparison to neat PLA

5.5. Thermal Stability

5.5.1. TGA

Figure 5.6 depicts the weight loss and derivative TGA thermograms for the prepared PLA-NHA in comparison to neat PLA. In general, one-step degradation process was observed for all the nanocomposites. The TGA thermograms show that the degradation of the nanocomposites started around 330°C and is completed around 390°C. As mentioned in section 4.4.4, the NHA nanofiller does not undergo thermal degradation within this range of temperature. Hence, the drastic weight loss is caused by the complete

degradation of the neat PLA at a high temperature (Liu, Chen et al. 2015). In addition, Table 5.1 summaries the data obtained from the weight loss and derivative TGA thermograms in respect to the thermal properties of the synthesised NHA reported in chapter 4.

The maximum weight loss of the neat PLA was observed to take place at temperature (T_{max}) of 367.5°C (Liu et al. 2010). Addition of NHA into the PLA matrix caused the T_{max} to shift within the range of ~363-369.5°C. Generally, incorporating nanofiller in the PLA matrix restricts the PLA chain mobility, causing the viscosity to increase, mainly at higher NHA loading. This was observed from the mixing torque reported in section 5.2, whereby as the NHA loading increased the mixing torque was increased. Thus, when the PLA chain movement is restricted, higher temperature is required to melt the composite and making it viscous. As a result, all the PLA-NHA nanocomposites displayed equal or higher T_{max} compared to neat PLA, except for PLA-1wt%NHA. This is because, addition of 1wt% was not enough to restrict the PLA, just like the mixing torque was not increased when only 1wt% NHA was added. However, further addition of NHA resulted in delay in temperature of the initial weight losses, as evidenced by the 5wt% ($T_{5\%}$), 10wt% ($T_{10\%}$) and 50wt% ($T_{50\%}$) of the PLA-NHA nanocomposites compared to the neat PLA. The ~5°C increase in the $T_{5\%}$, $T_{10\%}$ and $T_{50\%}$ can be attributed to restriction of the PLA chain mobility due to the presence of NHA (Wan, Wu et al. 2015). This in turn, indicates the thermal stability of PLA improved upon addition of NHA. It was also noted that the remaining weight of the nanocomposite increased proportionally with NHA loading. This is credited to the remaining weight of 72wt% after the degradation of the NHA (discussed in section 4.4.4).
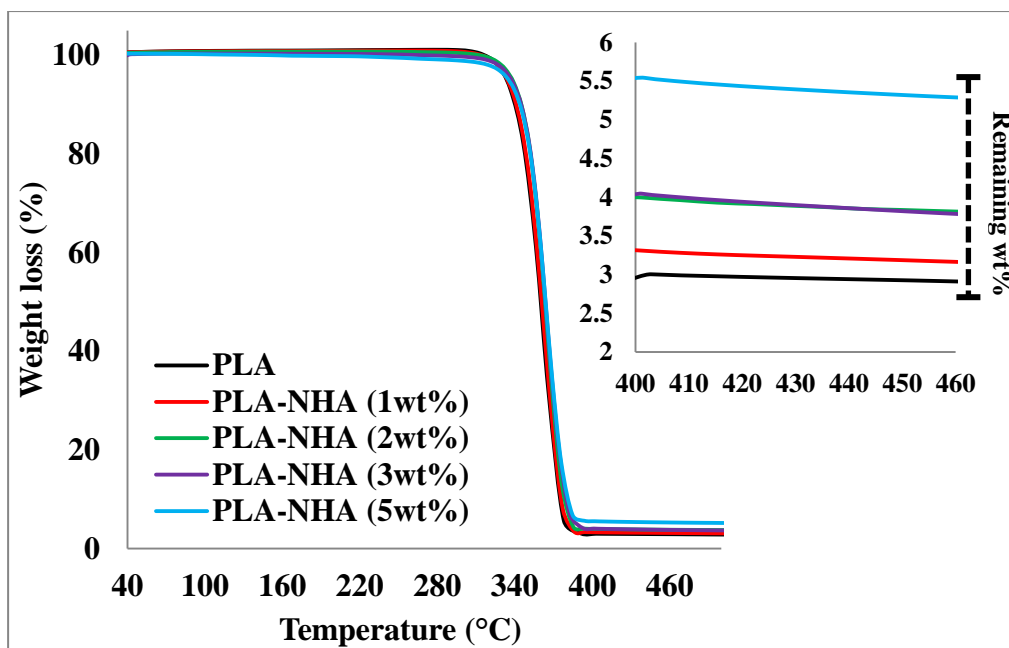
(a)
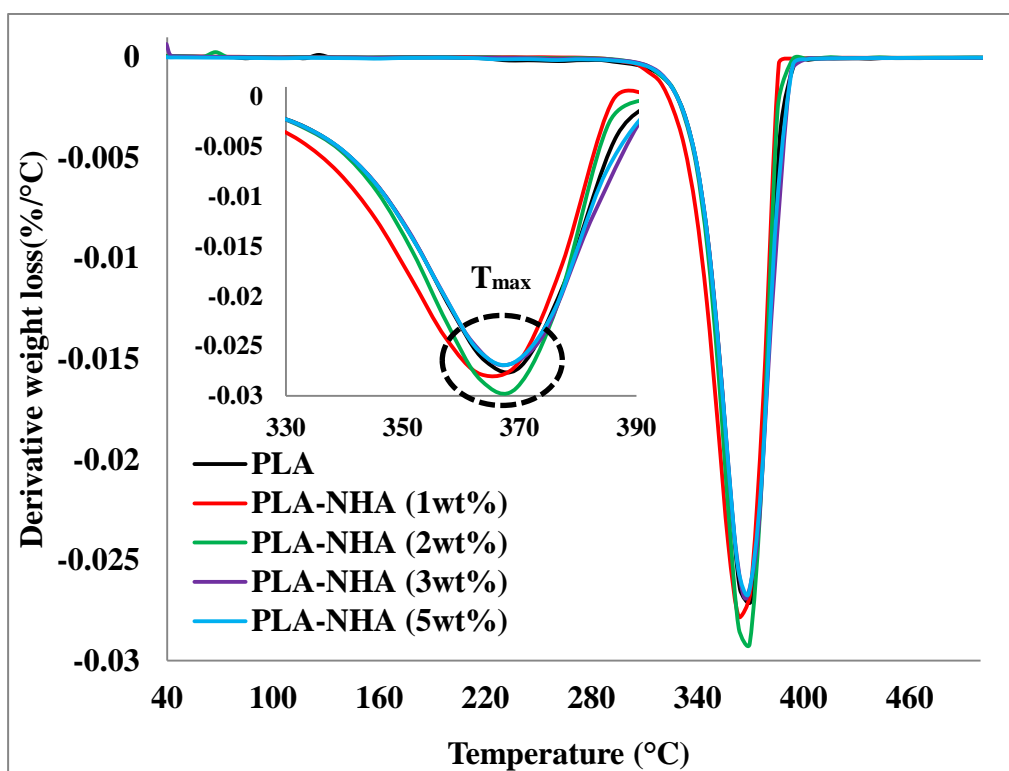
(b)

Figure 5.6: TGA thermogram for PLA-NHA nanocomposites in comparison to neat PLA (a) weight loss curve and (b) derivative curve

Table 5.1: Degradation temperatures and remaining weight of the PLA-NHA nanocomposites in respect to the PLA and NHA (chapter 4)

Sample	Degradation Temperature (°C)				Remaining wt (%)
	$T_{5\%}$	$T_{10\%}$	$T_{50\%}$	T_{max}	
NHA	89.23	209.96	-	671.2	72.0847
PLA	332.8	339.4	360.1	367.5	2.91
PLA-1wt% NHA	332.5	339.1	360.8	363.4	3.15
PLA-2wt% NHA	339.3	345.6	363.4	369.5	3.79
PLA-3wt% NHA	338.9	345.2	364.6	367.8	3.79
PLA-5wt% NHA	332.8	339.4	360.1	368.9	5.29

5.5.2. DSC

Figure 5.7 illustrates DSC curves for the PLA-NHA nanocomposites in comparison to neat PLA**.** From the figure, two peaks were observed, each representing the crystallisation (T_c) and melting (T_m) temperatures of the nanocomposites. Table 5.2 summaries the data obtained from the DSC curves. Generally, the T_c of the nanocomposites was observed to decrease while the T_m increased with addition of NHA. The T_c and T_m of the neat PLA were recorded as 120.2°C and 151.8°C, respectively. The T_c of the nanocomposites was observed to decrease to ~118°C while the T_m increased to ~160°C. However, both temperatures of the nanocomposites remained unaltered upon further addition of NHA.

As mentioned in section 2.7.1, T_c is the temperature at which polymers start to form crystals whereas T_m is the temperature at which the polymer starts to change from solid to liquid. Hence, upon addition of NHA, the formation of PLA crystals is facilitated, thus the T_c for the nanocomposites is reduced by 7°C. This is due to the nucleating effect of the NHA as a nanofiller (Balakrishnan et al. 2010, Persson et al. 2013). That being said, the nucleation process is strongly affected by the dispersion of the NHA in the PLA matrix. In other words, formation of NHA agglomerates can delay the formation of PLA crystals. Moreover, the formation of PLA crystals makes the melting behaviour much more complex, causing hindrance in the PLA chain mobility within the

nanocomposite (Phang et al. 2004). This led to the increase in melting temperature by ~8°C with addition of NHA in comparison to neat PLA.
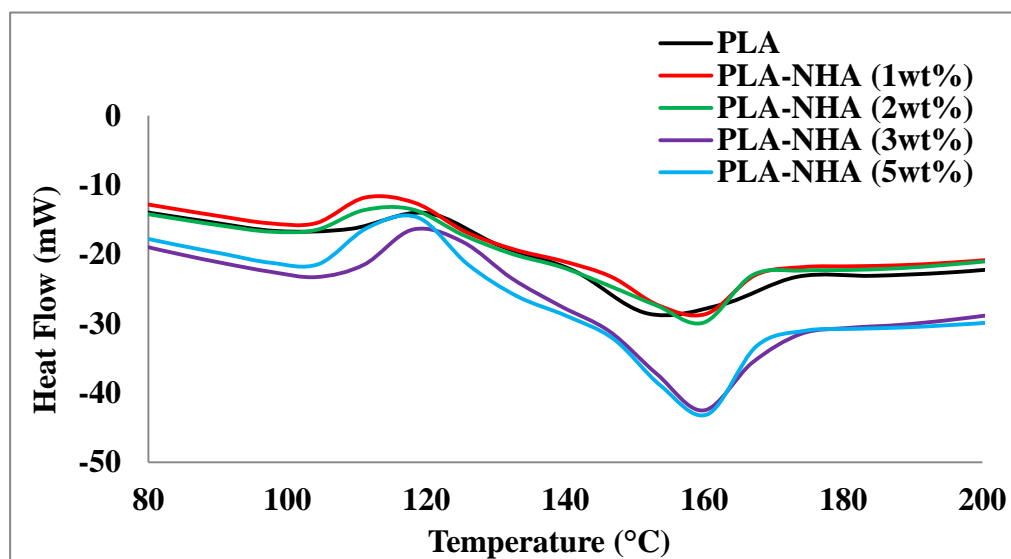
Figure 5.7: DSC curve for PLA-NHA nanocomposites in comparison to neat PLA

Table 5.2: DSC analysis of the PLA-NHA nanocomposites in respect to the PLA

Sample	Crystallisation Peak		Melting Peak	
	T_c (°C)	HF (mW)	T_m	HF (mW)
PLA	120.2	-17.19	151.8	-28.53
PLA-1wt% NHA	118.4	-12.61	160.3	-28.58
PLA-2wt% NHA	118.0	-13.54	160.2	-29.41
PLA-3wt% NHA	118.9	-21.44	160.4	-43.07
PLA-5wt% NHA	118.8	-14.69	160.5	-43.08

5.6. Fracture Surface Morphology

Figure 5.8 depicts the FESEM micrographs of the impact fractured PLA-NHA nanocomposites with 1, 3, 5wt% NHA loading in respect to neat PLA. It can be seen that neat PLA exhibits a relatively smooth fracture with folds of wavy lines, indicating typical brittle fracture behaviour (Figure 5.8 (a)). Compared to the neat PLA, the fracture surfaces of PLA-NHA nanocomposites showed

considerably different fractured surfaces whereby much rougher fracture surfaces are observed as the loading of NHA increased (Figure 5.8 (b-d)).

Upon addition of 3wt% NHA, presence of void around the NHA agglomerate can be observed (as shown by the circle) in Figure 5.8 (c). Formation of more agglomerates were observed with further increase in NHA loading (5wt%), as indicated by the circles in Figure 5.8 (d). Moreover, the poor interfacial adhesion of the PLA matrix with the NHA at a higher loading (3 and 5wt%) is observed in Figure 5.8 (c and d). These observations are in line with the decrease in mechanical properties observed with addition of 5wt% of NHA.
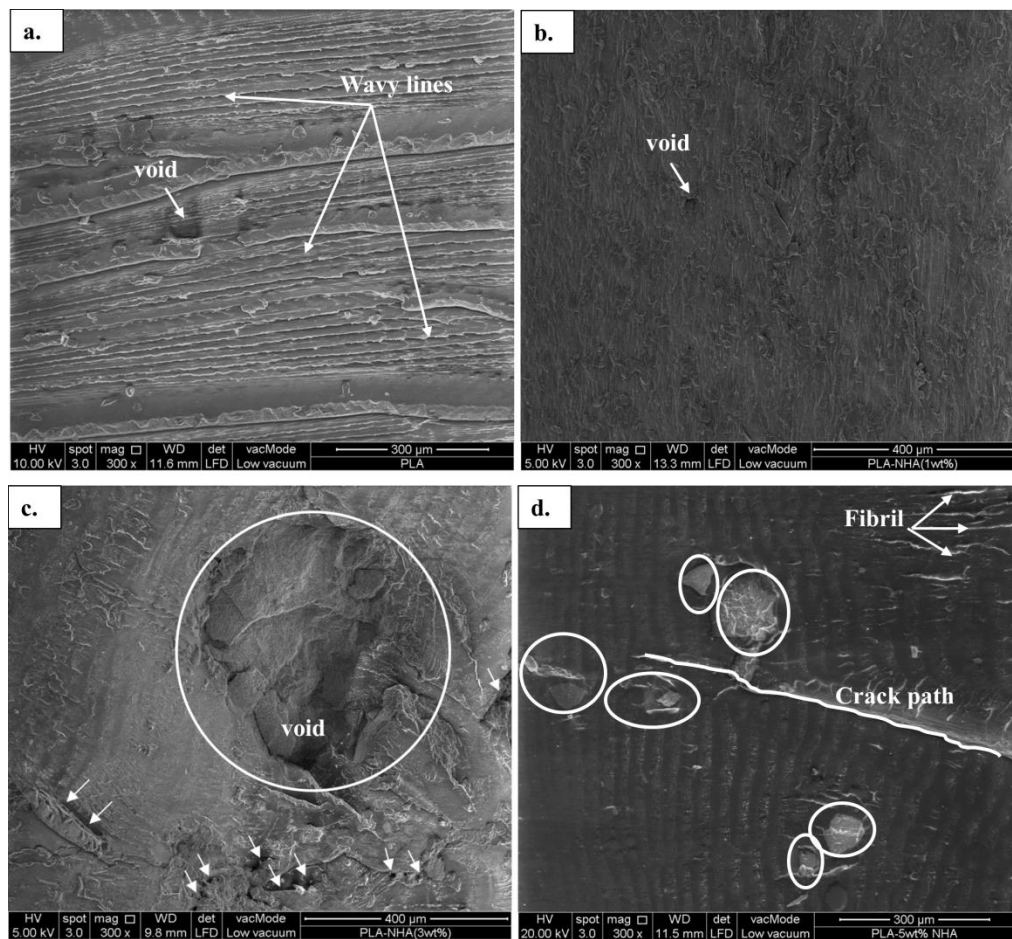
Figure 5.8: Impact fracture surface of (a) neat PLA, (b) PLA-1wt%NHA, (c) PLA-3wt%NHA and (d) PLA-5wt%NHA

5.7. Summary

Addition of NHA improved the mechanical and thermal properties of PLA-NHA nanocomposites. Results on the TGA and DSC revealed that the thermal stability exhibited slight improvement upon addition of NHA. Similarly, the results for impact strength suggested the brittleness behaviour reduced as the NHA loading increased. In contrast, the tensile properties were improved only at a lower NHA loading (1wt%), whereby upon higher loading the properties deteriorated. The FESEM microstructural images showed formation of NHA agglomerates as well as poor interfacial adhesion between the PLA matrix and NHA, hence explaining the reduction in tensile properties.

CHAPTER 6

PREPARATION OF POLY-LACTIC ACID NANOCOMPOSITES REINFORCED WITH SURFACE MODIFIED NHA (mNHA)

6.1. Introduction

This chapter addresses the third objective of this study, whereby the surface modification of the NHA prior to the reinforcement of PLA matrix is discussed. Judging from the mechanical, thermal and morphological properties of the PLA-NHA nanocomposites, it is apparent that the interfacial adhesion of these two components was poor. As a result, it is important to improve the interfacial adhesion between the NHA (hydrophilic) and PLA (hydrophobic) by chemically modifying the NHA. Neat PLA and PLA-5wt%NHA were used as control samples in this chapter. Three different chemicals were used to surface treat the NHA, namely, 3-aminopropyl triethoxysilane (APTES), sodium n-dodecyl sulfate (SDS) and polyethylenimine (PEI). APTES has acted as a silane coupling agent, whereby the amine and ethoxy groups of the APTES react with the PLA matrix and NHA, respectively. The loading of the mNHA (APTES) was varied at 5, 10, 20, 30wt%. The SDS is an anionic surfactant with a sodium salt head and a polar hydrocarbon tail, which has potential to reduce the surface tension of NHA prior to mixing with PLA. PEI on the other hand, is a polymer that has acted as binding agent between the NHA and PLA matrix. For comparison purpose, the selected loading for mNHA (SDS) and mNHA (PEI) are 5wt% and 30wt%. The mixing torques, mechanical, dynamic mechanical, thermal and morphological properties of the PLA-mNHA nanocomposites are discussed here.

6.2. Surface Modification Process

The greatest challenge faced during preparation of the nanocomposites is the interfacial adhesion between the hydrophilic and the hydrophobic biomaterials (Cai et al. 2008). Adhesion means the tendency of unlike biomaterials or surfaces to stick to one another (Kuilla et al. 2010, Udensi and Nnanna 2011). Hence, improving the interfacial adhesion between the biomaterials can lead to a considerable enhancement in the properties of the nanocomposite (Rong et al. 2006, Bula et al. 2007, Kango et al. 2013). Thus, the interfacial adhesion can be improved by either (1) reducing the loading of the nanofiller, (2) surface

modifying of the nanofiller and (3) introducing a third component which exhibits a good adhesion to either the filler and polymer (Rong, Zhang et al. 2006). Figure 6.1 shows the chemical structure of the PLA and the NHA. Due to their nature as hydrophobic (PLA) and hydrophilic (NHA), these biomaterials have poor interfacial interaction, resulting in poor mechanical properties, as reported in chapter 5. Consequently, the NHA was surface treated with APTES, SDS and PEI in order to attain a hydrophobic surface that can bind with the hydrophobic side of the PLA.

PLA   **NHA**
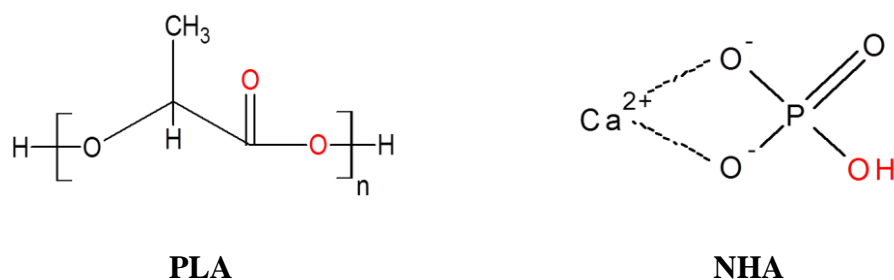
Figure 6.1: Chemical structure of the PLA and NHA

APTES is a silane coupling agent which is commonly used in surface treatment of various substrates. APTES has two functional groups, represented by OR_1 (C_2H_5OH) and R_2 ($C_3H_7NH_2$) in Figure 6.2. Generally, the reactive amine group, R_2, is bonded to silicon atom via short aliphatic chain, whereas the OR_1 group is the hydrolysing alcohol group. The activated silane coupling agent is then bonded to the surface of the NHA through OR_1 groups while R_2 groups react with the PLA matrix. Figure 6.2 (a-d) present the reaction schematic to surface treat the NHA with the APTES, which takes place in four stages. The first stage is the activation of APTES to reactive silanol, 3-Aminopropyl silanetriol (APS) through hydrolysis process by liberating ethanol (Figure 6.2 (a)). Then, the APS undergoes a self-condensation process, forming –Si–O–Si– and –Si–O–C– bonds (Figure 6.2 (b)). It is important to minimise the excess self-condensation process in order to leave the APS free for adsorption with the NHA. Due to the high affinity of the APS, the –Si–O–Si– bonds of APS will link with the hydroxyl bond of the NHA through hydrogen bond (Figure 6.2 (c)). During heating, these hydrogen bonds are converted to covalent bonds, forming –R_2– Si–O– bonds on the surface of NHA by liberating water (Figure 6.2 (d)). Finally,

these –R$_2$–Si–O– bonds on the surface of the NHA are linked with the -COO-bonds of PLA through hydrophobic interaction.
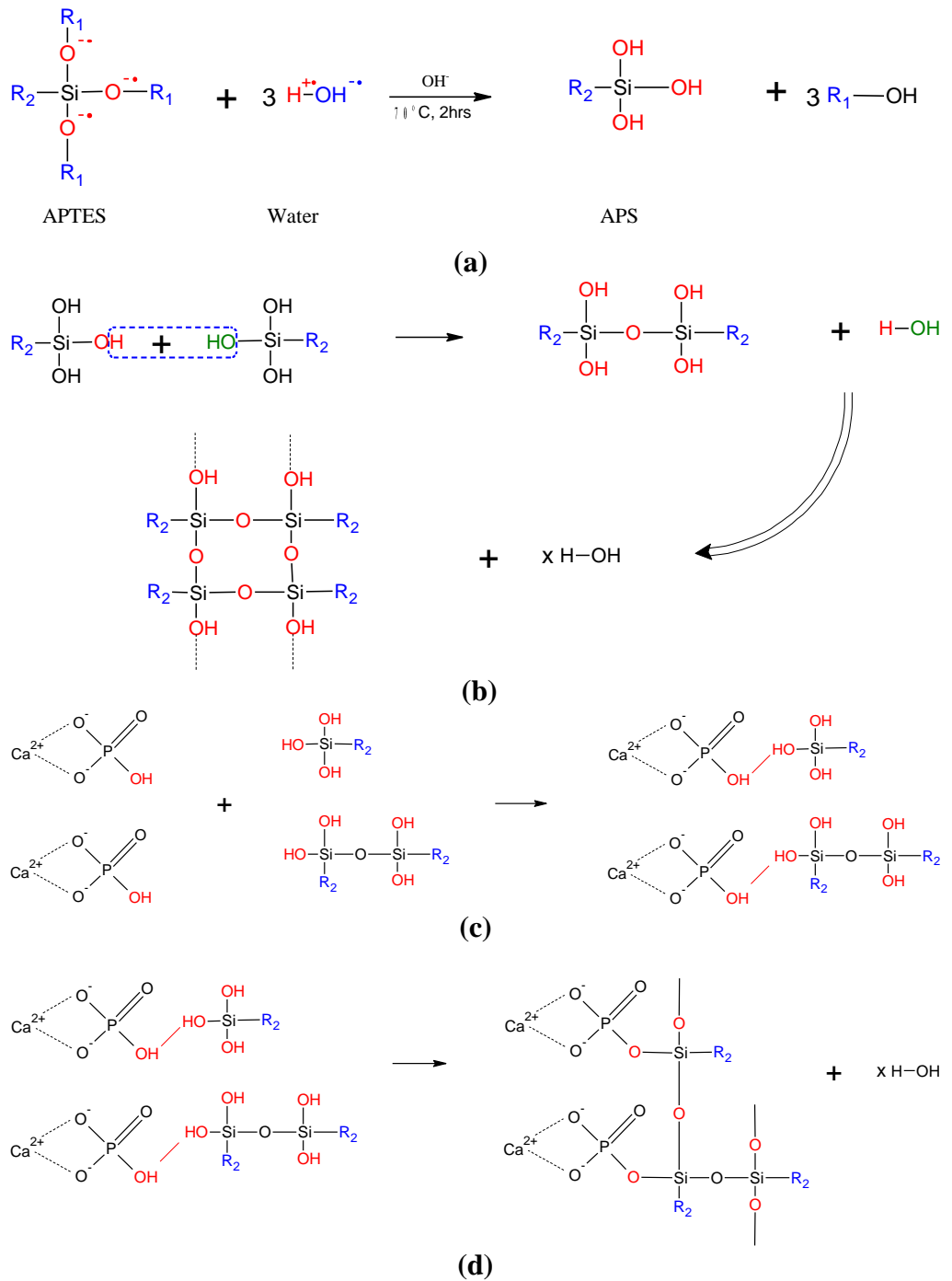
Figure 6.2: Schematic reaction of the surface modification of NHA using APTES through (a) hydrolysis, (b) self-condensation, (c) adsorption and (d) grafting

SDS is an anionic surfactant that lowers the surface tension of the nanoparticles. SDS consist a sodium salt and a polar hydrocarbon tail, R_3, ($C_{12}H_{25}$) attached to a sulfate group, as shown in Figure 6.3. Similar to APTES, SDS undergoes hydrolysis to yield sodium hydrogen sulfate and dodecanol (Figure 6.3 (a)). The anionic charged sodium hydrogen sulfate of the SDS is adsorbed by the cationic charge of the NHA (Ca^{2+}) due to electrostatic attractive force (Figure 6.3 (b)). The dodecanol on the other hand, is a by-product which happens to be insoluble in water. In addition, dodecanol has high surface activities, limiting the interface availability for the sodium hydrogen sulfate on the NHA surface. As a result, the dodecanol links with the hydroxyl group of the NHA through hydrogen bond (Figure 6.3 (b)). Upon heating, the hydrogen bond breaks and forms a hydrophobic bond on the surface of NHA (Figure 6.3 (c)). This in turn will allow the NHA to link with PLA via hydrophobic bond.

(a)

(b)

(c)
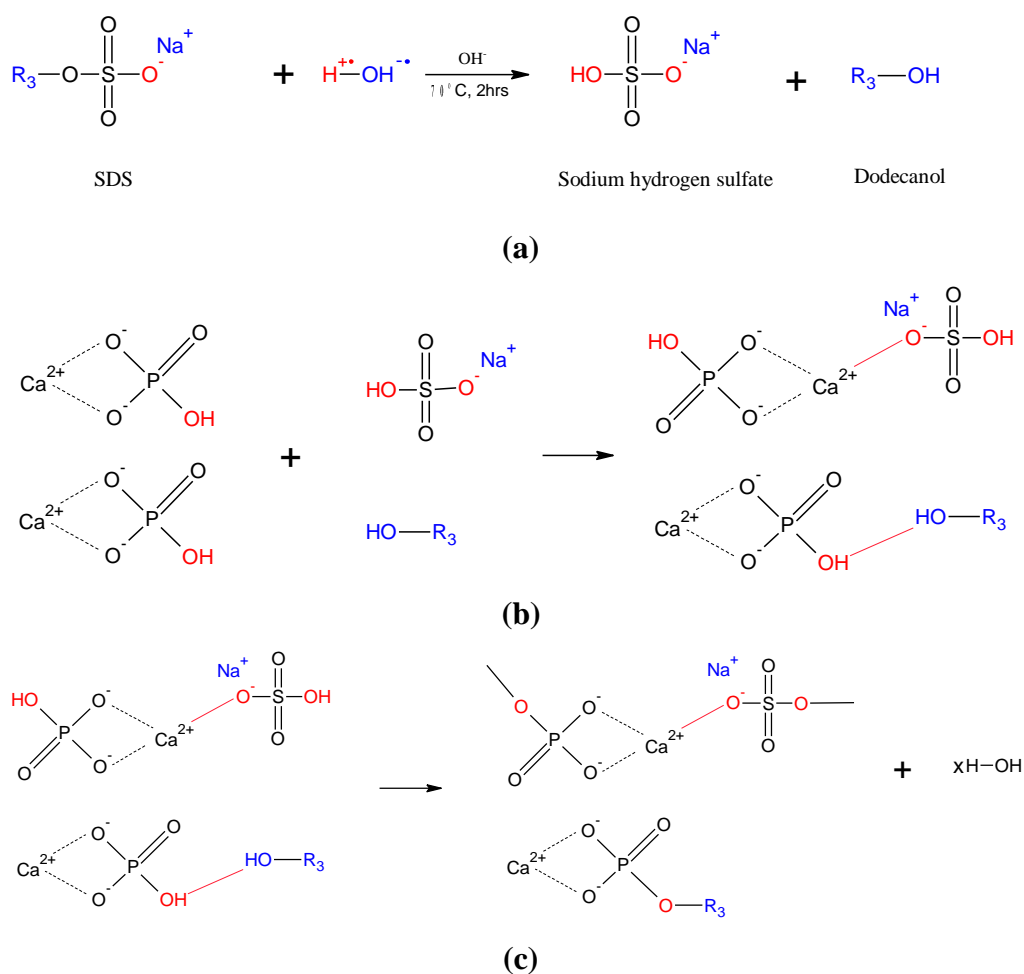
Figure 6.3: Schematic reaction of the surface modification of NHA using SDS through (a) hydrolysis, (b) adsorption and (c) grafting

PEI is polymer with repeating unit composed of amine groups spaced by two hydrocarbons (CH_2CH_2). PEI consist two types: linear ethylenimines (connected with each other in a linear fashion) and branching polyethylenimine (ethylenimines connected with each other in a branch fashion). The linear ethylenimine and branched polyethylenimine are presented by R_4 ($C_6H_{12}N_2H_2$), R_5 ($C_6H_{12}N(NH_2)_2$) and R_6 (C_4H_8NH) in Figure 6.4. Moreover, PEI is a high-charged cationic polymer that readily binds with highly anionic substrates. Thus, the cationic charge of PEI forms a bond with the hydroxyl group of the NHA as shown in Figure 6.4. Then, the amine groups present in the PEI bond with PLA, linking PLA with NHA in the process.
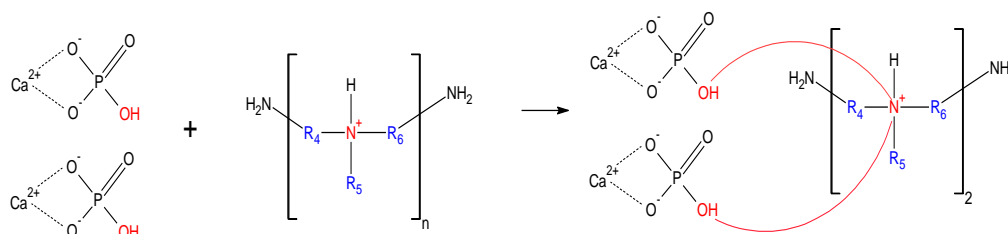
Figure 6.4: Schematic reaction of the surface modification of NHA using PEI

6.3. FTIR and Elemental analysis

Figure 6.5 presents the FTIR spectra of the NHA and the surface modified NHA (mNHA). As discussed in chapter 4, the peaks detected at ~1030cm^{-1} and ~603cm^{-1}, ~825cm^{-1}, ~1384cm^{-1} as well as ~3446cm^{-1} and ~1636cm^{-1} denote the stretching and bending modes of PO_4^{3-}, HPO_4^{2-}, NH_4^+ and the stretching and bending modes of OH^- in the NHA, respectively. It is observed that the peaks of the mNHA resemble the NHA peaks with some additional chemical functional groups.

FTIR spectrum of mNHA (APTES) revealed presence of S-O at 850cm^{-1}, Si–O–Si at 1100cm^{-1}, C-H at 1450cm^{-1} (bending mode) and 2900 cm^{-1} (stretching mode), N-H at 3200cm^{-1} along with Si-OH at 3436cm^{-1} wavelengths (Bahrami et al. , Kumar et al. , Saikia and Parthasarathy 2010). Moreover, the FTIR spectrum of mNHA (SDS) depicted presence of stretching and bending modes of C-H at 2924cm^{-1} and 1384cm^{-1}, respectively, and the stretching mode OH^- at

3437cm^{-1} wavelength. In addition, presence of stretching mode SO_2 from the SO_4 of SDS was detected at 1224cm^{-1} for the mNHA (SDS) (Ramimoghadam et al. 2012). Similarly, the FTIR spectrum of mNHA (PEI) identified presence of stretching mode C-N at 982cm^{-1}, bending and stretching modes C-H at 1484cm^{-1} and 2934cm^{-1}, respectively, as well as bending and stretching modes N-H at 1638cm^{-1} and 3248cm^{-1}, respectively (Wang et al. 2012). Hence, the formation of more functional groups in comparison to NHA, confirms the successful surface modification of NHA.

The FTIR spectrum of the NHA and mNHA was further complemented by the elemental analysis using EDX image obtained in Figure 6.6 (a-d). From the figures, the detection of Ca and P elements prove the synthesis of NHA. The extra elements (Si, N_2, and S) shown in Figure 6.6 (b-d) are due to the surface modifiers used to modify the NHA. For instance, presence of Si and N_2 compounds detected in Figure 6.6 (b) confirms the surface modification of the NHA with APTES. Similarly, Figure 6.6 (c) and (d) show presence of S and N_2, respectively, verifying the surface modification of NHA by SDS and PEI.

6.4. Mixing Torque

Figure 6.7 shows the mixing torque-time curve of PLA, PLA-5wt%NHA and PLA- (5-30wt%) mNHA (APTES) nanocomposites. As mentioned in section 5.2., the first peak at 30 seconds represents the loading peak of PLA, and ones the PLA underwent full melting and fusion, the mNHA was charged in at 2 minutes. The mixing torque was observed to increase slightly for 5wt% mNHA (APTES) loading. Further increase in mNHA (APTES) loading from 10wt% to 30wt% caused a significant increase in the mixing torque. This is due to the increased viscosity upon the addition of mNHA (APTES). After a few seconds, the torque is observed to decrease as PLA and mNHA (APTES) melted, suggesting the nanocomposite undergoes mixing and homogenisation.
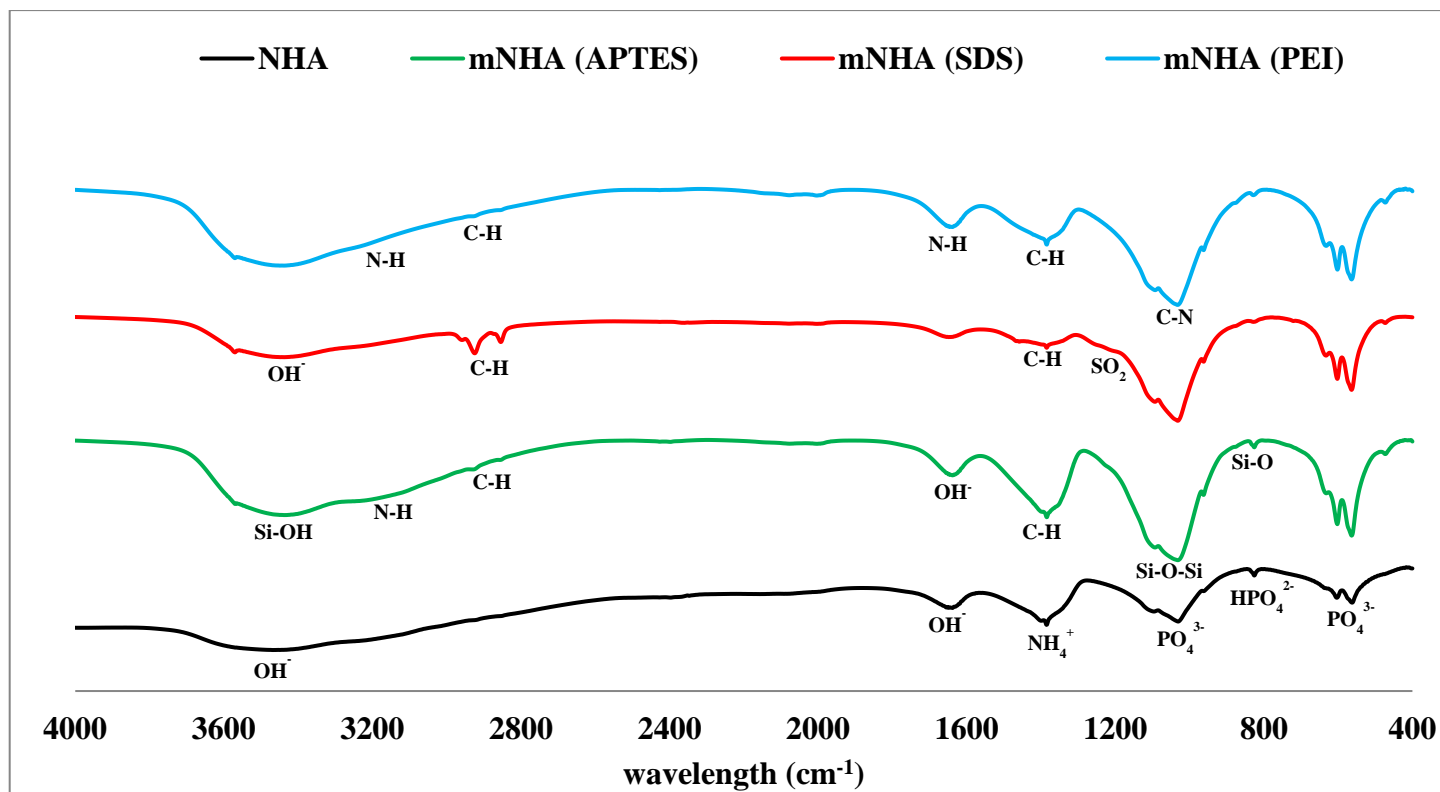
Figure 6.5: FTIR spectra for NHA and mNHA (APTES), mNHA (SDS) and mNHA (PEI)
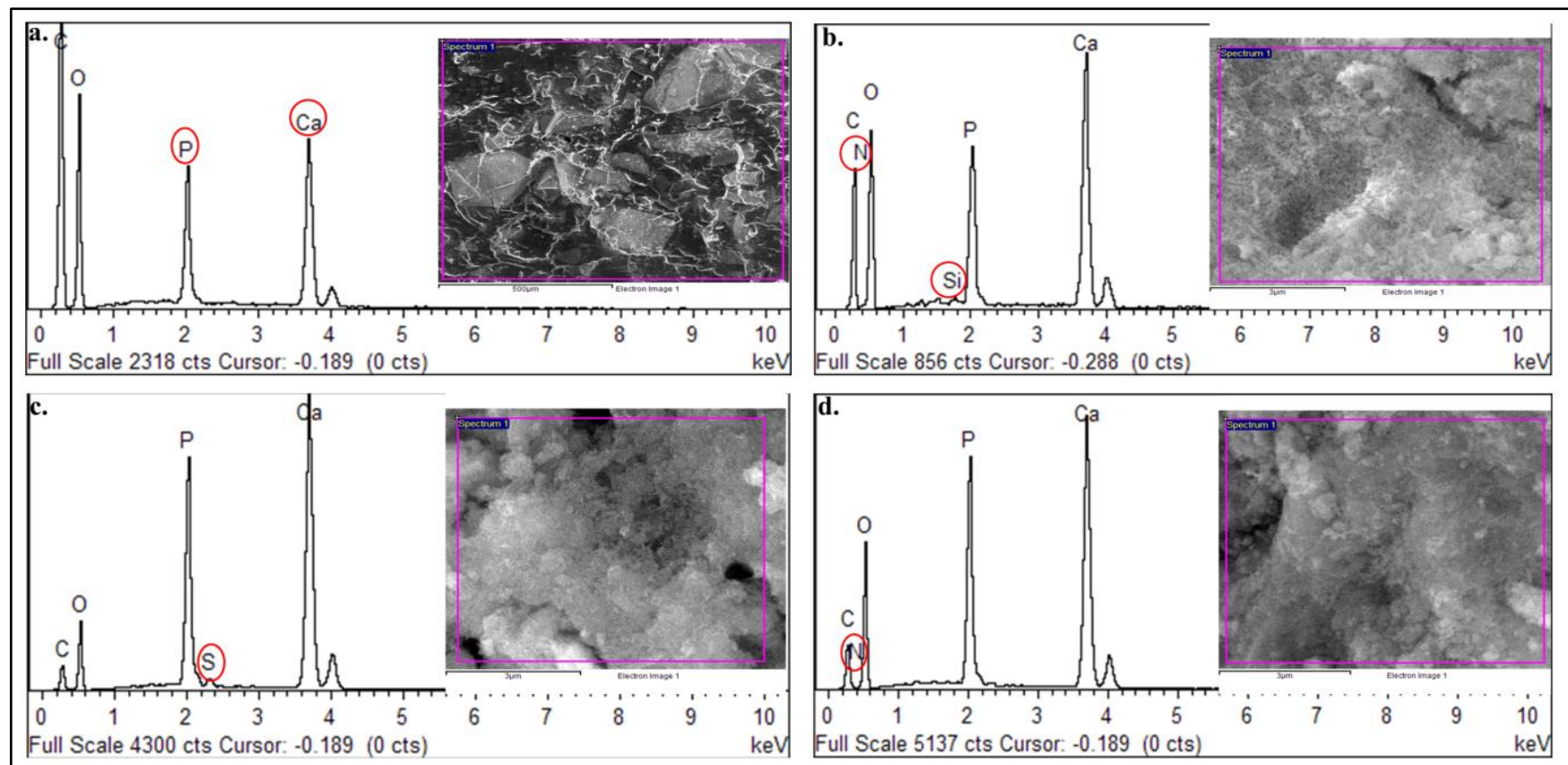
Figure 6.6: Microstructure image and EDX analysis of (a) NHA, (b) mNHA (APTES), (c) mNHA (SDS) and (d) mNHA (PEI)
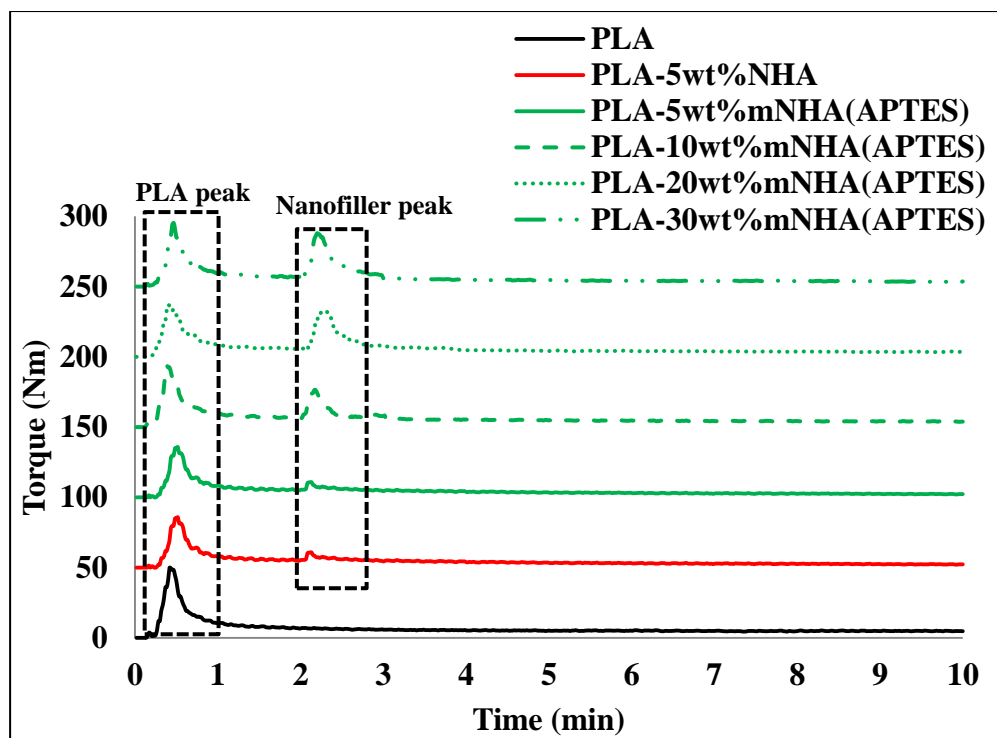
Figure 6.7: Mixing torque graph for PLA, PLA- 5wt%NHA and PLA- (5-30wt%) mNHA (APTES) nanocomposites

6.5. Mechanical Properties

6.5.1. Tensile Properties

Figure 6.8 depicts the tensile properties of the surface modified PLA-mNHA nanocomposites using APTES, SDS or PEI in comparison to neat PLA and unmodified PLA-5wt% NHA nanocomposite. Surface treatment of NHA caused considerable change on the tensile properties of nanocomposites. The tensile strength of neat PLA and PLA-5wt% NHA nanocomposite improved by 1.2% and 19.7%, respectively, compared to PLA-5wt%mNHA(APTES). The tensile strength of PLA-5wt%mNHA (SDS) nanocomposite increased by 10.6% compared to PLA-5wt% NHA, while decreasing by 6.5% in respect to neat PLA. In the contrary, the tensile strength of PLA-5wt%mNHA (PEI) decreased by 16.92% and 1.62% in comparison to neat PLA and PLA-5wt% NHA, respectively.

The improvements in the tensile strength upon surface treatment of NHA are attributed to the improved interfacial adhesion between the mNHA and

the PLA matrix (Harper et al. 2000). As mentioned in chapter 5, PLA and NHA are only capable of forming weak van der Waal forces since PLA happens to be hydrophobic while NHA is hydrophilic. This weak bond contributed in the poor interfacial adhesion between the NHA and PLA. In this chapter, the APTES treated NHA acquired hydrophobic chain through strong covalent bonding which further bonded with PLA, as discussed in section 6.2, thus improving the interfacial adhesion between PLA and mNHA (APTES). The improved interfacial adhesion further ensured efficient stress transfer between the biomaterials, allowing the nanocomposites to withstand higher amount of stress before failure. Similarly, the interaction between the SDS treated NHA and PLA was improved to some extend as the NHA was able to form hydrophobic chain by bonding with the dodecanol (by-product of SDS). However, the mNHA (SDS) still had a hydrophilic chain formed by the electrostatic force between the cationic charge of NHA and anionic charge of SDS. This could have caused the interfacial adhesion between the mNHA(SDS) and PLA to reduce compared to mNHA(APTES) and PLA. Furthermore, APTES has enabled the NHA to disperse in smaller size in the PLA matrix compared to SDS. This increases the effective surface area of interaction between the mNHA (APTES) and PLA matrix as shown from the FESEM micrographs of the fractured samples in section 6.8. Increase in the surface area of interaction along with good interfacial adhesion, increases the stress transfer feasibility between the nanofiller and PLA matrix, hence resulting in improved tensile strength of the PLA-5wt% mNHA(APTES) compared to PLA-5wt% mNHA(SDS). The PEI treated NHA on the other hand did not have a hydrophobic chain that could have linked with the PLA, thus, did not contribute in the improvement of interfacial adhesion between the mNHA (PEI) and PLA, thus, the drastic decrease in tensile strength of the PLA-5wt%mNHA(PEI).

The tensile modulus of the APTES and SDS treated nanocomposites improved by 8.46% and 9.71% as well as 2.37% and 3.55%, respectively, compared to neat PLA and PLA-5wt% NHA. The PEI treated nanocomposite, had the least tensile modulus, whereby a decrease of

17.55% and 16.12% was noted with respect to neat PLA and PLA-5wt% NHA. The increase in tensile modulus upon surface treatment of NHA with APTES and SDS is also attributed to the improved interfacial adhesion between mNHA and PLA matrix. This subsequently increases the hindrance effect of the mNHA in the PLA chain mobility.

Considering the tensile properties of the nanocomposites improved upon surface treating the NHA, the mNHA loading was further increased to 30wt%. Such attempt was made in order to make the nanocomposite suitable for bone implant with increased bone healing properties. However, further increase in mNHA loading to 30wt%, led to drastic decrease in tensile strength with a concomitant increase in the tensile modulus. This can be witnessed from Figure 6.8, whereby comparing the tensile strength of PLA-30wt%mNHA with PLA-5wt% mNHA exhibited a decrease of 34.02% (APTES), 29.65% (SDS), and 40.45% (PEI). In contrast to tensile strength, the tensile modulus of PLA-30wt% mNHA increased by 2.48% (APTES), 1.96% (SDS), and 1.24% (PEI) in comparison to their respective PLA-5wt% mNHA. The influence of mNHA loading on the tensile properties is elaborated more using Figure 6.9. It is obvious that the tensile strength decreases proportionally with the increase of mNHA(APTES) loading, while the tensile modulus is maintained. The reduction in tensile strength is attributed to the increased agglomeration of the mNHA at a higher loading (Wan, Wu et al. 2015). This is further elaborated by the FESEM images obtained in Section 6.8, where the agglomeration of mNHA particles were clearly detected. However, it is still important to note that, the tensile strength of PLA-30wt% mNHA (APTES and SDS) recorded in this study is higher than previous studies obtained for PLA-30wt% NHA (SDS) (Wan, Wu et al. 2015) and UHMWPE- 30wt% NHA (Fang, Leng et al. 2005).
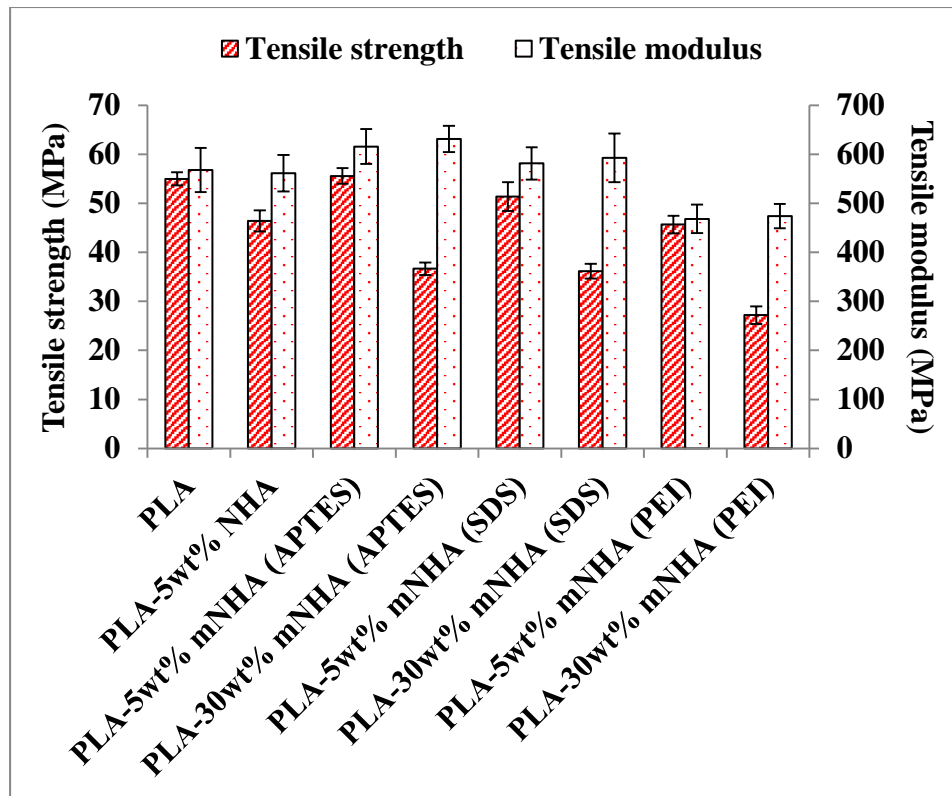
Figure 6.8: Tensile properties of the surface modified PLA-mNHA nanocomposites in comparison to neat PLA and PLA-5wt% NHA
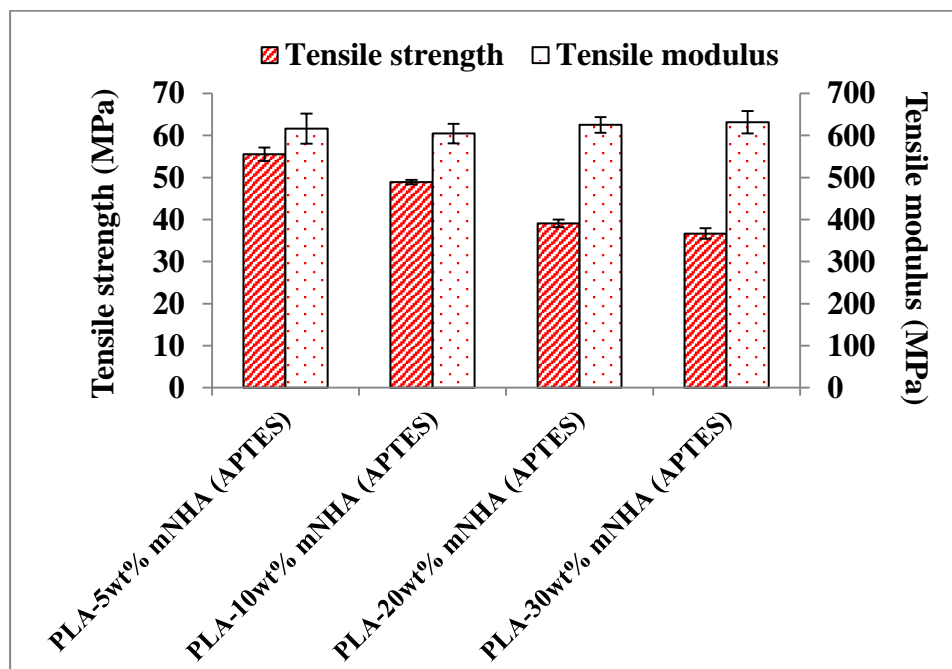
Figure 6.9: Tensile properties of the APTES treated PLA-mNHA nanocomposites at different loading

119

6.5.2. Impact Strength

Figure 6.10 shows the impact strength of the surface treated PLA-mNHA nanocomposites using APTES, SDS or PEI in comparison to neat PLA and PLA-5wt% NHA nanocomposite. The impact strength of PLA-5wt% mNHA(APTES) nanocomposite recorded 6.91% reduction compared to PLA-5wt% NHA, even though, the value is 13% higher than neat PLA. Similarly, the impact strength of PLA-5wt%mNHA(SDS) and PLA-5wt%mNHA(PEI) nanocomposites decreased by 2.52% and 31.56%, respectively, in comparison to PLA-5wt% NHA. In comparison to neat PLA, the impact strength of PLA-5wt%mNHA(SDS) was 18.49% higher whereas PLA-5wt%mNHA(PEI) decreased by 19.67% (lowest impact strength overall). Increase in mNHA loading had no significant effect on the APTES and SDS treated nanocomposite. This is more clarified in Figure 6.11. However, the impact strength of SDS treated PLA- 30wt% mNHA reduced by 15.57% compared to PLA- 5wt% mNHA. Generally, the decrease in impact strength of surface treated nanocomposites in comparison to the PLA-5wt%NHA indicate the brittleness increased, however, still is less brittle than the neat PLA with the exception of PLA-mNHA (PEI).
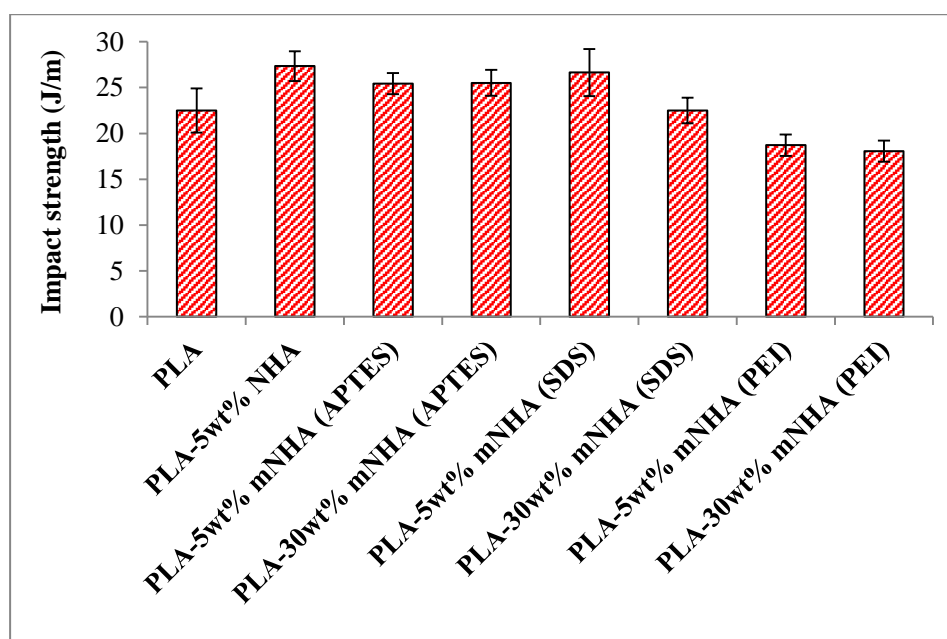
Figure 6.10: Impact strength of the surface modified PLA-mNHA nanocomposites in comparison to neat PLA and PLA-5wt% NHA
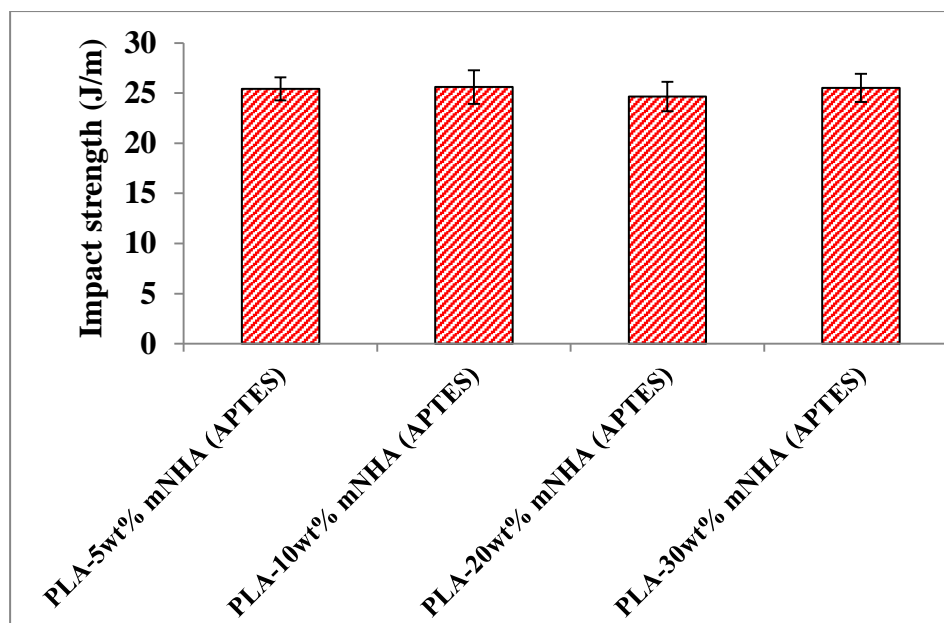
Figure 6.11: Impact strength of the APTES treated PLA-mNHA nanocomposites at different loading

6.6. Thermal Properties

6.6.1. TGA

The thermal stability of surface modified (PLA-mNHA) and unmodified (PLA-NHA) nanocomposites in respect to neat PLA is depicted in Figure 6.12 and tabulated in Table 6.1. The thermal stability of PLA improved with addition of surface modified NHA. The APTES and PEI treated nanocomposites improved the thermal stability at 5wt% mNHA loading, whereas the SDS treated nanocomposites, degraded compared to neat PLA and PLA-5wt%NHA. Generally, the thermal degradation temperature of polymer reduced when the interaction between the polymer and filler is poor (Ueda et al. 2016). It was mentioned in section 6.5.1., that the PLA and mNHA(APTES) had formed a strong covalent bond, which also means more energy/heat is required to make the PLA molecules to flow. Thus, resulting in the improved thermal stability by increasing the T_{max}, also meaning the maximum degradation temperature increased. However, the PLA and mNHA(SDS) attained poor interfacial adhesion due to the electrostatic force holding the biomaterials together. This also suggest that

the interaction is weak that the PLA can freely move when the temperature increased and the mNHA(SDS) does not have enough physical barrier to absorb some of the heat to delay the melting of PLA. Similarly, the remaining weight of the nanocomposites increased upon surface treatment of the NHA according to PLA-5wt% mNHA (APTES) > PLA-5wt%mNHA (PEI) > PLA-5wt%mNHA (SDS) > PLA-5wt%NHA > PLA.

The $T_{10\%}$, $T_{50\%}$ and T_{max} of the PLA-5wt% mNHA (APTES) nanocomposite increased by 1°C, 5°C and 4°C, respectively, despite the initial degradation temperature ($T_{5\%}$) decreasing by ~6°C in comparison to both neat PLA and PLA-5wt%NHA. Likewise, the thermal stability of PLA-5wt%mNHA (PEI) nanocomposite enhanced by 9°C ($T_{5\%}$), 8°C ($T_{10\%}$), 6°C ($T_{50\%}$) and 3°C (T_{max}). Nevertheless, the thermal stability of PLA-5wt%mNHA (SDS) nanocomposite showed drastic decrease of 21°C ($T_{5\%}$), 23°C ($T_{10\%}$), 28°C ($T_{50\%}$) and 32°C (T_{max}) in respect to both neat PLA and PLA-5wt%NHA.

Figure 6.13 shows the thermal stability of the PLA-30wt%mNHA nanocomposites. The $T_{5\%}$, $T_{10\%}$, $T_{50\%}$ and T_{max} and remaining weight of the nanocomposites are charted in Table 6.1. Overall, the thermal stability of the PLA-mNHA nanocomposites showed improvement as the mNHA loading increased from 5wt% to 30wt%. This reflected in the $T_{5\%}$, $T_{10\%}$, $T_{50\%}$ and T_{max} recorded, in which the enhancement of thermal stability of the nanocomposites was in the order of PLA-30wt%mNHA(APTES) > PLA-30wt%mNHA(PEI) > PLA-30wt%mNHA(SDS). The thermal stability of PLA-30wt%mNHA(APTES) nanocomposite showed an improvement of 6°C ($T_{5\%}$), 5°C ($T_{10\%}$), 7°C ($T_{50\%}$), whereas the T_{max} decreased by 4°C compared to PLA-5wt%mNHA(APTES) nanocomposite. In the same way, the thermal stability of the PLA-30wt% mNHA(SDS) nanocomposite improved by 18°C ($T_{5\%}$), 21°C ($T_{10\%}$), 36°C ($T_{50\%}$) and 25°C (T_{max}) in respect to PLA-5wt%mNHA(SDS) nanocomposite. The PLA-30wt%mNHA(PEI) nanocomposite, on the other hand, showed an initial decrease in the thermal stability whereby the $T_{5\%}$ and $T_{10\%}$ decreased by 10°C and 4°C, respectively, while an increase

of 2°C and 4°C was then observed for $T_{50\%}$ and T_{max}, respectively, in comparison to the PLA-5wt%mNHA (PEI). Similarly, the remaining weight of the nanocomposites also increased significantly with addition of 30wt% mNHA in the order of PLA-30wt%mNHA(SDS) > PLA-30wt%mNHA (APTES) > PLA-30wt%mNHA (PEI).

Figure 6.14 illustrates the influence of mNHA(APTES) loading (5wt%, 10wt%, 20wt% and 30wt%) on the thermal stability of the nanocomposites. The $T_{5\%}$, $T_{10\%}$, $T_{50\%}$ and T_{max} of the nanocomposites are tabulated in Table 6.1. As mentioned in section 6.4, the mixing torque was also observed to increase significantly as the mNHA(APTES) loading increase. As such, the viscosity of the PLA-mNHA increased at higher loading, leading to the increase in temperature. Hence, it is observed that increase in the mNHA (APTES) loading from 5wt% - 20wt% has improved the initial thermal degradation temperatures by 18°C ($T_{5\%}$) and 10°C ($T_{10\%}$), and 4°C ($T_{50\%}$). The T_{max} of both the nanocomposites with 10wt% and 20wt% mNHA(APTES) loading however reduced by 4°C. Further increase to 30wt% mNHA(APTES) loading resulted in the decrease of the initial degradation temperatures by 12°C ($T_{5\%}$) and 7°C ($T_{10\%}$) while maintaining the T_{max}, in respect to the nanocomposites with 10-20wt% mNHA(APTES) loadings. Similar observation was also reported when PLA-HA nanocomposites were prepared through melt-spun technique (Persson, Lorite et al. 2013). In reference to the remaining weight of the nanocomposites with respect to increase in mNHA (APTES) loading, Table 6.1 shows the remaining weight percentage of the nanocomposites increased proportionally with the increase in mNHA(APTES) loading. This can also be exemplified by the arrows presented in Figure 6.14 (a), whereby at every degradation stage, the remaining weight of the nanocomposite is higher as the mNHA (APTES) loading increased.
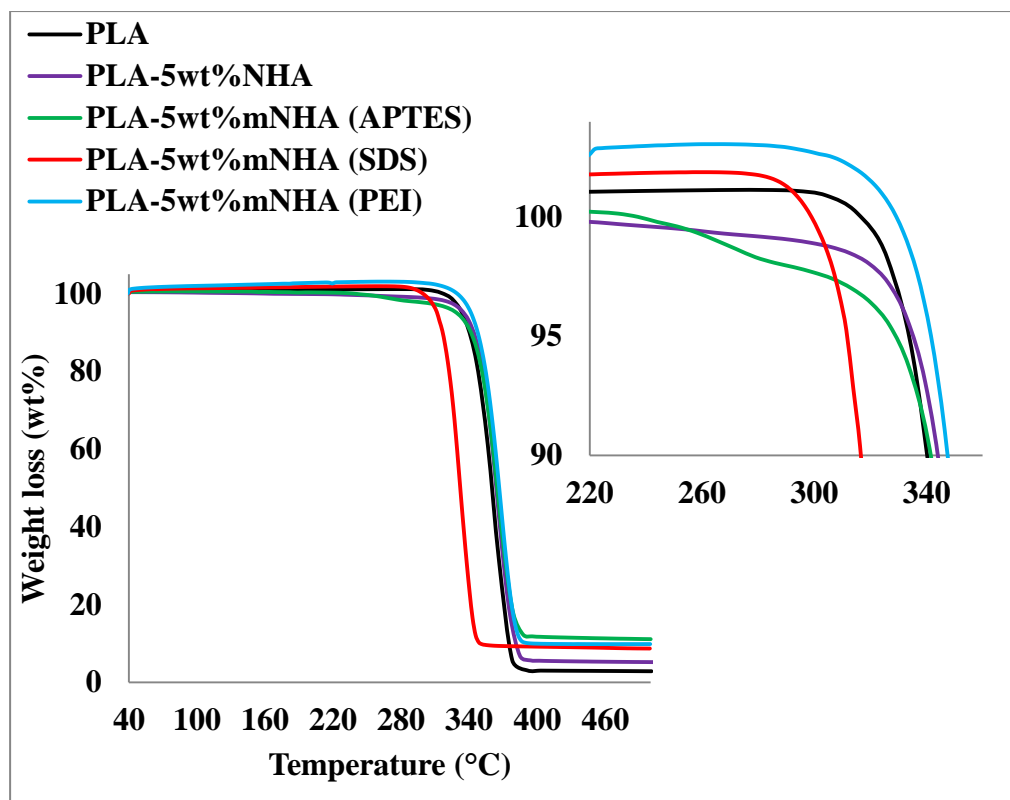
(a)
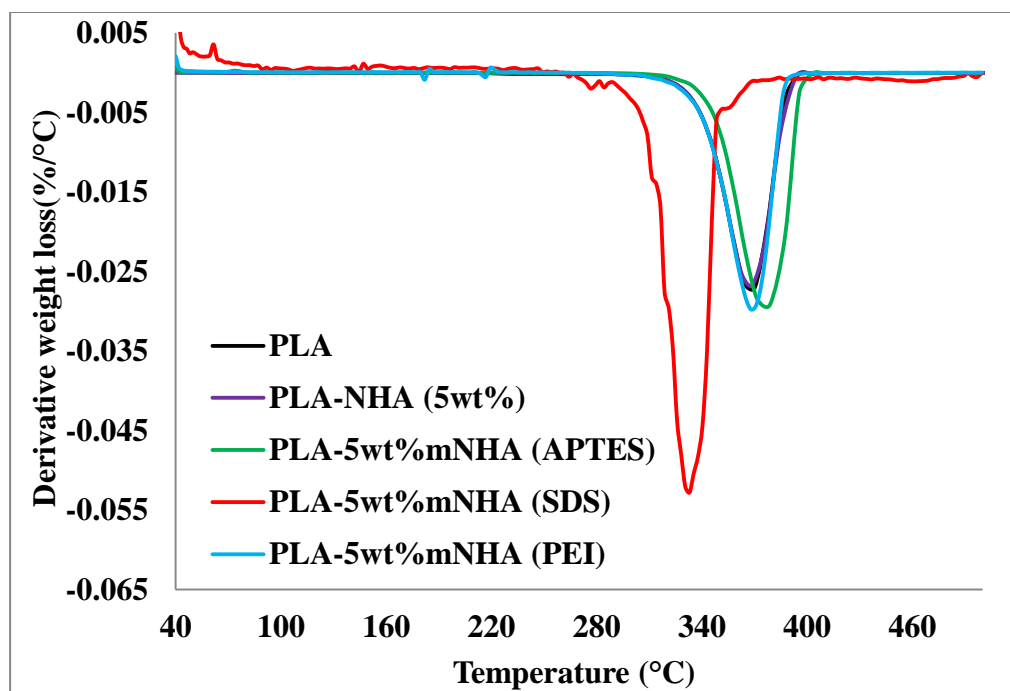
(b)

Figure 6.12: TGA thermogram for PLA-5wt%mNHA nanocomposites in comparison to neat PLA and PLA-5wt%NHA (a) weight loss curve and (b) derivative curve
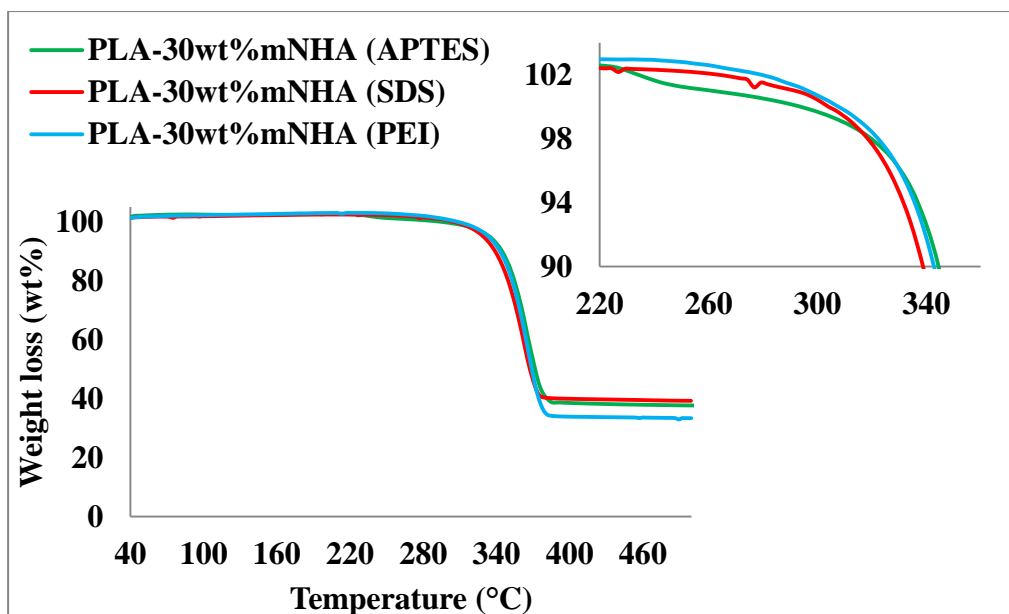
(a)
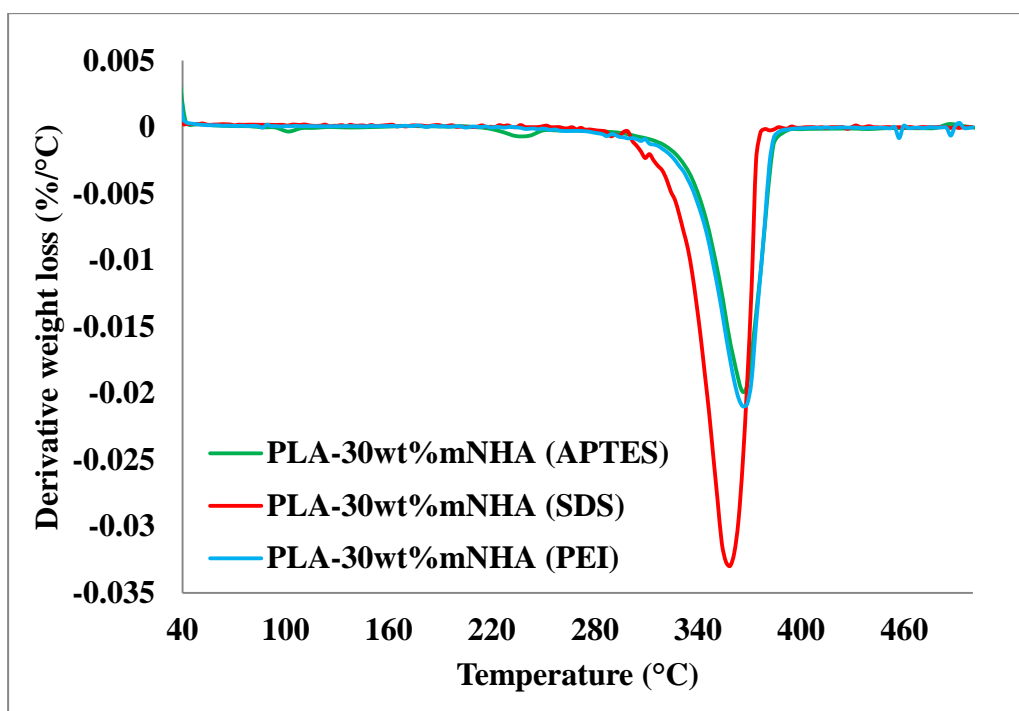
(b)

Figure 6.13: **TGA thermogram for PLA-30wt%mNHA nanocomposites (a) weight loss curve and (b) derivative curve**
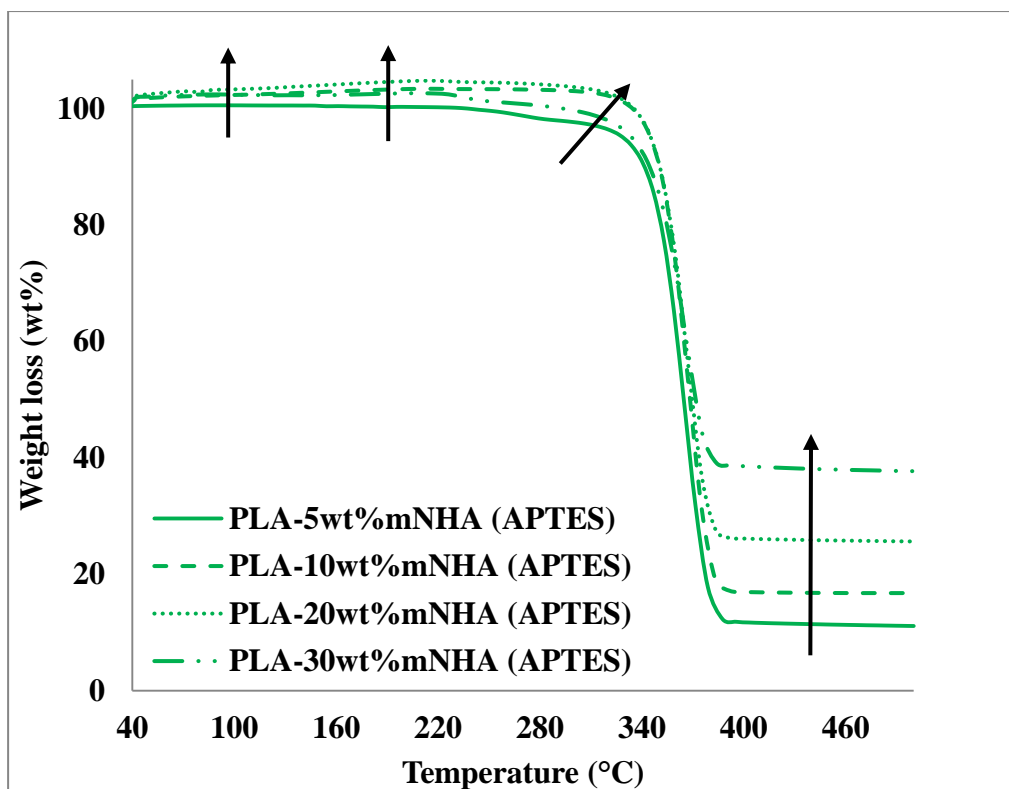
(a)
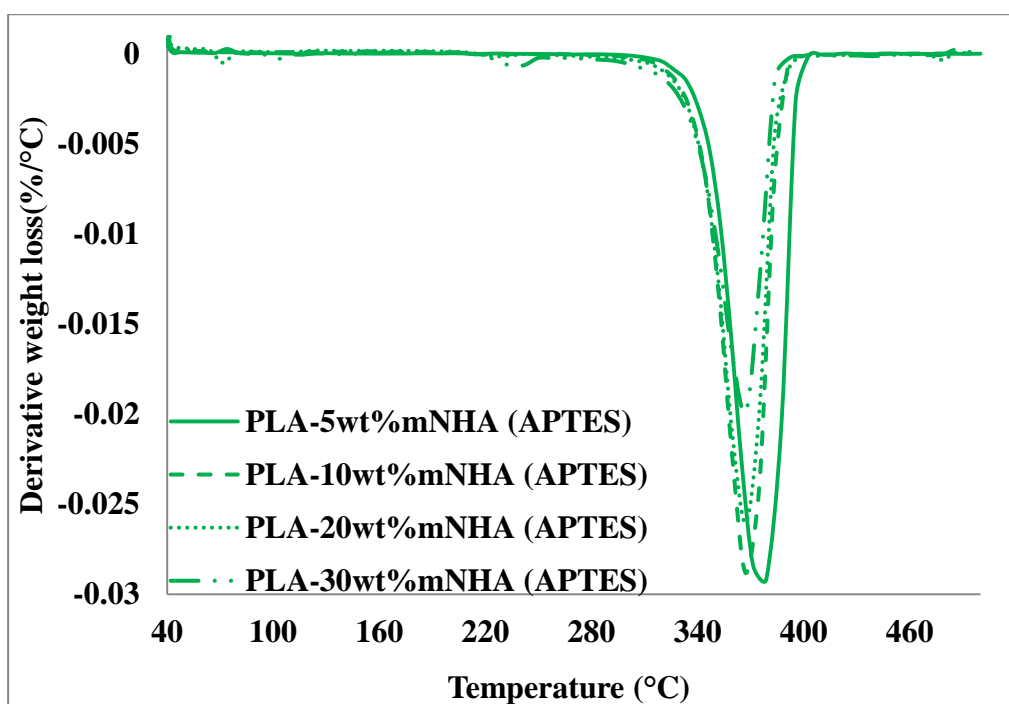
(b)

Figure 6.14: TGA thermogram (a) weight loss curve and (b) derivative curve for PLA-mNHA(APTES) nanocomposites at different mNHA (APTES) loading

Table 6.1: Degradation temperatures and remaining weight of the PLA-mNHA nanocomposites in respect to the PLA and PLA-5wt%NHA

Sample	Degradation Temperature (°C)				Remainin g wt (%)
	$T_{5\%}$	$T_{10\%}$	$T_{50\%}$	T_{max}	
PLA	332.8	339.4	360.1	367.5	2.91
PLA-5wt% NHA	332.8	339.4	360.1	368.9	5.29
PLA-5wt%mNHA(APTES)	326.9	340.4	364.9	371.5	11.09
PLA-10wt%mNHA(APTES)	344.5	350.2	368.3	367.3	16.92
PLA-20wt%mNHA(APTES)	344.7	351.6	369.8	367.5	26.11
PLA-30wt%mNHA(APTES)	332.4	344.6	371.8	367.8	37.69
PLA-5wt%mNHA(SDS)	311.5	316.4	331.7	335.4	8.68
PLA-30wt%mNHA(SDS)	329.2	337.8	367.5	360.3	39.27
PLA-5wt%mNHA(PEI)	341.6	346.9	366.4	370.4	9.83
PLA-30wt%mNHA(PEI)	331.8	342.6	368.6	366.1	33.38

6.6.2. DSC

Figure 6.15 shows the DSC curve for the surface modified PLA-5wt% mNHA and the unmodified PLA-5wt%NHA nanocomposites in comparison to neat PLA. Moreover, Table 6.2 lists the data obtained from the DSC curves, in which the T_c of the nanocomposites was observed to decrease while the T_m increased in contrast to neat PLA. The T_c and T_m of the PLA-5wt%mNHA nanocomposites are recorded as 127.4°C and 167.9°C (APTES), 114.2°C and 154.6°C (SDS), respectively, while the T_m of the PEI treated nanocomposite is 154.7°C. The T_c and T_m of PLA-5wt%NHA and neat PLA are listed as 118.8°C and 160.5°C as well as 120.2°C and 151.8°C, respectively.

As mentioned in section 5.5.2., presence of 5wt% NHA in the PLA matrix facilitated the formation of PLA crystals; hence, recording a reduction in the T_c of the nanocomposite. However, the improvement in the interfacial adhesion between the mNHA(APTES) and PLA matrix, is believed to increase the nucleating capacity of mNHA (APTES) compared to NHA. This in turn leads to an increased need for energy to form PLA crystals, translating in the increase of the T_c. Addition of 5wt%mNHA (SDS), on

the other hand, resulted in reduction of T_c of the nanocomposite in respect to both PLA-5wt%NHA and neat PLA. This could be due to the increased brittleness of PLA-5wt%mNHA (SDS) and poor interfacial adhesion between mNHA(SDS) and PLA matrix, which also reflected in the mechanical properties of the nanocomposite. Moreover, surface treatment of NHA with PEI led to the disappearance of the T_c, indicating poor nucleation effect of mNHA(PEI). In general, the nucleating capacity of the nanofillers is arranged in the order of mNHA(APTES) > NHA> mNHA(SDS) > mNHA(PEI).

It is evident that all the nanocomposites obtained melting temperature higher than the neat PLA. This is due to the presence of nanofillers, causing hindrance in the mobility of the PLA chain. Similar to the T_c, the T_m of the nanocomposites is greatly affected by the nanofillers nucleation effect and the interfacial adhesion between the nanofiller and polymer matrix. Thus, smoothed/improved nucleation or strong interfacial adhesion contributes to lower chain mobility of PLA, hence, elevating the melting temperature of the nanocomposite. As a result, the PLA-5wt%mNHA (APTES) nanocomposite attained the highest melting temperature due to the improved interfacial adhesion, followed by the PLA-5wt%NHA nanocomposite as a result of strong nucleating effect of NHA. However, both PLA-5wt%mNHA (SDS) and PLA-5wt%mNHA (PEI) achieved the lowest melting temperature, close to neat PLA. This is credited to both the poor interfacial adhesion and weak nucleating effect of mNHA(SDS) and mNHA (PEI).

Figure 6.16 illustrates the DSC curve for the APTES, SDS and PEI surface treated PLA-30wt%mNHA nanocomposites, where the data are summarised in Table 6.2. It is observed that the T_c of all the PLA-30wt%mNHA nanocomposites disappeared. The T_m of the SDS and PEI treated PLA-30wt%mNHA remained unchanged compared to their respective PLA-5wt%mNHA. Figure 6.17 clarifies the T_c and T_m changes that took place as the mNHA(APTES) loading increased at an interval of 10wt%. It is noted that the T_c of the APTES treated nanocomposites

decreased by 10°C as the mNHA(APTES) loading increased to 20wt%, gradually disappearing at 30wt% loading. Moreover, the T_m beyond 10wt% mNHA(APTES) loading attained constant value of 155°C, which is also 10°C lower than the PLA-5wt%mNHA (APTES) nanocomposite. This is due to the increased formation of agglomerates at a higher mNHA loading, causing the T_c and T_m of the nanocomposites to decrease, which is in line with the mechanical properties reported in section 6.5. The presence of agglomeration and the poor interfacial adhesion between the PLA matrix and mNHA at a higher loading can be observed in the FESEM micrographs, discussed later in section 6.8.
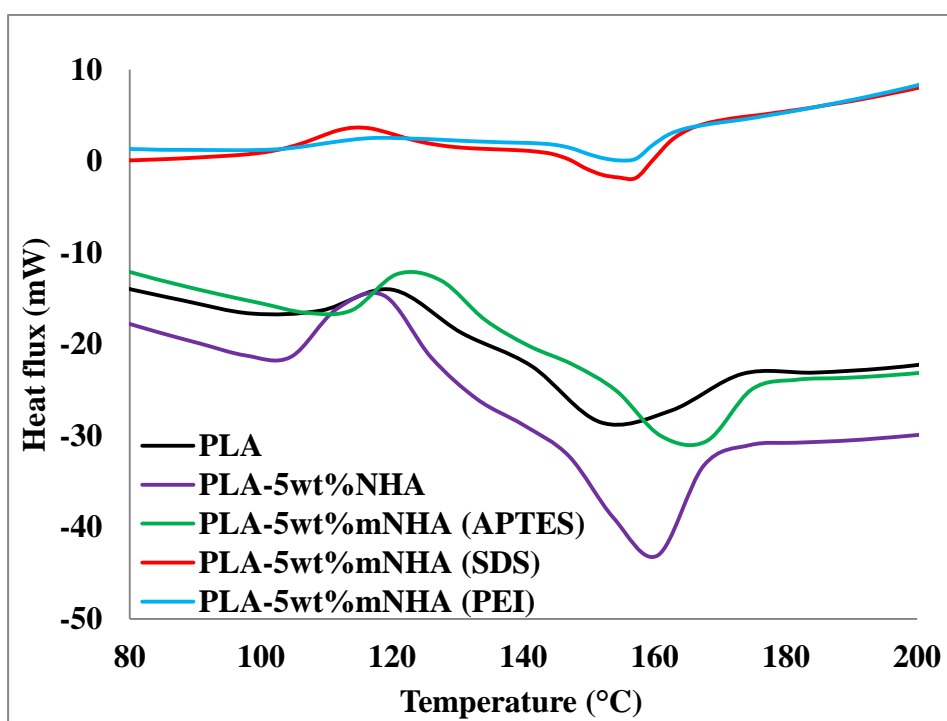
Figure 6.15: DSC curve for PLA-5wt%mNHA nanocomposites in comparison to neat PLA and PLA-5wt%NHA
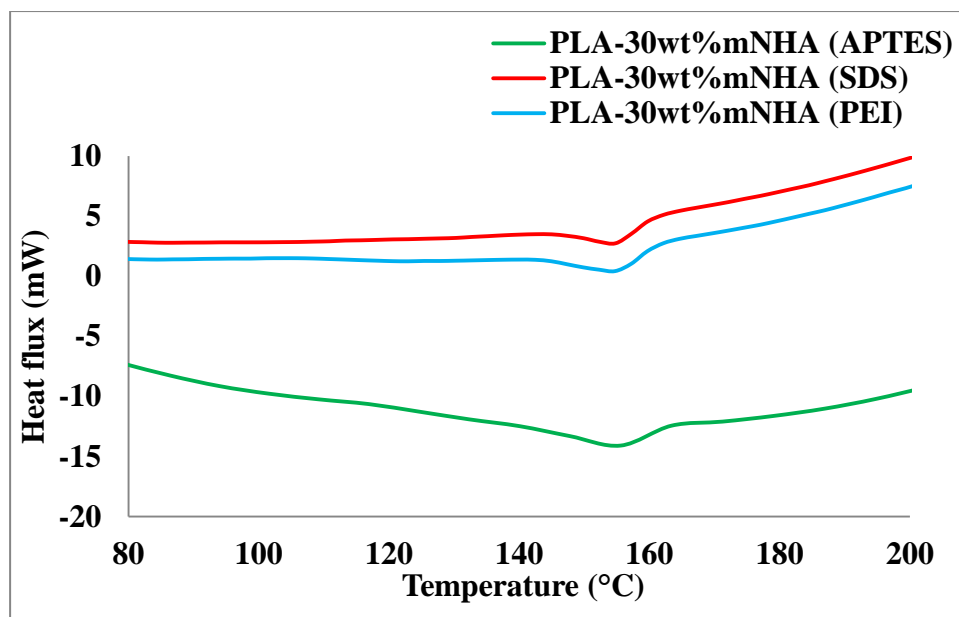
Figure 6.16: DSC curve for APTES, SDS and PEI treated PLA-30wt% mNHA nanocomposites
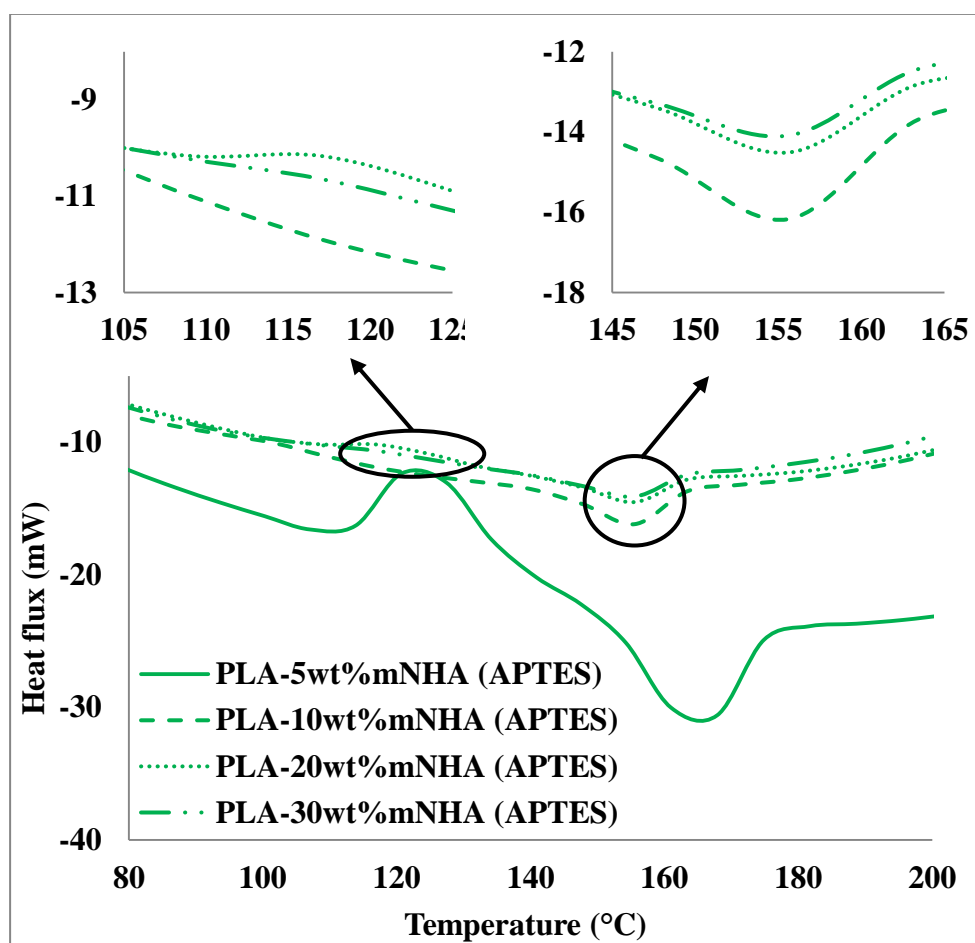
Figure 6.17: DSC curve for PLA-mNHA(APTES) nanocomposites at different mNHA(APTES) loading

Table 6.2: DSC analysis of the PLA-mNHA nanocomposites in respect to the PLA and PLA-5wt%NHA

Sample	Crystallisation Peak		Melting Peak	
	T_c (°C)	HF (mW)	T_m	HF (mW)
PLA	120.2	-17.19	151.8	-28.53
PLA-5wt% NHA	118.8	-14.69	160.5	-43.08
PLA-5wt%mNHA(APTES)	127.4	-13.04	167.9	-30.60
PLA-10wt%mNHA(APTES)	-	-	155.6	-16.22
PLA-20wt%mNHA(APTES)	116.9	-10.6	155.6	-14.53
PLA-30wt%mNHA(APTES)	-	-	155.6	-14.09
PLA-5wt%mNHA(SDS)	114.2	3.66	154.6	-1.79
PLA-30wt%mNHA(SDS)	-	-	154.7	0.43
PLA-5wt%mNHA(PEI)	-	-	154.7	0.08
PLA-30wt%mNHA(PEI)	-	-	154.7	2.75

6.7. Dynamic Mechanical Properties

Polymers possess viscoelastic behaviour when undergoing deformation; exhibiting both viscose and elastic characteristics. The viscoelastic properties can be studied using a technique known as dynamic mechanical analysis (DMA). DMA combines both mechanical and rheological characterisations of the polymer; tested as a function of temperature, time and frequency of an applied deformation force. The properties are expressed in terms of storage modulus and tan delta. The storage modulus determines the ability of the polymer to absorb or store energy. In addition, storage modulus is often associated with the stiffness (tensile modulus) of the polymer and is proportional to the energy stored during loading cycle. Tan delta on the other hand, signifies the ratio of dissipated energy to the stored energy per cycle of sample deformation at the glass transition temperature (T_g) and can be related to the impact strength of the material. Tan delta less than unity indicate elastic-dominant (solid-like) behaviour and values greater than unity indicate viscous-dominant (liquid-like) behaviour (Nammakuna et al. 2015). In addition, height of the tan delta peak can give information on the interfacial adhesion between the polymer

matrix and nanofiller, whereby lower height suggests improved interfacial adhesion.

Moreover, DMA can provide the information regarding the deformation properties of the polymer in terms of creep. As highlighted in section 2.7.2., creep is one of the essential properties to study when preparing nanocomposite for load bearing bone implant. This is because the degree of deformation of the biomaterials is dependent on several factors such as types of biomaterials used, magnitude of load, temperature and time. Moreover, for nanocomposites, the nanofillers loading can also influence the degree of deformation.

6.7.1.   Storage Modulus

Figure 6.18 depicts the storage modulus of the PLA-5wt%mNHA nanocomposites in respect to neat PLA and PLA-5wt%NHA. In all cases, the storage modulus decreases with temperature. It is also observed that the highest storage modulus values are obtained at the glassy regions (40°C) while rapid decrease is noted around the transition region (above 60°C). This can be noted from the calculated storage modulus retention percentage, listed in Table 6.3. For instance, the neat PLA recorded a drop of 89.7% as the temperature increased from 60°C to 70°C (transition region). Similar observation is made for the nanocomposites as well, recording a significant drop in storage modulus around the transition region compared to the glassy region. This is because, increasing the temperature reduces the stiffness of the nanocomposite due to increased PLA chain mobility at higher temperature; as mentioned in the thermal properties section.

Table 6.3 also lists the storage modulus of the nanocomposites, before and after surface modification at different loading mNHA loading. The storage modulus of the neat PLA is lower than most of the nanocomposites at all the temperatures. This is because addition of nanofiller increases the stiffness the PLA matrix. Optimum storage modulus was recorded for the PLA-5wt%NHA nanocomposite at both the glassy and transition regions. The storage modulus of PLA-5wt%NHA nanocomposite was 28.2%

higher than the neat PLA. However, the storage modulus of the nanocomposites decreased upon surface treatment of NHA. As a result, the storage modulus of PLA-5wt%mNHA(APTES) nanocomposite recorded reduction of 28% compared to the PLA-5wt% NHA, even though it was retained 3.4% higher than the neat PLA. In contrast, the storage modulus of SDS and PEI treated PLA-5wt%mNHA decreased drastically by 59.27% and 45.60%, respectively, in comparison to PLA-5wt%NHA and 46.16% and 28.08%, respectively, in comparison to neat PLA. Comparing to PLA-5wt%mNHA (APTES) nanocomposite, the storage modulus decreased by 47.94% (SDS) and 30.45% (PEI).

The reduction in storage modulus of the surface treated nanocomposites compared to the PLA-5wt% NHA, is credited to the improved interfacial adhesion between the mNHA(APTES) and the PLA matrix. This in turn caused the PLA chain mobility to increase, hence, reducing the storage modulus. However, PLA-5wt%mNHA (APTES) still obtained higher the storage modulus than neat PLA. This is again due to the presence of mNHA (APTES) as nanofiller within the PLA matrix, slightly restricting the mobility of the PLA chain.

Figure 6.19 illustrates the storage modulus of the APTES, SDS and PEI surface modified PLA-30wt%mNHA nanocomposites and the data are listed in Table 6.3. The increase in the mNHA loading from 5wt% to 30wt% contributed to a higher storage modulus. The APTES treated PLA-30wt%mNHA nanocomposite attained higher storage modulus, followed by the SDS treated PLA-30wt%mNHA and PEI treated PLA-30wt%mNHA nanocomposites. This can be due to the increased stiffness of the PLA matrix with the reinforcement effect imparted by the mNHA (APTES). Moreover, this increase in storage modulus of the PLA-30wt%mNHA (APTES) nanocomposite complemented the improvement in tensile modulus and impact strength of the nanocomposites, as described in mechanical properties section. The storage modulus of PLA-30wt% mNHA (SDS) was sustained in respect to neat PLA, whereby PLA-30wt% mNHA (PEI) nanocomposite obtained 20.5% less than the neat PLA. Similarly, the decrease in storage modulus for these two nanocomposites

further explains the decrease in tensile modulus and impact strength reported for both nanocomposites.

The effectiveness of the NHA and mNHA on the storage modulus of the nanocomposite can be expressed by a coefficient C. This effectiveness is calculated by Equation 6.1, whereby E'_G and E'_R denote the storage modulus at the glassy (T=40°C) and rubbery (T=80°C) state, respectively. The lower the C value, the higher the effectiveness of the nanofiller. In other words, lower C value indicates the significant reinforcement ability of the nanofiller on the polymer matrix. Table 6.3 lists the calculated C values of all the nanocomposites. It can be observed that the PLA-5wt% NHA nanocomposite attained the lowest C value. This however contradicts the assumptions made earlier regarding NHA not being suitable to reinforce PLA matrix due to poor interfacial adhesion. The C values of the surface treated nanocomposites at higher nanofiller loading decreased with increase in mNHA (APTES, SDS, and PEI) loading from 5wt% to 30wt%. This is because at a higher mNHA loading, the PLA matrix rich region becomes less, contributing to the lower C values, thus, improving the effectiveness of mNHA at a higher loading.

$$C = \frac{(E'_G/E'_R)_{nanocomposite}}{(E'_G/E'_R)_{neat\ PLA}} \qquad \textbf{Equation 6.1}$$
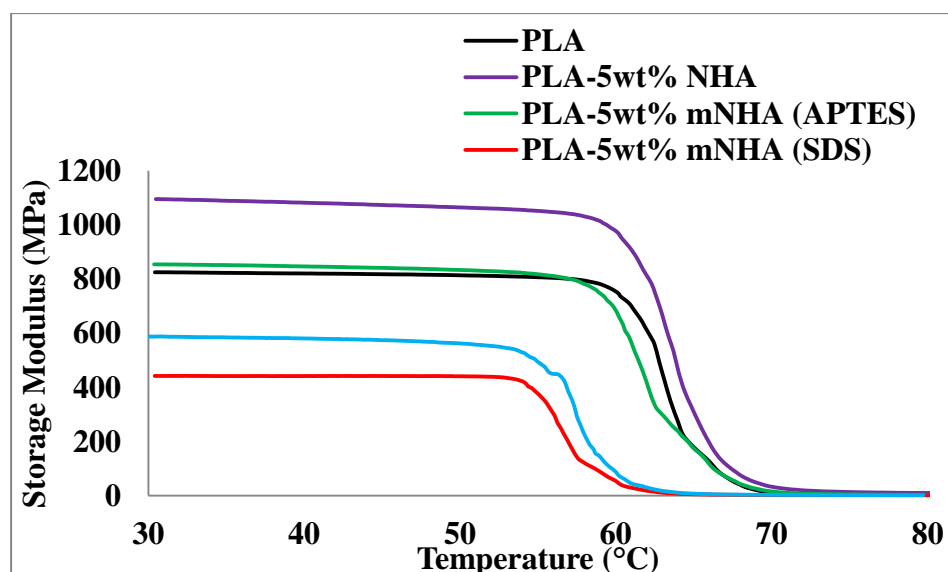
Figure 6.18: Storage modulus of the PLA-5wt%mNHA treated with APTES, SDS and PEI in respect to neat PLA and PLA-5wt%NHA
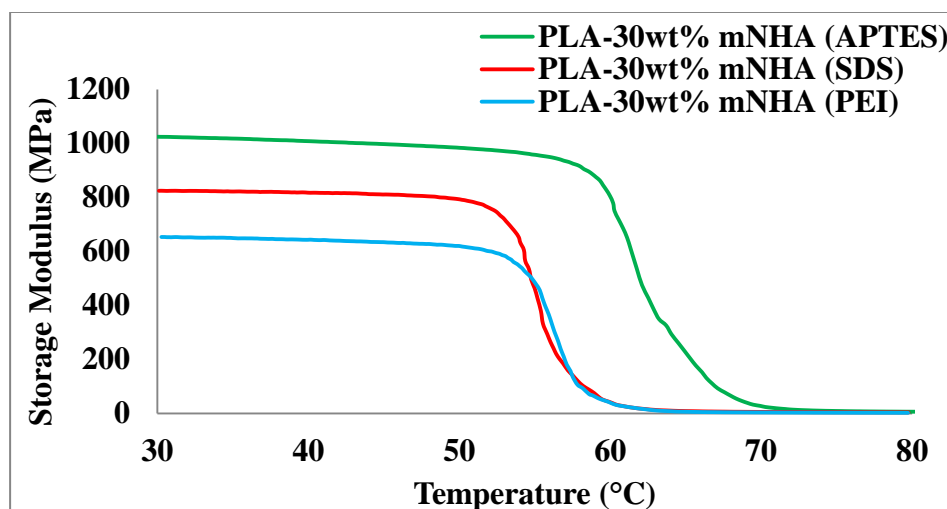
Figure 6.19: Storage modulus of the APTES, SDS and PEI surface treated PLA-30wt% mNHA

6.7.2. Tan Delta

Figure 6.20 portrays the tan delta of the PLA-5wt%mNHA nanocomposites in comparison to neat PLA and PLA-5wt%NHA. The tan delta and T_g values are also listed in Table 6.3. All the nanocomposites acquired lower tan delta peak height compared to the neat PLA. This is due to the increased stiffness of the material. Lower tan delta also indicates the increase in the elasticity of the nanocomposite, thus, justifying the reported increase in tensile modulus and storage modulus. In other words, the more elastic the nanocomposite is, the more energy is stored. Upon surface treatment, the tan delta peak height of the PLA-5wt% mNHA (APTES, SDS and PEI) nanocomposites decreased significantly compared to PLA-5wt%NHA. It is important to note that decrease in tan delta peak height indicates better interfacial adhesion between the nanofiller and the polymer matrix. The tan delta peak height of PLA-5wt%mNHA (APTES) recorded the lowest tan delta value, decreasing by 45% compared to PLA-5wt%NHA. Hence, justifying the suggested improvement of the interfacial adhesion between mNHA(APTES) and PLA matrix.

135

Figure 6.21 depicts the tan delta of the APTES, SDS and PEI treated PLA-30wt%mNHA nanocomposites, and the data are summarised in Table 6.3. The PLA-30wt%mNHA nanocomposites exhibit lower tan delta peak height than their respective PLA-5wt%mNHA, whereby a decrease of 11.6% (SDS) and 9.9% (PEI) was noted. However, the tan delta of the mNHA(APTES) increased upon increase in the mNHA loading, contradicting the fact that tan delta should have decreased upon higher loading.

In contrast to tan delta, T_g of the PLA-5wt%NHA nanocomposite showed no significant change compared to neat PLA (Salerno et al. 2014). The T_g of APTES treated PLA-5wt%mNHA recorded slight decrease (0.9%) while SDS and PEI treated PLA-5wt%mNHA nanocomposites noted drastic decrease of 9.3% and 7.3%, respectively compared to PLA-5wt%NHA nanocomposite. Further increase in the mNHA loading showed no difference in the T_g values. It is important to note that, reduction in T_g values are also a measure of poor interfacial adhesion between PLA matrix and mNHA(SDS) and mNHA(PEI).
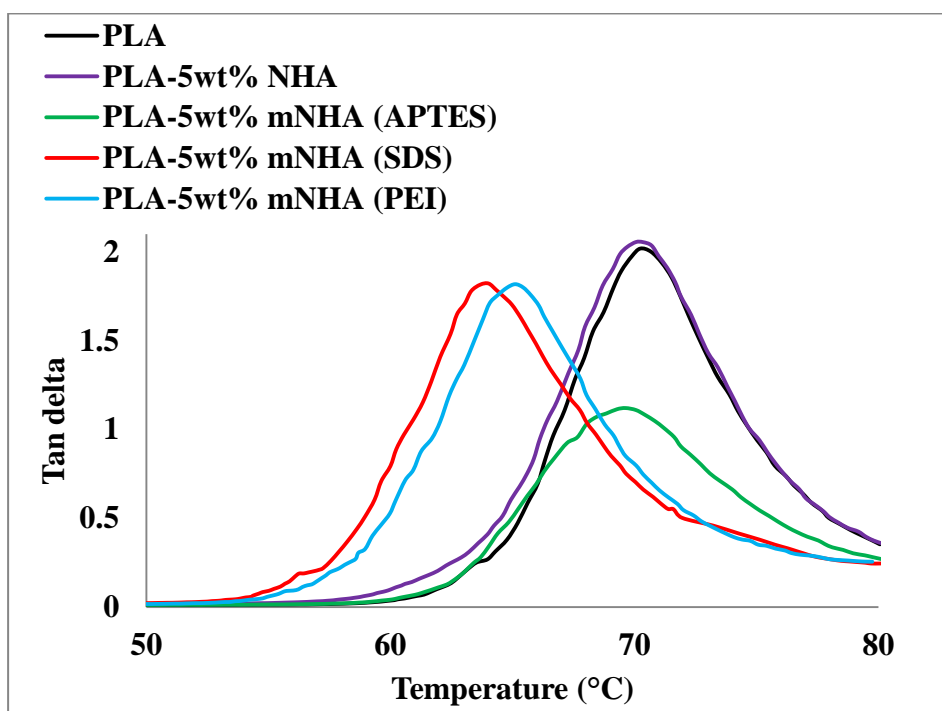
Figure 6.20: Tan delta of the PLA-5wt%mNHA treated with APTES, SDS and PEI in respect to neat PLA and PLA-5wt%NHA
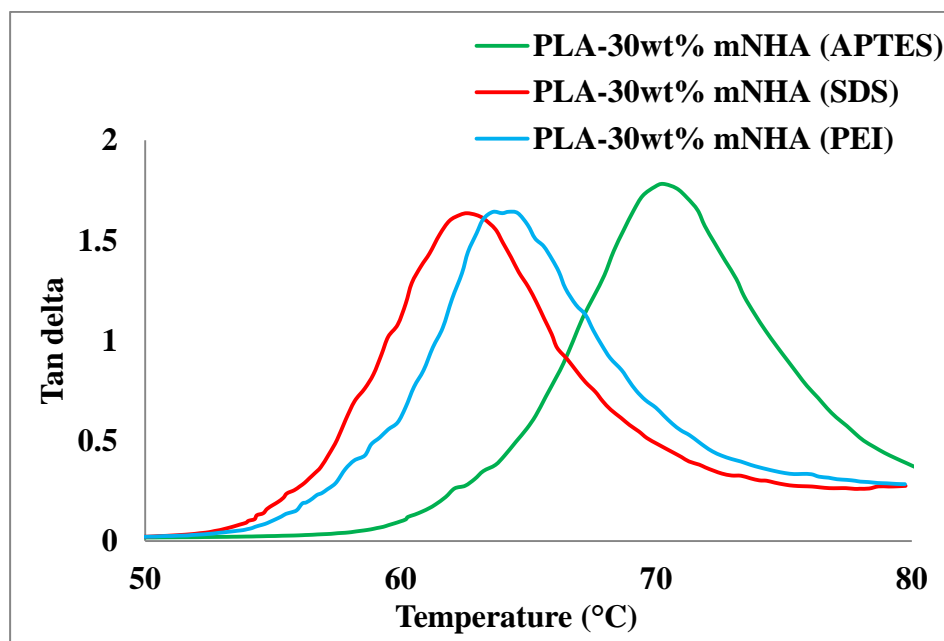
Figure 6.21: Tan delta of the PLA-30wt%mNHA treated with APTES, SDS and PEI

Table 6.4 outlines the storage modulus, tan delta, T_g, variation of the storage modulus retention of the nanocomposites and the effectiveness of the mNHA(APTES). It is evident that the storage modulus increased with increase in the mNHA (APTES) loading, while the tan delta decreased compared to neat PLA with the exception of 5wt%mNHA(APTES) reinforced nanocomposite. As mentioned in section 6.7.2, reduction in tan delta height is an indication of improved interfacial adhesion between the PLA matrix and mNHA. It also means, the stiffness of the martial improved, justifying the increased storage modulus and the tensile modulus. This is because, as mentioned in section 6.7.1, the PLA matrix rich region becomes less as the mNHA loading increased to up to 30wt%, thus resulting in the increased storage modulus. This was complemented by the calculated C values of the PLA-mNHA(APTES), which suggested that effectiveness of mNHA (APTES) improved with the increase in mNHA loading, whereby, the 30wt% mNHA (APTES) was more effective as a filler compared to the lower loading.

Table 6.3: Effectiveness of surface modifiers on the dynamic mechanical properties

Sample	Tan delta	T_g (°C)	Storage modulus (MPa)	C	Storage modulus retention (%)			
					$E'_{50°C}/E'_{40°C}$	$E'_{60°C}/E'_{40°C}$	$E'_{70°C}/E'_{40°C}$	$E'_{80°C}/E'_{40°C}$
PLA	2.04	70.24	821.58	-	99	91	1.3	0.3
PLA-5wt%NHA	2.04	70.06	1086.13	0.37	98	90	3	0.9
PLA-5wt%mNHA(APTES)	1.12	69.64	849.61	0.81	98	80	1.8	0.4
PLA-30wt%mNHA(APTES)	1.76	70.28	1013.32	0.59	98	77	2.3	0.6
PLA-5wt%mNHA(SDS)	1.81	63.69	442.32	0.85	99	12.4	0.6	0.4
PLA-30wt%mNHA(SDS)	1.60	63.24	824.38	0.77	97	4.5	0.6	0.4
PLA-5wt%mNHA(PEI)	1.82	64.11	590.88	0.87	97	12.6	0.5	0.4
PLA-30wt%mNHA(PEI)	1.64	63.98	653.14	1.10	96	5.4	0.5	0.3

Table 6.4: Effectiveness of nanofillers loading on the dynamic mechanical properties

Sample	Tan delta	T_g (°C)	Storage modulus (MPa)	C	Storage modulus retention (%)			
					$E'_{50°C}/E'_{40°C}$	$E'_{60°C}/E'_{40°C}$	$E'_{70°C}/E'_{40°C}$	$E'_{80°C}/E'_{40°C}$
PLA-5wt%mNHA(APTES)	1.12	69.64	849.61	0.81	98	80	1.8	0.4
PLA-10wt%mNHA(APTES)	1.99	70.65	924.18	0.80	98	84	1.8	0.4
PLA-20wt%mNHA(APTES)	1.76	70.75	947.45	0.59	99	89	2.9	0.6
PLA-30wt%mNHA(APTES)	1.76	70.28	1013.32	0.58	98	77	2.3	0.6

6.7.3. Creep

An ideal creep and recovery curve for viscoelastic material is illustrated schematically in Figure 6.22. OA represents the instant creep strain which reflects the elastic properties of the materials at t=0. As the time of loading continues, the strain is observed to increase non-linearly (AB) and eventually a linear (BC) increase appears. AB is referred as the delayed elastic strain which can fully be recovered, while BC is an irreversible strain. Upon the removal of the constant load, an instant recovery strain is generated (CD), which is usually equal to the instant creep strain (OA). As the time for recovery continues, the AB region decreases to zero (DE) and the BC will remain as residual strain (EF).
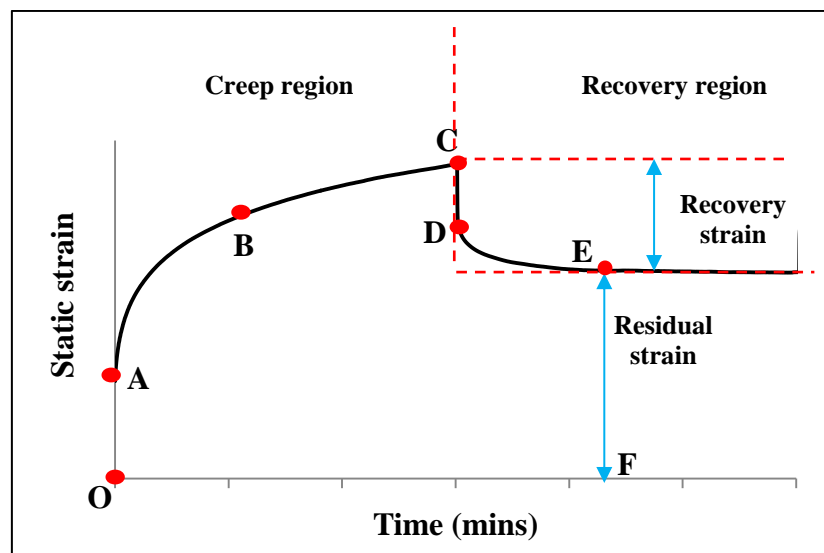
Figure 6.22: Typical creep and recovery curves of viscoelastic material under constant stress

Figures 6.23 – 6.27 depict the creep and recovery curves of the nanocomposites in comparison to neat PLA. In this study, a constant static load of 0.5N (10% of tensile strength of PLA) was applied to the neat PLA and nanocomposites for 20 mins. The effect of temperature on the creep properties was further analysed for PLA-5wt%NHA and PLA-5wt%mNHA(APTES). In addition, the influence of mNHA loading on the creep properties was investigated. Table 6.5 summarises the creep, recovery and residual strains of the nanocomposites including neat PLA. From Figure 6.23, it can be observed that the nanocomposites displayed similar creep behaviour as the neat PLA. However,

the creep and recovery strains of the nanocomposites were lower than that of the neat PLA; implying improved creep properties of the nanocomposite due to the presence of nanofillers. For instance, upon addition of 5wt% NHA, the creep and recovery strains at T_g (70°C) recorded a reduction of 89.1% and 89.45%, respectively, in comparison to neat PLA. This also indicates improved elasticity. Significant reduction of 88.1% in the residual strain of the PLA-5wt%NHA nanocomposite was also noted compared to neat PLA; suggesting minimum permanent deformation took place. Meanwhile, the creep and residual strains of the surface treated PLA-5wt% mNHA nanocomposites recorded no significant changes compared to PLA-5wt%NHA (less than ~1%). The recovery strains on the other hand noted reduction of 23.4%. Thus, based on the creep and recovery strains obtained, the optimum improved creep properties were achieved for the PLA-5wt%mNHA (APTES) nanocomposite.
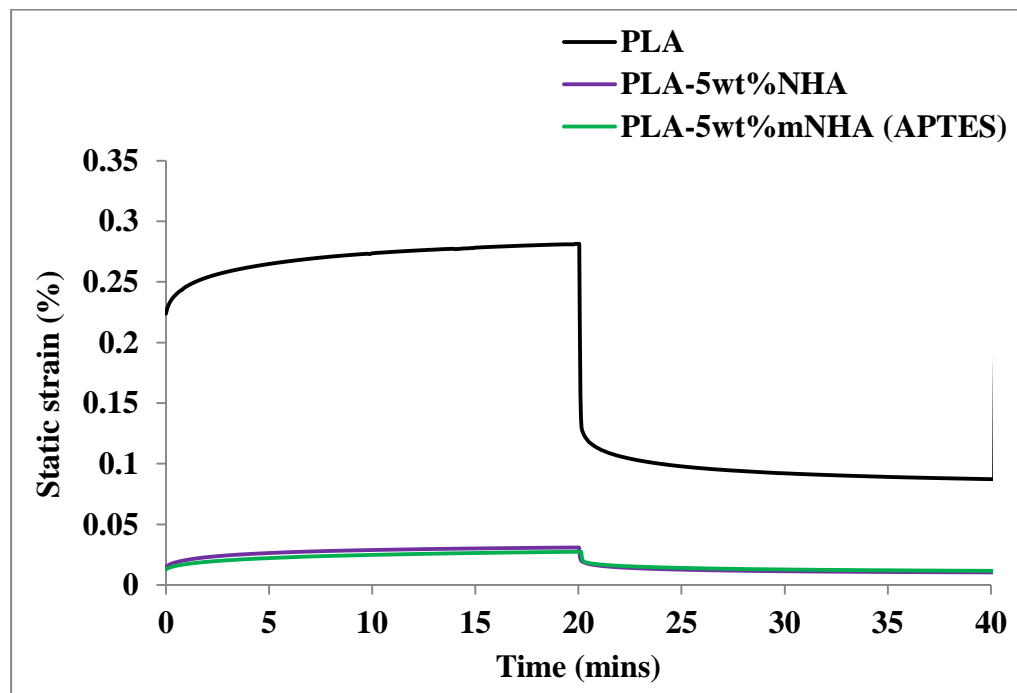
Figure 6.23: Creep and recovery curve of the nanocomposites before and after surface modification in comparison to neat PLA

Figure 6.24 compares the creep properties of the before and after surface treated nanocomposites conducted at different temperatures. As expected, creep strain increased with temperature. It is evident that changing the temperature from 60°C to 80°C increased the creep strain by 31.7% (PLA-5wt%NHA) and

537.7% (PLA-5wt%mNHA(APTES)), at t= 20mins, which is not favourable. In addition, a large permanent deformation (residual strain) was observed at T=80°C despite most of the strains being recovered. This shows that creep properties are sensitive towards change in temperature.
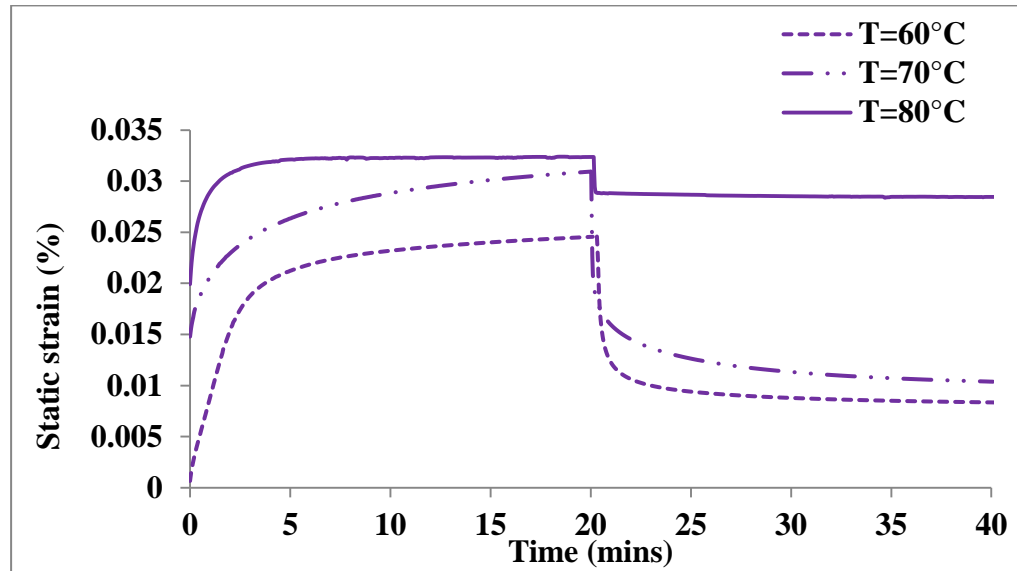
(a)
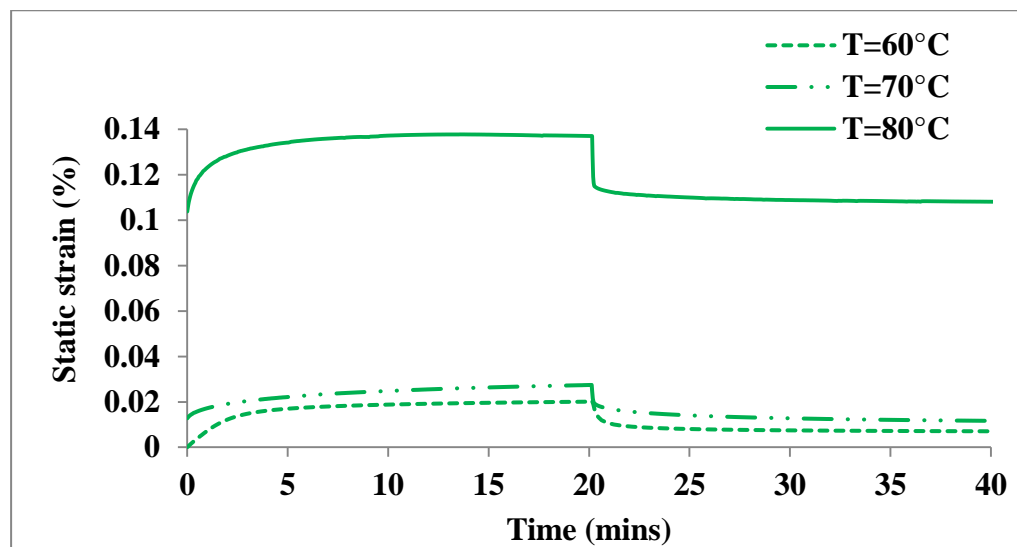
(b)

Figure 6.24: Effect of temperature on the creep and recovery curve of (a) PLA-5wt%NHA and (b) PLA-5wt%mNHA(APTES)

Figures 6.25 – 6.26 show the creep properties of APTES, SDS and PEI treated PLA-5wt%mNHA and PLA30wt%mNHA nanocomposites, respectively. Compared to PLA-5wt%mNHA(APTES), the creep properties of the SDS

treated nanocomposite had no significant changes. Meanwhile, PEI treated PLA-5wt%mNHA nanocomposite attained higher creep strain (9.9%) and recovery strain (22.9%) and lower residual strain (7.7%) than APTES treated PLA-5wt%mNHA. The increased recoverable strain of the PLA-5wt%mNHA(PEI) could be as a result of poor interfacial adhesion between mNHA(PEI) and PLA matrix. Similarly, the creep properties of PLA-30wt%mNHA followed the trend of PLA-5wt%mNHA.

Figure 6.27 illustrates the influence of mNHA (APTES) loading on the creep properties of the nanocomposites. It is found that the creep properties were greatly affected by the mNHA loading as can be seen in Table 6.5. Increasing the mNHA loading from 5wt% to 10wt% reduced the creep properties of the PLA-mNHA(APTES) by 14.6% (creep strain), 17.2% (recovery strain) and 11.1% (residual strain). This means that the PLA-10wt%mNHA(APTES) nanocomposite creep properties (more elastic and minimum permanent deformation) than PLA-5wt%mNHA(APTES). Further increase in mNHA loading to 20wt% and 30wt% resulted in the increase of creep strain (5.4% and 1.4%) and recovery strain (9.6% and 3.8%). Moreover, the PLA-30wt%mNHA recorded an increase of 8.5% in residual strain; indicating the permanent deformation is high. Thus, overall the PLA-10wt%mNHA attained the most favourable creep properties.
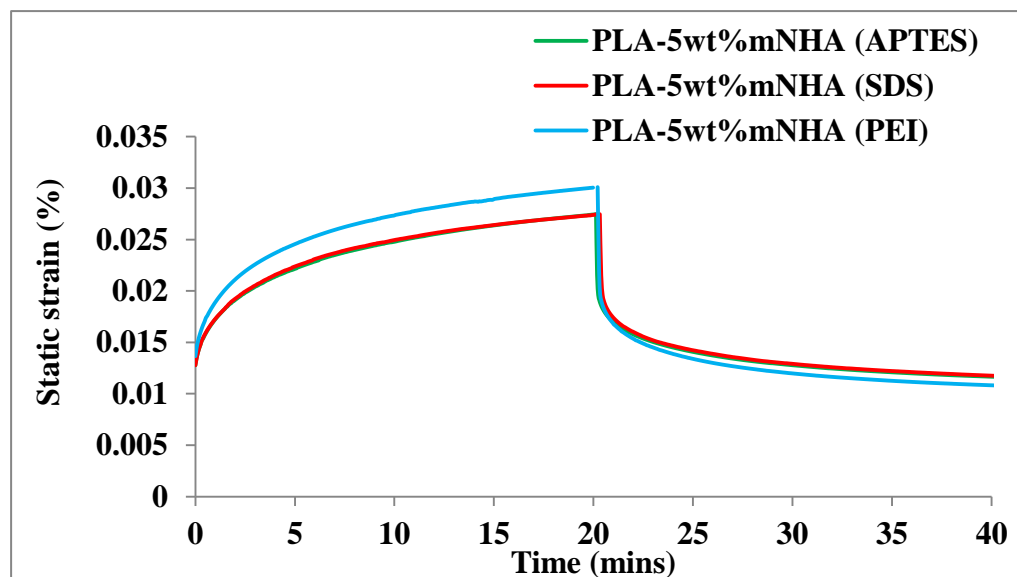
Figure 6.25: Creep and recovery curve of APTES, SDS and PEI surface treated PLA-5wt%mNHA nanocomposites
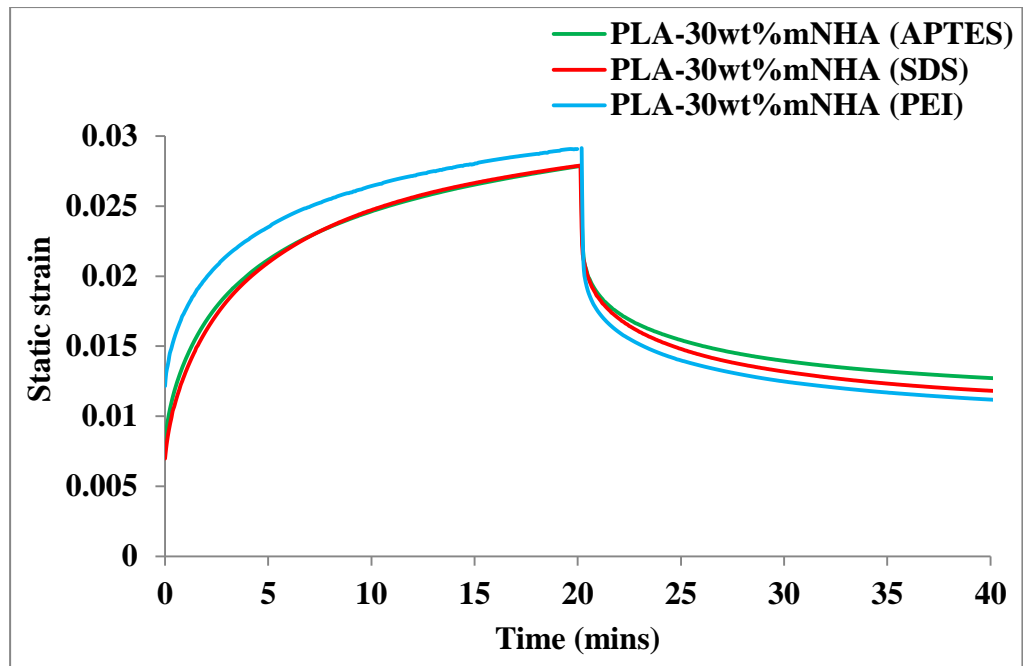
Figure 6.26: Creep and recovery curve of APTES, SDS and PEI surface treated PLA-30wt%mNHA nanocomposites
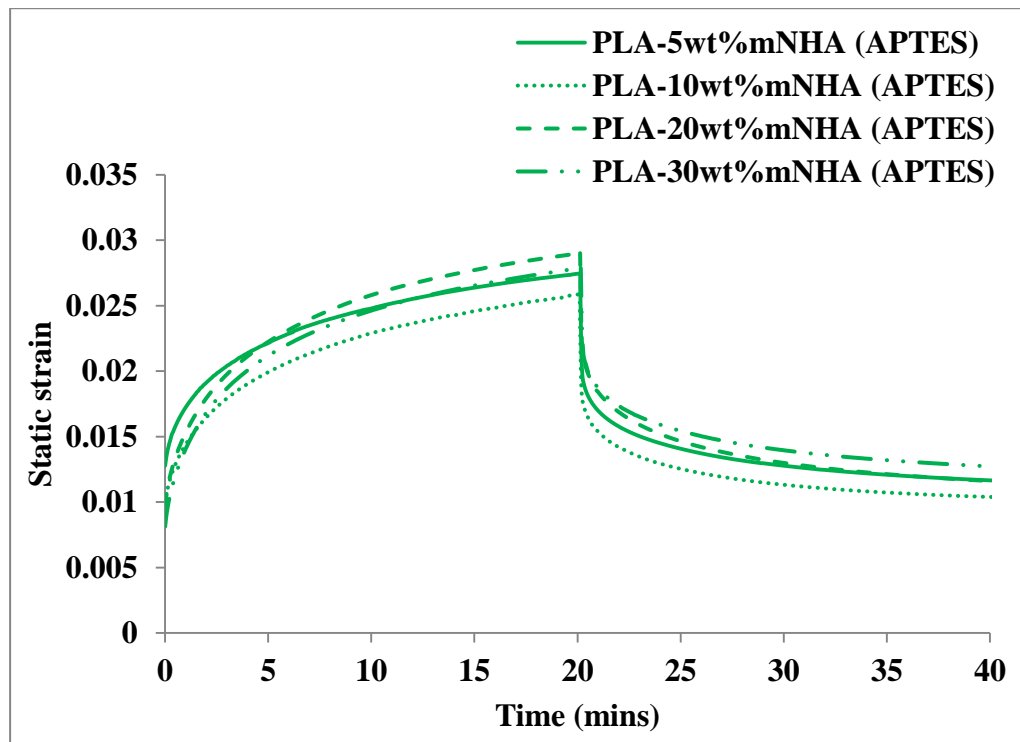
Figure 6.27: Effect of mNHA(APTES) loading on the creep and recovery curve of the PLA-mNHA (APTES) nanocomposites

Table 6.5: Creep analysis of the nanocomposites in comparison to neat PLA

Sample	Condition	Creep Strain	Recovery Strain	Residual Strain
PLA	**T=70°C**	0.2814	0.1940	0.0874
PLA-5wt% NHA	**T=60°C**	0.0246	0.0162	0.0084
	T=70°C	0.0309	0.0205	0.0104
	T=80°C	0.0324	0.0039	0.0285
PLA-5wt%mNHA(APTES)	**T=60°C**	0.0215	0.0144	0.0071
	T=70°C	0.0274	0.0157	0.0117
	T=80°C	0.1371	0.0290	0.1081
PLA-10wt%mNHA(APTES)	**T=70°C**	0.0234	0.0130	0.0104
PLA-20wt%mNHA(APTES)	**T=70°C**	0.0289	0.0172	0.0117
PLA-30wt%mNHA(APTES)	**T=70°C**	0.0278	0.0151	0.0127
PLA-5wt%mNHA(SDS)	**T=70°C**	0.0275	0.0157	0.0118
PLA-30wt%mNHA(SDS)	**T=70°C**	0.0279	0.0161	0.0118
PLA-5wt%mNHA(PEI)	**T=70°C**	0.0301	0.0193	0.0108
PLA-30wt%mNHA(PEI)	**T=70°C**	0.0291	0.0179	0.0112

6.8. Fracture Surface Morphology

As discussed in previous chapter (section 5.6), the microstructure images of the neat PLA suggested a brittle fracture surface, while PLA-5wt%NHA nanocomposite had weak interfacial adhesion between the nanofiller and PLA matrix. Moreover, agglomeration of the NHA filler in the PLA matrix and lack of fibril upon fracture was observed, contributing in the deterioration of the tensile strength of the PLA matrix. Figure 6.28 shows the microstructural images of the impact fractured surface of the APTES, SDS and PEI surface treated PLA-mNHA (5 and 30wt%) nanocomposites in comparison to neat PLA and PLA-5wt%NHA.

Figure 6.28 (a) displays lack of agglomerates and voids, hence improving the interfacial adhesion between the mNHA(APTES) and the PLA matrix. The presence of fibril suggested that the nanocomposite became less brittle compared to the NHA reinforced PLA nanocomposite. This further

complements the improvement in mechanical properties of PLA-5wt% mNHA (APTES). Increasing the loading of mNHA (APTES) to 30wt%, however, caused the nanofillers to agglomerate (Figure 6.28 (b)). As mentioned in chapter 5, these agglomerates are weak points in the nanocomposite and can break easily when stress is applied, hence produce a weaker nanocomposite. In addition, absence of fibril formation as the 30wt% mNHA(APTES) reinforced nanocomposite is an indication of increased brittle nature, explaining the drop in tensile strength of the nanocomposite compared to PLA-5wt%mNHA (APTES).

The surface treatment of NHA with SDS improved the interfacial adhesion; hence there are no voids in the fractured sample as shown in Figure 6.28 (c). This contributed in the increase of the mechanical properties of PLA-5wt% mNHA(SDS) in comparison to PLA-5wt% NHA. The presence of agglomerates of the mNHA (SDS) indicated by the circles in the Figure 6.28 (c), however, led to the decrease in mechanical properties of PLA-5wt% mNHA(SDS) compared to PLA-5wt%mNHA(APTES). Increasing the mNHA (SDS) loading from 5wt% to 30wt%, increased the agglomerates and the fibril disappeared as shown in Figure 6.28 (d). This resulted in the deterioration of mechanical properties of PLA-30wt%mNHA (SDS) as compared to PLA-5wt%mNHA (SDS).

Similarly, the treatment of NHA with PEI resulted in the improvement of the interfacial adhesion between NHA and PLA as indicted by the absence of voids in Figure 6.28 (e and f). In spite of that, the aggregation of mNHA particles was observed (indicated by circles). The size of the agglomerated 5wt% mNHA (PEI) particles in the PLA matrix is bigger compared to 5wt% mNHA (SDS). This was caused by the interaction the mNHA particles through the polyethylenomine group. Thus, the nanocomposite with mNHA (PEI) attained the least mechanical properties for both 5wt% and 30wt%.
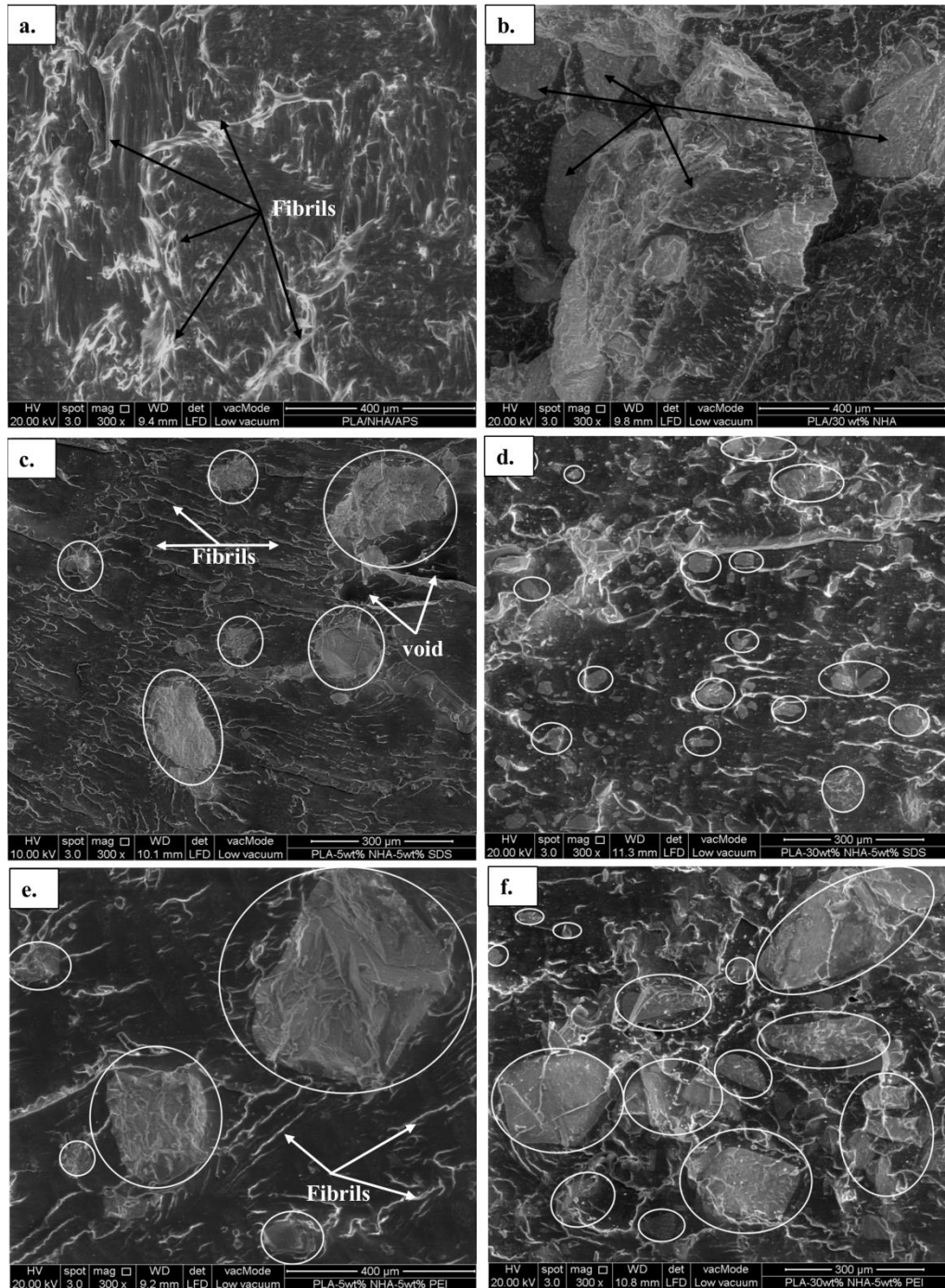
Figure 6.28: Microstructural images of the impact fractured samples (a) PLA-5wt% mNHA (APTES), (b) PLA-30wt% mNHA (APTES), (c) PLA-5wt% mNHA (SDS), (d) PLA-30wt% mNHA (SDS), (e) PLA-5wt% mNHA (PEI) and (f) PLA-30wt% mNHA (PEI)

6.9. Summary

The APTES has successfully surface modified the NHA and improved the interfacial adhesion between the mNHA (APTES) and PLA matrix. SDS also surface modified the NHA and to some extent contributed in the enhancement of the interfacial adhesion between the mNHA (SDS) and PLA matrix. PEI, however, failed to improve the interfacial adhesion in this study due to the lack of hydrophobic chain that could have formed strong bond with the PLA. Judging from the mechanical properties, the 5wt% of both mNHA (APTES) and mNHA (SDS) reinforced nanocomposite, achieved within the acceptable limit of cortical bones strength requirements. Even though the tensile strength decreased at higher mNHA loading, the 10-30wt% APTES and SDS treated nanocomposites can still be used as implants for trabecular bones. Moreover, APTES treated nanocomposites attained better thermal and dynamic mechanical properties as the mNHA(APTES) loading increased, while SDS and PEI resulted in the decrease of the properties of their respective surface treated nanocomposites.

CHAPTER 7

PREPARATION OF POLY-LACTIC ACID NANOCOMPOSITES REINFORCED WITH mNHA AND GRAPHENE NANOPLATELETS

7.1. Introduction

This chapter addresses the fourth objective of this study; which is the reinforcement of PLA matrix with nanohybrid filler. The previous chapter has reported slight improvement on the mechanical, thermal and dynamic mechanical properties of the mNHA (APTES) reinforced PLA nanocomposite. In this chapter, the nanohybrid is prepared by mixing the mNHA (APTES) with graphene nanoplatelets (GNP). This is because, in recent years, graphene has attracted great attention as it is one of the stiffest (modulus of 1 TPa) and strongest (strength 100GPa) materials (Grantab et al. 2010). In addition, it also happens to be biocompatible (Machado and Serp 2012). To date, significant improvement in mechanical properties of the graphene reinforced polymer nanocomposites has been reported (Kim et al. 2010, Chieng et al. 2014, Wang and Lin 2014). As a result, in this chapter the GNP loading was varied at 0.01wt%, 0.05wt% and 0.1wt% while the mNHA-GNP is kept constant at 5wt%. The neat PLA and PLA-5wt%mNHA(APTES) were used as control samples. The impact of mNHA-GNP nanohybrid and increasing the GNP loading on the mechanical, thermal and dynamic mechanical properties of PLA nanocomposites are reported in this chapter.

7.2. Mechanical Properties

7.2.1. Tensile Properties

Figure 7.1 shows the tensile properties of the mNHA-GNP reinforced PLA nanocomposites, in respect to neat PLA and PLA-5wt%mNHA(APTES) nanocomposite. It is observed that the tensile properties of the nanocomposites decreased with the addition of GNP. The tensile strength of PLA-5wt%mNHA reinforced with 0.01wt% GNP recorded a reduction of 8.7% and 9.7% in comparison to neat PLA and PLA-5wt%mNHA(APTES), respectively. It is known that the stress transfer between the nanofiller and the polymer matrix is greatly influenced by the interfacial adhesion and dispersion between both biomaterials. Hence, the reduction noted in this study could be as a result of

insufficient amount of GNP infused within the network of PLA, or/and poor interaction between the mNHA-GNP and PLA matrix.

Other factor that can impact the reinforcement of the polymer is also the nanofiller loading (as discussed in chapter 5 and 6). Given the large surface area of GNP and its rigidity, a significant improvement in the mechanical strength was expected to be seen, especially at a lower loading. This is because at lower loading, GNP can be fully exfoliated in the polymer matrix and effective reinforcement can be achieved. Increasing the GNP loading however, can cause the stacking of the GNP sheets due to strong van der Waals forces among them (Dai and Mishnaevsky 2014). These changes are evident from the FESEM micrographs of the mNHA-GNP nanofillers which have been clearly elaborated in section 7.5. Thus, further increase in the GNP loading caused the tensile strength to reduce by 10.8% (0.05wt% GNP) and 14.8% (0.1wt% GNP), in comparison to the 0.01wt% GNP reinforced nanocomposite. Similarly, a reduction in the tensile strength of PLA-epoxidised palm oil matrix was reported when reinforced with 0.1-0.5wt% of GNP (Chieng et al. 2012). In other studies, the tensile strength of epoxy nanocomposites was observed to improve only after addition of 0.5wt% GNP loading (Chatterjee et al. 2012, Prolongo et al. 2013) while Nylon-6 improved with addition of 0.1wt% GNP (Xu and Gao 2010).

The tensile modulus of the PLA-mNHA-GNP nanocomposites decreased by 16.9% and 23.4% (0.01wt% GNP), 22.8% and 28.8% (0.05wt% GNP) and 25.1% and 30.9% (0.1wt% GNP), compared to the neat PLA and PLA-5wt%mNHA(APTES), respectively, indicating the PLA-mNHA-GNP nanocomposites became less stiffer (Chieng et al. 2014). The reductions in tensile properties upon addition of GNP can also be attributed to the technique used to prepare the nanocomposite, which is melt mixing (Papageorgiou et al. 2015). The high shear forces applied by the twin-screw can cause buckling or shortening of graphene sheets, thus reducing its area-to-volume and aspect ratio and limiting the ability of GNP to reinforce the polymer (Bhattacharya 2016).
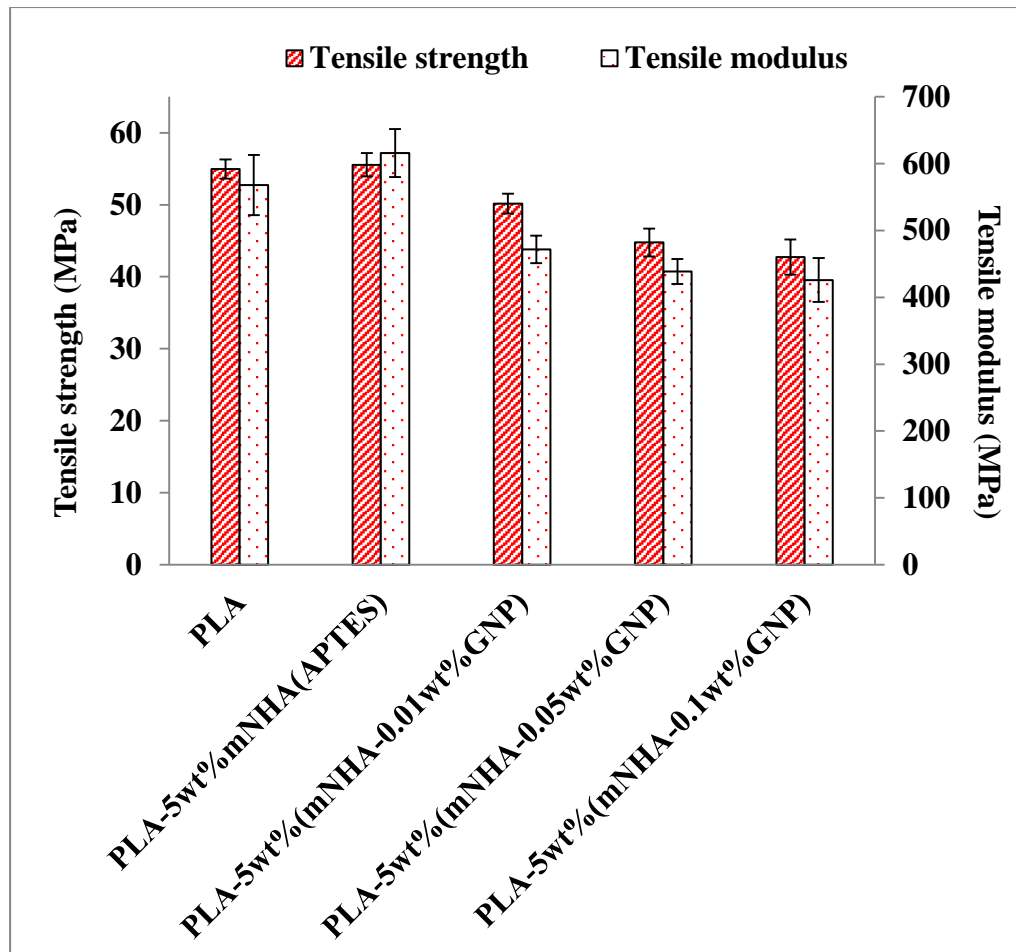
Figure 7.1: Tensile properties of PLA-5wt%(mNHA-(0.01-0.1wt%) GNP) nanocomposites in comparison to neat PLA and PLA-5wt%mNHA (APTES)

7.2.2. Impact Strength

Figure 7.2 depicts the impact strength of PLA nanocomposites reinforced with mNHA-GNP in comparison to neat PLA and PLA-5wt%mNHA(APTES) nanocomposite. In contrast to tensile properties, the impact strength of the 0.01wt% GNP reinforced PLA-5wt%(mNHA-GNP) showed significant increase of 22.1% compared to neat PLA while only 7.9% increase was recorded in contrast to PLA-5wt%mNHA (APTES). This can be accredited to the mNHA-GNP nanofiller absorbing the energy and acting as crack deflectors and crack bridging mechanisms at a lower loading. This in turn, indicates that the PLA was reinforced well and that the mNHA-GNP provided enough interface to allow load transfer from the PLA matrix to the mNHA-GNP filler.

Similar results were reported for epoxy-graphene nanocomposite (Liu et al. 2014).

Further increase in GNP loading on the other hand, resulted in reduction of the impact strength by 7.9% (0.05wt% GNP) and 25.7% (0.1wt% GNP), compared to 0.01wt% GNP. This is due the increased van der Waals forces binding the mNHA-GNP nanofiller with the PLA matrix at a higher loading (Pinto and Leszczynski 2014). These forces do not have sufficient magnitude to transfer the load between the biomaterials. Moreover, the stacking of graphene sheets at higher loading can lead to the formation of voids or agglomeration of particles. These agglomerates can act as stress concentrators allowing the crack to propagate faster, hence lower energy required for the nanocomposite to fracture. Similar observation were reported for both PP-graphene and epoxy-graphene nanocomposites at higher loading (Chaharmahali et al. 2014, Liu, Wu et al. 2014).
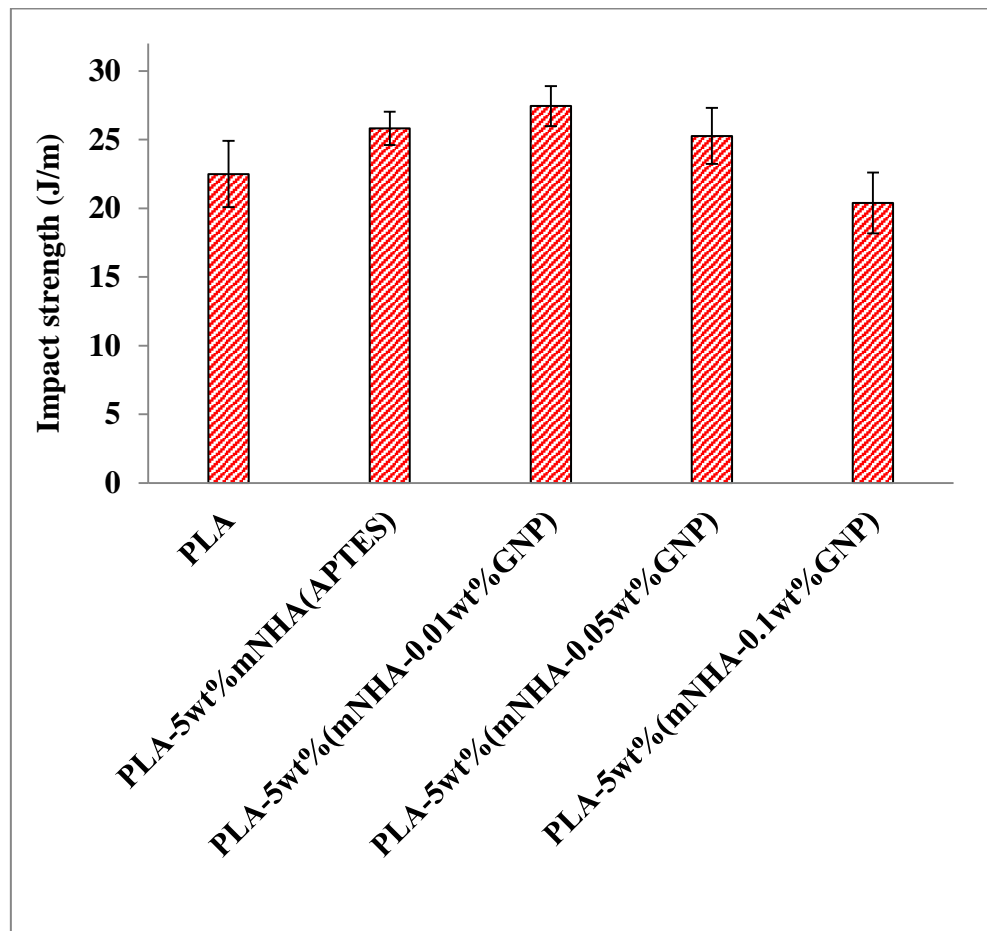
Figure 7.2: Impact strength of the PLA-5wt%(mNHA-(0.01-0.1wt%) GNP) nanocomposites in comparison to neat PLA and PLA-5wt%mNHA (APTES)

7.3. Thermal properties

The thermal properties of the mNHA-GNP reinforced PLA was investigated at 3°C and 10°C heating rate. In order to study the influence of GNP on the thermal properties of PLA nanocomposite, the TGA and DSC thermograms of PLA-mNHA(APTES) and neat PLA are also included.

7.3.1. TGA

Figures 7.3 – 7.4 present the TGA thermograms of the mNHA-GNP nanohybrid reinforced PLA nanocomposite at different heating rates. These figures elaborate the thermal stability of the nanocomposites at heating rates of 10°C/min (Figure 7.3) and 3°C/min (Figure 7.4). In addition, the $T_{5\%}$, $T_{10\%}$, $T_{50\%}$ and T_{max} and the remaining weight of the nanocomposites are listed in Table 7.1. At 10°C/min heating rate, the thermal stability of the PLA-5wt% (mNHA-0.01wt%GNP) nanocomposite decreased in respect to both neat PLA and PLA-5wt%mNHA (APTES) nanocomposite. This can be noted from the $T_{10\%}$, $T_{50\%}$ and T_{max} recorded in Table 7.1. Meanwhile, from Figure 7.3 (a), the $T_{5\%}$ of the PLA-5wt%mNHA (APTES) nanocomposite decreased drastically, due to excess lattice water removal. As mentioned in section 4.4.4., this lattice water is in fact found within the NHA and that the removal process is reversible. Thus, at around 280°C, the PLA-5wt%mNHA(APTES) noted the decrease. Upon addition of GNP however, the initial thermal stability ($T_{5\%}$) improved due to GNP's ability to act as physical barrier and absorb the heat. At slower heating rate (3°C/min), the initial degradation temperatures ($T_{5\%}$, $T_{10\%}$ and $T_{50\%}$) of the mNHA-GNP nanocomposite noted no significant difference compared to neat PLA, while showed no improvement compared to PLA-5wt%mNHA nanocomposites. However, the T_{max} of the 0.01wt% GNP reinforced nanocomposite was observed to increase, suggesting improvement in thermal stability of the PLA-5wt%(mNHA-0.01wt%GNP). This is also attributed to the increased ability of GNP to act as physical barrier at a slower heating rate, consequently delaying the maximum degradation of the PLA matrix.

Figure 7.5 illustrates the impact of GNP loading on the thermal stability of PLA matrix at heating rate of 3°C/min. The thermal stability of the PLA-mNHA-

GNP nanocomposite was observed to improve with increased GNP loading. This is evident from the $T_{5\%}$, $T_{10\%}$, $T_{50\%}$ and T_{max} recorded in Table 7.1. The enhancement in the thermal stability of the PLA-mNHA-GNP nanocomposite (0.1wt% > 0.05wt% > 0.01wt% GNP) can be attributed to the increased physical barrier effect of GNP sheets.
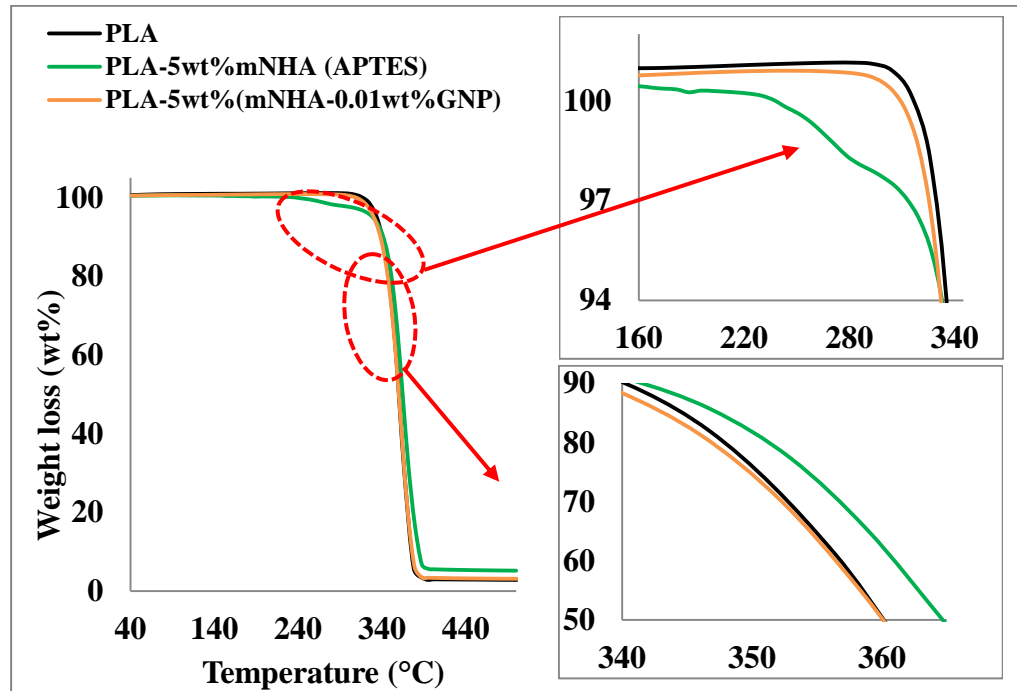
(a)
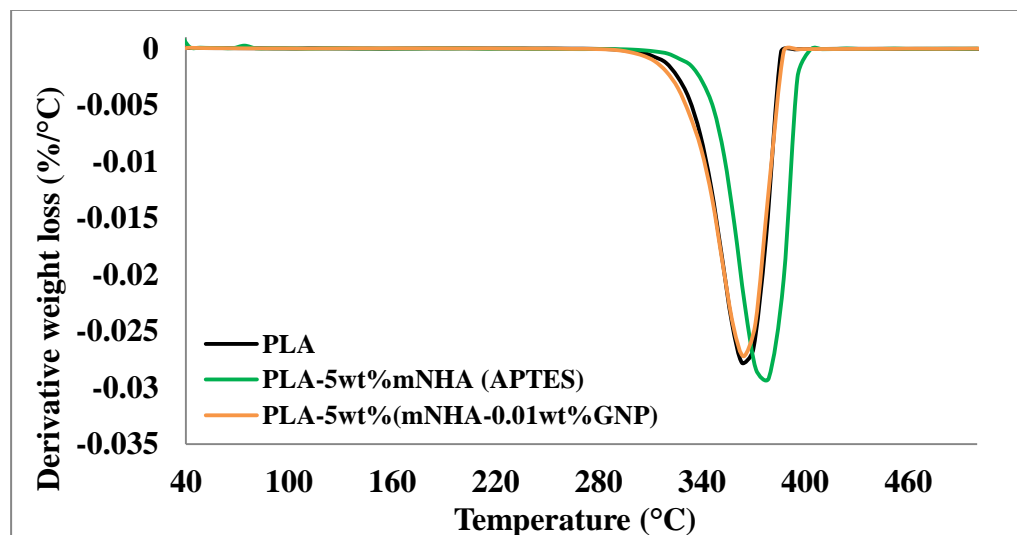
(b)

Figure 7.3: TGA thermograms of PLA-mNHA-GNP nanocomposite in comparison to PLA-mNHA(APTES) and neat PLA; heating rate at 10°C/min (a) weight loss curve and (b) derivative curve

154
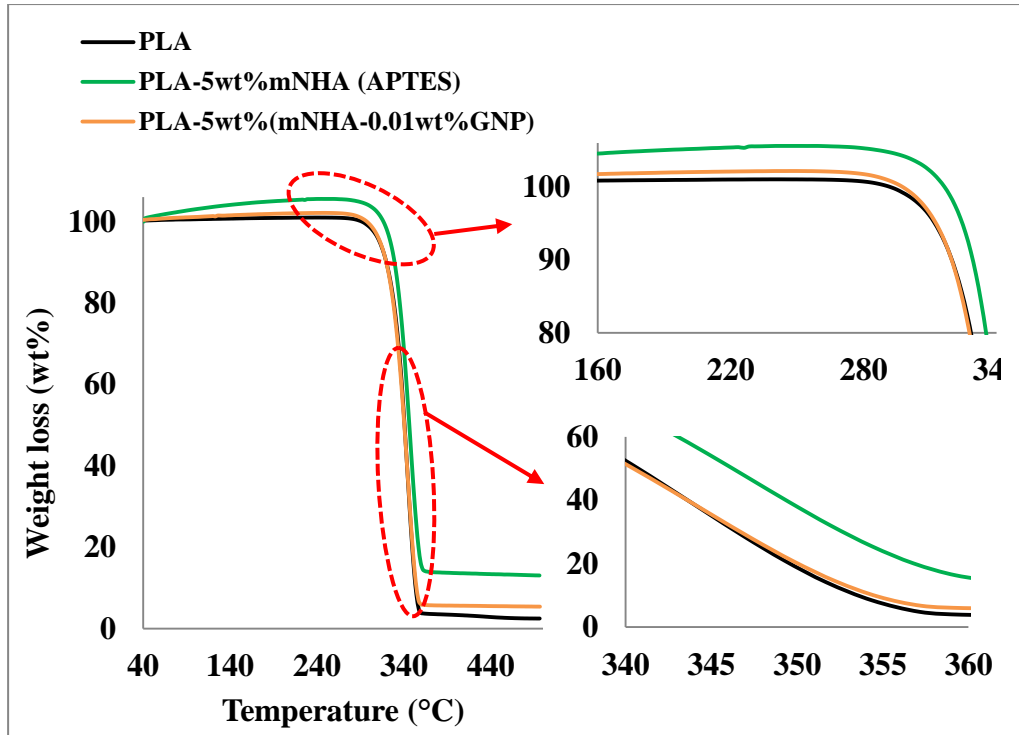
(a)
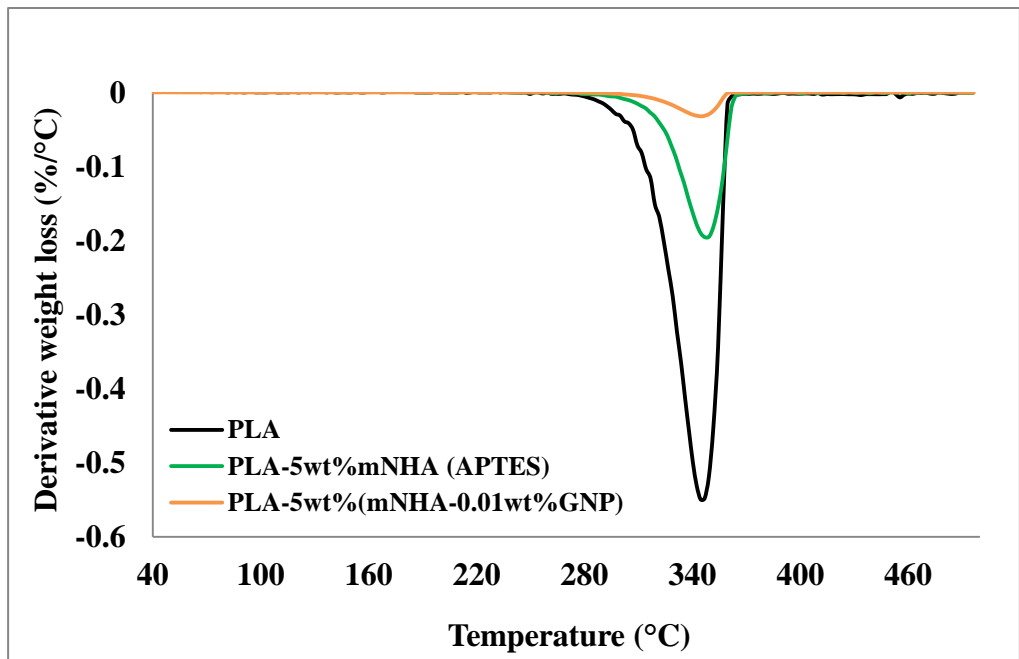
(b)

Figure 7.4: TGA thermograms of PLA-mNHA-GNP nanocomposite in comparison to PLA-mNHA(APTES) and neat PLA; heating rate at 3°C/min (a) weight loss curve and (b) derivative curve
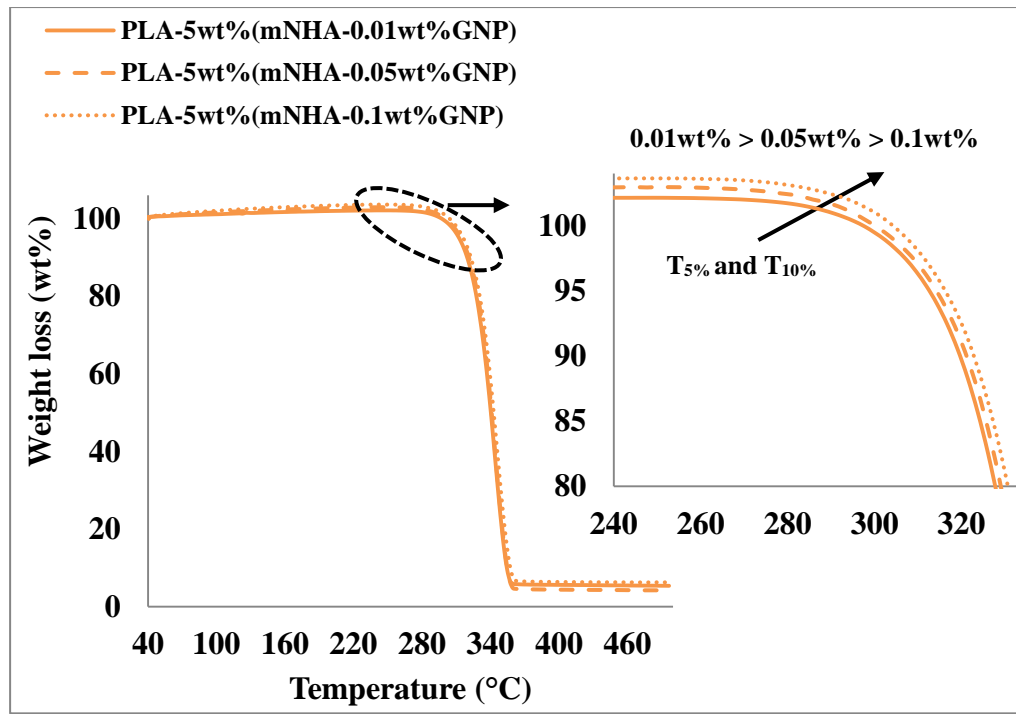
(a)
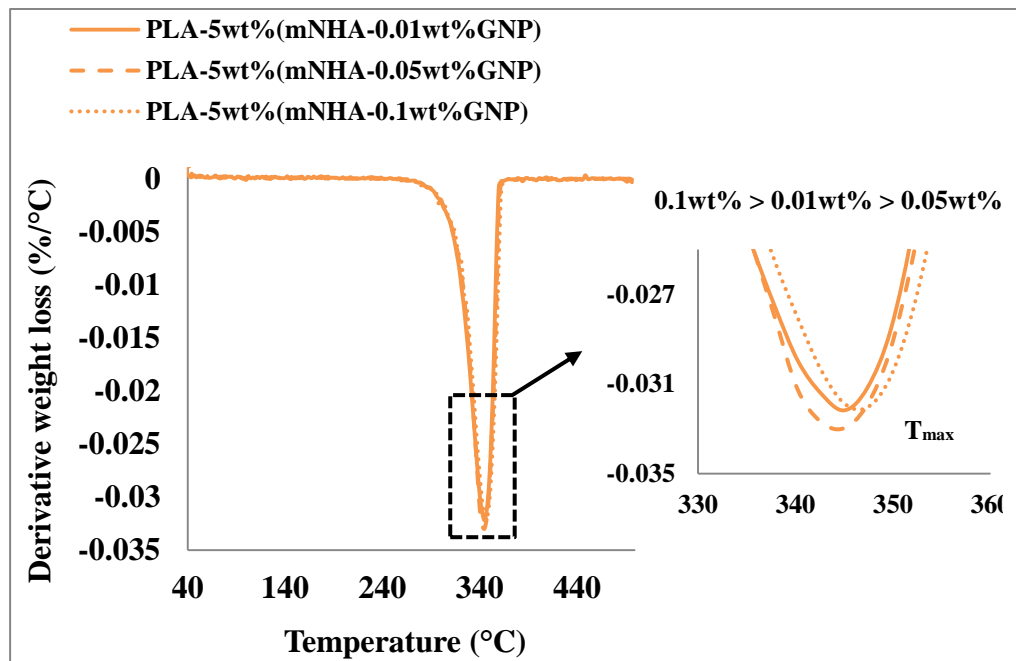
(b)

Figure 7.5: TGA thermograms of PLA-mNHA-GNP nanocomposites at different GNP loading; heating rate at 3°C/min (a) weight loss curve and (b) derivative curve

7.3.2. DSC

Figure 7.6 shows the DSC curve of the PLA-mNHA-GNP nanocomposites in association to PLA-5wt%mNHA(APTES) and neat PLA at different heating rates. The T_c and T_m temperatures are summarised in Table 7.2. For both heating rates, the highest T_c was recorded upon addition of 0.01wt% GNP. However, at 3°C/min heating rate, crystallisation peak for PLA- 5wt%mNHA (APTES) nanocomposite was observed to disappear. However, even though the T_m of the PLA-5wt%(mNHA-0.01wt%GNP) nanocomposite attained higher value than the neat PLA, it was still maintained lower than the PLA-5wt%mNHA(APTES) nanocomposite. Similarly, in other study PLAgMA reinforced with GO reported increase in T_c while the T_m decreased (Wang and Lin 2014).

As revealed in section 6.6.2., the T_c and T_m of the nanocomposite improve due to increased nucleating capacity of the nanofiller and strong interfacial adhesion between the nanofiller and polymer matrix. Hence, upon addition of 0.01wt% GNP, the nucleating capacity of mNHA-GNP nanofiller is believed to have increased, thus contributing in the increase the T_c of the PLA-5wt%(mNHA-0.01wt%GNP). Similarly, the increase in T_m in respect to neat PLA is due to the increased restriction of PLA chain mobility upon addition of mNHA-0.01wt%GNP nanofiller, however, the poor interfacial adhesion between mNHA and GNP could have caused the reduction in T_m compared to PLA-5wt%mNHA nanocomposite.

Figure 7.7 further demonstrates the influence of GNP loading on the DSC properties of the PLA-mNHA-GNP nanocomposites. Both temperatures (T_c and T_m) of the nanocomposites decrease with increased GNP loading (Table 7.2). It is apparent that the reduction in both temperatures is due to the formation of stacked graphene sheets and GNP induced defected microstructures within the PLA matrix discussed in section 7.5.
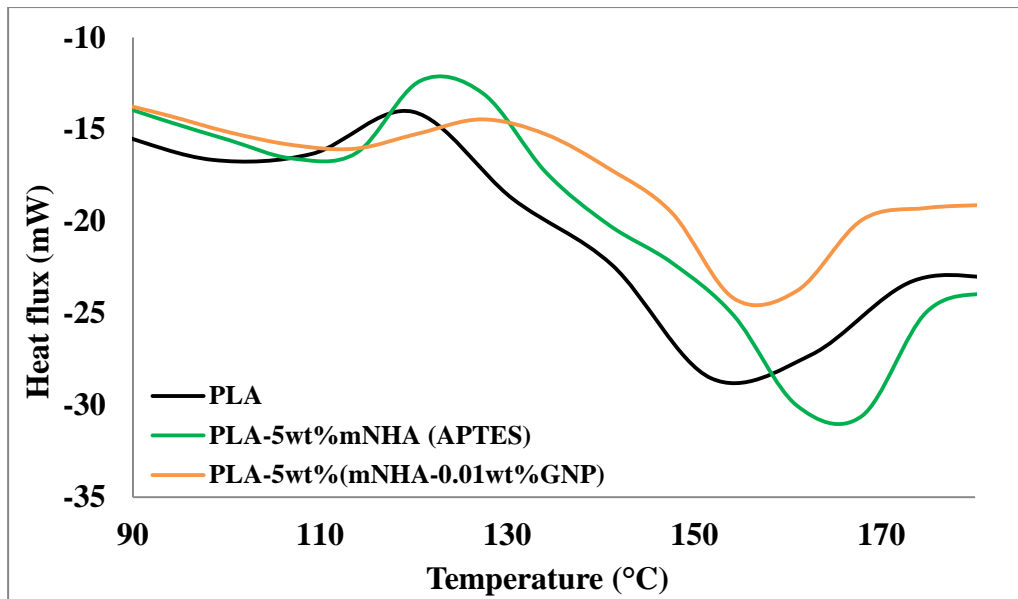
(a)
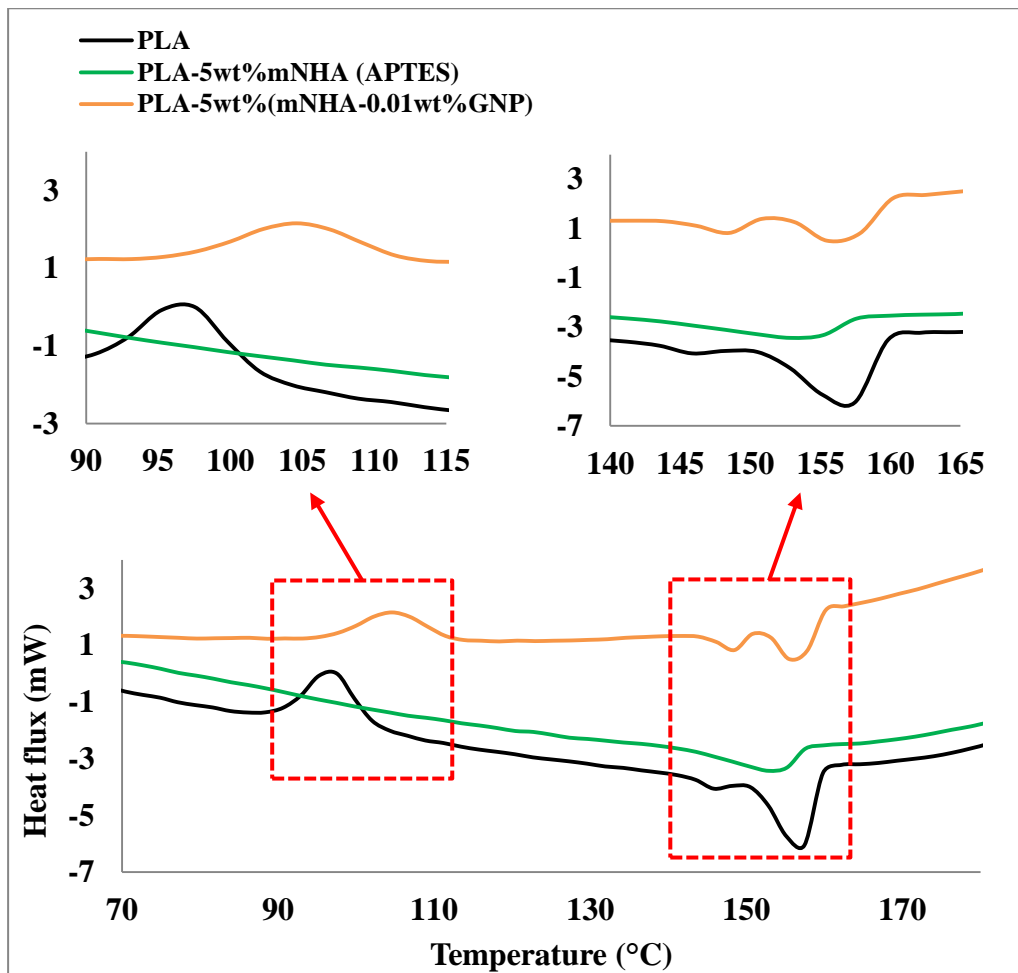
(b)

Figure 7.6: DSC curve for PLA-mNHA-GNP nanocomposites in comparison to PLA-mNHA(APTES) and neat PLA; heating rate at (a) 10°C/min and (b) 3°C/min
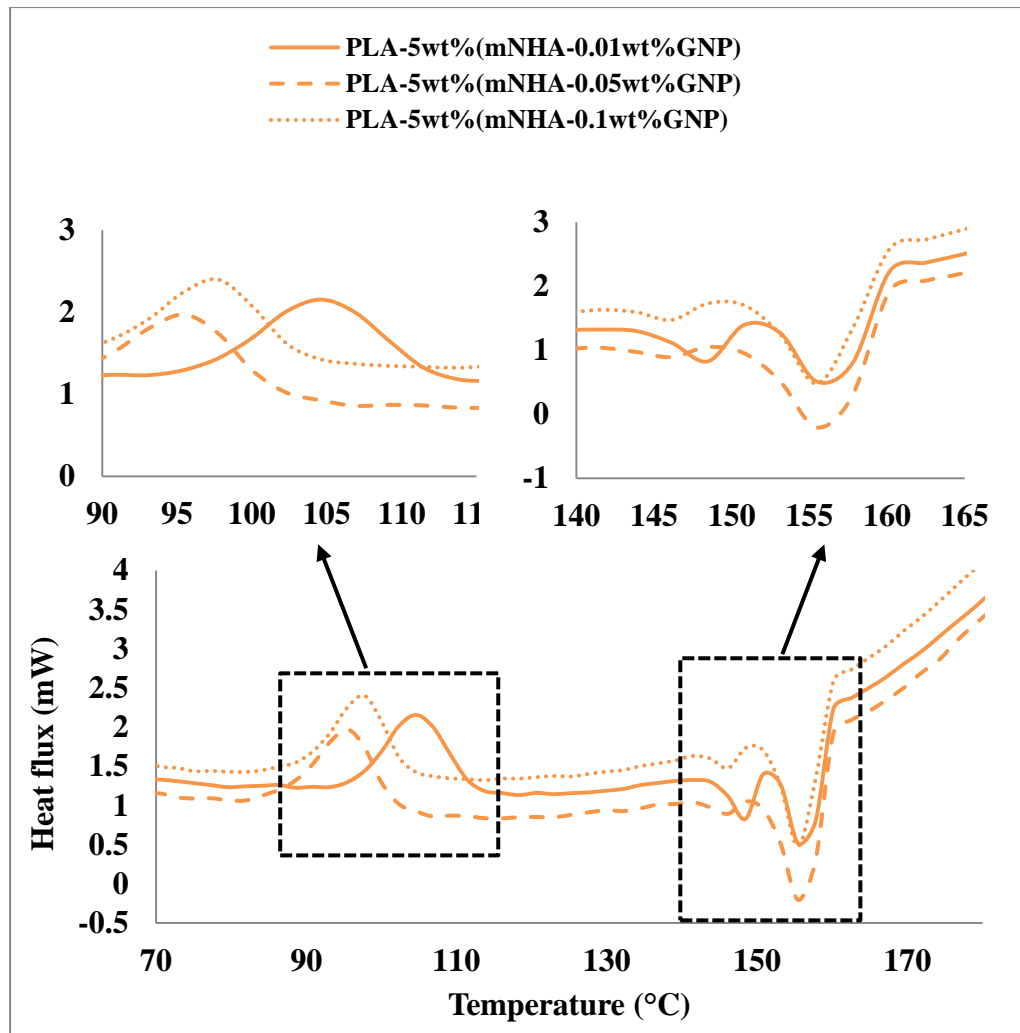
Figure 7.7: DSC curve for PLA-mNHA-GNP nanocomposites; heating rate at 3°C/min

Table 7.1: Degradation temperatures and remaining weight of the PLA nanocomposites

Sample	Heating Rate (°C/mins)	Degradation Temperature (°C)				Remaining wt (%)
		$T_{5\%}$	$T_{10\%}$	$T_{50\%}$	T_{max}	
PLA	10	332.8	339.4	360.1	364.51	2.91
PLA-5wt%mNHA(APTES)		326.9	340.4	364.9	371.50	11.09
PLA-5wt%mNHA(APTES)-0.01wt%GNP		329.6	336.3	360.5	364.42	3.13
PLA-5wt%mNHA(APTES)-0.05wt%GNP		333.6	340.4	361.3	370.11	2.95
PLA-5wt%mNHA(APTES)-0.1wt%GNP		333.8	340.6	359.5	363.47	2.90
PLA	3	311.9	319.3	340.2	344.65	2.48
PLA-5wt%mNHA(APTES)		324.6	328.1	345.9	344.76	13.06
PLA-5wt%mNHA(APTES)-0.01wt%GNP		311.9	319.1	340.2	345.37	9.83
PLA-5wt%mNHA(APTES)-0.05wt%GNP		313.2	320.3	341.1	344.87	8.42
PLA-5wt%mNHA(APTES)-0.1wt%GNP		315.6	322.7	342.7	347.48	10.29

Table 7.2: DSC analysis of the PLA nanocomposites

Sample	Heating Rate (°C/mins)	Crystallisation Peak		Melting Peak			
		T_c (°C)	HF (mW)	T_{m1}	HF (mW)	T_{m2}	HF (mW)
PLA	10	120.2	-17.19	-	-	151.8	-28.53
PLA-5wt%mNHA(APTES)		127.4	-13.04	-	-	167.9	-30.60
PLA-5wt%mNHA(APTES)-0.01wt%GNP		134.1	-15.25	-	-	161.2	-23.76
PLA-5wt%mNHA(APTES)-0.05wt%GNP		118.7	-9.66	-	-	160.5	-22.40
PLA-5wt%mNHA(APTES)-0.1wt%GNP		113.9	-6.19	-	-	160.9	-22.40
PLA	3	97.5	0	145.8	-4.06	157.5	-6.05
PLA-5wt%mNHA(APTES)		-	-	-	-	155.9	-3.32
PLA-5wt%mNHA(APTES)-0.01wt%GNP		104.6	2.16	148.9	0.83	157.8	1.35
PLA-5wt%mNHA(APTES)-0.05wt%GNP		95.5	1.97	146.1	0.89	155.5	-0.20
PLA-5wt%mNHA(APTES)-0.1wt%GNP		97.8	2.40	146.2	1.48	155.5	0.48

7.4. Dynamic Mechanical Properties

7.4.1. Storage modulus

Figures 7.8 and 7.9 depict the storage modulus of the PLA-mNHA-GNP nanocomposites in respect to the neat PLA and PLA-5wt%mNHA (APTES) nanocomposite. It is evident from the Figure 7.8, the storage modulus of PLA-5wt%(mNHA-0.01wt%GNP) nanocomposite increased in the glassy region, attaining the highest value compared to the neat PLA and PLA-5wt%mNHA (APTES) nanocomposite. The storage modulus around the transition region on the other hand is observed to decrease upon addition of 0.01wt% GNP. From Figure 7.9 it can be noted that increasing the GNP loading to 0.05wt% slightly improved the storage modulus in the glassy region but a significant decrease was observed at the transition region. The general increase in the storage modulus at the glassy region with the addition of GNP could be due to GNP contributing in the restriction of the PLA chains mobility leading to the formation of a stiffened nanocomposite. The reduction in storage modulus at transition region is resulted by the increased mobility of the PLA chains at higher temperature (above T_g).

The stiffness of the nanocomposite was affected by the dispersion of the mNHA-GNP in the PLA matrix and the degree of exfoliation of GNP sheets. It is believed that homogeneously dispersed and highly exfoliated GNP will always lead to an impressive increase in storage modulus of polymer/GNP nanocomposites (Li and Zhong 2011). However, the PLA-mNHA-GNP nanocomposite above 0.05wt% GNP loading attained poorly dispersed mNHA-GNP and lower degree of GNP exfoliation due to the van der Waals forces binding the GNP sheets together at higher loading (which will be discussed in section 7.5). As a result, increase to 0.1wt% GNP loading resulted in further deterioration of the storage modulus in both the glassy and transition regions. Table 7.3 summarises the calculated C coefficients of the PLA-5wt% mNHA (APTES) and PLA-mNHA-GNP nanocomposites. The increase in the C value of the PLA-mNHA-GNP compared to PLA-5wt%mNHA (APTES) indicate the effectiveness of mNHA-GNP as a filler is lower than mNHA. This explains the reduction in storage modulus recorded upon addition of GNP at higher loading.
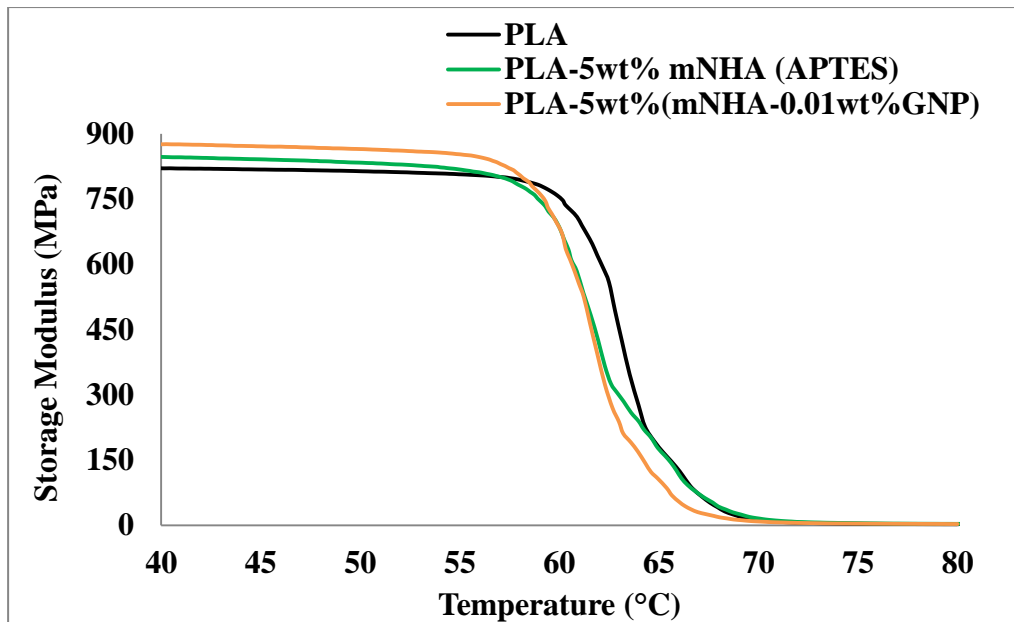
Figure 7.8: Storage modulus of PLA-mNHA-GNP nanocomposite in comparison to PLA-mNHA(APTES) and neat PLA
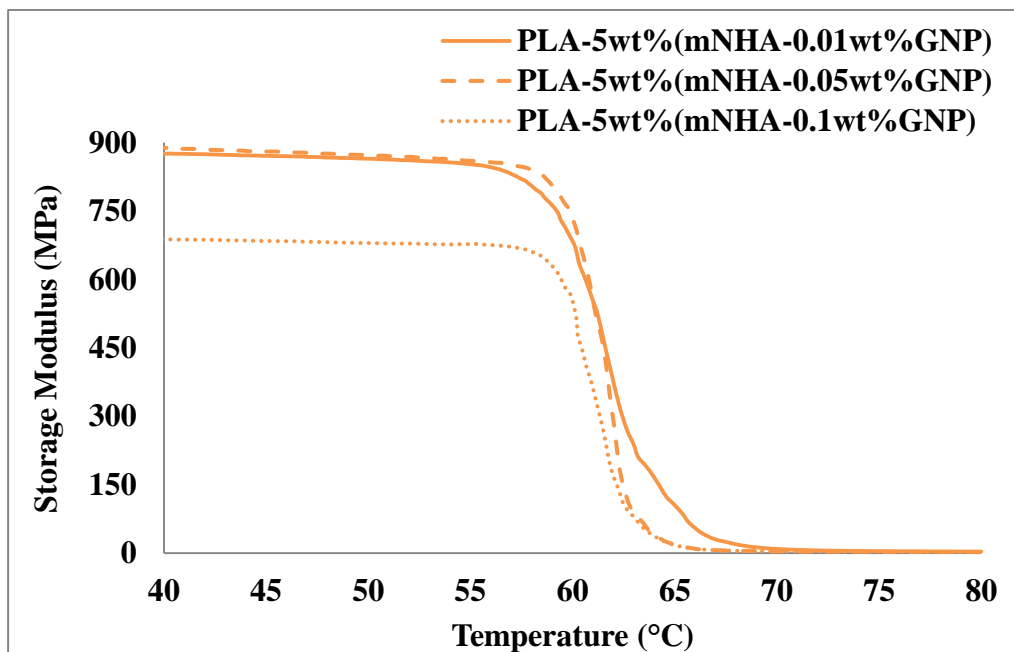
Figure 7.9: Storage modulus of PLA-mNHA-GNP nanocomposites at different GNP loading

7.4.2. Tan Delta

Figures 7.10 and 7.11 present the tan delta of the PLA-mNHA-GNP nanocomposites in comparison to neat PLA and PLA-5wt%mNHA(APTES).

The height and the temperatures at which the tan delta peaks are located (T_g) are also listed in Table 7.3. It is expected for the height of the tan delta peaks of the PLA-mNHA-GNP nanocomposites to be lower than the neat PLA due to the decreased matrix rich region upon incorporation of nanofillers. However, in comparison to PLA-5wt%mNHA, the PLA-mNHA-GNP nanocomposites obtained higher tan delta peak height. This suggests the interfacial adhesion between PLA and mNHA-GNP nanohybrid is weaker than PLA and mNHA(APTES). This also complements the reported lower effectiveness of mNHA-GNP nanohybrid as filler.

The T_g value of the PLA-5wt%(mNHA-0.01wt%GNP) nanocomposite showed no significant change in comparison to PLA-5wt%mNHA(APTES). However, upon addition of 0.05wt% GNP and beyond, the T_g value shifted to a lower temperature. This reduction in T_g is also highlights the poor interfacial adhesion reported between the PLA matrix and mNHA-GNP nanohybrid (Thomas et al. 2009).
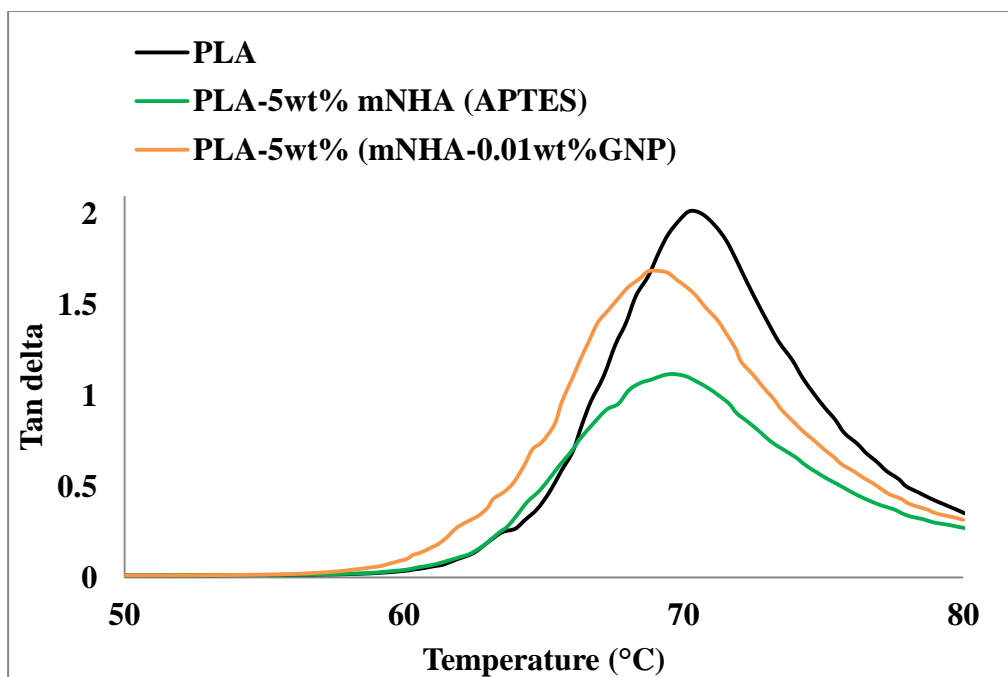
Figure 7.10: Tan delta PLA-mNHA-GNP nanocomposite in comparison to PLA-mNHA (APTES) and neat PLA
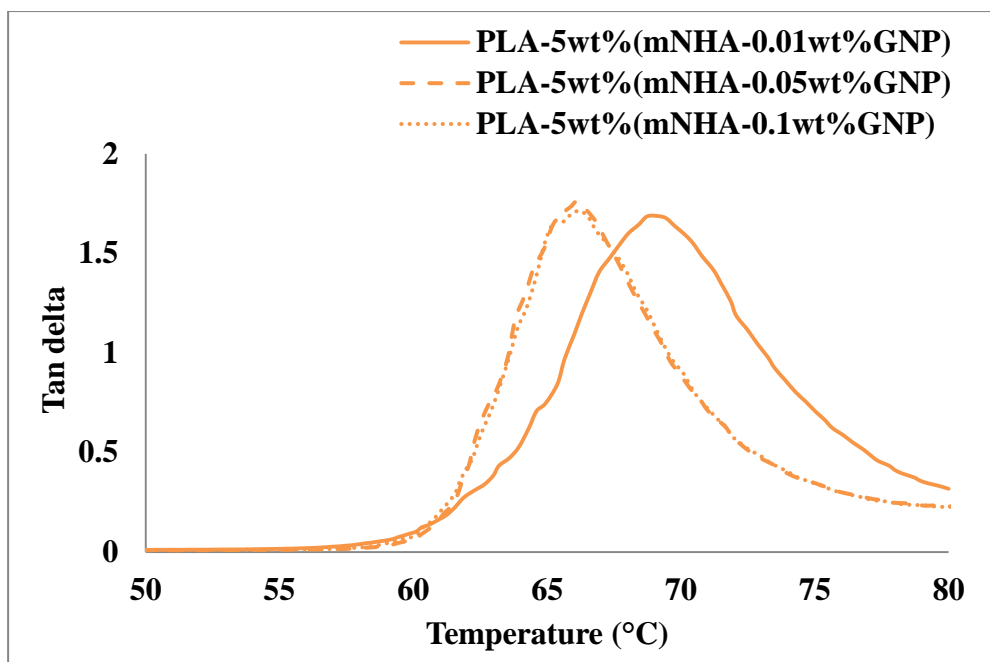
Figure 7.11: Tan delta of PLA-mNHA-GNP nanocomposites at different GNP loading

7.4.3. Creep

Figure 7.12 presents the creep properties of the PLA-5wt%(mNHA-0.01wt%GNP) nanocomposite in comparison to PLA-5wt%mNHA(APTES) and neat PLA. The creep properties are summarised in Table 7.4. Similar to the creep properties reported in section 6.7.3., it can be observed that the creep and recovery strains of the PLA-mNHA-GNP nanocomposite were lower than that of the neat PLA. A significant reduction of 88.9% (creep strain), 89.2% (recovery strain) and 88.2% (residual strain) was recorded in comparison to neat PLA; an indication of improved elasticity. However, in respect to PLA-5wt% mNHA(APTES), slight reduction of 13.9% (creep strain), 33.1% (recovery strain) and 11.9% (residual strain) was recorded. It is important to note that the PLA-mNHA-GNP nanocomposite obtained a minimum permanent deformation compared to both neat PLA and PLA-5wt%mNHA(APTES) nanocomposite

Table 7.3: Effectiveness of GNP loading on the dynamic mechanical properties

Sample	Tan delta	T_g (°C)	Storage modulus (MPa)	C	Storage modulus retention (%)			
					$E'_{50°C}/E'_{40°C}$	$E'_{60°C}/E'_{40°C}$	$E'_{70°C}/E'_{40°C}$	$E'_{80°C}/E'_{40°C}$
PLA-5wt%mNHA(APTES)	1.12	69.64	849.61	0.81	98	80	1.8	0.4
PLA-5%(mNHA-0.01wt%GNP)	1.69	69.15	881.74	0.92	98.7	77.4	0.01	0.04
PLA-5%(mNHA-0.05wt%GNP)	1.71	66.20	896.65	1.22	98.1	82.2	0.004	0.003
PLA-5%(mNHA-0.1wt%GNP)	1.70	65.88	691.98	0.99	98.8	78.6	0.006	0.003

Figure 7.13 illustrates the effect of GNP loading on the creep properties of PLA-mNHA-GNP nanocomposites, where the data are listed in Table 7.4. With addition of 0.05wt% GNP, the creep properties of the PLA-mNHA-GNP nanocomposite improved by 8%, 9% and 5.8%, for the creep, recovery and residual strains, respectively, compared to 0.01wt% GNP loading. Upon further increase of GNP loading to 0.1wt%, slight improvement in the creep strain (1.6%) and recovery strain (4.3%) was recorded, while the residual strain increased by 3.9%, attaining higher permanent deformation compared to 0.01wt% GNP nanocomposite. Thus, an optimum enhancement in creep properties was achieved by the PLA-5wt%(mNHA-0.05wt%GNP) nanocomposite. However, this contradicts with the mechanical properties obtained in section 7.2, whereby the reduction in mechanical properties with GNP loading was suggested to be due to poor interfacial adhesion between the mNHA-GNP and PLA matrix.
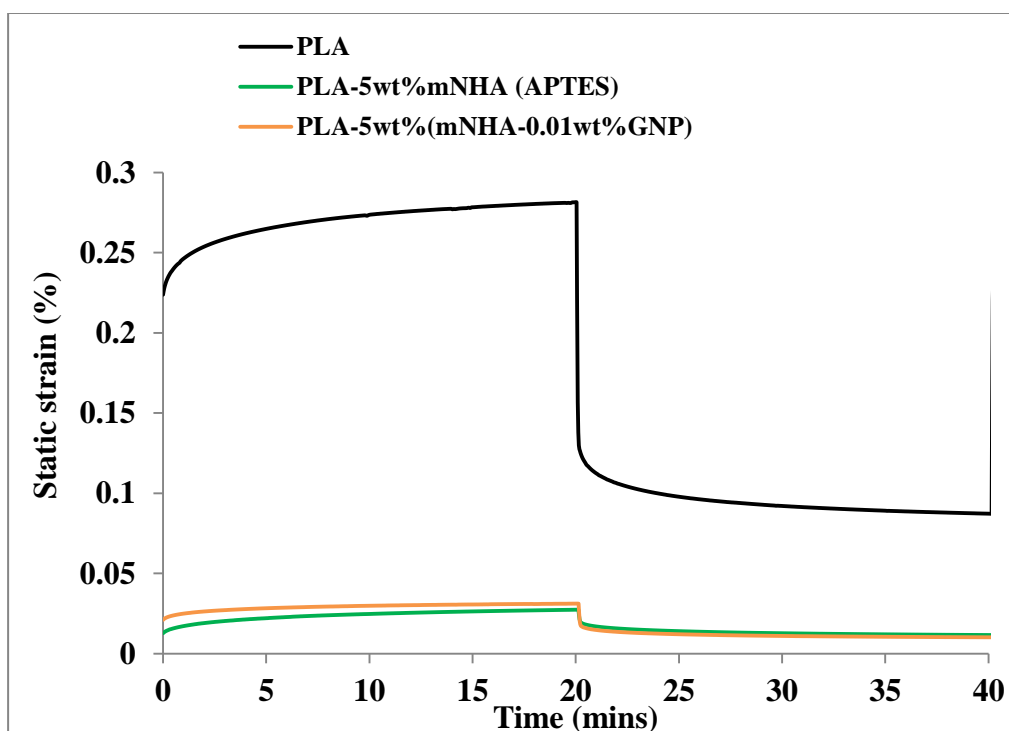
Figure 7.12: Creep and recovery curve of PLA-5wt%(mNHA-0.01wt%GNP) nanocomposites in comparison to PLA-5wt%mNHA(APTES) nanocomposite and neat PLA
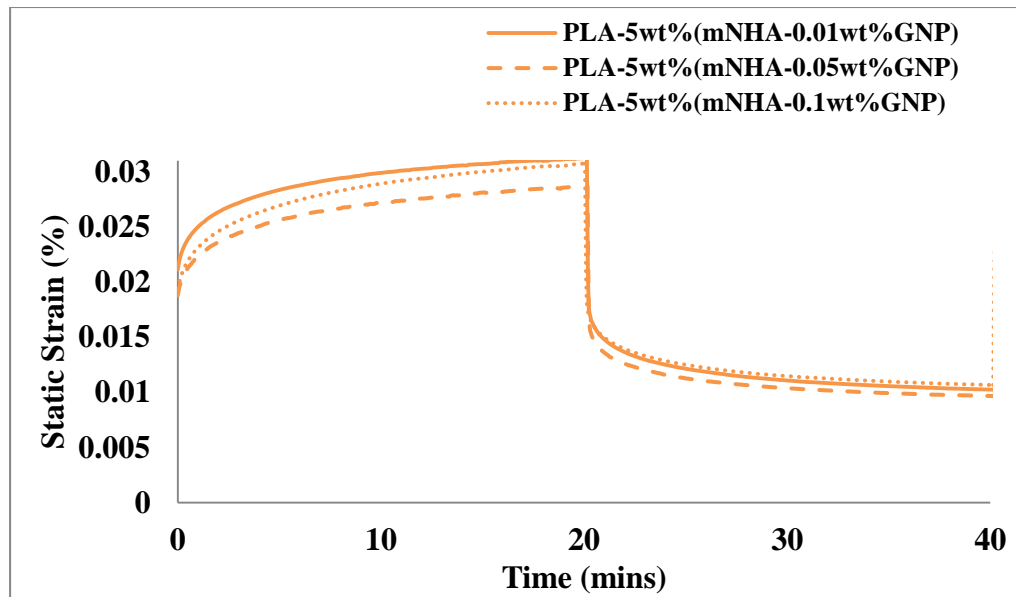
Figure 7.13: Creep and recovery curve of PLA-mNHA-GNP nanocomposites in comparison to PLA-5wt%mNHA(APTES) nanocomposite and neat PLA

Table 7.4: Creep analysis of the nanocomposites in comparison to neat PLA and PLA-5wt% mNHA(APTES)

Sample	Creep strain	Recovery Strain	Residual Strain
PLA	0.2814	0.1940	0.0874
PLA-5wt%mNHA(APTES)	0.0274	0.0157	0.0117
PLA-5wt%(mNHA-0.01wt%GNP)	0.0312	0.0209	0.0103
PLA-5wt%(mNHA-0.05wt%GNP)	0.0287	0.0190	0.0097
PLA-5wt%(mNHA-0.1wt%GNP)	0.0307	0.0200	0.0107

7.5. Fracture Surface Morphology

Figure 7.14 depicts the FESEM microstructural images of the mNHA-GNP nanohybrid filler prepared at different GNP loading. It is observed that the mNHA are well embedded onto the GNP particles. However, upon increase of GNP loading, the van der Waals forces between the GNP particles becomes stronger and causes the particles to overlap with one another, as indicated by the arrows in Figure 7.14 (b) and (c). This complements the reduction of the

mechanical properties of the PLA-mNHA-GNP nanocomposites reported in section 7.2.

Figure 7.15 shows the FESEM microstructural images obtained for the impact fractured surface of PLA reinforced with mNHA-GNP nanohybrid. Presence of fibril is detected in all the mNHA-GNP reinforced nanocomposites. The nanocomposite with 0.01wt% GNP loading had the closest resembles to the neat PLA (Figure 5.8). The nanocomposite displayed wavy lines along with tiny fibril structures. However, an agglomerate of mNHA-GNP particle was noticed as shown by the circle in the Figure 7.15 (a). The 0.05wt% and 0.1wt% GNP reinforced nanocomposites, however, exhibited formation of fibril structures without any wavy lines present. In addition, presence of voids and more agglomerated particles were detected as shown by the circles in Figure 7.15 (b) and (c). This could be the reason behind the good mechanical properties of the PLA-5wt% (mNHA-0.01wt%GNP) nanocomposite compared to the 0.05wt% and 0.1wt% GNP reinforced nanocomposites.
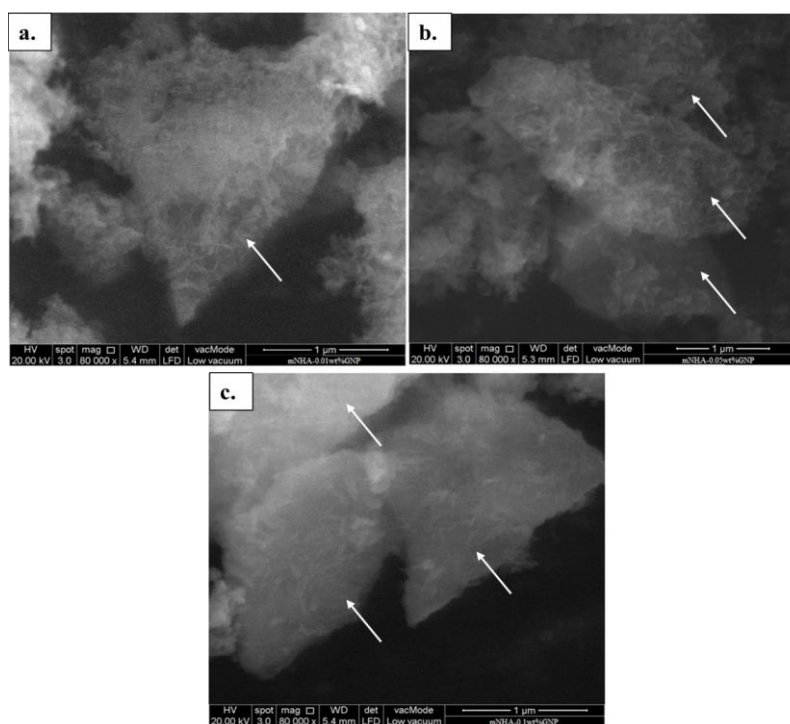
Figure 7.14: FESEM microstructural images of the mNHA-GNP nanofillers (a) 0.01wt%GNP, (b) 0.05wt%GNP, and (c) 0.1wt%GNP loadings
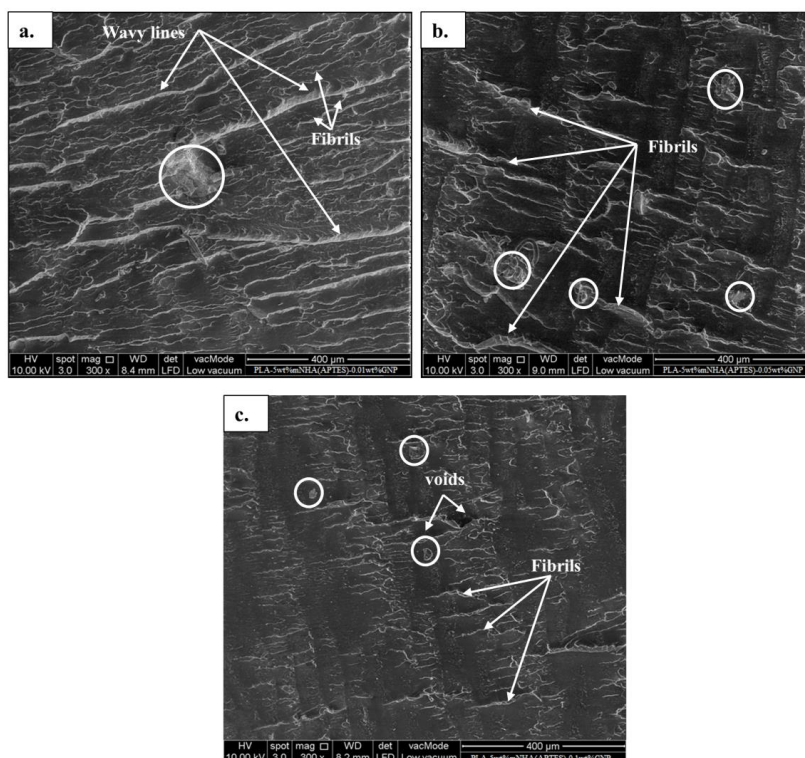
Figure 7.15: FESEM microstructural images of the impact fractured samples for PLA-5wt%mNHA(APTES) with (a) 0.01wt%GNP, (b) 0.05wt%GNP, and (c) 0.1wt%GNP loadings

7.6. Summary

The reinforcement of PLA with mNHA-GNP nanohybrid was greatly impacted by the GNP loading and the nanocomposite preparation technique. However, melt mixing technique might have limited the ability of GNP to reinforce the PLA-mNHA nanocomposite by buckling or shortening of graphene sheets, thus reducing its surface area-to-volume and aspect ratio. As a result, the tensile properties were observed to decrease upon addition of mNHA-GNP nanohybrid filler compared to mNHA nanofiller.

The PLA-mNHA-GNP nanocomposite showed improved impact strength, thermal stability, and dynamic mechanical properties at 0.01wt% GNP loading compared to PLA-5wt%mNHA nanocomposite. Judging from the FESEM images of mNHA-GNP nanohybrid, the GNP sheets were observed to overlap at higher loading due to increased van der Waals forces binding them together. This reflected in the deterioration of mechanical strength and dynamic

mechanical properties. However, the thermal properties of the 0.05wt% and 0.1wt% GNP reinforced PLA-mNHA-GNP nanocomposites showed significant improvement compared to the 0.01wt% GNP.

CHAPTER 8

IN-VITRO ANALYSIS OF THE
NANOCOMPOSITES

8.1. Introduction

To this point, the mechanical properties of the prepared nanocomposites are within the required limit of the cortical or cancellous bones (referring to the previous chapters (5, 6 and 7). Thus, in this chapter, the final objective of this study is addressed; which is the *in-vitro* analysis on the prepared PLA, PLA-NHA, PLA-mNHA and PLA-mNHA-GNP nanocomposites. This is important because to design a successful bone implant is not only about meeting the mechanical requirements of the bones, but also the biomaterials should be biocompatible with the body (mentioned in the chapter 1 and 2).

In this chapter, the biocompatibility of the prepared nanocomposites was conducted based on three *in-vitro* assays namely cell adhesion test, cell proliferation test and early differentiation test. Cell line used for these assays was MG63 osteoblastic cells; which is a common cell model for biocompatibility evaluation for bone regenerative applications (Mayr-Wohlfart et al. 2001). In cell adhesion test, the surface morphology of cells on different nanocomposites after 4-hr incubation was evaluated by using FESEM. The cell proliferation was measured through MTT assay- a colorimetric test used to determine the cell metabolic activity, after 3, 5 and 7 days of incubation. Meanwhile, the cells differentiation was measured by using ALP assay; which is a technique used to assess the presence of alkaline phosphatase in cells cultured on the nanocomposites after 7, 14, 21 and 28 days of culture. Cells cultured directly on tissue culture plate were used as control for comparison purpose. The results obtained are discussed here.

8.2. Cell Adhesion

Figure 8.1 presents FESEM images of MG63 cells on nanocomposites. The shape of cells cultured on neat PLA was rather spherical as shown in Figure 8.1 (a). This was indicative of less favourable adhesion. Unlike cells on neat PLA, cells adhered well on all the nanocomposites. They spread widely on the surface of the nanocomposites as indicated with arrows in Figure 8.1. However, there

is a variation on the degree at which the cells spread on the surface of the nanocomposites. In particular, cells cultured on PLA-5wt%NHA nanocomposite showed higher degree of spreading compared to those on the neat PLA. In other words, larger surface area of the nanocomposite was covered by the cells, indicating the cells had better interaction with the PLA-5wt%NHA than the neat PLA. This can be credited to the presence of NHA which likely enhanced the interaction between the cells and the nanocomposite (Cui et al. 2009).

The interaction of cells with the polymer is greatly influenced by the hydrophilicity of the polymer. This is because, cells adhere well on to moderately hydrophilic surface (Vladkova 2010). In other words, polymer surfaces with chemical functional groups of hydroxyl, carbonyl, carboxyl and amine promote cell adhesion. Also, it is suggested that surface modification on implant materials can improve the interaction between cells and the nanocomposites (Pae et al. 2011). As a result, among all the nanocomposites, both the PLA-mNHA(APTES) nanocomposites (5wt% and 30wt%) attained the highest degree of cells spreading on the nanocomposites (Figure 8.1 (c) and (d)). In addition, cells on both PLA-mNHA-GNP nanocomposites also exhibited higher degree of spreading on the surface (Figure 8.1 (e) and (f)). This could be due to the improved interaction between the PLA and APTES treated mNHA which added chemical functional groups like hydroxyl and amine (as mentioned in section 6.2). Thus, this affirmed the good interaction and between the nanocomposites and the cells.
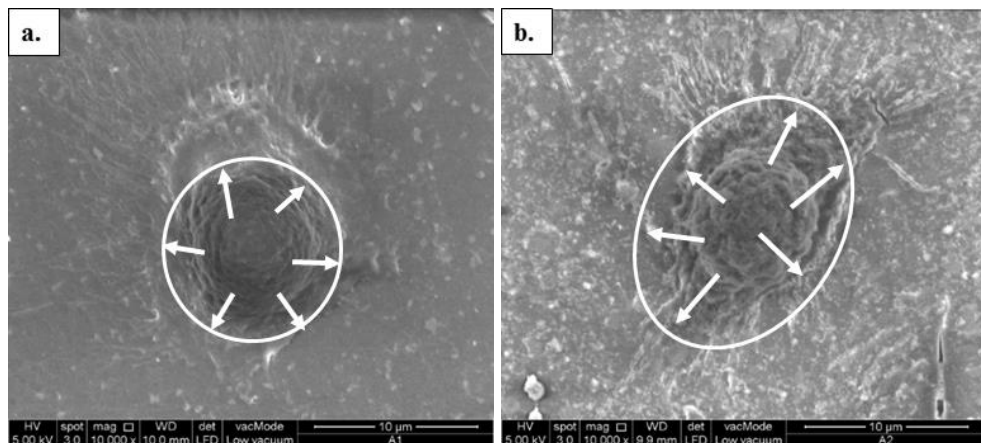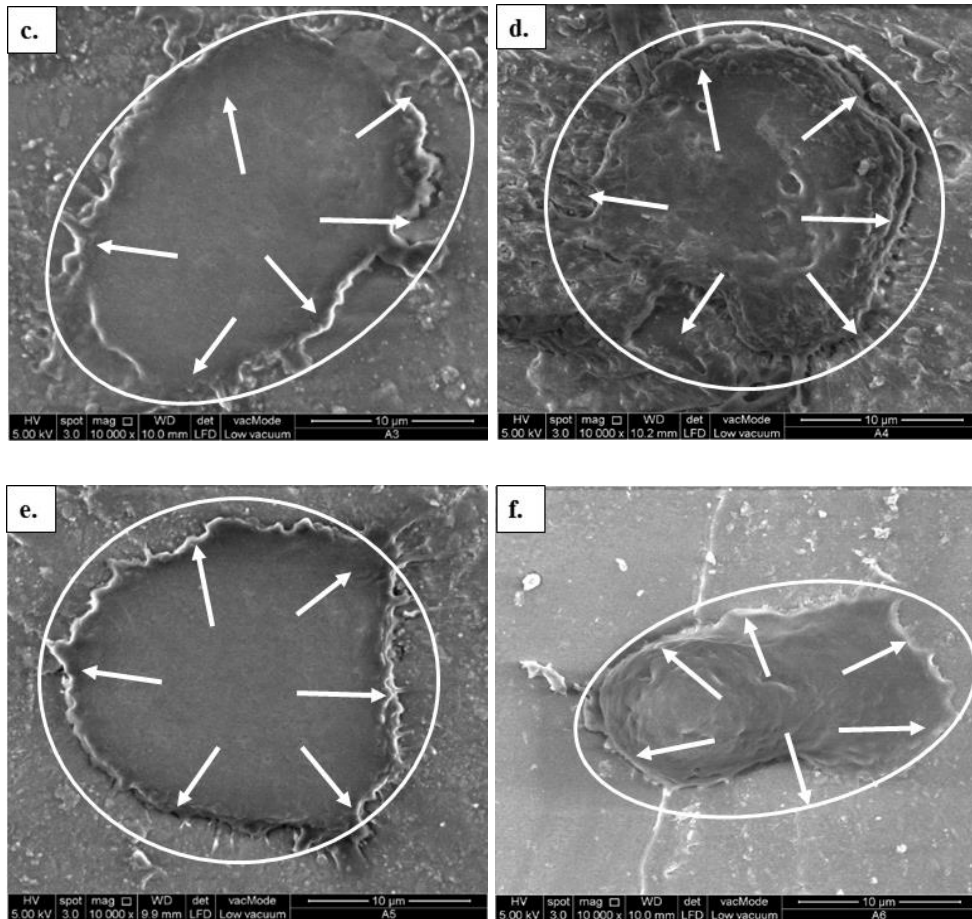
Figure 8.1: FESEM images showing the morphology of cells cultured on the nanocomposites; (a) PLA (A1), (b) PLA-5wt%NHA (A2), (c) PLA5wt% mNHA (APTES) (A3), (d) PLA-30wt%mNHA(APTES) (A4), (e) PLA-5wt% (mNHA-0.01wt%GNP) (A5) and (f) PLA-5wt%(mNHA-0.1wt%GNP) (A6) after 4-hour incubation

8.3. Cell Proliferation

Upon confirming good cells-nanocomposite interaction, further analysis on the cells proliferation was conducted by using MTT assay. Cell proliferation is referred to an increase in the number of cells as a result of cell growth. Hence, the proliferation of cells was determined in term of optical density at wavelength of 570 nm after the cells were cultured on all the nanocomposites for 3, 5 and 7 days. Figure 8.2 shows the MTT results of the nanocomposites in respect to neat PLA and control for all incubation periods. The ANOVA analysis of the MTT results is also presented in the appendix Table A.6 - Table A.14. Generally, the cell proliferation showed to increase with increase in culturing days. According to the results, there were slight difference in the cells proliferation rate between

the control and the neat PLA; for all the incubation periods. However, the cell proliferation rate of the nanocomposites exhibited great improvement in comparison to the neat PLA and the control as the incubation period increased (Kim et al. 2006, Cui, Liu et al. 2009). This is credited to the presence of NHA within the PLA matrix; whereby the NHA was able to chemically bond with the MG63 cells encouraging cell growth and proliferation upon cell seeding on the nanocomposites. This is because, as mentioned in section 2.3.1.1., ceramics such as hydroxyapatite are bioactive materials with hydrophilic chain (discussed in chapter 6) that can form chemical bond with MG63 cells.

As a result, even though at day 3, the cell proliferation rate of the nanocomposites did not show any significant changes ($p>0.05$), at day 5 and 7, the cells proliferation rate was seen to increase significantly, attaining maximum value at day 7. For instance, the cells proliferation rate of the nanocomposites recorded an increase of 132.8% (PLA-5wt% NHA), 151.7% (PLA-5wt%mNHA (APTES)), 132.4% (PLA-30wt%mNHA (APTES)), 103.7% (PLA-5wt% (mNHA-0.01wt%GNP)) and 135.1% (PLA-5wt%(mNHA-0.1wt%GNP)) in comparison to day 3, while the neat PLA recorded only 24.7% increase ($p>0.05$). This is because, as mentioned above NHA bonded with the cells chemically, encouraging the MG63 cells proliferation upon seeding on the nanocomposites with time compared to neat PLA.

In addition, the proliferation rate of the nanocomposites is generally affected by different factors such as interfacial adhesion (Lee et al. 2007), particle sizes (Shi et al. 2009) and filler loading (Xiaochen Liu 2011). These factors are greatly influenced through surface modification of the filler; whereby upon surface modification, the interfacial adhesion and dispersion of the filler is expected to have improved (as reported in chapter 6). Thus, at day 7, PLA-5wt%mNHA (APTES) nanocomposite was able to promote the highest cells proliferation rate compared to the PLA-5wt%NHA. This can be credited to the improved interfacial adhesion between mNHA (APTES) and PLA matrix as discussed in section 6.5.1; which in turn contributed in the improved cell proliferation rate.

It was also expected at higher mNHA loading, the cell proliferation rate would have improved as the nanocomposite would have more hydroxyapatite within the matrix; encouraging the cell growth. However, the cell growth of 30wt% mNHA reinforced nanocomposite was 5.7% less than 5wt% reinforced nanocomposite. Similarly, in other studies, the cell proliferation rate was observed to decrease with increased NHA loading (Ramires et al. 2001, Xiaochen Liu 2011). This is because, the mNHA did not disperse homogeneously and started to agglomerate when the loading increase from 5wt% to 30wt% (as discussed in section 6.8). This limited the amount of mNHA that could have interacted with the cell and encouraged the cell growth; thus lowering the cell proliferation.

GNP content on the other hand, had significant effect on the cells proliferation rate of the PLA-mNHA-GNP nanocomposites. For instance, upon the addition of 0.01wt%GNP, the cells proliferation rate of PLA-mNHA-GNP was observed to decrease by 16.9% compared to PLA-5wt%mNHA(APTES). Meanwhile, when the GNP loading increased to 0.1wt%, the cells proliferation rate increased, attaining comparable values as the PLA-mNHA(APTES) nanocomposites. Similarly, other studies reported that graphene at higher loading promoted better cell proliferation (Fan et al. 2010, Zuo et al. 2013, Singh 2016). However, to date, even though many studies have proven that graphene is biocompatible and capable of cell adhesion as well as proliferation; its contribution to bone tissue engineering is still quite new and knowledge on the effects of graphene is limited (Gu et al. 2014, Elkhenany et al. 2015)
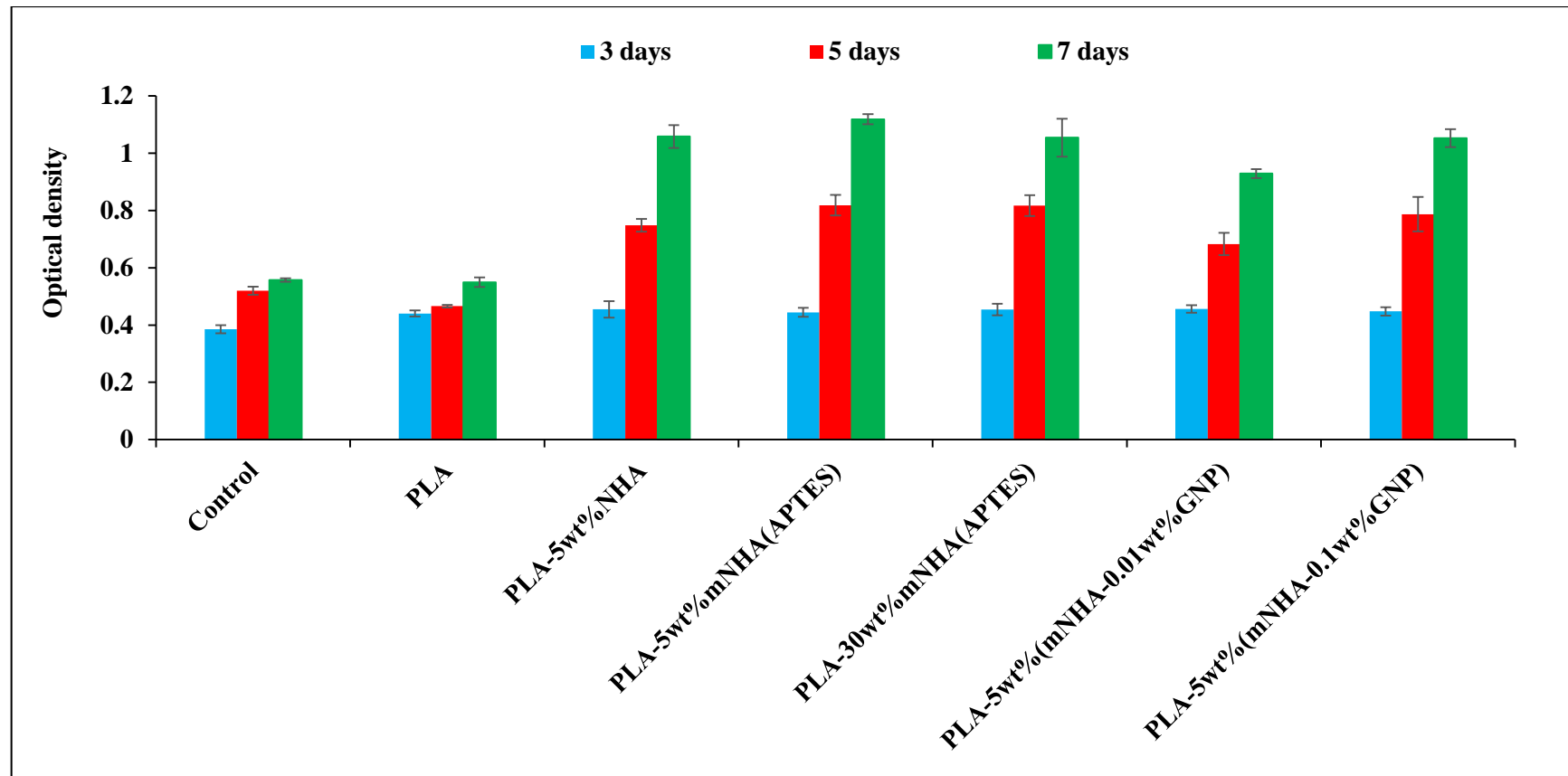
Figure 8.2: Proliferation of MG63 on nanocomposites, neat PLA and control after 3, 5 and 7 days of incubation in term of optical density at wavelength of 570 nm.

8.4. Early Cell Differentiation

Cell differentiation is a process by which one cell changes from one type to another. For instance, the MG63 cells can differentiate into variety of tissue types, including bone, cartilage, nerve and so on. However, these biological activity of the cells depends mainly on the three-dimensional pore microstructure of the nanocomposites which can be categories as having either open pores (inter-connecting) or closed pores (non-connecting). The presence of these pores on the nanocomposites would have allowed the cells to penetrate through the nanocomposite and encourage the differentiation of the cells (Karageorgiou and Kaplan 2005). Consequently, in *in-vitro* analysis, lower porosity is preferred as it improves the cell proliferation and forcing cell aggregation. Thus, a nanocomposites used for bone implants should possess a three dimensionally porous structure with porosity no less than 70% and pore size ranging from 50-900µm (Wang, Li et al. 2007). The higher the porosity of these nanocomposites, the wider the path for mass transport improving cell survival and also differentiation within the nanocomposite.

Hence, the early differentiation of the MG63 cells on the prepared nanocomposites was assessed by measuring the ALP level after 7, 14, 21 and 28 days. Figure 8.3 relates the ALP activity of cells cultured on all the nanocomposites and control with respect to the incubation period. Meanwhile, Figure A.3 (a-d) in the appendix section compares the ALP activity of cells cultured on each nanocomposite with the control well at a given culturing day. Moreover, the ANOVA analysis of the ALP results are shown in the appendix Table A.19 -Table A.22. The ALP level of the control well in Figure 8.3 recorded higher values than the nanocomposites for all the culturing days, indicating the cells seeded on the control wells showed higher differentiation rate than the nanocomposites (Deligianni et al. 2000). In other words, the smooth surface of the prepared nanocomposites; that is non porous structure, contributed in the slower cell differentiation rate (Lincks et al. 1998, Gittens et al. 2011). However, the ALP levels of the nanocomposites were still encouraging as the cells started to differentiate.

As a result, the ALP levels of cells cultured on the nanocomposites increased considerably with respect to incubation days, that is up to 21 days (*p<0.05*). For instance, the ALP levels of cells cultured on the nanocomposites increased by 20.3% (neat PLA), 19.7% (PLA-5wt% NHA), 19.8% (PLA-5wt%mNHA (APTES)), 23.9% (PLA-30wt%mNHA(APTES)), 14.4% (PLA-5wt%(mNHA-0.01wt% GNP)) and 11.1% (PLA-5wt%(mNHA-0.1wt%GNP)) for the 14 days in comparison to 7 days of incubation. The optimum ALP levels for the nanocomposites however was attained at day 21, in which an increase of 0.2% (neat PLA), 3.9% (PLA-5wt%NHA), 13.9% (PLA-5wt%mNHA (APTES)), 3.8% (PLA-5wt%(mNHA-0.01wt%GNP)) and 6.5% (PLA-5wt% (mNHA-0.1wt%GNP)) was recorded in comparison to 14 days of culturing, except for the PLA-30wt%mNHA (APTES) nanocomposite which recorded a reduction of 2.4%. These increase in ALP levels with time suggests that the nanocomposites aided in promoting early differentiation of MG63. Meanwhile, the reduction in the ALP level for PLA-30wt%mNHA(APTES) could be due to the nanocomposite undergoing mineralisation process; which is the process of depositing minerals (calcium phosphates) in the newly formed bone. This can be complemented from results obtained in another study, where PLGA-HA nanocomposite started undergoing mineralisation process after 21 days of incubation period (Lv et al. 2014). Lv *et. al.* (2014) initially reported that the ALP levels of PLGA-HA nanocomposite increased until 21 days of incubation period, attaining higher value than neat PLAGA. Furthermore, upon examining the mineralisation process using Alizarin red staining to visualise the calcium deposited onto the nanocomposite, both PLAGA-HA and PLAGA nanocomposites demonstrated visible red staining on the surface at day 21 of incubation period; suggesting calcium deposition took place on both nanocomposites, however, the staining on PLAGA-HA was more intense than PLAGA nanocomposite due to the presence of HA. As a result, in this study the ALP levels of nanocomposites decreased drastically by day 28; recording 7.7% (neat PLA), 13.7% (PLA-5wt%NHA), 23.4% (PLA-5wt% mNHA(APTES)), 12.9% (PLA-30wt% mNHA(APTES)), 10.3% (PLA-5wt%(mNHA-0.01wt%GNP)) and 11.8% (PLA-5wt%(mNHA-0.1wt%GNP)) decrease compared to 21 days of incubation period. This decrease in ALP level could be associated to the bone mineralisation process as the deposition of calcium is

observed to take place after 21 days of incubation period in other study (Lv, Yu et al. 2014).

In comparison to the neat PLA, the ALP levels of cells cultured on the nanocomposites showed no significant improvement at day 7 (*p>0.05*). Meanwhile, at day 14, all the nanocomposites showed slight increase in the ALP levels compared to neat PLA (*p<0.05*). By day 21, maximum ALP levels were attained especially by PLA-5wt%NHA and PLA-5wt%mNHA(APTES) nanocomposites. This is due to the presence of nanofiller in the PLA matrix; especially considering hydroxyapatite is an osteoinductive material and can stimulate cells to differentiate (Kong et al. 2006). Among these two nanocomposites, the PLA-5wt%mNHA(APTES) had the highest ALP level. This could be as a result of the improved interaction between the nanofiller and PLA matrix, complementing the statement made in chapter 5, where improved interaction between polymer matrix and nanofiller can not only enhance the mechanical properties but also the biocompatibility. Moreover, at day 28, the ALP levels of the nanocomposites were lower than the neat PLA. In other words, the mineral deposition process of the nanocomposites was faster upon addition of NHA/mNHA. These accelerated mineral deposition observed on the nanocomposites imply incorporation of hydroxyapatite into the PLA matrix improved the bioactivity in terms of mineral deposition. This is because NHA is bioactive in nature, which was discussed in the section 2.3.1.1. Thus, the capability of NHA to form apatite mineral on the nanocomposite surface has enhanced the bioactivity of the nanocomposites, making it favourable for bone implant application.
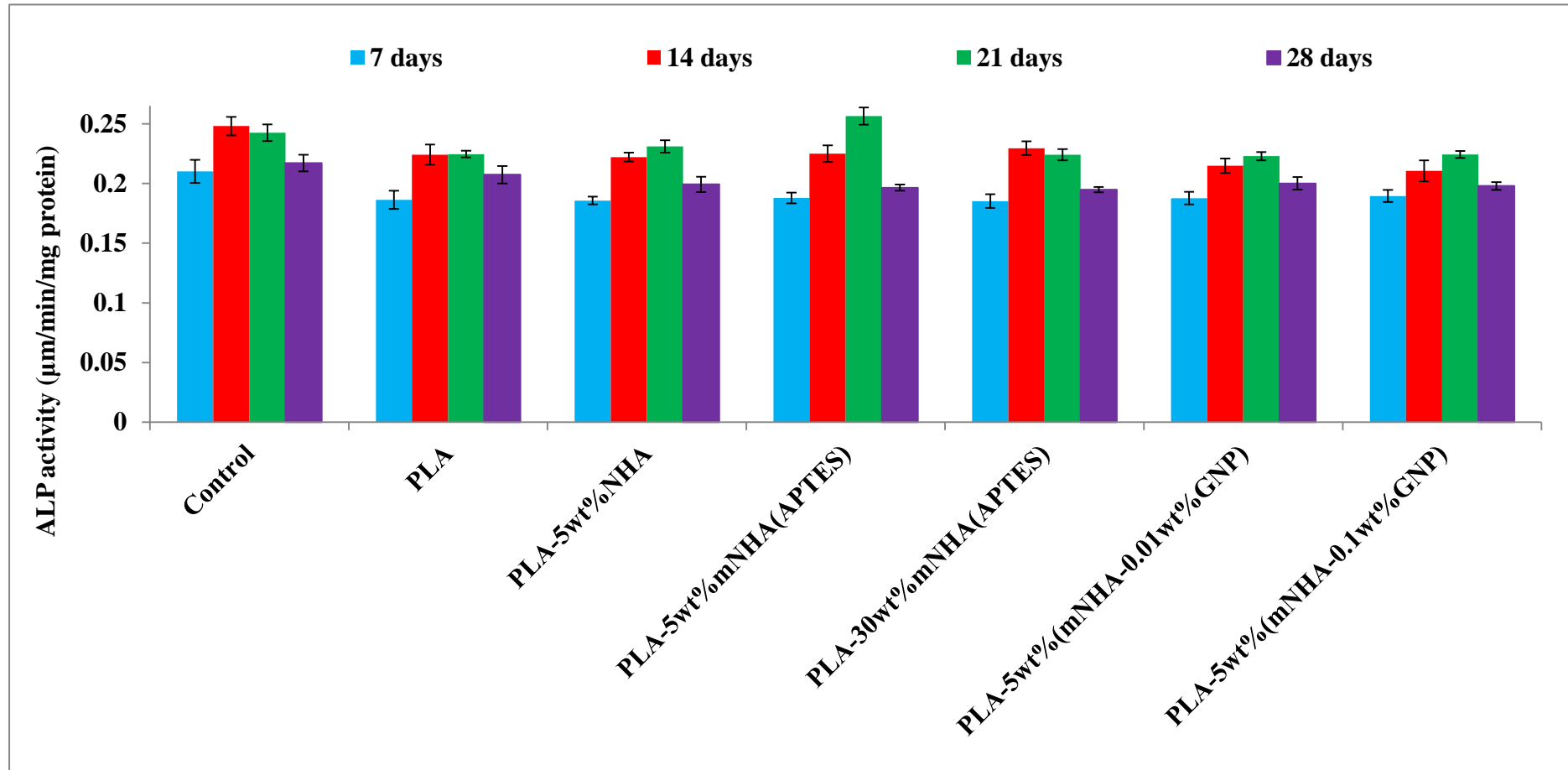
Figure 8.3: ALP activity of cells cultured on nanocomposites and control after 7, 14, 21 and 28 days of incubation

8.5. Summary

In this study, the MG63 cells adhered and spread well on the nanocomposites. The cells were also observed to proliferate, attaining optimum value by day 7. Moreover, the nanocomposites encouraged early differentiation by day 21. Therefore, the *in-vitro* analysis proved that the prepared nanocomposites are indeed biocompatible.

CHAPTER 9

CONCLUSIONS AND RECOMMENDATION FOR FUTURE WORKS

9.1. Principal findings

Three different nanofillers (NHA, mNHA and mNHA-GNP) were prepared and characterised successfully. The NHA was synthesised at optimised process parameters using precipitation method aided with ultrasonication, mNHA nanofiller was prepared by surface modifying the NHA using 5wt% of three different modifiers (APTES, SDS and PEI), and lastly, mNHA-GNP nanofiller was prepared by mixing the surface modified NHA (mNHA(APTES)) with 0.01wt%, 0.05wt% and 0.1wt% GNP loading in ethanol. Based on EDX, FTIR, BET, zetasizer, FESEM and TEM results obtained, the synthesised NHAs all displayed the properties of hydroxyapatite present in the human bone, chemically and morphologically.

PLA nanocomposites were compounded and characterised with 1wt%, 2wt%, 3wt% and 5wt% NHA loading. The PLA-NHA nanocomposites exhibited improved impact strength and thermal properties with increased NHA loading. In contrast to impact strength, the tensile strength of the PLA-NHA were observed to deteriorate beyond 1wt% NHA loading. In addition, the PLA matrix had poor interfacial adhesion with the NHA nanofiller. At higher NHA loading (above 1wt%), the NHA particles were observed to agglomerate.

Three different surface modifiers (APTES, SDS and PEI) were employed to improve the interfacial adhesion and properties of the PLA-NHA nanocomposites by surface treating the NHA. PLA-mNHA nanocomposites were compounded and characterised for 5wt%, 10wt%, 20wt% and 30wt% mNHA loading. Among these modifiers, APTES effectively improved the interfacial adhesion between the mNHA and PLA matrix, leading to improved mechanical, thermal and dynamic mechanical properties at 5wt% mNHA loading. The thermal and dynamic mechanical properties were further improved with increased mNHA loading. However, at higher mNHA loading (above 5wt%), mNHA particles were still observed to agglomerate, which resulted in the decrease of the mechanical properties. Nonetheless, the mechanical strength attained by the PLA-30wt%mNHA(APTES) is within the natural bone limit. SDS also surface modified the NHA and to some extent contributed in the enhancement of the interfacial adhesion while PEI failed to improve the

interfacial adhesion. However, both SDS and PEI did not improve the mechanical properties of PLA-mNHA nanocomposites in this study.

Graphene is known for its excellent properties among which includes mechanical and thermal properties. Thus, to further enhance the properties of the PLA-mNHA(APTES) nanocomposite, PLA was reinforced with a nanohybrid filler (mNHA-GNP). However, the reinforcement ability of GNP was limited due to its preparation technique (melt-mixing). It was suggested that the GNP sheets buckled or shortened—reducing its surface area-to-volume and aspect ratio. This led to a slight decrease in tensile properties upon addition of mNHA-GNP nanohybrid filler compared to mNHA nanofiller. Nonetheless, the impact strength improved for the lower loading (0.01wt% GNP). In addition, the GNP sheets were observed to overlap at higher loading due to increased van der Waals forces binding them together, resulting in the reduction of mechanical, thermal and dynamic mechanical properties of the 0.05wt% and 0.1wt% GNP reinforced PLA-mNHA-GNP nanocomposites.

In-vitro analysis was used to aid in the final objective of this study. The biocompatibility of the prepared nanocomposites was determined based on their ability to attach with MG63 cell; thus allowing the cells to proliferate, and enhance their ability to differentiate. Hence, on observation of the FESEM images of the cells-nanocomposites, as well as results of the MTT and ALP assays, the nanocomposites were confirmed to be biocompatible with the cells.

Therefore, the findings of this study so far suggest that the aim to develop nanocomposites that met the mechanical strength and biocompatibility requirements of the natural bones is achieved successfully. Subsequently, contributing to the current body of knowledge for developing bone implants.

9.2. Recommendation for future works

Bone implants are materials developed to perform in the body as devices able to support and induce bone repair. These bone implants should be biocompatible to integrate well within the tissue host without provoking any immune reaction

and biodegradable into forms of carbon dioxide and water. In addition, bone implants should possess an open pore and fully interconnected with highly porous structures which are the fundamental characteristic for providing available space for the cells to survive, grow and differentiate. Furthermore, the larger surface area to volume ratio available, the more cell interactions will take place. Lastly, bone implants should also have the mechanical strength that will retain its structure after implantation, mainly for the load bearing bones. Thus, it is important to choose the right material for bone implant application.

Biodegradable and biocompatible polymers are widely studied for bone implants. The stiffness limitation of these polymers is addressed through ceramic reinforcement. As a result, the polymer-ceramic nanocomposites have presented an alternative to the existing metals-ceramic or metals-polymers nanocomposites for bone implant applications. In addition, fabricating bone implants from polymer-ceramic nanocomposites has shown to be a smart way to overcome the negative implications of metals nanocomposites such as the lack of biocompatibility.

The findings from this study suggest that the prepared polymer-ceramic (PLA-NHA, PLA-mNHA and PLA-mNHA-GNP) nanocomposites meet the initial requirements of bone implants; mechanical strength and biocompatibility. Hence, the recommendations for future works are discussed based on these findings.

The biocompatibility of the bone implant depends mainly on its three-dimensional (3D) pore microstructure which can be categories as having either open pores (inter-connecting) or closed pores (non-connecting). The presence of these pores allows cells to penetrate through the bone implant and encourage the healing or regeneration process of bones. Meanwhile, presence of pores can also influence the mechanical strength of the bone implants. Thus, 3D printed porous bone implant with controlled pore size using the prepared PLA-NHA, PLA-mNHA and PLA-mNHA-GNP nanocomposites, can provide a better understanding on the mechanical strength and biocompatibility of the bone implant.

Lastly, developing a successful bone implant is also about balancing the bone healing rate with the degradation rate of the bone implant. The advantage of using biodegradable and biocompatible polymers is their ability to alter the chemical properties in order to adjust the degradation rate from weeks to years. In addition, the bone implants degrade via de-esterification process, whereby the end products are removed in form of carbon dioxide and water from the body. Thus, the biodegradation rate of the 3D printed bone implant should also be studied.

REFERENCES

Abu Bakar, M. S., P. Cheang and K. A. Khor (2003). "Mechanical properties of injection molded hydroxyapatite-polyetheretherketone biocomposites." Composites Science and Technology **63**(3–4): 421-425.

Abu Bakar, M. S., M. H. W. Cheng, S. M. Tang, S. C. Yu, K. Liao, C. T. Tan, K. A. Khor and P. Cheang (2003). "Tensile properties, tension–tension fatigue and biological response of polyetheretherketone–hydroxyapatite composites for load-bearing orthopedic implants." Biomaterials **24**(13): 2245-2250.

Agrawal, K., G. Singh, D. Puri and S. Prakash (2011). "Synthesis and characterization of hydroxyapatite powder by sol-gel method for biomedical application." Journal of Minerals and Materials Characterization and Engineering **10**: 727.

Akkapeddi, M. (2000). "Glass fiber reinforced polyamide-6 nanocomposites." Polymer Composites **21**(4): 576-585.

Allaoui, A., S. Bai, H. M. Cheng and J. B. Bai (2002). "Mechanical and electrical properties of a MWNT/epoxy composite." Composites Science and Technology **62**(15): 1993-1998.

Ambre, A. H., K. S. Katti and D. R. Katti (2010). "Nanoclay Based Composite Scaffolds for Bone Tissue Engineering Applications." Journal of Nanotechnology in Engineering and Medicine **1**(3): 031013-031013.

Amini, A. R., D. J. Adams, C. T. Laurencin and S. P. Nukavarapu (2012). "Optimally porous and biomechanically compatible scaffolds for large-area bone regeneration." Tissue Engineering Part A **18**(13-14): 1376-1388.

Andrews, R., D. Jacques, D. Qian and T. Rantell (2002). "Multiwall Carbon Nanotubes: Synthesis and Application." Accounts of Chemical Research **35**(12): 1008-1017.

Ansari, M., S. M. Naghib, F. Moztarzadeh and A. Salati (2011). "synthesis and characterisation of hydroxyapatite-calcium hydroxide for dental composites." Ceramics-Silikáty **55**(2): 123-126.

Ansari, M., S. M. Naghib, F. Moztarzadeh and A. Salati (2011). "Synthesis and characterisation of hydroxyapatite-calcium hydroxide for dental composites " Ceramics-Silikáty **55**(2): 123-126.

Armentano, I., M. Dottori, E. Fortunati, S. Mattioli and J. Kenny (2010). "Biodegradable polymer matrix nanocomposites for tissue engineering: a review." Polymer degradation and stability **95**(11): 2126-2146.

Bahrami, Z., A. Badiei and F. Atyabi "Surface functionalization of SBA-15 nanorods for anticancer drug delivery." Chemical Engineering Research and Design **92**(7): 1296-1303.

Balakrishnan, H., A. Hassan, M. U. Wahit, A. A. Yussuf and S. B. A. Razak (2010). "Novel toughened polylactic acid nanocomposite: Mechanical, thermal and morphological properties." Materials & Design **31**(7): 3289-3298.

Batra, S. K. a. U. (2010). "Preparation and bioactivity evaluation of bone like hydroxyapatite-bioglass composite." International Journal of chemical and biologial engineering **3**(1).

Bezerra, M. A., R. E. Santelli, E. P. Oliveira, L. S. Villar and L. A. Escaleira (2008). "Response surface methodology (RSM) as a tool for optimization in analytical chemistry." Talanta **76**(5): 965-977.

Bhattacharya, M. (2016). "Polymer Nanocomposites—A Comparison between Carbon Nanotubes, Graphene, and Clay as Nanofillers." Materials **9**(4): 262.

Bonfield, W. and I. R. Gibson (2003). Method for the preparation of carbonated hydroxyapatite compositions, Google Patents.

Bonfield, W., M. Grynpas, A. Tully, J. Bowman and J. Abram (1981). "Hydroxyapatite reinforced polyethylene—a mechanically compatible implant material for bone replacement." Biomaterials **2**(3): 185-186.

Bono, C. M. and T. A. Einhorn (2003). "Overview of osteoporosis: pathophysiology and determinants of bone strength." European Spine Journal **12**(2): S90-S96.

Bouyer, E., F. Gitzhofer and M. Boulos (2000). "Morphological study of hydroxyapatite nanocrystal suspension." Journal of Materials Science: Materials in Medicine **11**(8): 523-531.

Bula, K., T. Jesionowski, A. Krysztafkiewicz and J. Janik (2007). "The effect of filler surface modification and processing conditions on distribution behaviour of silica nanofillers in polyesters." Colloid and Polymer Science **285**(11): 1267-1273.

Cai, X., B. Riedl, S. Y. Zhang and H. Wan (2008). "The impact of the nature of nanofillers on the performance of wood polymer nanocomposites." Composites Part A: Applied Science and Manufacturing **39**(5): 727-737.

Campbell, P., P. E. Beaulé, E. Ebramzadeh, M. LeDuff, K. De Smet, Z. Lu and H. C. Amstutz (2006). "The John Charnley Award: a study of implant failure in metal-on-metal surface arthroplasties." Clinical orthopaedics and related research **453**: 35-46.

Cengiz, B., Y. Gokce, N. Yildiz, Z. Aktas and A. Calimli (2008). "Synthesis and characterization of hydroxyapatite nanoparticles." Colloids and Surfaces A: Physicochemical and Engineering Aspects **322**(1–3): 29-33.

Chaharmahali, M., Y. Hamzeh, G. Ebrahimi, A. Ashori and I. Ghasemi (2014). "Effects of nano-graphene on the physico-mechanical properties of bagasse/polypropylene composites." Polymer Bulletin **71**(2): 337-349.

Chan, M.-l., K.-t. Lau, T.-t. Wong, M.-p. Ho and D. Hui (2011). "Mechanism of reinforcement in a nanoclay/polymer composite." Composites Part B: Engineering **42**(6): 1708-1712.

Chandrasekar, A., S. Sagadevan and A. Dakshnamoorthy (2013). "Synthesis and characterization of nano-hydroxyapatite (n-HAP) using the wet chemical technique." International journal of physical Sciences **8**(32): 1639-1645.

Charnley, J. (1960). "Surgery of the Hip-joint." British Medical Journal **1**(5176): 821-826.

    IMAGES:

Chatterjee, S., F. Nafezarefi, N. H. Tai, L. Schlagenhauf, F. A. Nüesch and B. T. T. Chu (2012). "Size and synergy effects of nanofiller hybrids including graphene nanoplatelets and carbon nanotubes in mechanical properties of epoxy composites." Carbon **50**(15): 5380-5386.

Chen, X., W. Wang, Z. Song and J. Wang (2011). "Chitosan/carbon nanotube composites for the isolation of hemoglobin in the presence of abundant proteins." Analytical Methods **3**(8): 1769-1773.

Chieng, B. W., N. A. Ibrahim, W. M. Z. Wan Yunus, M. Z. Hussein and V. Silverajah (2012). "Graphene nanoplatelets as novel reinforcement filler in poly (lactic acid)/epoxidized palm oil green nanocomposites: Mechanical properties." International journal of molecular sciences **13**(9): 10920-10934.

Chieng, B. W., N. A. Ibrahim, W. M. Z. W. Yunus, M. Z. Hussein and Y. Y. Loo (2014). "Effect of graphene nanoplatelets as nanofiller in plasticized poly (lactic acid) nanocomposites." Journal of Thermal Analysis and Calorimetry **118**(3): 1551-1559.

Chieng, B. W., N. A. Ibrahim, W. M. Z. W. Yunus, M. Z. Hussein, Y. Y. Then and Y. Y. Loo (2014). "Effects of Graphene Nanoplatelets and Reduced Graphene Oxide on Poly (lactic acid) and Plasticized Poly (lactic acid): A Comparative Study." Polymers **6**(8): 2232-2246.

Chronakis, I. S. (2005). "Novel nanocomposites and nanoceramics based on polymer nanofibers using electrospinning process—A review." Journal of Materials Processing Technology **167**(2–3): 283-293.

Clarke, B. (2008). "Normal bone anatomy and physiology." Clinical journal of the American Society of Nephrology **3**(Supplement 3): S131-S139.

Coleman, J. N., U. Khan, W. J. Blau and Y. K. Gun'ko (2006). "Small but strong: A review of the mechanical properties of carbon nanotube–polymer composites." Carbon **44**(9): 1624-1652.

Cui, Y., Y. Liu, Y. Cui, X. Jing, P. Zhang and X. Chen (2009). "The nanocomposite scaffold of poly(lactide-co-glycolide) and hydroxyapatite surface-grafted with l-lactic acid oligomer for bone repair." Acta Biomaterialia **5**(7): 2680-2692.

Currey, J. (1998). Cortical bone. Handbook of biomaterial properties, Springer**:** 3-14.

Currey, J. D. (2013). Bones: Structure and Mechanics, Princeton University Press.

Custers, R., D. Saris, W. Dhert, A. Verbout, M. Van Rijen, S. Mastbergen, F. Lafeber and L. Creemers (2009). "Articular cartilage degeneration following the treatment of focal cartilage defects with ceramic metal implants and compared with microfracture." The Journal of Bone & Joint Surgery **91**(4): 900-910.

Dai, G. and L. Mishnaevsky (2014). "Graphene reinforced nanocomposites: 3D simulation of damage and fracture." Computational Materials Science **95**: 684-692.

Dai, J., Q. Wang, W. Li, Z. Wei and G. Xu (2007). "Properties of well aligned SWNT modified poly (methyl methacrylate) nanocomposites." Materials Letters **61**(1): 27-29.

Das, S., S. J. Hollister, C. Flanagan, A. Adewunmi, K. Bark, C. Chen, K. Ramaswamy, D. Rose and E. Widjaja (2003). "Freeform fabrication of Nylon-6 tissue engineering scaffolds." Rapid Prototyping Journal **9**(1): 43-49.

Dash, M., F. Chiellini, R. M. Ottenbrite and E. Chiellini (2011). "Chitosan—A versatile semi-synthetic polymer in biomedical applications." Progress in Polymer Science **36**(8): 981-1014.

Datta, N., H. L. Holtorf, V. I. Sikavitsas, J. A. Jansen and A. G. Mikos (2005). "Effect of bone extracellular matrix synthesized in vitro on the osteoblastic differentiation of marrow stromal cells." Biomaterials **26**(9): 971-977.

Deligianni, D. D., N. D. Katsala, P. G. Koutsoukos and Y. F. Missirlis (2000). "Effect of surface roughness of hydroxyapatite on human bone marrow cell adhesion, proliferation, differentiation and detachment strength." Biomaterials **22**(1): 87-96.

Dhandayuthapani, B., Y. Yoshida, T. Maekawa and D. S. Kumar (2011). "Polymeric scaffolds in tissue engineering application: a review." International Journal of Polymer Science **2011**.

Elkhenany, H., L. Amelse, A. Lafont, S. Bourdo, M. Caldwell, N. Neilsen, E. Dervishi, O. Derek, A. S. Biris and D. Anderson (2015). "Graphene supports in vitro proliferation and osteogenic differentiation of goat adult mesenchymal stem cells: potential for bone tissue engineering." Journal of Applied Toxicology **35**(4): 367-374.

Eslami, H., M. Solati-Hashjin, M. Tahriri and F. Bakhshi (2010). "Synthesis and characterization of nanocrystalline hydroxyapatite obtained by the wet chemical technique." Materials Science-Poland **28**(1): 5-13.

Fan, H., L. Wang, K. Zhao, N. Li, Z. Shi, Z. Ge and Z. Jin (2010). "Fabrication, mechanical properties, and biocompatibility of graphene-reinforced chitosan composites." Biomacromolecules **11**(9): 2345-2351.

Fang, L., Y. Leng and P. Gao (2005). "Processing of hydroxyapatite reinforced ultrahigh molecular weight polyethylene for biomedical applications." Biomaterials **26**(17): 3471-3478.

Fang, L., Y. Leng and P. Gao (2006). "Processing and mechanical properties of HA/UHMWPE nanocomposites." Biomaterials **27**(20): 3701-3707.

Fischer, J. E. (2006). Carbon nanotubes: structure and properties, CRC Press, Boca Raton, USA.

Fu, J. and H. E. Naguib (2006). "Effect of nanoclay on the mechanical properties of PMMA/clay nanocomposite foams." Journal of cellular plastics **42**(4): 325-342.

Fu, S.-Y., X.-Q. Feng, B. Lauke and Y.-W. Mai (2008). "Effects of particle size, particle/matrix interface adhesion and particle loading on mechanical properties of particulate–polymer composites." Composites Part B: Engineering **39**(6): 933-961.

Gentile, P., M. Mattioli-Belmonte, V. Chiono, C. Ferretti, F. Baino, C. Tonda-Turo, C. Vitale-Brovarone, I. Pashkuleva, R. L. Reis and G. Ciardelli (2012). "Bioactive glass/polymer composite scaffolds mimicking bone tissue." Journal of Biomedical Materials Research Part A **100A**(10): 2654-2667.

Gittens, R. A., T. McLachlan, R. Olivares-Navarrete, Y. Cai, S. Berner, R. Tannenbaum, Z. Schwartz, K. H. Sandhage and B. D. Boyan (2011). "The effects of combined micron-/submicron-scale surface roughness and nanoscale features on cell proliferation and differentiation." Biomaterials **32**(13): 3395-3403.

Gloria, A., F. Causa, R. De Santis, P. Netti and L. Ambrosio (2007). "Dynamic-mechanical properties of a novel composite intervertebral disc prosthesis." Journal of Materials Science: Materials in Medicine **18**(11): 2159-2165.

Gopi, D., K. Govindaraju, C. A. P. Victor, L. Kavitha and N. Rajendiran (2008). "Spectroscopic investigations of nanohydroxyapatite powders synthesized by conventional and ultrasonic coupled sol–gel routes." Spectrochimica Acta Part A: Molecular and Biomolecular Spectroscopy **70**(5): 1243-1245.

Gorbunov, A. A., R. Friedlein, H.-D. Bauer, M. Golden, R. Scharfenberg, J. Fink and W. Pompe (1999). Synthesis of single-wall carbon nanotubes by laser ablation. 6th International Conference on Industrial Lasers and Laser Applications' 98, International Society for Optics and Photonics.

Gorustovich, A. A., J. A. Roether and A. R. Boccaccini (2009). "Effect of bioactive glasses on angiogenesis: a review of in vitro and in vivo evidences." Tissue Engineering Part B: Reviews **16**(2): 199-207.

Granados-Correa, F., J. Bonifacio-Martinez and J. Serrano-Gomez (2010). "Synthesis and characterization of calcium phosphate and its relation to Cr (VI) adsorption properties." Revista Internacional de Contaminacion Ambiental **26**(2): 129-134.

Grantab, R., V. B. Shenoy and R. S. Ruoff (2010). "Anomalous strength characteristics of tilt grain boundaries in graphene." Science **330**(6006): 946-948.

Gross, K. A., V. Gross and C. C. Berndt (1998). "Thermal analysis of amorphous phases in hydroxyapatite coatings." Journal of the American Ceramic Society **81**(1): 106-112.

Gu, M., Y. Liu, T. Chen, F. Du, X. Zhao, C. Xiong and Y. Zhou (2014). "Is graphene a promising nano-material for promoting surface modification of implants or scaffold materials in bone tissue engineering?" Tissue Engineering Part B: Reviews **20**(5): 477-491.

Guarino, V., F. Causa and L. Ambrosio (2007). "Bioactive scaffolds for bone and ligament tissue." Expert Review of Medical Devices **4**(3): 405-418.

Habibovic, P., D. C. Bassett, C. J. Doillon, C. Gerard, M. D. McKee and J. E. Barralet (2010). "Collagen biomineralization in vivo by sustained release of inorganic phosphate ions." Advanced Materials **22**(16): 1858-1862.

Han, J.-K., H.-Y. Song, F. Saito and B.-T. Lee (2006). "Synthesis of high purity nano-sized hydroxyapatite powder by microwave-hydrothermal method." Materials Chemistry and Physics **99**(2–3): 235-239.

Hapuarachchi, T. D. and T. Peijs (2010). "Multiwalled carbon nanotubes and sepiolite nanoclays as flame retardants for polylactide and its natural fibre reinforced composites." Composites Part A: Applied Science and Manufacturing **41**(8): 954-963.

Haque, A., M. Shamsuzzoha, F. Hussain and D. Dean (2003). "S2-glass/epoxy polymer nanocomposites: manufacturing, structures, thermal and mechanical properties." Journal of Composite materials **37**(20): 1821-1837.

Harper, E., M. Braden and W. Bonfield (2000). "Mechanical properties of hydroxyapatite reinforced poly (ethylmethacrylate) bone cement after immersion in a physiological solution: influence of a silane coupling agent." Journal of Materials Science: Materials in Medicine **11**(8): 491-497.

Harrison, B. S. and A. Atala (2007). "Carbon nanotube applications for tissue engineering." Biomaterials **28**(2): 344-353.

He, L.-H., O. C. Standard, T. T. Huang, B. A. Latella and M. V. Swain (2008). "Mechanical behaviour of porous hydroxyapatite." Acta Biomaterialia **4**(3): 577-586.

He, L., L. Yao, D. Yang, Q. Cheng, J. Sun, R. Song and Y. Hao (2011). "Preparation and Characterization of Chitosan-Blended Multiwalled Carbon Nanotubes." Journal of Macromolecular Science, Part B **50**(12): 2454-2463.

Hoidy, W. H., M. B. Ahmad, E. A. J. Al-Mulla and N. A. B. Ibrahim (2010). "Preparation and characterization of polylactic acid/polycaprolactone clay nanocomposites." Journal of Applied sciences **10**(2): 97-106.

Hong, Z., P. Zhang, C. He, X. Qiu, A. Liu, L. Chen, X. Chen and X. Jing (2005). "Nano-composite of poly(l-lactide) and surface grafted hydroxyapatite: Mechanical properties and biocompatibility." Biomaterials **26**(32): 6296-6304.

Hu, Q., B. Li, M. Wang and J. Shen (2004). "Preparation and characterization of biodegradable chitosan/hydroxyapatite nanocomposite rods via in situ hybridization: a potential material as internal fixation of bone fracture." Biomaterials **25**(5): 779-785.

Hudson Zanin, E. S., Fernanda Roberta Marciano, Helder Jose Ceragioli, Alessandro Eustaquio Campos Granato, Marimelia Porcionatto and Anderson Oliveira Lobo (2013). "Fast preparation of nano-hydroxyapatite/superhydrophilic reduced graphene oxide composites for bioactive applications." Journal of Materials Chemistry B.

Hui, P., S. Meena, G. Singh, R. Agarawal and S. Prakash (2010). "Synthesis of hydroxyapatite bio-ceramic powder by hydrothermal method." Journal of Minerals and Materials Characterization and Engineering **9**: 683.

Hussain, F., M. Hojjati, M. Okamoto and R. E. Gorga (2006). "Review article: Polymer-matrix Nanocomposites, Processing, Manufacturing, and Application: An Overview." Journal of Composite Materials **40**(17): 1511-1575.

Hussain, M., M. Kabir and A. Sood (2009). "On the cytotoxicity of carbon nanotubes." Current science **96**(5): 664-673.

Hutmacher, D. W. (2001). "Scaffold design and fabrication technologies for engineering tissues—state of the art and future perspectives." Journal of Biomaterials Science, Polymer Edition **12**(1): 107-124.

Hutmacher, D. W., J. T. Schantz, C. X. F. Lam, K. C. Tan and T. C. Lim (2007). "State of the art and future directions of scaffold-based bone engineering from a biomaterials perspective." Journal of tissue engineering and regenerative medicine **1**(4): 245-260.

Islam, M. S. and M. Todo (2016). "Effects of sintering temperature on the compressive mechanical properties of collagen/hydroxyapatite composite scaffolds for bone tissue engineering." Materials Letters **173**: 231-234.

Ismail Zainol, F. A. Z., Mohd Razif Saliman and Mohd Affandi Derman (2008). "Preparation and characterisation of chitosan/nanohydroxyapatite composites." Solid State Science and Technology **16**(No. 1): 153-159.

Jang, J.-H., O. Castano and H.-W. Kim (2009). "Electrospun materials as potential platforms for bone tissue engineering." Advanced drug delivery reviews **61**(12): 1065-1083.

Jiang, L., Y. Li, X. Wang, L. Zhang, J. Wen and M. Gong (2008). "Preparation and properties of nano-hydroxyapatite/chitosan/carboxymethyl cellulose composite scaffold." Carbohydrate Polymers **74**(3): 680-684.

Jiao, T., J. Hu, Q. Zhang and Y. Xiao (2015). "Preparation and Self-assembly of Functionalized Nanocomposites and Nanomaterials–Relationship Between Structures and Properties."

Jo, J.-H., E.-J. Lee, D.-S. Shin, H.-E. Kim, H.-W. Kim, Y.-H. Koh and J.-H. Jang (2009). "In vitro/in vivo biocompatibility and mechanical properties of bioactive glass nanofiber and poly(ε-caprolactone) composite materials." Journal of Biomedical Materials Research Part B: Applied Biomaterials **91B**(1): 213-220.

Jo, J. H., E. J. Lee, D. S. Shin, H. E. Kim, H. W. Kim, Y. H. Koh and J. H. Jang (2009). "In vitro/in vivo biocompatibility and mechanical properties of bioactive glass nanofiber and poly (ε-caprolactone) composite materials." Journal of Biomedical Materials Research Part B: Applied Biomaterials **91**(1): 213-220.

Journet, C., W. Maser, P. Bernier, A. Loiseau, M. L. De La Chapelle, d. l. S. Lefrant, P. Deniard, R. Lee and J. Fischer (1997). "Large-scale production of single-walled carbon nanotubes by the electric-arc technique." Nature **388**(6644): 756-758.

K.A. Dubey, Y. K. B., C.V. Chaudhari, Virendra Kumar, N.K. Goel, S. Sabharwal (2009). "Radiation processed ethylene vinyl acetate-multiple walled carbon nanotube nano-composites: Effect of MWNT addition on the gel content and crosslinking density." eXPRESS Polymer Letters **3**: 492-500.

Kalia, P., G. Vizcay-Barrena, J. P. Fan, A. Warley, L. Di Silvio and J. Huang (2014). "Nanohydroxyapatite shape and its potential role in bone formation: an analytical study." Journal of the Royal Society Interface **11**(93): 20140004.

Kanagaraj, S., F. R. Varanda, T. V. Zhil'tsova, M. S. Oliveira and J. A. Simões (2007). "Mechanical properties of high density polyethylene/carbon nanotube composites." Composites Science and Technology **67**(15): 3071-3077.

Kane, R. J., G. L. Converse and R. K. Roeder (2008). "Effects of the reinforcement morphology on the fatigue properties of hydroxyapatite reinforced polymers." Journal of the Mechanical Behavior of Biomedical Materials **1**(3): 261-268.

Kango, S., S. Kalia, A. Celli, J. Njuguna, Y. Habibi and R. Kumar (2013). "Surface modification of inorganic nanoparticles for development of organic–inorganic nanocomposites—A review." Progress in Polymer Science **38**(8): 1232-1261.

Karageorgiou, V. and D. Kaplan (2005). "Porosity of 3D biomaterial scaffolds and osteogenesis." Biomaterials **26**(27): 5474-5491.

Kashiwagi, T., J. Fagan, J. F. Douglas, K. Yamamoto, A. N. Heckert, S. D. Leigh, J. Obrzut, F. Du, S. Lin-Gibson, M. Mu, K. I. Winey and R. Haggenmueller (2007). "Relationship between dispersion metric and properties of PMMA/SWNT nanocomposites." Polymer **48**(16): 4855-4866.

Keaveny, T. (1998). Cancellous bone. Handbook of biomaterial properties, Springer**:** 15-23.

Keaveny, T. M., E. F. Morgan and O. C. Yeh (2004). "Bone mechanics."

Ker, R. (2008). Damage and fatigue. Collagen, Springer**:** 111-131.

Kim, B. K., J. W. Seo and H. M. Jeong (2003). "Morphology and properties of waterborne polyurethane/clay nanocomposites." European Polymer Journal **39**(1): 85-91.

Kim, G.-M., A. S. Asran, G. H. Michler, P. Simon and J.-S. Kim (2008). "Electrospun PVA/HAp nanocomposite nanofibers: biomimetics of mineralized hard tissues at a lower level of complexity." Bioinspiration & biomimetics **3**(4): 046003.

Kim, H.-W., J. C. Knowles and H.-E. Kim (2004). "Hydroxyapatite/poly (ε-caprolactone) composite coatings on hydroxyapatite porous bone scaffold for drug delivery." Biomaterials **25**(7): 1279-1287.

Kim, H., A. A. Abdala and C. W. Macosko (2010). "Graphene/Polymer Nanocomposites." Macromolecules **43**(16): 6515-6530.

Kim, H. W., H. H. Lee and J. Knowles (2006). "Electrospinning biomedical nanocomposite fibers of hydroxyapatite/poly (lactic acid) for bone regeneration." Journal of Biomedical Materials Research Part A **79**(3): 643-649.

Kokubo, T. (1991). "Bioactive glass ceramics: properties and applications." Biomaterials **12**(2): 155-163.

Kong, J., A. M. Cassell and H. Dai (1998). "Chemical vapor deposition of methane for single-walled carbon nanotubes." Chemical Physics Letters **292**(4–6): 567-574.

Kong, L., Y. Gao, G. Lu, Y. Gong, N. Zhao and X. Zhang (2006). "A study on the bioactivity of chitosan/nano-hydroxyapatite composite scaffolds for bone tissue engineering." European Polymer Journal **42**(12): 3171-3179.

Konidari, M. V., D. N. Soulas, K. G. Papadokostaki and M. Sanopoulou (2012). "Study of the effect of modified and pristine carbon nanotubes on the properties of poly(vinyl alcohol) nanocomposite films." Journal of Applied Polymer Science **125**(S1): E471-E477.

Koutsopoulos, S. (2002). "Synthesis and characterization of hydroxyapatite crystals: a review study on the analytical methods." Journal of biomedical materials research **62**(4): 600-612.

Kuilla, T., S. Bhadra, D. Yao, N. H. Kim, S. Bose and J. H. Lee (2010). "Recent advances in graphene based polymer composites." <u>Progress in Polymer Science</u> **35**(11): 1350-1375.

Kumar, D., I. Mutreja, P. C. Keshvan, M. Bhat, A. K. Dinda and S. Mitra "Organically Modified Silica Nanoparticles Interaction with Macrophage Cells: Assessment of Cell Viability on the Basis of Physicochemical Properties." <u>Journal of Pharmaceutical Sciences</u> **104**(11): 3943-3951.

Kumar, M., S. Mohanty, S. K. Nayak and M. Rahail Parvaiz (2010). "Effect of glycidyl methacrylate (GMA) on the thermal, mechanical and morphological property of biodegradable PLA/PBAT blend and its nanocomposites." <u>Bioresource Technology</u> **101**(21): 8406-8415.

Kumar, M. N. R. (2000). "A review of chitin and chitosan applications." <u>Reactive and functional polymers</u> **46**(1): 1-27.

Kurtz, S. M., O. K. Muratoglu, M. Evans and A. A. Edidin (1999). "Advances in the processing, sterilization, and crosslinking of ultra-high molecular weight polyethylene for total joint arthroplasty." <u>Biomaterials</u> **20**(18): 1659-1688.

Lau, K.-t., M. Lu, L. Chun-ki, H.-y. Cheung, F.-L. Sheng and H.-L. Li (2005). "Thermal and mechanical properties of single-walled carbon nanotube bundle-reinforced epoxy nanocomposites: the role of solvent for nanotube dispersion." <u>Composites Science and Technology</u> **65**(5): 719-725.

Lee, H. J., S. E. Kim, H. W. Choi, C. W. Kim, K. J. Kim and S. C. Lee (2007). "The effect of surface-modified nano-hydroxyapatite on biocompatibility of poly(ε-caprolactone)/hydroxyapatite nanocomposites." <u>European Polymer Journal</u> **43**(5): 1602-1608.

Lee, K.-L., M. Baldassarri, N. Gupta, D. Pinisetty, M. N. Janal, N. Tovar and P. G. Coelho (2012). "Nanomechanical Characterization of Canine Femur Bone for Strain Rate Sensitivity in the Quasistatic Range under Dry versus Wet Conditions." <u>International Journal of Biomaterials</u> **2012**: 6.

Li, B. and W.-H. Zhong (2011). "Review on polymer/graphite nanoplatelet nanocomposites." <u>Journal of Materials Science</u> **46**(17): 5595-5614.

Li, X., H. Gao, W. A. Scrivens, D. Fei, V. Thakur, M. A. Sutton, A. P. Reynolds and M. L. Myrick (2005). "Structural and mechanical characterization of nanoclay-reinforced agarose nanocomposites." <u>Nanotechnology</u> **16**(10): 2020.

Li, X., L. Wang, Y. Fan, Q. Feng, F. Z. Cui and F. Watari (2013). "Nanostructured scaffolds for bone tissue engineering." Journal of Biomedical Materials Research Part A.

Li, Z., L. Yubao, Y. Aiping, P. Xuelin, W. Xuejiang and Z. Xiang (2005). "Preparation and in vitro investigation of chitosan/nano-hydroxyapatite composite used as bone substitute materials." Journal of Materials Science: Materials in Medicine **16**(3): 213-219.

Liao, C. Z., K. Li, H. M. Wong, W. Y. Tong, K. W. K. Yeung and S. C. Tjong (2013). "Novel polypropylene biocomposites reinforced with carbon nanotubes and hydroxyapatite nanorods for bone replacements." Materials Science and Engineering: C **33**(3): 1380-1388.

Liao, S., G. Xu, W. Wang, F. Watari, F. Cui, S. Ramakrishna and C. K. Chan (2007). "Self-assembly of nano-hydroxyapatite on multi-walled carbon nanotubes." Acta Biomaterialia **3**(5): 669-675.

Lichte, P., H. C. Pape, T. Pufe, P. Kobbe and H. Fischer (2011). "Scaffolds for bone healing: Concepts, materials and evidence." Injury **42**(6): 569-573.

Liebschner, M. and M. Wettergreen (2003). "Optimization of bone scaffold engineering for load bearing applications." Topics in tissue engineering: 1-39.

Lincks, J., B. Boyan, C. Blanchard, C. Lohmann, Y. Liu, D. Cochran, D. Dean and Z. Schwartz (1998). "Response of MG63 osteoblast-like cells to titanium and titanium alloy is dependent on surface roughness and composition." Biomaterials **19**(23): 2219-2232.

Ling, C., W. Shing-Chung and P. Sreekumar (2003). "Fracture properties of nanoclay-filled polypropylene." Journal of Applied Polymer Science **88**(14): 3298-3305.

Liu, I. Y. Phang, L. Shen, S. Y. Chow and W.-D. Zhang (2004). "Morphology and Mechanical Properties of Multiwalled Carbon Nanotubes Reinforced Nylon-6 Composites." Macromolecules **37**(19): 7214-7222.

Liu, D.-M., Q. Yang, T. Troczynski and W. J. Tseng (2002). "Structural evolution of sol–gel-derived hydroxyapatite." Biomaterials **23**(7): 1679-1687.

Liu, H. S., T. S. Chin, L. S. Lai, S. Y. Chiu, K. H. Chung, C. S. Chang and M. T. Lui (1997). "Hydroxyapatite synthesized by a simplified hydrothermal method." Ceramics International **23**(1): 19-25.

Liu, J., X. Ye, H. Wang, M. Zhu, B. Wang and H. Yan (2003). "The influence of pH and temperature on the morphology of hydroxyapatite synthesized by hydrothermal method." Ceramics International **29**(6): 629-633.

Liu, L., A. H. Barber, S. Nuriel and H. D. Wagner (2005). "Mechanical Properties of Functionalized Single-Walled Carbon-Nanotube/Poly (vinyl alcohol) Nanocomposites." Advanced Functional Materials **15**(6): 975-980.

Liu, X., S. Khor, E. Petinakis, L. Yu, G. Simon, K. Dean and S. Bateman (2010). "Effects of hydrophilic fillers on the thermal degradation of poly(lactic acid)." Thermochimica Acta **509**(1–2): 147-151.

Liu, X. and P. Ma (2004). "Polymeric Scaffolds for Bone Tissue Engineering." Annals of Biomedical Engineering **32**(3): 477-486.

Liu, Y., J. Lim and S.-H. Teoh (2013). "Review: Development of clinically relevant scaffolds for vascularised bone tissue engineering." Biotechnology Advances **31**(5): 688-705.

Liu, Y., H. Wu and G. Chen (2014). "Enhanced mechanical properties of nanocomposites at low graphene content based on in situ ball milling." Polymer Composites.

Liu, Z., Y. Chen, W. Ding and C. Zhang (2015). "Filling behavior, morphology evolution and crystallization behavior of microinjection molded poly (lactic acid)/hydroxyapatite nanocomposites." Composites Part A: Applied Science and Manufacturing **72**: 85-95.

Lordan, S., J. E. Kennedy and C. L. Higginbotham (2011). "Cytotoxic effects induced by unmodified and organically modified nanoclays in the human hepatic HepG2 cell line." Journal of Applied Toxicology **31**(1): 27-35.

Lv, Q., X. Yu, M. Deng, L. Nair and C. Laurencin (2014). "Evaluation of PLAGA/n-HA Composite Scaffold Bioactivity in vitro." Bioceram Dev Appl **4**(080): 2.

Machado, B. F. and P. Serp (2012). "Graphene-based materials for catalysis." Catalysis Science & Technology **2**(1): 54-75.

Mahyudin, F., L. Widhiyanto and H. Hermawan (2016). Biomaterials in Orthopaedics. Biomaterials and Medical Devices, Springer**:** 161-181.

Maisanaba, S., S. Pichardo, M. Puerto, D. Gutiérrez-Praena, A. M. Cameán and A. Jos (2015). "Toxicological evaluation of clay minerals and derived nanocomposites: A review." Environmental Research **138**: 233-254.

Malinowski, R., P. Rytlewski and M. Żenkiewicz (2011). "Effects of electron radiation on properties of PLA." Arch. Mater. Sci. Eng **49**(1): 25-32.

Manchado, M. A. L., L. Valentini, J. Biagiotti and J. M. Kenny (2005). "Thermal and mechanical properties of single-walled carbon nanotubes–polypropylene composites prepared by melt processing." Carbon **43**(7): 1499-1505.

Marchi, J., A. Dantas, P. Greil, J. Bressiani, A. Bressiani and F. Müller (2007). "Influence of Mg-substitution on the physicochemical properties of calcium phosphate powders." Materials research bulletin **42**(6): 1040-1050.

Marcolongo, M., P. Ducheyne, J. Garino and E. Schepers (1998). "Bioactive glass fiber/polymeric composites bond to bone tissue." Journal of biomedical materials research **39**(1): 161-170.

Marrs, B., R. Andrews, T. Rantell and D. Pienkowski (2006). "Augmentation of acrylic bone cement with multiwall carbon nanotubes." Journal of Biomedical Materials Research Part A **77A**(2): 269-276.

Mayr-Wohlfart, U., J. Fiedler, K. P. Günther, W. Puhl and S. Kessler (2001). "Proliferation and differentiation rates of a human osteoblast-like cell line (SaOS-2) in contact with different bone substitute materials." Journal of biomedical materials research **57**(1): 132-139.

Michael, F. M., M. Khalid, C. Ratnam, C. Y. Chee, W. Rashmi and M. Hoque (2016). "Sono-synthesis of nanohydroxyapatite: Effects of process parameters." Ceramics International **42**(5): 6263-6272.

Michael, F. M., M. Khalid, C. T. Ratnam, W. Rashmi, M. E. Hoque and M. R. Ketabchi (2016). "Nanohydroxyapatite synthesis using optimized process parameters for load-bearing implant." Bulletin of Materials Science: 1-13.

Michael, F. M., M. Khalid, R. Walvekar, C. T. Ratnam, S. Ramarad, H. Siddiqui and M. E. Hoque (2016). "Effect of nanofillers on the physico-mechanical properties of load bearing bone implants." Materials Science and Engineering: C **67**: 792-806.

Minkova, L., Y. Peneva, E. Tashev, S. Filippi, M. Pracella and P. Magagnini (2009). "Thermal properties and microhardness of HDPE/clay nanocomposites compatibilized by different functionalized polyethylenes." Polymer Testing **28**(5): 528-533.

Mozafari, M., M. Rabiee, M. Azami and S. Maleknia (2010). "Biomimetic formation of apatite on the surface of porous gelatin/bioactive glass nanocomposite scaffolds." Applied Surface Science **257**(5): 1740-1749.

Muisener, P. A. O. R., L. Clayton, J. D'Angelo, J. P. Harmon, A. K. Sikder, A. Kumar, A. M. Cassell and M. Meyyappan (2002). "Effects of gamma radiation on poly(methyl methacrylate)/single-wall nanotube composites." Journal of Materials Research **17**(10): 2507-2513.

Murugan, R. and S. Ramakrishna (2005). "Development of nanocomposites for bone grafting." Composites Science and Technology **65**(15): 2385-2406.

Mutlu, G. k. M., G. S. Budinger, A. A. Green, D. Urich, S. Soberanes, S. E. Chiarella, G. F. Alheid, D. R. McCrimmon, I. Szleifer and M. C. Hersam (2010). "Biocompatible nanoscale dispersion of single-walled carbon nanotubes minimizes in vivo pulmonary toxicity." Nano letters **10**(5): 1664-1670.

Naffakh, M., A. M. Diez-Pascual and M. A. Gómez-Fatou (2011). "New hybrid nanocomposites containing carbon nanotubes, inorganic fullerene-like WS2 nanoparticles and poly (ether ether ketone)(PEEK)." Journal of Materials Chemistry **21**(20): 7425-7433.

Nammakuna, N., S. A. Barringer and P. Ratanatriwong (2015). "The effects of protein isolates and hydrocolloids complexes on dough rheology, physicochemical properties and qualities of gluten-free crackers." Food Science & Nutrition.

Narang, S. and V. Chava (2000). "Biomaterials used as bone graft substitutes." Ann Dent Univ Malaya **7**: 36-42.

Navarro, M., A. Michiardi, O. Castano and J. Planell (2008). "Biomaterials in orthopaedics." Journal of the Royal Society Interface **5**(27): 1137-1158.

Navarro, M., A. Michiardi, O. Castaño and J. Planell (2008). "Biomaterials in orthopaedics." Journal of the Royal Society, Interface/the Royal Society **5**(27): 1137-1158.

Nerem, R. M. and A. Sambanis (1995). "Tissue engineering: from biology to biological substitutes." Tissue Engineering **1**(1): 3-13.

Nielsen, L. E. (1969). "Cross-Linking–Effect on Physical Properties of Polymers." Journal of Macromolecular Science, Part C **3**(1): 69-103.

Ogle, M. F., M. S. Reimink and R. F. Schroeder (2001). Medical devices with metal/polymer composites, Google Patents.

Oliveira, M. and A. Machado (2013). "Preparation of polymer-based nanocomposites by different routes." Nanocomposites: synthesis, characterization and applications: 1-22.

Onuki, Y., U. Bhardwaj, F. Papadimitrakopoulos and D. J. Burgess (2008). "A Review of the Biocompatibility of Implantable Devices: Current Challenges to Overcome Foreign Body Response." Journal of Diabetes Science and Technology **2**(6): 1003-1015.

Pae, A., S. Kim, H. Kim and Y. Woo (2011). "Osteoblast-like cell attachment and proliferation on turned, blasted, and anodized titanium surfaces." The International journal of oral & maxillofacial implants **26**(3): 475.

Paiva, M., B. Zhou, K. Fernando, Y. Lin, J. Kennedy and Y.-P. Sun (2004). "Mechanical and morphological characterization of polymer–carbon nanocomposites from functionalized carbon nanotubes." Carbon **42**(14): 2849-2854.

Pang, X. and I. Zhitomirsky (2007). "Electrophoretic deposition of composite hydroxyapatite-chitosan coatings." Materials Characterization **58**(4): 339-348.

Papageorgiou, D. G., I. A. Kinloch and R. J. Young (2015). "Graphene/elastomer nanocomposites." Carbon **95**: 460-484.

Pappas, J., K. Patel and E. Nauman (2005). "Structure and properties of phenolic resin/nanoclay composites synthesized by in situ polymerization." Journal of applied polymer science **95**(5): 1169-1174.

Parchi, P., O. Vittorio, L. Andreani, N. Piolanti, G. Cirillo, F. Iemma, S. Hampel and M. Lisanti (2013). "How nanotechnology can really improve the future of orthopedic implants and scaffolds for bone and cartilage defects." Journal of Nanomedicine & Biotherapeutic Discovery **2013**.

Parhi, P., A. Ramanan and A. R. Ray (2004). "A convenient route for the synthesis of hydroxyapatite through a novel microwave-mediated metathesis reaction." Materials letters **58**(27): 3610-3612.

Park, G. E. and T. J. Webster (2005). "A review of nanotechnology for the development of better orthopedic implants." Journal of Biomedical Nanotechnology **1**(1): 18-29.

Park, J.-E. and M. Todo (2011). "Development and characterization of reinforced poly (l-lactide) scaffolds for bone tissue engineering." Journal of Materials Science: Materials in Medicine **22**(5): 1171-1182.

Park, J. H. and S. C. Jana (2003). "The relationship between nano- and micro-structures and mechanical properties in PMMA–epoxy–nanoclay composites." Polymer **44**(7): 2091-2100.

Park, J. H. and S. C. Jana (2003). "The relationship between nano-and micro-structures and mechanical properties in PMMA–epoxy–nanoclay composites." Polymer **44**(7): 2091-2100.

Paul, W. and C. P. Sharma (2006). "Nanoceramic matrices: biomedical applications." Am J Biochem Biotechnol **2**(2): 41-48.

Persson, M., G. S. Lorite, S.-W. Cho, J. Tuukkanen and M. Skrifvars (2013). "Melt spinning of poly (lactic acid) and hydroxyapatite composite fibers: Influence of the filler content on the fiber properties." ACS applied materials & interfaces **5**(15): 6864-6872.

Phang, I. Y., K. Pramoda, T. Liu and C. He (2004). "Crystallization and melting behavior of polyester/clay nanocomposites." Polymer international **53**(9): 1282-1289.

Piggott, M., P. Chua and D. Andison (1985). "The interface between glass and carbon fibers and thermosetting polymers." Polymer composites **6**(4): 242-248.

Pinto, H. P. and J. Leszczynski (2014). "Fundamental properties of graphene." Handbook of Carbon Nano Materials:(In 2 Volumes) Volume 5: Graphene—Fundamental PropertiesVolume 6: Graphene—Energy and Sensor Applications.

Polikeit, A., L. P. Nolte and S. J. Ferguson (2003). "The effect of cement augmentation on the load transfer in an osteoporotic functional spinal unit: finite-element analysis." Spine **28**(10): 991-996.

Polo-Corrales, L., M. Latorre-Esteves and J. E. Ramirez-Vick (2014). "Scaffold design for bone regeneration." Journal of nanoscience and nanotechnology **14**(1): 15-56.

Pradhan, S., J. Hedberg, E. Blomberg, S. Wold and I. Odnevall Wallinder (2016). "Effect of sonication on particle dispersion, administered dose and metal release of non-functionalized, non-inert metal nanoparticles." Journal of Nanoparticle Research **18**(9): 285.

Pradhan, S., R. Lach, H. H. Le, W. Grellmann, H.-J. Radusch and R. Adhikari (2013). "Effect of Filler Dimensionality on Mechanical Properties of Nanofiller Reinforced Polyolefin Elastomers." ISRN Polymer Science **2013**: 9.

Pramanik, S., A. K. Agarwal, K. Rai and A. Garg (2007). "Development of high strength hydroxyapatite by solid-state-sintering process." Ceramics International **33**(3): 419-426.

Pramanik, S., A. K. Agarwal, K. N. Rai and A. Garg (2007). "Development of high strength hydroxyapatite by solid-state-sintering process." Ceramics International **33**(3): 419-426.

Pramoda, K. P., T. Liu, Z. Liu, C. He and H.-J. Sue (2003). "Thermal degradation behavior of polyamide 6/clay nanocomposites." Polymer degradation and stability **81**(1): 47-56.

Prolongo, S. G., A. Jimenez-Suarez, R. Moriche and A. Ureña (2013). "In situ processing of epoxy composites reinforced with graphene nanoplatelets." Composites Science and Technology **86**: 185-191.

Puvvada, N., P. K. Panigrahi, H. Kalita, K. R. Chakraborty and A. Pathak (2013). "Effect of temperature on morphology of triethanolamine-assisted synthesized hydroxyapatite nanoparticles." Applied Nanoscience **3**(3): 203-209.

Qi, B., Q. Zhang, M. Bannister and Y.-W. Mai (2006). "Investigation of the mechanical properties of DGEBA-based epoxy resin with nanoclay additives." Composite Structures **75**(1): 514-519.

Rahaman, M. N., D. E. Day, B. Sonny Bal, Q. Fu, S. B. Jung, L. F. Bonewald and A. P. Tomsia (2011). "Bioactive glass in tissue engineering." Acta Biomaterialia **7**(6): 2355-2373.

Ramay, H. R. and M. Zhang (2003). "Preparation of porous hydroxyapatite scaffolds by combination of the gel-casting and polymer sponge methods." Biomaterials **24**(19): 3293-3302.

Rámila, A., F. Balas and M. Vallet-Regí (2002). "Synthesis Routes for Bioactive Sol−Gel Glasses: Alkoxides versus Nitrates." Chemistry of Materials **14**(2): 542-548.

Ramimoghadam, D., M. Z. B. Hussein and Y. H. Taufiq-Yap (2012). "The effect of sodium dodecyl sulfate (SDS) and cetyltrimethylammonium bromide (CTAB) on the properties of ZnO synthesized by hydrothermal method." International journal of molecular sciences **13**(10): 13275-13293.

Ramires, P. A., A. Romito, F. Cosentino and E. Milella (2001). "The influence of titania/hydroxyapatite composite coatings on in vitro osteoblasts behaviour." Biomaterials **22**(12): 1467-1474.

Ramírez, C., C. Albano, A. Karam, N. Domínguez, Y. Sánchez and G. González (2005). "Mechanical, thermal, rheological and morphological behaviour of irradiated PP/HA composites." Nuclear Instruments and Methods in Physics Research Section B: Beam Interactions with Materials and Atoms **236**(1–4): 531-535.

Ren, Y., F. Li, H.-M. Cheng and K. Liao (2003). "Tension–tension fatigue behavior of unidirectional single-walled carbon nanotube reinforced epoxy composite." Carbon **41**(11): 2177-2179.

Rezler, T. (2011). "Orthopedic implants- A global market overview." Retrieved 12/1, 2017.

Rezwan, K., Q. Chen, J. Blaker and A. R. Boccaccini (2006). "Biodegradable and bioactive porous polymer/inorganic composite scaffolds for bone tissue engineering." Biomaterials **27**(18): 3413-3431.

Rezwan, K., Q. Z. Chen, J. J. Blaker and A. R. Boccaccini (2006). "Biodegradable and bioactive porous polymer/inorganic composite scaffolds for bone tissue engineering." Biomaterials **27**(18): 3413-3431.

Rhee, S.-H. (2002). "Synthesis of hydroxyapatite via mechanochemical treatment." Biomaterials **23**(4): 1147-1152.

Roeder, R. K., G. L. Converse, R. J. Kane and W. Yue (2008). "Hydroxyapatite-reinforced polymer biocomposites for synthetic bone substitutes." Jom **60**(3): 38-45.

Rong, M., M. Zhang and W. Ruan (2006). "Surface modification of nanoscale fillers for improving properties of polymer nanocomposites: a review." Materials science and technology **22**(7): 787-796.

Saeed, K. and S.-Y. Park (2007). "Preparation of multiwalled carbon nanotube/nylon-6 nanocomposites by in situ polymerization." Journal of applied polymer science **106**(6): 3729-3735.

Saikia, B. J. and G. Parthasarathy (2010). "Fourier transform infrared spectroscopic characterization of kaolinite from Assam and Meghalaya, Northeastern India." Journal of Modern Physics **1**(04): 206.

Salehi Vaziri, H., M. Abadyan, M. Nouri, I. A. Omaraei, Z. Sadredini and M. Ebrahimnia (2011). "Investigation of the fracture mechanism and mechanical properties of polystyrene/silica nanocomposite in various silica contents." Journal of Materials Science **46**(17): 5628-5638.

Salerno, A., M. Fernández-Gutiérrez, J. S. R. del Barrio and C. D. Pascual (2014). "Macroporous and nanometre scale fibrous PLA and PLA–HA composite scaffolds fabricated by a bio safe strategy." RSC Advances **4**(106): 61491-61502.

Sargeant, A. and T. Goswami (2006). "Hip implants: Paper V. Physiological effects." Materials & Design **27**(4): 287-307.

Scalera, F., F. Gervaso, K. Sanosh, A. Sannino and A. Licciulli (2013). "Influence of the calcination temperature on morphological and mechanical properties of highly porous hydroxyapatite scaffolds." Ceramics International **39**(5): 4839-4846.

Seitz, H., W. Rieder, S. Irsen, B. Leukers and C. Tille (2005). "Three-dimensional printing of porous ceramic scaffolds for bone tissue engineering." Journal of Biomedical Materials Research Part B: Applied Biomaterials **74**(2): 782-788.

Sen, R., B. Zhao, D. Perea, M. E. Itkis, H. Hu, J. Love, E. Bekyarova and R. C. Haddon (2004). "Preparation of single-walled carbon nanotube reinforced polystyrene and polyurethane nanofibers and membranes by electrospinning." Nano Letters **4**(3): 459-464.

Shi, X., B. Sitharaman, Q. P. Pham, P. P. Spicer, J. L. Hudson, L. J. Wilson, J. M. Tour, R. M. Raphael and A. G. Mikos (2008). "In vitro cytotoxicity of single-walled carbon nanotube/biodegradable polymer nanocomposites." Journal of Biomedical Materials Research Part A **86**(3): 813-823.

Shi, Z., X. Huang, Y. Cai, R. Tang and D. Yang (2009). "Size effect of hydroxyapatite nanoparticles on proliferation and apoptosis of osteoblast-like cells." Acta Biomaterialia **5**(1): 338-345.

Singh, A. (2012). "Hydroxyapatite, a biomaterial: Its chemical synthesis, characterization and study of biocompatibility prepared from shell of garden snail, Helix aspersa." Bulletin of Materials Science **35**(6): 1031-1038.

Singh, M. K., T. Shokuhfar, J. J. d. A. Gracio, A. C. M. de Sousa, J. M. D. F. Fereira, H. Garmestani and S. Ahzi (2008). "Hydroxyapatite Modified with Carbon-Nanotube-Reinforced Poly(methyl methacrylate): A Nanocomposite Material for Biomedical Applications." Advanced Functional Materials **18**(5): 694-700.

Singh, Z. (2016). "Applications and toxicity of graphene family nanomaterials and their composites." Nanotechnology, science and applications **9**: 15.

Smart, S., A. Cassady, G. Lu and D. Martin (2006). "The biocompatibility of carbon nanotubes." Carbon **44**(6): 1034-1047.

Srinivasan, S., R. Jayasree, K. P. Chennazhi, S. V. Nair and R. Jayakumar (2012). "Biocompatible alginate/nano bioactive glass ceramic composite scaffolds for periodontal tissue regeneration." Carbohydrate Polymers **87**(1): 274-283.

Tabata, Y. (2003). "Tissue regeneration based on growth factor release." Tissue Engineering **9**(4, Supplement 1): 5-15.

Takayama, T., M. Todo and A. Takano (2009). "The effect of bimodal distribution on the mechanical properties of hydroxyapatite particle filled poly (L-lactide) composites." Journal of the mechanical behavior of biomedical materials **2**(1): 105-112.

Tanniru, M., Q. Yuan and R. Misra (2006). "On significant retention of impact strength in clay–reinforced high-density polyethylene (HDPE) nanocomposites." Polymer **47**(6): 2133-2146.

Taurozzi, J. S., V. A. Hackley and M. R. Wiesner (2011). "Ultrasonic dispersion of nanoparticles for environmental, health and safety assessment–issues and recommendations." Nanotoxicology **5**(4): 711-729.

Teo, A. J. T., A. Mishra, I. Park, Y.-J. Kim, W.-T. Park and Y.-J. Yoon (2016). "Polymeric Biomaterials for Medical Implants and Devices." ACS Biomaterials Science & Engineering **2**(4): 454-472.

Thein-Han, W. W. and R. D. K. Misra (2009). "Biomimetic chitosan–nanohydroxyapatite composite scaffolds for bone tissue engineering." Acta Biomaterialia **5**(4): 1182-1197.

Thomas, S., M. Idicula and K. Joseph (2009). "Mechanical performance of short banana/sisal hybrid fibre reinforced polyester composites." Journal of reinforced plastics and composites.

Torabinejad, B., J. Mohammadi-Rovshandeh, S. M. Davachi and A. Zamanian (2014). "Synthesis and characterization of nanocomposite scaffolds based on triblock copolymer of L-lactide, ε-caprolactone and nano-hydroxyapatite for bone tissue engineering." Materials Science and Engineering: C **42**: 199-210.

Turner, C., T. Wang and D. Burr (2001). "Shear strength and fatigue properties of human cortical bone determined from pure shear tests." Calcified tissue international **69**(6): 373-378.

Udensi, S. C. and L. A. Nnanna (2011). "Sem Studies of Tensile Fractured Surfaces of Expanded Graphite/Acrylonitrile/Methyl Methacrylate Nanocomposites Prepared via in-Situ Polymerization." American Journal of Materials Science **1**(2): 123-127.

Ueda, K., K. Tanaka and Y. Chujo (2016). "Remarkably high miscibility of octa-substituted POSS with commodity conjugated polymers and molecular fillers for the improvement of homogeneities of polymer matrices." Polym J **48**(12): 1133-1139.

Unnikrishnan, L., S. Mohanty, S. K. Nayak and A. Ali (2011). "Preparation and characterization of poly(methyl methacrylate)–clay nanocomposites via melt intercalation: Effect of organoclay on thermal, mechanical and flammability properties." Materials Science and Engineering: A **528**(12): 3943-3951.

Ventura, M., O. C. Boerman, C. de Korte, M. Rijpkema, A. Heerschap, E. Oosterwijk, J. A. Jansen and X. F. Walboomers (2014). "Preclinical imaging in bone tissue engineering." Tissue Engineering Part B: Reviews **20**(6): 578-595.

Vergaro, V., E. Abdullayev, Y. M. Lvov, A. Zeitoun, R. Cingolani, R. Rinaldi and S. Leporatti (2010). "Cytocompatibility and uptake of halloysite clay nanotubes." Biomacromolecules **11**(3): 820-826.

Verma, N. K., E. Moore, W. Blau, Y. Volkov and P. Ramesh Babu (2012). "Cytotoxicity evaluation of nanoclays in human epithelial cell line A549 using high content screening and real-time impedance analysis." Journal of Nanoparticle Research **14**(9): 1-11.

Vladkova, T. G. (2010). "Surface Engineered Polymeric Biomaterials with Improved Biocontact Properties." International Journal of Polymer Science **2010**.

Wan, Y., C. Wu, G. Xiong, G. Zuo, J. Jin, K. Ren, Y. Zhu, Z. Wang and H. Luo (2015). "Mechanical properties and cytotoxicity of nanoplate-like hydroxyapatite/polylactide nanocomposites prepared by intercalation technique." Journal of the Mechanical Behavior of Biomedical Materials **47**: 29-37.

Wang, F., P. Liu, T. Nie, H. Wei and Z. Cui (2012). "Characterization of a polyamine microsphere and its adsorption for protein." International journal of molecular sciences **14**(1): 17-29.

Wang, H., Y. Li, Y. Zuo, J. Li, S. Ma and L. Cheng (2007). "Biocompatibility and osteogenesis of biomimetic nano-hydroxyapatite/polyamide composite scaffolds for bone tissue engineering." Biomaterials **28**(22): 3338-3348.

Wang, M. and W. Bonfield (2001). "Chemically coupled hydroxyapatite–polyethylene composites: structure and properties." Biomaterials **22**(11): 1311-1320.

Wang, P., C. Li, H. Gong, X. Jiang, H. Wang and K. Li (2010). "Effects of synthesis conditions on the morphology of hydroxyapatite nanoparticles produced by wet chemical process." Powder Technology **203**(2): 315-321.

Wang, Q., J. Dai, W. Li, Z. Wei and J. Jiang (2008). "The effects of CNT alignment on electrical conductivity and mechanical properties of SWNT/epoxy nanocomposites." Composites Science and Technology **68**(7): 1644-1648.

Wang, S.-F., L. Shen, W.-D. Zhang and Y.-J. Tong (2005). "Preparation and Mechanical Properties of Chitosan/Carbon Nanotubes Composites." Biomacromolecules **6**(6): 3067-3072.

Wang, X., Y. Li, J. Wei and K. de Groot (2002). "Development of biomimetic nano-hydroxyapatite/poly (hexamethylene adipamide) composites." Biomaterials **23**(24): 4787-4791.

Wang, X., J. Nyman, X. Dong, H. Leng and M. Reyes (2010). "Fundamental biomechanics in bone tissue engineering." Synthesis Lectures on Tissue Engineering **2**(1): 1-225.

Wang, Y. and C.-S. Lin (2014). "Preparation and characterization of maleated polylactide-functionalized graphite oxide nanocomposites." Journal of Polymer Research **21**(1): 1-14.

Wang, Z., Z. Liang, B. Wang, C. Zhang and L. Kramer (2004). "Processing and property investigation of single-walled carbon nanotube (SWNT) buckypaper/epoxy resin matrix nanocomposites." Composites Part A: Applied Science and Manufacturing **35**(10): 1225-1232.

Wetzel, B., F. Haupert, K. Friedrich, M. Q. Zhang and M. Z. Rong (2002). "Impact and wear resistance of polymer nanocomposites at low filler content." Polymer Engineering & Science **42**(9): 1919-1927.

Wick, P., P. Manser, L. K. Limbach, U. Dettlaff-Weglikowska, F. Krumeich, S. Roth, W. J. Stark and A. Bruinink (2007). "The degree and kind of agglomeration affect carbon nanotube cytotoxicity." Toxicology Letters **168**(2): 121-131.

Wong, K. L., C. T. Wong, W. C. Liu, H. B. Pan, M. K. Fong, W. M. Lam, W. L. Cheung, W. M. Tang, K. Y. Chiu, K. D. K. Luk and W. W. Lu (2009). "Mechanical properties and in vitro response of strontium-containing hydroxyapatite/polyetheretherketone composites." Biomaterials **30**(23–24): 3810-3817.

Wu, C.-S. and H.-T. Liao (2007). "Study on the preparation and characterization of biodegradable polylactide/multi-walled carbon nanotubes nanocomposites." Polymer **48**(15): 4449-4458.

Wu, T. Y., N. Guo, C. Y. Teh and J. X. W. Hay (2013). Theory and fundamentals of ultrasound. Advances in ultrasound technology for environmental remediation, Springer**:** 5-12.

Xiaochen Liu, J. W., and Shicheng Wei (2011). "Biological Effects of Osteoblast-Like Cells on Nanohydroxyapatite Particles at a Low Concentration Range." Journal of Nanomaterials **2011**.

Xie, X.-L., Y.-W. Mai and X.-P. Zhou (2005). "Dispersion and alignment of carbon nanotubes in polymer matrix: a review." Materials Science and Engineering: R: Reports **49**(4): 89-112.

Xu, T., Z. Tang and J. Zhu (2012). "Synthesis of polylactide-graft-glycidyl methacrylate graft copolymer and its application as a coupling agent in polylactide/bamboo flour biocomposites." Journal of Applied Polymer Science **125**(S2).

Xu, Z. and C. Gao (2010). "In situ Polymerization Approach to Graphene-Reinforced Nylon-6 Composites." Macromolecules **43**(16): 6716-6723.

Yamaguchi, I., K. Tokuchi, H. Fukuzaki, Y. Koyama, K. Takakuda, H. Monma and J. Tanaka (2001). "Preparation and microstructure analysis of chitosan/hydroxyapatite nanocomposites." Journal of biomedical materials research **55**(1): 20-27.

Yaszemski, M. J., R. G. Payne, W. C. Hayes, R. Langer and A. G. Mikos (1996). "Evolution of bone transplantation: molecular, cellular and tissue strategies to engineer human bone." Biomaterials **17**(2): 175-185.

Yoo, J. J. and S. H. Rhee (2004). "Evaluations of bioactivity and mechanical properties of poly (ε-caprolactone)/silica nanocomposite following heat treatment." Journal of Biomedical Materials Research Part A **68**(3): 401-410.

Zainuddin, S., M. V. Hosur, Y. Zhou, A. T. Narteh, A. Kumar and S. Jeelani (2010). "Experimental and numerical investigations on flexural and thermal properties of nanoclay–epoxy nanocomposites." Materials Science and Engineering: A **527**(29–30): 7920-7926.

Zhang, W. D., L. Shen, I. Y. Phang and T. Liu (2004). "Carbon nanotubes reinforced nylon-6 composite prepared by simple melt-compounding." Macromolecules **37**(2): 256-259.

Zhou, H. and J. Lee (2011). "Nanoscale hydroxyapatite particles for bone tissue engineering." Acta Biomaterialia **7**(7): 2769-2781.

Zhou, L., S. Fang, J. Tang, L. Gao and J. Yang (2012). "Synthesis and characterization of multiwalled carbon nanotube/polyurethane composites via surface modification multiwalled carbon nanotubes using silane coupling agent." Polymer Composites **33**(11): 1866-1873.

Zhu, H. W., C. L. Xu, D. H. Wu, B. Q. Wei, R. Vajtai and P. M. Ajayan (2002). "Direct Synthesis of Long Single-Walled Carbon Nanotube Strands." <u>Science</u> **296**(5569): 884-886.

Zhu, M., J. Zhang, Y. Zhou, Y. Liu, X. He, C. Tao and Y. Zhu (2013). "Preparation and Characterization of Magnetic Mesoporous Bioactive Glass/Carbon Composite Scaffolds." <u>Journal of Chemistry</u> **2013**: 11.

Zia, K. M., M. Zuber, M. Barikani, R. Hussain, T. Jamil and S. Anjum (2011). "Cytotoxicity and mechanical behavior of chitin–bentonite clay based polyurethane bio-nanocomposites." <u>International Journal of Biological Macromolecules</u> **49**(5): 1131-1136.

Zou, C., W. Weng, X. Deng, K. Cheng, X. Liu, P. Du, G. Shen and G. Han (2005). "Preparation and characterization of porous β-tricalcium phosphate/collagen composites with an integrated structure." <u>Biomaterials</u> **26**(26): 5276-5284.

Zuo, P.-P., H.-F. Feng, Z.-Z. Xu, L.-F. Zhang, Y.-L. Zhang, W. Xia and W.-Q. Zhang (2013). "Fabrication of biocompatible and mechanically reinforced graphene oxide-chitosan nanocomposite films." <u>Chemistry Central Journal</u> **7**(1): 1.

APPENDIX

Dissolve MEM powder in 1L autoclaved distilled water and add 2.2g NaHCO$_3$; stir for 2hrs then filter

Add filtered sodium pyruvate (10ml) and Pen-strep antibiotics (10ml)

Add filtered FBS (5wt%)
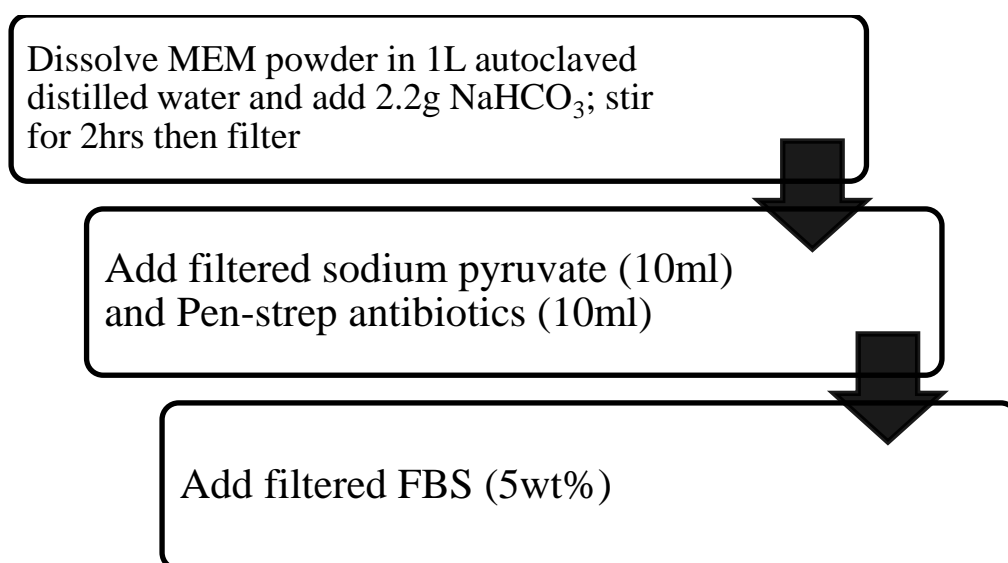
Figure A.1: Preparation of complete MEM (MEM+5%FBS)

Autoclave

1.44g Na$_2$HPO$_4$

0.2g KCl

0.24g KH$_2$PO$_4$

8g NaCl

HCl (pH=7.4)

1L distilled water
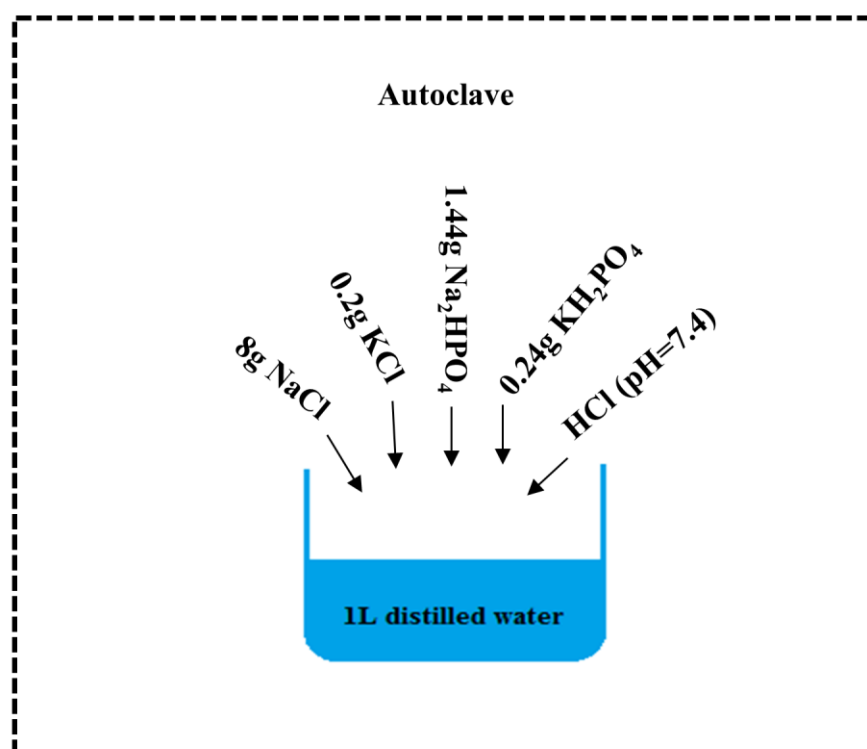
Figure A.2: Preparation of PBS

Table A.1: MTT results for the control after 3, 5 and 7 days of incubation in term of optical density at wavelength of 570 nm

3 day	5 days	7 days
0.385732	0.500532	0.552048
0.396387	0.510156	0.556652
0.390233	0.548721	0.555304
0.399731	0.51663	0.566118
0.390523	0.518105	0.538854
0.390158	0.523794	0.534289
0.354566	0.51378	0.532486
0.37546	0.52476	0.532476
0.3786	0.53487	0.54277
0.38534875	**0.51955975**	**0.5575305**
0.014382339	**0.014091238**	**0.006042406**

Table A.2: ANOVA analysis on the MTT results for the control after 3, 5 and 7 days of incubation in term of optical density at wavelength of 570 nm

SUMMARY

Groups	Count	Sum	Average	Variance
3 days	9	3.46139	0.3846	0.00019
5 days	9	4.69135	0.52126	0.0002

ANOVA

Source of Variation	SS	df	MS	F	P-value	F crit
Between Groups	0.08404	1	0.08404	435.639	5E-13	4.494
Within Groups	0.00309	16	0.00019			
Total	0.08713	17				

SUMMARY

Groups	Count	Sum	Average	Variance
5 days	9	4.69135	0.52126	0.0002
7 days	9	4.911	0.54567	0.00015

ANOVA

Source of Variation	SS	df	MS	F	P-value	F crit
Between Groups	0.00268	1	0.00268	15.3007	0.00124	4.494
Within Groups	0.0028	16	0.00018			
Total	0.00548	17				

SUMMARY

Groups	Count	Sum	Average	Variance
3 days	9	3.46139	0.3846	0.00019
7 days	9	4.911	0.54567	0.00015

ANOVA

Source of Variation	SS	df	MS	F	P-value	F crit
Between Groups	0.11674	1	0.11674	693.615	1.3E-14	4.494
Within Groups	0.00269	16	0.00017			
Total	0.11944	17				

Table A.3: MTT results for the PLA and nanocomposites after 3 days of incubation in term of optical density at wavelength of 570 nm

Sets	PLA	PLA-5wt% NHA	PLA-5wt% mNHA(APTES)	PLA-30wt% mNHA(APTES)	PLA-5wt%(mNHA-0.01wt%GNP)	PLA-5wt%(mNHA-0.1wt%GNP)
A	0.431755	0.461737	0.432123	0.450611	0.459682	0.447116
	0.452604	0.472718	0.454592	0.466876	0.473101	0.462869
	0.428588	0.475296	0.450228	0.461391	0.469486	0.461201
B	0.437869	0.400712	0.459635	0.480374	0.439615	0.441354
	0.439753	0.41032	0.466008	0.462659	0.459441	0.461158
	0.427106	0.480254	0.453665	0.463298	0.433178	0.453681
C	0.436952	0.461517	0.433424	0.444274	0.454605	0.421188
	0.457139	0.465171	0.4215	0.409644	0.458621	0.45032
	0.451834	0.465438	0.428948	0.444548	0.456661	0.43057
Average	**0.4404**	**0.454795889**	**0.444458111**	**0.453741667**	**0.456043333**	**0.447717444**
Standard deviation	**0.011008923**	**0.028738027**	**0.015640631**	**0.020123717**	**0.012739023**	**0.014461428**

Table A.4: MTT results for the PLA and nanocomposites after 5 days of incubation in term of optical density at wavelength of 570 nm

Sets	PLA	PLA-5wt% NHA	PLA-5wt% mNHA(APTES)	PLA-30wt% mNHA(APTES)	PLA-5wt%(mNHA-0.01wt%GNP)	PLA-5wt%(mNHA-0.1wt%GNP)
A	0.462278	0.733249	0.85251	0.844438	0.705194	0.739417
	0.472981	0.74247	0.870444	0.823556	0.719571	0.722841
	0.459876	0.749185	0.844869	0.855758	0.733937	0.755182
B	0.467336	0.727996	0.796367	0.832014	0.692252	0.846939
	0.469477	0.737732	0.806626	0.851696	0.684482	0.878241
	0.462424	0.719705	0.748633	0.835582	0.672726	0.862973
C	0.463281	0.757438	0.827225	0.769675	0.692276	0.767168
	0.467524	0.77952	0.814752	0.762334	0.625235	0.780289
	0.466745	0.784116	0.805642	0.780404	0.619269	0.731299
Average	0.465769111	0.747934556	0.818563111	0.817273	0.682771333	0.787149889
Standard deviation	0.004131344	0.022199913	0.03591293	0.036467716	0.038894006	0.059815497

Table A.5: MTT results for the PLA and nanocomposites after 7 days of incubation in term of optical density at wavelength of 570 nm

Sets	PLA	PLA-5wt% NHA	PLA-5wt% mNHA(APTES)	PLA-30wt% mNHA(APTES)	PLA-5wt%(mNHA-0.01wt%GNP)	PLA-5wt%(mNHA-0.1wt%GNP)
A	0.537623	1.06485	1.14617	0.989904	0.924062	1.06336
	0.53704	1.03878	1.12092	0.994048	0.911996	1.06648
	0.528539	1.01728	1.13091	0.999573	0.916208	1.07672
B	0.563726	1.07306	1.10199	1.12465	0.919376	1.02209
	0.555512	1.10776	1.10155	1.11644	0.932494	1.00522
	0.550299	1.13292	1.10996	1.10187	0.927849	1.0825
C	0.569643	1.03881	1.11617	0.960917	0.94246	1.05876
	0.571317	1.02602	1.12549	0.945949	0.921561	1.09387
	0.530156	1.02757	1.14821	0.948721	0.96378	1.05163
Average	0.549317222	1.058561111	1.118583333	1.054414167	0.928865111	1.052728333
Standard deviation	0.016697498	0.039850415	0.017653702	0.066099201	0.015926802	0.03149553

Table A.6: ANOVA analysis on the MTT results for the neat PLA after 3, 5 and 7 days of incubation in term of optical density at wavelength of 570 nm

SUMMARY

Groups	Count	Sum	Average	Variance
3 days	9	3.9636	0.4404	0.00012
5 days	9	4.19192	0.46577	1.7E-05

ANOVA

Source of Variation	SS	df	MS	F	P-value	F crit
Between Groups	0.0029	1	0.0029	41.8931	7.70E-06	4.494
Within Groups	0.00111	16	6.9E-05			
Total	0.004	17				

SUMMARY

Groups	Count	Sum	Average	Variance
5 days	9	4.19192	0.46577	1.7E-05
7 days	9	4.94386	0.54932	0.00028

ANOVA

Source of Variation	SS	df	MS	F	P-value	F crit
Between Groups	0.03141	1	0.03141	212.329	1.1791E-10	4.494
Within Groups	0.00237	16	0.00015			
Total	0.03378	17				

SUMMARY

Groups	Count	Sum	Average	Variance
3 days	9	3.9636	0.4404	0.00012
7 days	9	4.94386	0.54932	0.00028

ANOVA

Source of Variation	SS	df	MS	F	P-value	F crit
Between Groups	0.05338	1	0.05338	266.915	2.1087E-11	4.494
Within Groups	0.0032	16	0.0002			
Total	0.05658	17				

Table A.7: ANOVA analysis on the MTT results for the PLA-5wt%NHA after 3, 5 and 7 days of incubation in term of optical density at wavelength of 570 nm

SUMMARY

Groups	Count	Sum	Average	Variance
3 days	9	4.09316	0.4548	0.00083
5 days	9	6.73141	0.74793	0.00049

ANOVA

Source of Variation	SS	df	MS	F	P-value	F crit
Between Groups	0.38669	1	0.38669	586.461	4.9183E-14	4.494
Within Groups	0.01055	16	0.00066			
Total	0.39724	17				

SUMMARY

Groups	Count	Sum	Average	Variance
5 days	9	6.73141	0.74793	0.00049
7 days	9	9.52705	1.05856	0.00159

ANOVA

Source of Variation	SS	df	MS	F	P-value	F crit
Between Groups	0.4342	1	0.4342	417.321	6.8997E-13	4.494
Within Groups	0.01665	16	0.00104			
Total	0.45085	17				

SUMMARY

Groups	Count	Sum	Average	Variance
3 days	9	4.09316	0.4548	0.00083
7 days	9	9.52705	1.05856	0.00159

ANOVA

Source of Variation	SS	df	MS	F	P-value	F crit
Between Groups	1.6404	1	1.6404	1359.11	6.6316E-17	4.494
Within Groups	0.01931	16	0.00121			
Total	1.65971	17				

Table A.8: ANOVA analysis on the MTT results for the PLA-5wt%mNHA (APTES) after 3, 5 and 7 days of incubation in term of optical density at wavelength of 570 nm

SUMMARY

Groups	Count	Sum	Average	Variance
3 days	9	4.00012	0.44446	0.00024
5 days	9	7.36707	0.81856	0.00129

ANOVA

Source of Variation	SS	df	MS	F	P-value	F crit
Between Groups	0.6298	1	0.6298	820.918	3.5344E-15	4.494
Within Groups	0.01227	16	0.00077			
Total	0.64207	17				

SUMMARY

Groups	Count	Sum	Average	Variance
5 days	9	7.36707	0.81856	0.00129
7 days	9	10.1014	1.12237	0.0003

ANOVA

Source of Variation	SS	df	MS	F	P-value	F crit
Between Groups	0.41536	1	0.41536	524.188	1.17895E-13	4.494
Within Groups	0.01268	16	0.00079			
Total	0.42803	17				

SUMMARY

Groups	Count	Sum	Average	Variance
3 days	9	4.00012	0.44446	0.00024
7 days	9	10.1014	1.12237	0.0003

ANOVA

Source of Variation	SS	df	MS	F	P-value	F crit
Between Groups	2.06807	1	2.06807	7664.45	6.97214E-23	4.494
Within Groups	0.00432	16	0.00027			
Total	2.07238	17				

Table A.9: ANOVA analysis on the MTT results for the PLA-30wt%mNHA (APTES) after 3, 5 and 7 days of incubation in term of optical density at wavelength of 570 nm

SUMMARY

Groups	Count	Sum	Average	Variance
3 days	9	4.08368	0.45374	0.0004
5 days	9	7.35546	0.81727	0.00133

ANOVA

Source of Variation	SS	df	MS	F	P-value	F crit
Between Groups	0.5947	1	0.5947	685.586	1.45163E-14	4.494
Within Groups	0.01388	16	0.00087			
Total	0.60858	17				

SUMMARY

Groups	Count	Sum	Average	Variance
5 days	9	7.35546	0.81727	0.00133
7 days	9	9.18207	1.02023	0.00538

ANOVA

Source of Variation	SS	df	MS	F	P-value	F crit
Between Groups	0.18536	1	0.18536	55.2854	1.41417E-06	4.494
Within Groups	0.05365	16	0.00335			
Total	0.23901	17				

SUMMARY

Groups	Count	Sum	Average	Variance
3 days	9	4.08368	0.45374	0.0004
7 days	9	9.18207	1.02023	0.00538

ANOVA

Source of Variation	SS	df	MS	F	P-value	F crit
Between Groups	1.44409	1	1.44409	499.623	1.71189E-13	4.494
Within Groups	0.04625	16	0.00289			
Total	1.49034	17				

Table A.10: ANOVA analysis on the MTT results for the PLA-5wt%(mNHA-0.01wt%GNP) after 3, 5 and 7 days of incubation in term of optical density at wavelength of 570 nm

SUMMARY

Groups	Count	Sum	Average	Variance
3 days	9	4.10439	0.45604	0.00016
5 days	9	6.14494	0.68277	0.00151

ANOVA

Source of Variation	SS	df	MS	F	P-value	F crit
Between Groups	0.23133	1	0.23133	276.205	1.62705E-11	4.494
Within Groups	0.0134	16	0.00084			
Total	0.24473	17				

SUMMARY

Groups	Count	Sum	Average	Variance
5 days	9	6.14494	0.68277	0.00151
7 days	9	8.35979	0.92887	0.00025

ANOVA

Source of Variation	SS	df	MS	F	P-value	F crit
Between Groups	0.27253	1	0.27253	308.57	7.00375E-12	4.494
Within Groups	0.01413	16	0.00088			
Total	0.28666	17				

SUMMARY

Groups	Count	Sum	Average	Variance
3 days	9	4.10439	0.45604	0.00016
7 days	9	8.35979	0.92887	0.00025

ANOVA

Source of Variation	SS	df	MS	F	P-value	F crit
Between Groups	1.00602	1	1.00602	4837.27	2.74421E-21	4.494
Within Groups	0.00333	16	0.00021			
Total	1.00935	17				

Table A.11: ANOVA analysis on the MTT results for the PLA-5wt%(mNHA-0.1wt%GNP) after 3, 5 and 7 days of incubation in term of optical density at wavelength of 570 nm

SUMMARY

Groups	*Count*	*Sum*	*Average*	*Variance*
3 days	9	4.02946	0.44772	0.00021
5 days	9	7.08435	0.78715	0.00358

ANOVA

Source of Variation	*SS*	*df*	*MS*	*F*	*P-value*	*F crit*
Between Groups	0.51846	1	0.51846	273.811	1.73809E-11	4.494
Within Groups	0.0303	16	0.00189			
Total	0.54876	17				

SUMMARY

Groups	*Count*	*Sum*	*Average*	*Variance*
5 days	9	7.08435	0.78715	0.00358
7 days	9	9.52063	1.05785	0.00081

ANOVA

Source of Variation	*SS*	*df*	*MS*	*F*	*P-value*	*F crit*
Between Groups	0.32975	1	0.32975	150.41	1.49985E-09	4.494
Within Groups	0.03508	16	0.00219			
Total	0.36483	17				

SUMMARY

Groups	*Count*	*Sum*	*Average*	*Variance*
3 days	9	4.02946	0.44772	0.00021
7 days	9	9.52063	1.05785	0.00081

ANOVA

Source of Variation	*SS*	*df*	*MS*	*F*	*P-value*	*F crit*
Between Groups	1.67517	1	1.67517	3297.87	5.81172E-20	4.494
Within Groups	0.00813	16	0.00051			
Total	1.68329	17				

Table A.12: ANOVA analysis on the MTT results for the nanocomposites in comparison to the control and neat PLA after 3 days of incubation in term of optical density at wavelength of 570 nm

SUMMARY

Groups	Count	Sum	Average	Variance
Control	9	3.46139	0.384598889	0.000186
PLA	9	3.9636	0.4404	0.000121
PLA-5wt%NHA	9	4.093163	0.454795889	0.000826
PLA-5wt%mNHA(APTES)	9	4.000123	0.444458111	0.000245
PLA-30wt%mNHA(APTES)	9	4.083675	0.453741667	0.000405
PLA-5wt%(mNHA-0.01wt%GNP)	9	4.10439	0.456043333	0.000162
PLA-5wt%(mNHA-0.1wt%GNP)	9	4.029457	0.447717444	0.000209

ANOVA

Source of Variation	SS	df	MS	F	P-value	F crit
Between Groups	0.034322	6	0.005720365	18.58869	9.43E-12	2.265567
Within Groups	0.017233	56	0.000307734			
Total	0.051555	62				

SUMMARY

Groups	Count	Sum	Average	Variance
PLA	9	3.9636	0.4404	0.000121
PLA-5wt%NHA	9	4.093163	0.454795889	0.000826
PLA-5wt%mNHA(APTES)	9	4.000123	0.444458111	0.000245
PLA-30wt%mNHA(APTES)	9	4.083675	0.453741667	0.000405
PLA-5wt%(mNHA-0.01wt%GNP)	9	4.10439	0.456043333	0.000162
PLA-5wt%(mNHA-0.1wt%GNP)	9	4.029457	0.447717444	0.000209

ANOVA

Source of Variation	SS	df	MS	F	P-value	F crit
Between Groups	0.001802	5	0.000360463	1.098929	0.373377	2.408514
Within Groups	0.015745	48	0.000328013			
Total	0.017547	53				

Table A.13: ANOVA analysis on the MTT results for the nanocomposites in comparison to the control and neat PLA after 5 days of incubation in term of optical density at wavelength of 570 nm

SUMMARY

Groups	Count	Sum	Average	Variance
Control	9	4.691348	0.521261	0.0002
PLA	9	4.191922	0.465769	1.71E-05
PLA-5wt%NHA	9	6.731411	0.747935	0.000493
PLA-5wt%mNHA(APTES)	9	7.367068	0.818563	0.00129
PLA-30wt%mNHA(APTES)	9	7.355457	0.817273	0.00133
PLA-5wt%(mNHA-0.01wt%GNP)	9	6.144942	0.682771	0.001513
PLA-5wt%(mNHA-0.1wt%GNP)	9	7.084349	0.78715	0.003578

ANOVA

Source of Variation	SS	df	MS	F	P-value	F crit
Between Groups	1.118787	6	0.186464	155.0186	5.11E-33	2.265567
Within Groups	0.06736	56	0.001203			
Total	1.186146	62				

SUMMARY

Groups	Count	Sum	Average	Variance
PLA	9	4.191922	0.465769	1.71E-05
PLA-5wt%NHA	9	6.731411	0.747935	0.000493
PLA-5wt%mNHA(APTES)	9	7.367068	0.818563	0.00129
PLA-30wt%mNHA(APTES)	9	7.355457	0.817273	0.00133
PLA-5wt%(mNHA-0.01wt%GNP)	9	6.144942	0.682771	0.001513
PLA-5wt%(mNHA-0.1wt%GNP)	9	7.084349	0.78715	0.003578

ANOVA

Source of Variation	SS	df	MS	F	P-value	F crit
Between Groups	0.814369	5	0.162874	118.8835	7.82E-26	2.408514
Within Groups	0.065761	48	0.00137			
Total	0.88013	53				

Table A.14: ANOVA analysis on the MTT results for the nanocomposites in comparison to the control and neat PLA after 7 days of incubation in term of optical density at wavelength of 570 nm

SUMMARY

Groups	Count	Sum	Average	Variance
Control	9	4.691348	0.521261	0.0002
PLA	9	4.191922	0.465769	1.71E-05
PLA-5wt%NHA	9	6.731411	0.747935	0.000493
PLA-5wt%mNHA(APTES)	9	7.367068	0.818563	0.00129
PLA-30wt%mNHA(APTES)	9	7.355457	0.817273	0.00133
PLA-5wt%(mNHA-0.01wt%GNP)	9	6.144942	0.682771	0.001513
PLA-5wt%(mNHA-0.1wt%GNP)	9	7.084349	0.78715	0.003578

ANOVA

Source of Variation	SS	df	MS	F	P-value	F crit
Between Groups	1.118787	6	0.186464	155.0186	5.11E-33	2.265567389
Within Groups	0.06736	56	0.001203			
Total	1.186146	62				

SUMMARY

Groups	Count	Sum	Average	Variance
PLA	9	4.191922	0.465769	1.71E-05
PLA-5wt%NHA	9	6.731411	0.747935	0.000493
PLA-5wt%mNHA(APTES)	9	7.367068	0.818563	0.00129
PLA-30wt%mNHA(APTES)	9	7.355457	0.817273	0.00133
PLA-5wt%(mNHA-0.01wt%GNP)	9	6.144942	0.682771	0.001513
PLA-5wt%(mNHA-0.1wt%GNP)	9	7.084349	0.78715	0.003578

ANOVA

Source of Variation	SS	df	MS	F	P-value	F crit
Between Groups	0.814369	5	0.162874	118.8835	7.82E-26	2.408514119
Within Groups	0.065761	48	0.00137			
Total	0.88013	53				

Table A.15: ALP results for the PLA and nanocomposites after 7 days of incubation in term of optical density at wavelength of 405 nm

Sets	PLA	PLA-5wt% NHA	PLA-5wt% mNHA(APTES)	PLA-30wt% mNHA(APTES)	PLA-5wt%(mNHA-0.01wt%GNP)	PLA-5wt%(mNHA-0.1wt%GNP)
A	0.191861	0.190747	0.184528	0.195818	0.182842	0.185727
	0.200886	0.189184	0.181309	0.194947	0.181461	0.188301
	0.201988	0.190015	0.182253	0.200396	0.182287	0.202559
B	0.187397	0.187183	0.182198	0.187941	0.187607	0.195127
	0.186587	0.182172	0.18337	0.176493	0.196115	0.199473
	0.184768	0.188025	0.18356	0.179574	0.192517	0.205462
Average	**0.18638**	**0.18573**	**0.18296**	**0.18526**	**0.18779**	**0.18954**
Standard deviation	**0.00759**	**0.00329**	**0.00448**	**0.00577**	**0.00625**	**0.00756**

Table A.16: ALP results for the PLA and nanocomposites after 14 days of incubation in term of optical density at wavelength of 405 nm

Sets	PLA	PLA-5wt% NHA	PLA-5wt% mNHA(APTES)	PLA-30wt% mNHA(APTES)	PLA-5wt%(mNHA-0.01wt%GNP)	PLA-5wt%(mNHA-0.1wt%GNP)
A	0.221321	0.219715	0.218827	0.223535	0.211964	0.200171
	0.221737	0.222861	0.21711	0.228201	0.20465	0.204962
	0.218918	0.226203	0.222056	0.226999	0.21504	0.207421
B	0.215456	0.223273	0.225885	0.226045	0.221612	0.217922
	0.229198	0.216041	0.232645	0.233964	0.224924	0.217678
	0.238776	0.224859	0.233753	0.238951	0.211447	0.215533
Average	**0.22423**	**0.22216**	**0.22505**	**0.22962**	**0.21494**	**0.21061**
Standard deviation	**0.00844**	**0.00371**	**0.007**	**0.00574**	**0.00736**	**0.00747**

Table A.17: ALP results for the PLA and nanocomposites after 21 days of incubation in term of optical density at wavelength of 405 nm

Sets	PLA	PLA-5wt% NHA	PLA-5wt% mNHA(APTES)	PLA-30wt% mNHA(APTES)	PLA-5wt%(mNHA-0.01wt%GNP)	PLA-5wt%(mNHA-0.1wt%GNP)
A	0.229448	0.231036	0.256679	0.227892	0.227464	0.233408
	0.225269	0.226479	0.256572	0.223713	0.21884	0.21567
	0.225515	0.229267	0.261371	0.222161	0.219451	0.215243
B	0.221742	0.233463	0.247979	0.221364	0.224807	0.227498
	0.222609	0.226422	0.249662	0.218325	0.221798	0.224499
	0.223406	0.239924	0.267148	0.231214	0.225121	0.229699
Average	0.22466	0.2311	0.25657	0.22411	0.22291	0.22434
Standard deviation	0.00277	0.0051	0.00716	0.00468	0.00343	0.00747

Table A.18: ALP results for the PLA and nanocomposites after 28 days of incubation in term of optical density at wavelength of 405 nm

Sets	PLA	PLA-5wt% NHA	PLA-5wt% mNHA(APTES)	PLA-30wt% mNHA(APTES)	PLA-5wt%(mNHA-0.01wt%GNP)	PLA-5wt%(mNHA-0.1wt%GNP)
A	0.212409	0.200044	0.203313	0.199856	0.204694	0.201174
	0.218342	0.20041	0.203368	0.204301	0.193216	0.188394
	0.217883	0.199388	0.199927	0.200661	0.19644	0.192282
B	0.200012	0.21291	0.20173	0.195163	0.205414	0.19342
	0.201711	0.205106	0.205164	0.198748	0.207774	0.197232
	0.203919	0.206266	0.201775	0.197121	0.204119	0.195941
Average	**0.20739**	**0.19933**	**0.19649**	**0.19487**	**0.20011**	**0.19793**
Standard deviation	**0.00732**	**0.00642**	**0.00261**	**0.00222**	**0.00565**	**0.00323**

Table A.19: ANOVA analysis on the ALP results for the nanocomposites in comparison to the control and neat PLA after 7 days of incubation in term of optical density at wavelength of 405 nm

SUMMARY

Groups	Count	Sum	Average	Variance
Control	6	1.321121	0.220187	2.79E-05
PLA	6	1.173487	0.195581	6.19E-05
PLA-5wt%NHA	6	1.127326	0.187888	9.51E-06
PLA-5wt%mNHA(APTES)	6	1.157218	0.19287	1.35E-06
PLA-30wt%mNHA(APTES)	6	1.135169	0.189195	9.16E-05
PLA-5wt%(mNHA-0.01wt%GNP)	6	1.122829	0.187138	3.68E-05
PLA-5wt%(mNHA-0.1wt%GNP)	6	1.176649	0.196108	6.2E-05

ANOVA

Source of Variation	SS	df	MS	F	P-value	F crit
Between Groups	0.004706	6	0.000784	18.86152	1.17E-09	2.371781
Within Groups	0.001455	35	4.16E-05			
Total	0.006161	41				

SUMMARY

Groups	Count	Sum	Average	Variance
PLA	6	1.173487	0.195581	6.19E-05
PLA-5wt%NHA	6	1.127326	0.187888	9.51E-06
PLA-5wt%mNHA(APTES)	6	1.157218	0.19287	1.35E-06
PLA-30wt%mNHA(APTES)	6	1.135169	0.189195	9.16E-05
PLA-5wt%(mNHA-0.01wt%GNP)	6	1.122829	0.187138	3.68E-05
PLA-5wt%(mNHA-0.1wt%GNP)	6	1.176649	0.196108	6.2E-05

ANOVA

Source of Variation	SS	df	MS	F	P-value	F crit
Between Groups	0.000463	5	9.26E-05	2.110398	0.091587	2.533555
Within Groups	0.001316	30	4.39E-05			
Total	0.001779	35				

Table A.20: ANOVA analysis on the ALP results for the nanocomposites in comparison to the control and neat PLA after 14 days of incubation in term of optical density at wavelength of 405 nm

SUMMARY

Groups	Count	Sum	Average	Variance
Control	6	6	1.499049	0.249842
PLA	6	6	1.345406	0.224234
PLA-5wt%NHA	6	6	1.332952	0.222159
PLA-5wt%mNHA(APTES)	6	6	1.350276	0.225046
PLA-30wt%mNHA(APTES)	6	6	1.377695	0.229616
PLA-5wt%(mNHA-0.01wt%GNP)	6	6	1.289637	0.21494
PLA-5wt%(mNHA-0.1wt%GNP)	6	6	1.263687	0.210615

ANOVA

Source of Variation	SS	df	MS	F	P-value	F crit
Between Groups	0.00573	6	0.000955	21.6034	1.97E-10	2.371781
Within Groups	0.001547	35	4.42E-05			
Total	0.007277	41				

SUMMARY

Groups	Count	Sum	Average	Variance
PLA	6	1.345406	0.224234	7.12E-05
PLA-5wt%NHA	6	1.332952	0.222159	1.38E-05
PLA-5wt%mNHA(APTES)	6	1.350276	0.225046	4.9E-05
PLA-30wt%mNHA(APTES)	6	1.377695	0.229616	3.29E-05
PLA-5wt%(mNHA-0.01wt%GNP)	6	1.289637	0.21494	5.42E-05
PLA-5wt%(mNHA-0.1wt%GNP)	6	1.263687	0.210615	5.57E-05

ANOVA

Source of Variation	SS	df	MS	F	P-value	F crit
Between Groups	0.001482	5	0.000296	6.421902	0.000363	2.533555
Within Groups	0.001384	30	4.61E-05			
Total	0.002866	35				

Table A.21: ANOVA analysis on the ALP results for the nanocomposites in comparison to the control and neat PLA after 21 days of incubation in term of optical density at wavelength of 405 nm

SUMMARY

Groups	Count	Sum	Average	Variance
Control	6	1.457733	0.242956	7.52E-05
PLA	6	1.347989	0.224665	7.66E-06
PLA-5wt%NHA	6	1.386591	0.231099	2.6E-05
PLA-5wt%mNHA(APTES)	6	1.539411	0.256569	5.13E-05
PLA-30wt%mNHA(APTES)	6	1.344669	0.224112	2.19E-05
PLA-5wt%(mNHA-0.01wt%GNP)	6	1.337481	0.222914	1.18E-05
PLA-5wt%(mNHA-0.1wt%GNP)	6	1.346017	0.224336	5.58E-05

ANOVA

Source of Variation	SS	df	MS	F	P-value	F crit
Between Groups	0.005885	6	0.000981	27.49192	7.15E-12	2.371781
Within Groups	0.001249	35	3.57E-05			
Total	0.007133	41				

SUMMARY

Groups	Count	Sum	Average	Variance
PLA	6	1.347989	0.224665	7.66E-06
PLA-5wt%NHA	6	1.386591	0.231099	2.6E-05
PLA-5wt%mNHA(APTES)	6	1.539411	0.256569	5.13E-05
PLA-30wt%mNHA(APTES)	6	1.344669	0.224112	2.19E-05
PLA-5wt%(mNHA-0.01wt%GNP)	6	1.337481	0.222914	1.18E-05
PLA-5wt%(mNHA-0.1wt%GNP)	6	1.346017	0.224336	5.58E-05

ANOVA

Source of Variation	SS	df	MS	F	P-value	F crit
Between Groups	0.005102	5	0.00102	35.08435	1.16E-11	2.533555
Within Groups	0.000872	30	2.91E-05			
Total	0.005974	35				

Table A.22: ANOVA analysis on the ALP results for the nanocomposites in comparison to the control and neat PLA after 28 days of incubation in term of optical density at wavelength of 405 nm

SUMMARY

Groups	Count	Sum	Average	Variance
Control	6	1.382921	0.230487	2.78E-05
PLA	6	1.254276	0.209046	6.75E-05
PLA-5wt%NHA	6	1.224124	0.204021	2.71E-05
PLA-5wt%mNHA(APTES)	6	1.215277	0.202546	3.25E-06
PLA-30wt%mNHA(APTES)	6	1.19585	0.199308	9.87E-06
PLA-5wt%(mNHA-0.01wt%GNP)	6	1.211657	0.201943	3.3E-05
PLA-5wt%(mNHA-0.1wt%GNP)	6	1.168443	0.194741	1.94E-05

ANOVA

Source of Variation	SS	df	MS	F	P-value	F crit
Between Groups	0.004876	6	0.000813	30.27548	1.81E-12	2.371781
Within Groups	0.00094	35	2.68E-05			
Total	0.005816	41				

SUMMARY

Groups	Count	Sum	Average	Variance
PLA	6	1.254276	0.209046	6.75E-05
PLA-5wt%NHA	6	1.224124	0.204021	2.71E-05
PLA-5wt%mNHA(APTES)	6	1.215277	0.202546	3.25E-06
PLA-30wt%mNHA(APTES)	6	1.19585	0.199308	9.87E-06
PLA-5wt%(mNHA-0.01wt%GNP)	6	1.211657	0.201943	3.3E-05
PLA-5wt%(mNHA-0.1wt%GNP)	6	1.168443	0.194741	1.94E-05

ANOVA

Source of Variation	SS	df	MS	F	P-value	F crit
Between Groups	0.000684	5	0.000137	5.124251	0.001631	2.533555
Within Groups	0.000801	30	2.67E-05			
Total	0.001484	35				
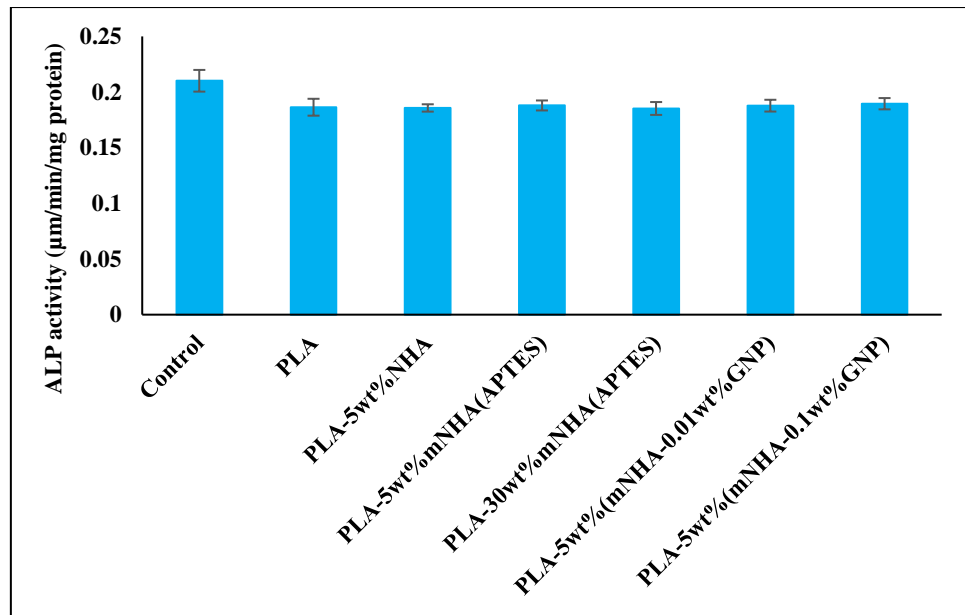
(a)
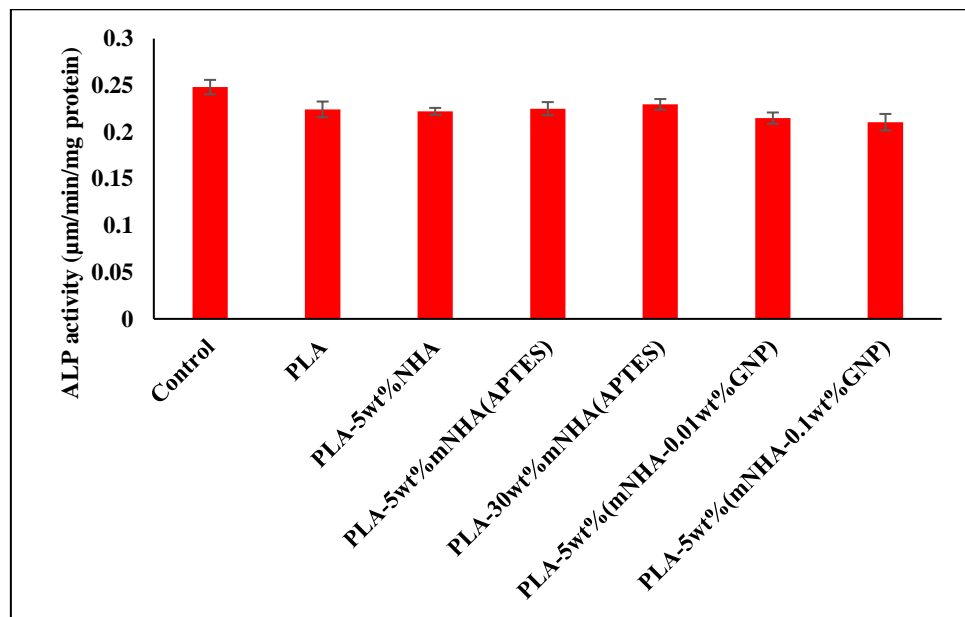
(b)
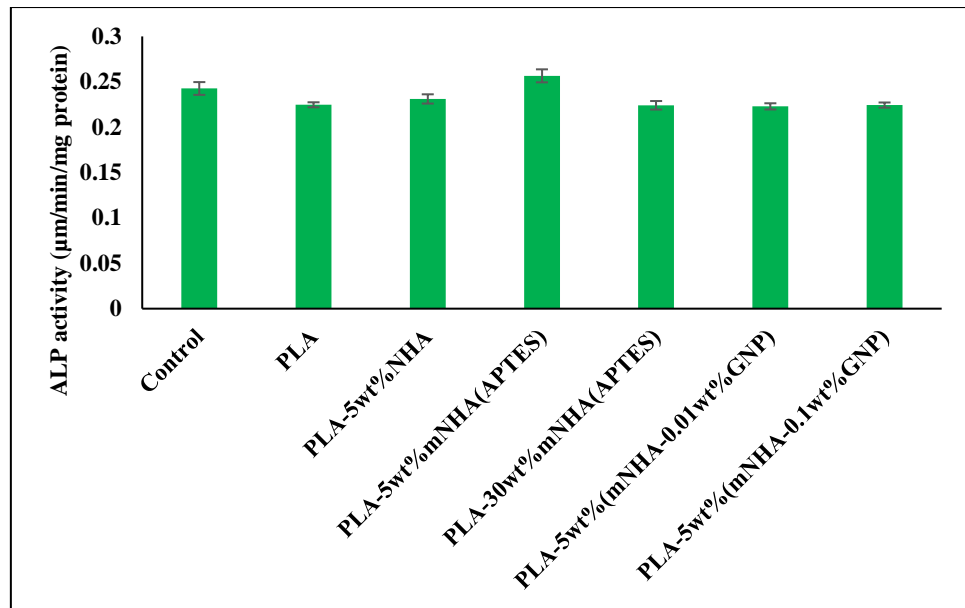
(c)

(d)

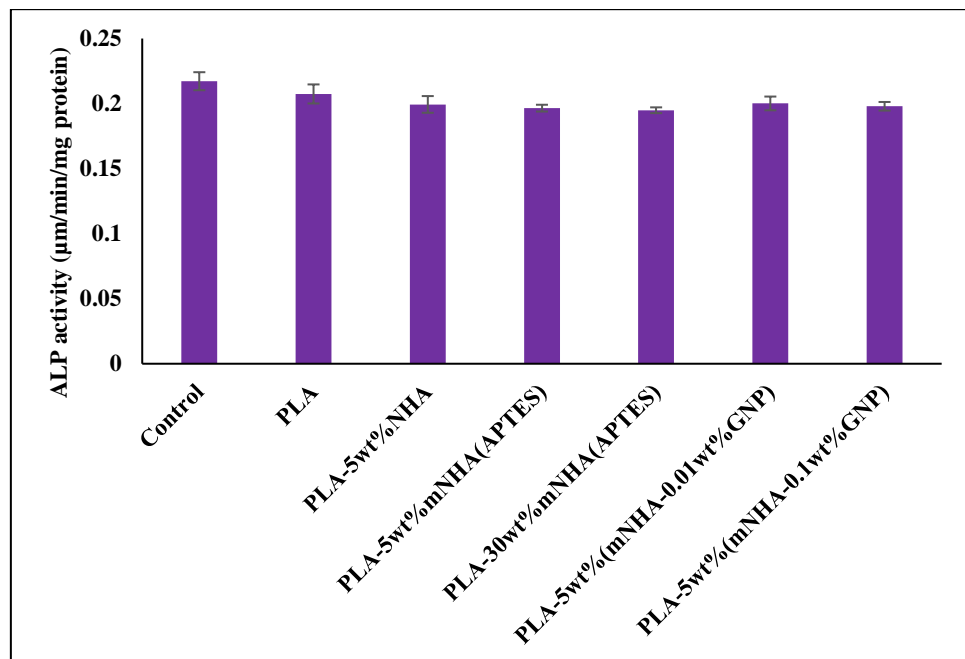**Figure A.3:** ALP analysis of the nanocomposites cultured after (a) 7 days, (b) 14 days, (c) 21 days and (d) 28 days